Flow through and over model porous media with or without inertial effects

By

James Kofi Arthur

A thesis submitted to the Faculty of Graduate Studies of
The University of Manitoba
In partial fulfilment of the requirements for the degree of

DOCTOR OF PHILOSOPHY

Department of Mechanical and Manufacturing Engineering
University of Manitoba
Winnipeg

Abstract

An experimental research program was designed to study laminar flows through and over models of porous media with or without inertial effects. The models used were made up of circular or square rods arranged to cover solid volume fraction ϕ ranging from 0.03 to 0.49, and filling fraction h / H ranging from 0.34 to 1 of the test channel. In this way, the ratios of the depth of the test section to the porous medium pore H / l ranged from 5.75 to 18.25. Three types of model porous media were tested: (1) two-dimensional 'horizontal' models, having rod axes aligned along the span of the channel in a staggered or non-staggered fashion; (2) three-dimensional 'vertical' models with rod axes aligned in the transverse direction; and (3) three-dimensional 'mesh' models with rod axes aligned along both transverse and spanwise directions. Using a pressure-driven viscous fluid, the bulk Reynolds number Re_{bulk} was varied from 0.1 to 10.3. Velocity measurements were obtained using particle image velocimetry at various streamwise-transverse planes of the test section. Differential pressure measurements were also obtained using electronic transducers. These measurements were used to determine relevant governing equations for the flow through the porous media; to characterize the effects of ϕ, rod shape and arrangement, h / H, H / l, porous media dimensionality, and Re_{bulk} on the flow; and to predict the flow at the porous medium-free flow interface.

The Izbash and quadratic Forchheimer equations were respectively found to describe well the flow through two- and three-dimensional porous media. Penetration of the free

flow into the porous medium varied with ϕ and rod arrangement, but was nearly independent of the rod shape. At the interface between the porous medium and the free flow, h / H and H / l effects were found to be counteractive. Penetration was highest for the vertical models compared with the mesh and horizontal models. Inertial dependence of interfacial flow was weak when porous medium conditions were considered. The interfacial flow was found to follow a dose response formulation with a predictable slip coefficient.

.

Acknowledgments

My utmost gratitude is to my LORD and my God, for every blessing and help in every way. I could not do anything without Him.

To Prof. D. W. Ruth and Prof. M. F. Tachie, my supervisors, I extend my profound appreciation for their professional guidance and mentoring throughout this research program. I am also indebted to the National Science and Engineering Research Council, Canada Foundation for Innovation, and the University of Manitoba for their financial support in diverse ways. I would also like to thank Prof. D. F. James, Prof. D. C. S. Kuhn and Dr. S. P. Clark for being part of my examining committee.

The contributions of the following people are additionally acknowledged with profound gratitude: Lucy and John Arthur for their kind support through my studies; Erwin Penner, John Finken and Paul Krueger for their technical assistance; and Dr. Kofi Adane for his initial contribution in developing the MATLAB script used in the calculation of averages of the velocity data.

Dedication

To my darling wife Dalen .....my precious son Isaac......and my dear mother Esther...

Contents

List of Tables

List of Figures

List of Symbols

ENGLISH SYMBOLS

a	Specific area, empirical constant, input image
a_1	Empirical constant
A	Area, fast Fourier transform functions
b	Empirical constant, image transfer function
b_1	Empirical constant
B	Bias limit
c	Constant, noise function
c_1	Empirical constant
C	Number of particles per unit fluid volume
d	Mean particle diameter, diameter of rod
d_1	Empirical constant
D	Fast Fourier transform function
Dp	Depth to porous medium pore ratio
E	Total uncertainty
e	Empirical constant
F	Empirical constant
e_1	Empirical constant

f_{f1}	Friction factor = $d/(2\rho_f U_d^2)(-dP_f/dx)$
f_{f2}	Friction factor = $d/(\rho_f U_d^2)\ (-dP_f/dx)$
f_{f2}	Friction factor =$\sqrt{k}/(\rho_f U_d^2)\ (-dP_f/dx)$
ff	Filling fraction
$f_{\#}$	Diaphragm aperture
g, g_1	Empirical constant
G	Empirical constant
G	Pressure Drop
h	Bed, porous medium or manometric height, empirical constant
h_1	Empirical constant
h_f	Depth of the channel of free flow
H	Total depth of test section
i_1	Empirical constant
I	Interrogation window size
k	Specific permeability, hydraulic conduction coefficient
K	Confidence coefficient
$\mathbf{K}$	Second-order permeability tensor
l	Spacing between adjacent rod centers
L	Length scale, channel length
Lo	Resolutions of the image
L_I	Charged camera device camera chip
m	Output image coordinate in streamwise direction
M	Mesh, image magnification

n	Output image coordinate in transverse direction, experimental rounds
n	Number of experimental rounds
N	Sample size
p	Microscopic pressure
P	Average pressure, precision limit
P_f	Intrinsic pressure
Q	Volumetric flow rate
r	Radius of rod
R	Multi-component parameter
R^2	Adjusted coefficient of determination for data
R^2_d	Adjusted coefficient of determination for non-dimensionalized data
Re	Reynolds number = UL/ν
Re_{bulk}	Bulk Reynolds number = Ud/ν or Us/ν
Re_{BL}	Modified Reynolds number = $U_d\, d/(\phi\nu)$
Re_d	Particle Reynolds number = $U_d\, d/\nu$
Re_i	Interstitial Reynolds number = $U_d\, d/(\varepsilon\nu)$
Re_k	Modified Reynolds number = $U_d \sqrt{k}/\nu$
Re_{pore}	Pore Reynolds number = $4\rho U_d \tau / (a_{vd}\, \mu(1\text{-}\varepsilon))$
Rd	Round
s	Side of square rod, displacement
Sq	Square
x	Streamwise direction
y, Y	Transverse direction

z	Spanwise direction
St	Staggered
S	Object to image scale factor
t	Time
u	Microscopic velocity in streamwise direction, total uncertainty
u	Coordinate in streamwise direction
$\mathbf{u}$	Three-dimensional microscopic velocity vector
U	Averaged velocity in streamwise direction, velocity scale
U_d	Darcy velocity
$\mathbf{U}$	Three-dimensional average velocity vector
$\mathbf{U}_f$	Three-dimensional intrinsic average velocity vector
$\mathbf{U}_{fs}$	Three-dimensional superficial average velocity vector
v	Microscopic velocity in transverse direction
v	Coordinate in transverse direction
V	Averaged velocity in transverse direction
w	Microscopic velocity in spanwise direction
W	Averaged velocity in spanwise direction, span of channel

GREEK SYMBOLS

α	Slip coefficient
β	Inertial (non-Darcy flow) coefficient
β_1	Empirical coefficient in boundary condition
β_2	Empirical coefficient in boundary condition

β_3	Empirical coefficient in boundary condition
δ	Transition layer thickness
δ_1	Transition layer thickness within the porous medium
∇	Gradient, displacement
ε	Porosity
ϕ	Solid volume fraction
ϕ_{ad}	Correlation function
Φ_{ad}	Coefficient function
$\dot{\gamma}$	Shear rate at interface
λ	Laser light wavelength
μ	Fluid dynamic viscosity
μ'	Apparent (Brinkman) viscosity
v	Kinematic viscosity
ρ_f	Fluid density
θ	Sensitivity coefficient
σ	Standard deviation of the measurements
τ	Dimensionless parameter, tortuosity, time
ψ	Microscopic quantity
Ψ	Averaged quantity

SUBSCRIPT

-	In the free zone
+	In the porous medium

a	Area average
BL	Blake
Bulk	Bulk
cr	Critical
d	Darcy
f	Intrinsic, Forchheimer, drag form
fs	Superficial
h	Empirical constant ranging from 1 to 2
f	Fluid
h	Horizontal
i	Interstitial
l	Line average
m	Mesh
max	Maximum
min	Minimum
p, part	Particle
pore	Pore
ΔP	Average differential pressure
r	Relative
R	Response
rev	Representative elementary volume
s	Slip
u	Streamwise velocity

v	Vertical, volume average, transverse velocity
x	Streamwise direction
y	Transverse direction

ACRONYMS

CCD	Charged coupled device
CTB	Cantor Taylor brush configuration
DPR	Ratio of test section depth to porous medium pore ratio (H / l)
F-C	Forchheimer cubic equation
FFT	Fast Fourier transforms
F-Q	Forchheimer quadratic equation
IA	Interrogation area
LDA	Laser Doppler anemometry
MBE	Modified Brinkman equation
Nd-YAG	Neodymium: yttrium-aluminium-garnet
PIV	Particle image velocimetry
REV	Representative elementary volume

List of Appendices

Chapter 1

Introduction

1.1 Overview

Flow through and over porous media has essential bearing on many engineering applications. Examples of these are groundwater hydrology, oil and gas exploration, permeable reactive barriers, binary alloy solidifications, and filtration technology.

While porous media flow phenomena are largely laminar in nature, they are typically conducted through tortuous paths of interconnected voids in complex networks of solid matrices. As a result, these flows are inherently complicated, and are still subject to many unresolved fundamental questions. Notable amongst these questions are the constitutive equations that govern the flow at the regime where the effects of inertia become significant. In cases where there is an adjoining free (or open) parallel flow, an additional difficulty that is presented is the proper definition of boundary conditions at the interface between the porous medium and the open flow. As these issues are still analytically and numerically formidable, there is a pressing demand for experimental studies to serve as a basis for further understanding of the underlying physics involved. This work therefore seeks to use an experimental approach to provide insights to help resolve these outstanding concerns pertaining to laminar flows through and over porous media (with or without inertial effects).

It is important to note that even though porous media flows are often multi-phase and may be compressible, and some may be driven by shear, this study is limited to single-phase, incompressible, pressure-driven flows. The insights gained from this single-phase consideration will nonetheless serve as a foundational knowledge base for multi-phase flow studies. It should also be pointed out that the regimes of porous media flow presently under consideration include the range in which inertial effects just become apparent, but for which the conditions of flow are still steady. This limitation has been put in place so that the issue of the onset of inertial effects can be specially tackled. Furthermore, as the focus of this study is to present experimental evidence for cases which lend themselves to analytical and numerical simulations, the porous media utilized are only models of real porous media. That, notwithstanding, the standard methods of averaging analysis applied in natural porous media still do hold as for real porous media.

The purpose of this introductory chapter is to provide brief background information to the problem at hand. To do this, basic descriptions of equations, notations and conventional approaches to the problem are given. This is followed by an outline of the objectives and scope of the study, and a description of the structure of the thesis.

1.2 Terms, Notations and Equations

In this section, some key terms, concepts, notations and equations used in the thesis are defined.

1.2.1 Flow through Porous Media

A porous medium may be defined as a material made up of a solid matrix with interconnected voids or pores (Nield and Bejan 2006). Such a material ranges from naturally occurring substances such as soils, granular crushed rocks, and mammalian hair, to fabrications such as cigarettes, filters and wire-crimps. The present study is limited to porous media that are rigid (*i.e.*, not moving), and that for which the flows through and over them are not affected by gravity.

Flow through porous media is of considerable interest in many natural and industrial areas. Examples include the flow of hydrocarbons in oil wells, groundwater flows through beds of rocks, as well as the transport of minerals and contaminants through the ground. One may also find this flow phenomenon directly relevant in gaseous or aqueous catalytic and inert packed bed reactors, flows through screens in filters, geothermal heat management, melting or solidification of binary alloys, trapping of soot in automobile emissions, heat exchanger technologies, and in lubrication.

There are a number of terms that are commonly used to describe porous media. One such term is the 'porosity', hereafter signified by ε. Porosity is defined as the fraction of the porous media volume occupied by voids. A complementary term of ε is the solid volume fraction, hereafter signified by ϕ. This is defined as the fraction of the porous medium occupied by the solid matrix. Solid volume fraction is therefore equivalent to (1-ε). In this thesis, frequent reference to porosity and solid volume fractions will be made to characterize the pore structure of porous media.

1.2.1.1. The Continuum Approach

The detailed solution of porous media flow is a formidable task. Even with the most sophisticated computing technique, direct numerical simulations of the micro-scale flow equations within the pores are hardly possible without first allowing for a great deal of simplification of the porous media structure at hand (Breugem 2004; Nield and Bejan 2006). Due to the complex structure of typical porous media, numerical simulations are usually limited to methods using simplified boundary conditions or methods premised on a conceptual continuum model so that the behaviour of the flow on a large (average) scale can be considered with spatially averaged Navier-Stokes equations (Whitaker 1999; Breugem 2004). Considering computational cost and realism, the latter method (which will hereafter be referred to as the 'continuum approach') is the more preferred option.

One of the advantages of the continuum approach is that it accounts for the wide range of length and time scales that are present in porous media flows. This approach is usually achieved by two averaging methods, namely spatial averaging, or statistical averaging. The present study limits its consideration to averaged quantities obtained by the spatial averaging method as that can be used readily without extra assumptions of statistical homogeneity. Nonetheless, the two methods yield equivalent flow quantities if the spatially averaged relationships are those of primary interest (Nield and Bejan 2006), as is the case in this study.

The resulting quantities of interest in a spatial averaging are those averaged over sufficient areas of pores that show changes only in a regular manner in spatial and temporal coordinates. When this is done, the flow is assumed to be following these averaged measurements over the sample. Spatial averaging yields averaged flow quantities over a representative elementary volume (REV) having length scales that are much larger than the scales at the pore level, and at the same time much smaller than those at the averaged scale of the total sample under investigation. This REV ought to be sufficiently large that the flow quantity computed is the value at its centroid (Nield and Bejan 2006). Thus, the average obtained is not dependent on the size of the volume element. In a single-phase porous media flow, the total volume of an REV is given by the sum of the volume occupied by the fluid and the volume occupied by the solid matrix.

In this thesis, all microscopic (pore-level) quantities will be denominated by lower case letters, and the corresponding averaged flow quantities by upper case letters. Thus, for example, in a Cartesian frame of reference, the components of microscopic velocity in the streamwise (x), transverse (y) and spanwise (w) directions are hereafter signified respectively by u, v, and w, and the corresponding averaged components by U, V, and W respectively. Microscopic and averaged pressures are also represented by p and P respectively.

1.2.1.2. The Onset of Inertia and Related Problems

Using spatial averaging in porous medium flow, the microscopic flow quantities in a finite microscopic elemental volume can be related to their respective averaged quantities in a defined REV by a superficial averaging method, or an intrinsic averaging method. In the superficial averaging method, a quantity Ψ_{fs} is obtained by averaging the respective microscopic quantity ψ in a volume element, over the entire elemental volume made up of fluid and solid parts. The averaged velocity obtained by this means is called the 'superficial velocity', $\mathbf{U}_{fs}$ (alternative terms for this velocity are: seepage velocity, volumetric flux density, and filtration velocity; Nield and Bejan 2006). The second kind of spatial averaging, called intrinsic averaging, is done by averaging all microscopic quantities only over the volume of the fluid of the volume element. The velocity obtained by this means is the 'intrinsic velocity', $\mathbf{U}_f$. In a Cartesian frame of reference the components of the porous media superficial velocity in the *x*, *y*, and *z* directions are hereafter signified respectively by U_{fs}, V_{fs}, and W_{fs}. Similarly, those of the intrinsic velocity in the *x*, *y*, and *z* directions are hereafter signified respectively by U_f, V_f, and W_f.

Using the continuum approach for a steady-state fluid flow of fluid density ρ_f, differential equations related to the continuity equation, and averaged momentum equations may be obtained (Whitaker 1996), and solved numerically using appropriate boundary conditions for whatever model of REV chosen. The results may then be validated using the empirical Darcy Law, which is known to be the constitutive equation that applies at a sufficiently low flow rate, if body forces are assumed to be negligible in the flow (Balhoff and Wheeler 2009). The Darcy Law may be written as (Nield and Bejan 2006)

$$\frac{1}{\mu}\mathbf{K}\cdot\nabla\mathbf{P}_f = \mathbf{U}_{fs} \tag{1.1}$$

where $\nabla\mathbf{P}_f$ is the applied pressure gradient across the porous medium, μ is the fluid dynamic viscosity, and $\mathbf{K}$ is a second-order permeability tensor. In an isotropic medium, the permeability is scalar, and the tensor $\mathbf{K}$ can be replaced by k, called the 'specific permeability' or 'Darcy permeability'. For such a medium in which the vector $\mathbf{U}_{fs}$ and the pressure gradient $\nabla\mathbf{P}_f$ are parallel along the stream, Darcy's law can be expressed as

$$-\frac{dP_f}{dx} = \mu\frac{U_d}{k} \tag{1.2}$$

where $-dP_f/dx$ is a constant gradient of the streamwise pressure drop, and U_d is a constant superficial streamwise Darcy velocity.

Although the Darcy law is generally accepted to govern porous media flow, it does not cover all the practical ranges of flow in porous media. As a result, areas of application such as those near well bores, fractures and tight screens of cryogenic propellant tanks, where seepage velocities are relatively high, may not be adequately modeled using the Darcy law. As seepage velocities increase, a gradual transition occurs, resulting in a flow in which the relationship between the averaged velocity and the pressure gradient is no longer linear. In this case inertia is no longer negligible, and has to be accounted for in the flow description.

To account for this non-linearity, a number of formulations have been suggested. The quadratic extension first proposed by Forchheimer (1901) is one of the most widely used. This equation, expressed in terms of Equation (1.2) is (Fourar *et al*. 2004)

$$-\frac{dP_f}{dx} = \frac{\mu}{k_f}U_d + (\beta\rho_f{U_d}^2) \tag{1.3}$$

where k_f is the equivalent Forchheimer permeability, and β is an inertial (non-Darcy flow) coefficient whose values are obtained through experimentation.

While this quadratic equation appears to have worked well for many inertial flows, its uniqueness in describing the inertial regime has been questioned (Ruth and Ma 1992). Furthermore, it has been found not to be universal in the inertial range, particularly at the onset of inertia, and in the regime where the inertial range approaches unsteady flow. Some researchers (*e.g.* Firdaous *et al.* 1997) have therefore proposed that the on-set of non-linearity be better represented by the following cubic law:

$$-\frac{dP_f}{dx} = \frac{\mu}{k} U_d + \left(\frac{\tau \rho_f^{\ 2}}{\mu} U_d^{\ 3}\right) \tag{1.4}$$

where τ is a dimensionless parameter. Between Equations (1.3) and (1.4), there has been a raging debate as to which of these equations is more representative of the flow phenomenon. While some efforts have been directed towards reconciling these problems, uncertainties still remain regarding the particular conditions (such as flow dimensions and porous media arrangement) under which the equations accurately apply. As a result, numerical modellers of such flow regimes are left to decide which model would be used in validating their results. This makes the provision of further benchmark experimental data a necessity.

1.2.2 Flow over Porous Media

As for flow through porous media, flow over porous media is also of essential value in a number of engineering applications. Applications include flows over river beds, fluid transport over biological membranes, flows over electronic cooling devices, permeable reactive barrier flow arrangements, flow over packed bed heat exchangers insulations, and fluid flow in chemical drying devices.

Attention is directed to Figure 1.1 where a typical single-phase laminar flow of identical fluids through and over a porous medium is schematically illustrated. Accurate solution of such a coupled flow is daunting. This is because it involves matching the coupled flow so that there is a detailed account of the transfer of momentum at the interface between the porous media section and the free zone. In order to tackle this problem, two main levels of descriptions are usually considered, namely the microscopic and averaged levels of descriptions.

At the microscopic levels of description, microscopic momentum equations are used to describe the flow in either the free zone flow, or the entire flow section. For a steady incompressible Newtonian flow (in the absence of body forces), the microscopic momentum equation that governs the flow is given by

$$\rho_f(\mathbf{u} \cdot \nabla \mathbf{u}) = -\nabla \mathbf{p} + \mu \nabla^2 \mathbf{u} \tag{1.5}$$

where $\mathbf{u} = (u, v, w)$ and $\nabla\, \mathbf{p} = (dp/dx,\ dp/dy,\ dp/dz)$ are the local (microscopic) velocity and pressure gradient vector values. This is an equation that may be used to describe the flow in the free zone and the porous medium section. In cases where the convective terms in Equation (1.5) are negligible, the equation reduces to

$$\nabla \mathbf{p} = \mu \nabla^2 \mathbf{u} \tag{1.6}$$

This is generally referred to as the ‘Stokes equation’.

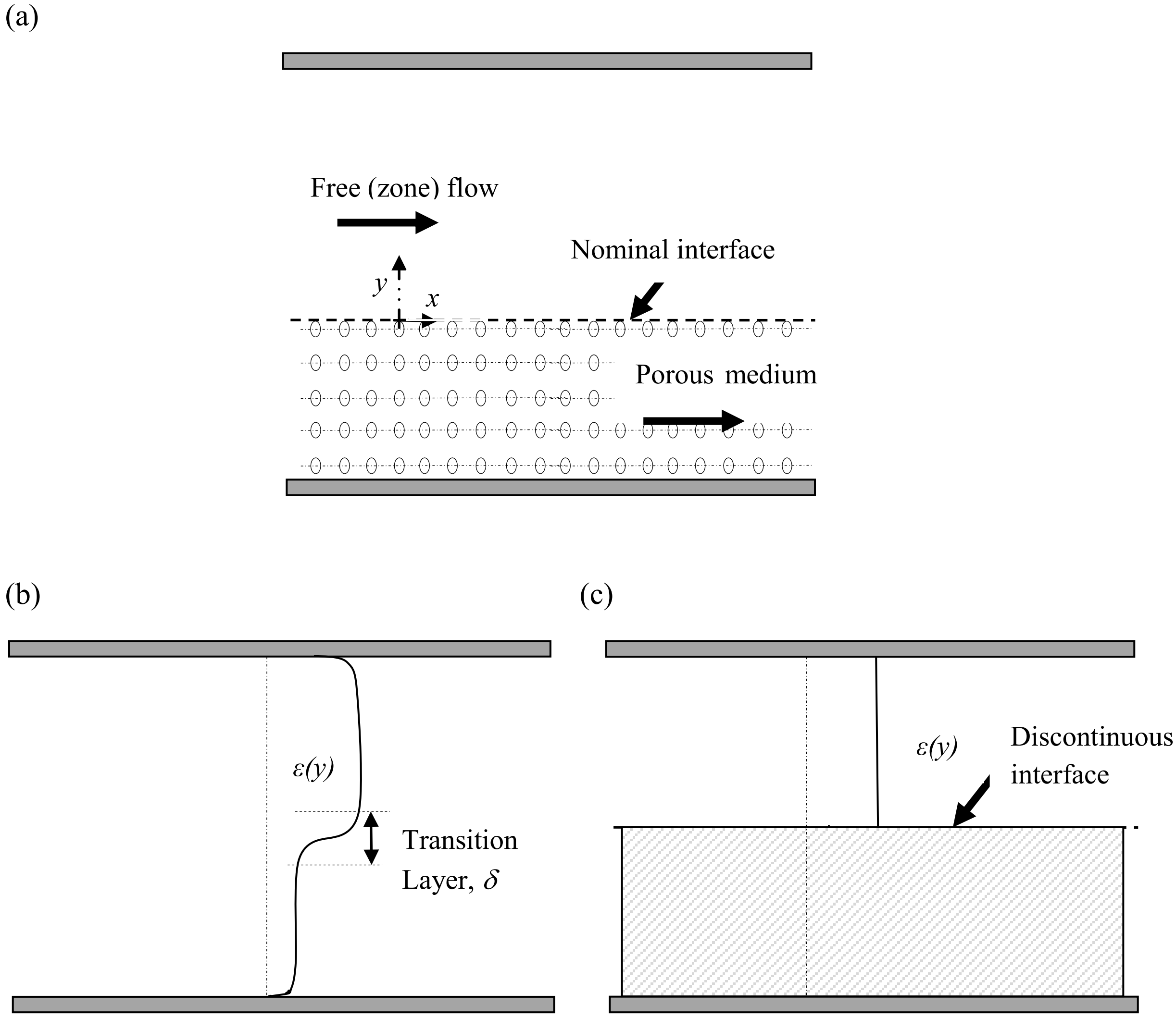

Figure 1.1: Flow through and over a model porous medium, as seen in the (a) microscopic level of description; (b) Mesoscopic description of (a) with a continuous transition layer; and (c) Macroscopic description of (a) with a discontinuous interface. The porosity profiles (in line) in (b) and (c) are only schematic. Located at the origin of the plot $\varepsilon(y)$ are the alternating short and long dashes.

When both flow domains (*i.e.* the free zone flow, and the porous medium flows) are described with microscopic equations, the flow in the whole section is solved using Equation (1.5) or its appropriate modification (such as Equation 1.6), together with suitable boundary conditions. Although this description generally leads to a detailed study of the physics of the flow, due to prohibitive computational costs of simulating the porous medium flow, it is not applicable for most practical cases (Chandesris and Jamet 2007). Such considerations are usually limited to simple two-dimensional porous media flows (Larson and Higdon 1986, 1987; Sahraoui and Kaviany 1992) and simple three-dimensional systems (Breugem 2004).

The practical limitations associated with representing local heterogeneities makes the use of a modified microscopic description more useful. In such a description, the flow in the porous medium is described by an averaged equation such as the Darcy's Law (Equation 1.2), or an appropriate extension that accounts for inertial effects (such as the Forchheimer equation, *i.e.* Equation 1.3).

Although this somewhat simplifies the description of flow within the porous medium in particular, the solution of the problem is still a challenge. This is because the averaged and microscopic governing equations of different orders of the respective flow domains (such as in the one first order differential averaged equation of the Darcy law in the porous medium, and the second order microscopic Stokes equation of the free zone) must be matched. Related to this problem is the consideration of complex interactions at a nominal interface between the two flow domains for which hydrodynamic boundary conditions are difficult to define.

For the case of a Stokes and Darcy coupled flow, one way to tackle the problem is to use a modified Darcian equation proposed by Brinkman (1947) in lieu of the Darcy law. The Brinkman equation may be expressed as

$$-\frac{dP_f}{dx} + \mu' \nabla^2 U_{fs} = \frac{\mu U_{fs}}{k} \tag{1.7}$$

Here, μ' is an apparent (Brinkman) viscosity – a parameter which depends on the fluid as well as the geometry and structure of the porous medium. With Equation (1.7), velocity and stress continuities may be assumed at the interface between the porous and the open medium (whose location is known *a priori*), so that together with the Stokes equation and other requisite boundary conditions, the flow can then be solved. While the Brinkman equation is widely used in the literature, there seems to be no consensus as to how its so-called apparent viscosity is to be modelled. The value of this viscosity, its variation, the range of porosity of its application, and even its potency to predict accurate velocity profiles have all been subjects of much debate (*e.g.* Lundgren 1972; Koplik *et al.* 1983; Kim and Russel 1985; Larson and Higdon 1986, 1987; Dulofski and Brady 1987; Basu and Khalili 1991; James and Davis 2001). This makes this method of solution an approximation at best, needing an alternative.

Another way to match the Stokes and Darcy coupled flow is to use an empirical interfacial boundary condition. Beavers and Joseph (1967) provided one of the first boundary conditions by reasoning that the classical no-slip condition is not applicable at the nominal interface of such a coupled flow due to a tangential slip velocity, U_s at the nominal interface which is related to the interfacial shear rate of the fluid ($du/dy\big|_{y=0-}$) in the following way

$$\left.\frac{du}{dy}\right|_{y=0-} = \frac{\alpha}{\sqrt{k}}(U_s - U_d) \tag{1.8}$$

The empirical parameter α in Equation (1.7) is a slip coefficient whose value is obtained from experiments – something which is still not adequately provided in the literature. Quite apart from this empirical limitation, the use of the slip boundary condition leads to a jump discontinuity in both velocity and stress at the interface, and therefore makes this approach unsuitable for flow modelling.

The issue of determining the boundary condition at the interface has led to the postulation of various formulations (*e.g.* Ochoa-Tapia and Whitaker 1995a, 1995b, 1998). But these methods are either limited to one particular kind of porous media model, or lead to unrealistic velocity and shear discontinuities at the interface, or are fraught with unknown coefficient of one kind or another which need experimental determination. This leaves the problem of laminar flow over porous media an unresolved one that needs to be addressed experimentally.

1.2.2.1. Averaged Levels of Descriptions and Related Problems

The scale limitations of the above-mentioned approaches of the microscopic levels of descriptions have necessitated the current use of two kinds of averaged descriptions (Ochoa-Tapia and Whitaker 1995a; Chandesris and Jamet 2006, 2009; Jamer *et al.* 2009). For convenience and simplicity, these descriptions will be referred to as the 'mesoscopic description', and the 'macroscopic description' (Chandesris and Jamet 2009). In either case, the flow in the entire flow section is described by spatially averaged transport equations. From these equations, the flow may be solved, or interfacial boundary conditions may be derived albeit with empirical coefficients (Ochoa-Tapia and Whitaker 1995a; Chandesris and Jamet 2006, 2007, 2009; Valdès-Parada *et al*. 2007; Jamet *et al.* 2009). .

The mesoscopic description is an extension of the continuum approach. In this case, the whole flow section is treated as a continuum, and the same volume averaging is applied over the whole flow section. Thus, the entire flow section is up-scaled to an equivalent medium consisting of a homogenous porous section and a homogenous free zone separated by a continuous heterogeneous transition zone with varying effective transport properties in which the same volume averaged transport equation (which is usually similar to the Brinkman equation) is valid everywhere. This is schematized in Figure 1.1(b). It should be noted however that for this type of averaged description, after the first averaging (up-scaling), what results is an intrinsic averaged momentum equation in which a closure problem is confronted at the transition zone whose effective properties are complex, and difficult to determine fully (Ochoa-Tapia and Whitaker 1995a; Valdès-Parada *et al*. 2007; Chandesris and Jamet 2006, 2009). Indeed, at the present time, no formal approach has been developed to these closure relations (Jamet and Chandesris 2009). Such a problem makes the experimental provision of detailed information in this zone vital.

In order to simplify the above-mentioned closure problem, fluid dynamists resort to the macroscopic description. In this mode, an additional up-scaling is performed in which the heterogeneous transition zone is substituted by a discontinuous interface with constant effective properties on either sides of the interface [as shown in Figure 1.1(c)]. This up-scaling is done by averaging over the transition layer thickness δ (which is defined as twice the transition layer thickness within the porous medium δ_1; Ochoa-Tapia and Whitaker 1995a). The main problem with this description however, is that appropriate boundary conditions still need to be specified. Furthermore, the second up-scaling associated with this description involves the knowledge of a transition layer thickness which still needs experimental determination (Ochoa-Tapia and Whitaker 1995a; Chandesris and Jamet 2006, 2009; Jamet *et al.* 2009). One other weakness of this description is that it ultimately leads to loss of information of the momentum transfer, and thereby provides at best, only an approximate account of the flow.

1.3 Summary of Research Goals

The present research program seeks to investigate experimentally single-phase laminar flow through and over porous media with or without inertial effects. The goals in summary are to characterize the flow with reference to various porous media parameters, to determine the governing equation that prevails at the onset of inertia within the porous medium, and to establish a workable boundary condition at the interface between a porous medium flow and an overlying free flow.

Circular and square rods arranged in simple and complex periodic patterns are used to model real porous media. The rods are arranged in a test channel so as to achieve solid volume fractions ranging from 0.03 to 0.49, and to fill 34% to 100% of the channel depth.

Using a refractive index matched viscous fluid as the working fluid, and pumping it through a system of valves and connectors, the flow is regulated so as to obtain flow through the porous medium up to the regime in which inertia is apparent. A high resolution planar particle image velocimetry technique is used to measure streamwise and transverse velocities across various spanwise sections of the porous media. In order not to lose detailed information at the interfacial region (as may result from the use of the macroscopic description), the velocity measurements are also spatially averaged in accordance with the mesoscopic level of description, and these averages are used to determine the requisite boundary conditions that apply at the interface. Using electronic pressure transducers, differential pressure measurements are also obtained. The velocity and pressure measurements provide a complete set of experimental data to characterize the flow through and over porous media.

The results of this experimental study are used to provide deeper insights into laminar flow through and over porous media. This work is expected to form a substantial basis for further experimental, theoretical and numerical studies of more complex cases of real porous media.

1.4 Thesis Structure

This report presents studies on laminar flow through and over porous media. Particular attention is focussed on the range of the laminar flow regime up to which inertia is just apparent. The chapter which follows reviews the pertinent literature regarding such flows. Chapter 3 then presents a description of the experimental set-up, measurement procedure, and preliminary checks. In Chapter 4 results of experiments are presented, together with a discussion, and then finally in Chapter 5, a summary of results and conclusions are given, together with some proposals that may be considered for future studies.

Chapter 2

Literature Review and Objectives

2.1 Overview

To put this study in the proper context of the present literature, this chapter reviews the pertinent works that have been published. The reviews are summarized in Tables 2.1 to 2.5. This is followed by an outline of the problem under study in this work, and the theoretical basis, scope and objectives of the present research work.

2.2 Flow through Porous Media

This section looks at relevant publications of flow through porous media, focusing particularly on the Darcy Law, the onset of inertia, and the Forchheimer equation. Following this is a summary of the literature reviewed.

2.2.1 The Darcy Law

When Darcy (1856) conducted his famous filtration experiments, his primary focus was the hydrological study of the fountains of Dijon. He therefore conducted unidirectional flow experiments in vertical homogenous randomly and loosely packed sand filter beds as shown schematically in Figure 2.1. The bed was of height h_1 and bounded by horizontal plane areas of equal size, A. Open manometer tubes were attached at the upper and lower boundaries of the filter bed so that water percolating through the bed rose through the tubes to heights h_3 and h_2 measured above an arbitrary datum level. Darcy's observation was that for a steady-state flow in a uniform porous medium, there is a linear relationship between the volumetric flow rate, Q and the applied pressure drop. The relationship was dependent on an unknown hydraulic conduction coefficient k. The relation, known as Darcy's law, is stated as:

$$Q = \frac{-kA(h_3 - h_2)}{h_1} \tag{2.1}$$

The hydraulic conduction coefficient (commonly referred to as the permeability) k in Equation (2.1) may also be interpreted as a parameter for describing resistance of flow through porous media. This is taken as a constant, depending on the properties of the porous medium. For porous media of packed beds or fibres, one other expression of the resistance of the medium is a dimensionless parameter called the friction factor, f (reference will be made to another significance of this parameter in due course).

The Darcy law has since been subjected to many experimental, numerical and theoretical treatments. Many derivations of the law have been done based upon hydrodynamic principles, using various conceptual models of porous media and related theorems or techniques (*e.g.* Kozeny 1927; Irmay 1958; Scheidegger 1960; Rumer, 1969; Whitaker 1986). It is not within the scope of this work to present a thorough review of all the reported treatments. But it suffices to note at this point that the Darcy law as stated in Equation (2.1) may be generalized by the differential equation given in Equation (1.1).

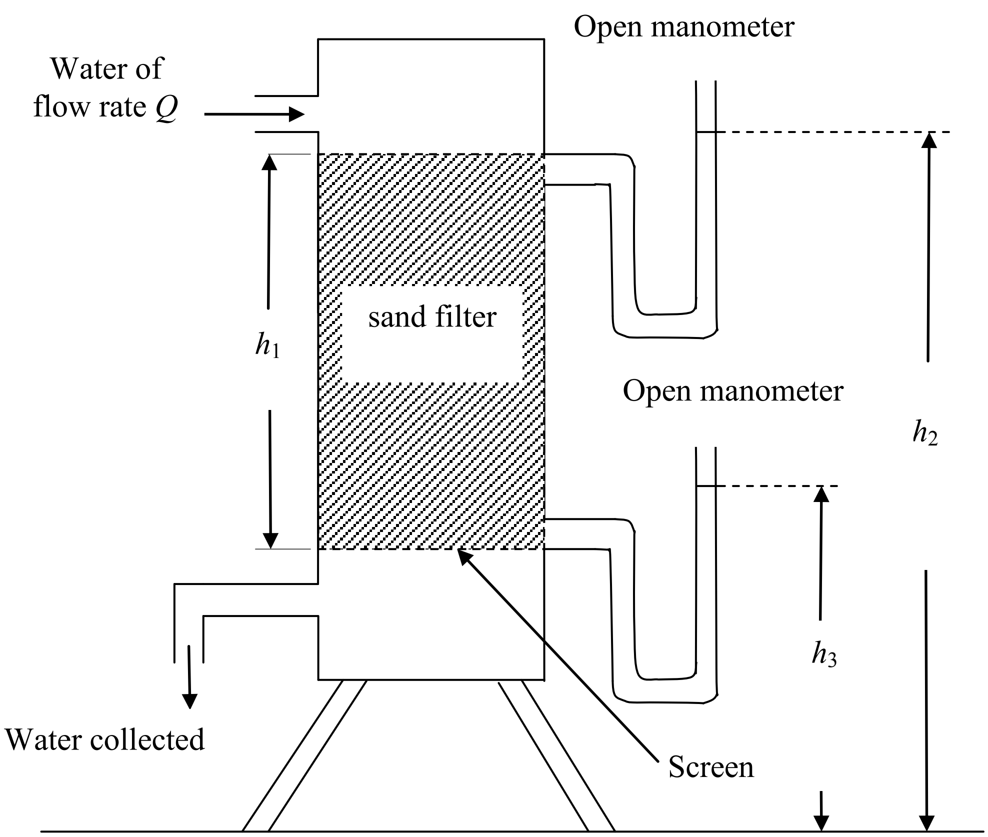

Figure 2.1: Schematic diagram of Darcy's experiment (Bear 1988).

2.2.2 The Evolution of Inertia

The regime of fluid motion where the Darcy law is applicable is called the creeping or Darcy flow regime (Huang and Ayoub 2008). For engineering and analytical purposes, this regime is often specified by a range of Reynolds numbers that is defined by an appropriate length scale, L (such as the mean particle diameter, d; the square root of the permeability $\sqrt{k}$; or the square root of the ratio of the permeability and the effective porosity, $\sqrt{(k / \varepsilon)}$; Hlushkou and Tallarek 2006), and a velocity scale, U (which is usually the seepage velocity, U_d). This Reynolds number, generically referred to as

$$Re = \frac{UL}{\nu} \tag{2.2}$$

where ν is the kinematic viscosity of the fluid), may be seen as the ratio of the inertial forces to the viscous forces in the flow. To appreciate the utility of this dimensionless number, consideration is now given to the role of the viscous and inertial forces. It is important to note that the viscous and inertial forces have opposing effects on the dynamics of the flow. The viscous forces of the flow on one hand are the flow's characteristic frictional forces, responsible for smoothening out the microscopic heterogeneous velocity scales at neighbouring points of the flow. Inertial forces, on the other hand, are the forces that bring about the transfer of energy from large-scale components to small-scale components, thereby ensuring a characteristic heterogeneity in the flow. The relative effects of these forces are defined in the Reynolds number. Three main kinds of Reynolds numbers are used in the literature to discuss porous media flows. They are namely (Huang and Ayoub 2008): the particle Reynolds number, $Re_d = U_d\, d/\nu$; the interstitial Reynolds number, $Re_i = U_d\, d/(\varepsilon\nu)$, and the so-called modified Reynolds numbers – such as that due to Blake (1922), $Re_{BL} = U_d\, d/(\phi\nu)$ and $Re_k = U_d \sqrt{k}\,/\nu$ (which is also known as the Darcian Reynolds number; Spena and Vacca 2001). Another Reynolds number that has been used is called the pore Reynolds number Re_{pore}. This is based on a model of porous media represented as a bundle of identical cylindrical tortuous pores of diameter d_{pore}, tortuosity τ, dynamic specific surface area, $a_{vd,}$ (*i.e.* an empirical quantity defined as the ratio of the actual surface area of the particle in the flow to the volume of the solid), so that Re_{pore} for Newtonian flow is $4\rho U_d\tau\, /\, (a_{vd}\, \mu(1\text{-}\varepsilon))$.

As shown in Figure 2.2, in the Darcy regime, Re is usually of a value close to zero (or for practical engineering applications $Re_i < 1$; Huang and Ayoub 2008). The flow in that regime is essentially viscous, so that inertia is negligible. This is what pertains in porous media flow where the flow is typically conducted through media of very low hydraulic permeabilities, which effectively yields low velocities.

Not all porous media flows, however, are characterized by very low velocities. In hydraulically fractured wells and condensate reservoirs for example, relatively high velocities of flow are encountered, and their related flow phenomena do not follow the Darcy law. Although the onset of this deviation is generally attributed to a more prominent inertial force (*e.g.* Chauveteau 1965), the actual origins of these inertial forces have been the object of many speculations (Hlushkou and Tallarek 2006). While some researchers ascribe this inertial force to pore roughness (Minsky 1951), others point out that this stems from such factors as the microscopic inertial force (Ma and Ruth 1993), inertial core development (Dybbs and Edwards 1984), interstitial pore space curvature (Hayes *et. al.* 1995), viscous boundary layer formation (Whitaker 1996), and the singularity of patterns of streamlines that is sometimes associated with microscale non-periodicity of flow

(Panfilov *et al.* 2003). Nonetheless, it must be emphasized that this deviation, being at a relatively low *Re* is certainly not the kind associated with the onset of turbulence (Scheidegger 1960; Bear 1988; Dullien 1992; *etc*).

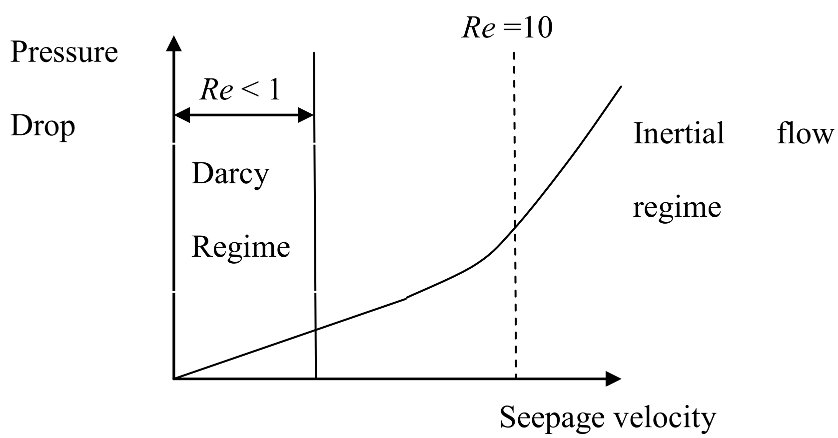

Figure 2.2: A schematic representation of the transition from Darcy flow to the inertial flow. The vertical dashed line represents the region where *Re* ~10 (Bear 1988).

In order to correct for the non-linearities in the inertial flow regime, Forchheimer (1901) proposed an *ad hoc* equation (Firdaouss *et al.* 1997) of the following form for an isotropic porous medium

$$-\frac{dP_f}{dx} = aU_d + bU_d^{\,2} \tag{2.3}$$

Here, a and b are constants to be determined from experiments. Equation (2.3) is equivalent to Equation (1.3), so that a is identically the ratio of the dynamic viscosity to the equivalent Forchheimer permeability, and b is the product of the inertial coefficient and the fluid density.

Although Equation (2.3) (also known as the Forchheimer or quadratic equation; Fourar *et al.* 2004) is often attributed to Forchheimer (1901), Dupuit (1863) had previously suggested a similar extension to Darcy's Law. Equation (2.3) is perhaps, the most widely used formulation for describing inertial effects in steady flow through porous media. This equation has also been extended to cover multi-dimensional flow. Joseph *et al.* (1982), for example, modified the Forchheimer equation for this purpose so that Equation (1.3) for media of homogenous permeability becomes

$$-\nabla \mathbf{P}_f = \frac{\mu}{k}\mathbf{U}_{fs} - \frac{c_f}{k^{0.5}}\left|\mathbf{U}_{fs}\right|\mathbf{U}_{fs} \tag{2.4}$$

where c_f is a dimensionless "drag-form constant". The regime of flow in which the Forchheimer equation applies is called the Forchheimer flow regime. This regime is a viscous-inertia regime, and it persists within the range of interstitial Reynolds numbers: $1 < Re_i < 150$. Beyond this range is a regime of a strong inertial unsteady laminar flow, characterized by wake oscillations and vortical development (Huang and Ayoub 2008). As the present study is limited to the regime of inertia onset, attention will be focussed on reviewing work done on porous media flow in the Forchheimer regime and particularly formulations governing that flow.

Although the Darcy regime and the Forchheimer regime appear to be clearly demarcated, the transition from one regime to the other is known to be a gradual one (Moutsopoulos and Tsihrintzis 2005). Plots of friction factor and the pore Reynolds number may be used as a convenient means of showing this transition (Comiti *et al.* 2000). Like the Reynolds number, the dimensionless friction factor also comes in various forms in the literature. It is given by $f_{f1} = (d/2\rho_f U_d^2)\ (-dP_f/dx)$ (for packed beds; Huang and Ayoub 2008) or by $f_{f2} = (d/\rho_f U_d^2)\ (-\,dP_f/dx)$ (Fourar *et al.* 2004), or even $f_{f3} = (\sqrt{k}/\rho_f U_d^2\ )(-dP_f/dx)$ (Nield and Bejan 2006). When f_{f1} versus pore Reynolds number is plotted logarithmically, the Darcy regime follows a straight line at low Reynolds number. This is followed by a region of deviation from this straight line due to an inertia effect. The point at which this deviation begins is thought to be the transition point from Darcy flow to Forchheimer flow (Comiti *et al.* 2000).

There has been a general inclination to define this transition by means of a critical Reynolds number Re_{cr}. (Bear 1988). However, there has been a wide range of values that have been proposed over the years to be the correct Re_{cr} mainly due to the varying definitions of Reynolds number. Dybbs and Edwards (1984) performed perhaps, the most detailed experiments in the literature covering the transition zone. They used laser Doppler anemometry (LDA) and flow visualization techniques to obtain two-dimensional measurements and dye streakline movies respectively. The porous media model utilized was plexiglass rods arranged in a complex three-dimensional geometrical array, and their working fluids were refractive index matched with respect to the rods. They concluded that this critical Reynolds number is within the range of $1 < Re_{cr} < 10$, where the Re_{cr} was defined in terms of the interstitial Reynolds number of particles Re_i (*i.e.*, $Re_{cr} = Re_{cr,i}$). In another study, Comiti *et al*. (2000) proposed that for engineering purposes, this Re_{cr} be defined as the point where the percentage of inertial effects in the pressure drop is greater than 5%. They suggested that numerically, the Re_{cr} for non-Newtonian flow be fixed at $Re_{pore} = 4.3$. More recently, Fourar *et al.* (2004) also showed that Re_{cr} may be assessed by considering the relative contributions of the pressure and drag terms of the governing equation of the flow. The Re_{cr} is the Reynolds number above which these terms are no longer proportional, but that the pressure drag increases faster than the viscous drag. They therefore proposed that Re_{cr} be seen to fall within the range of $2 < Re_{pore} < 4$.

2.2.3 Forchheimer Equation: Relevant Experimental Works

As reviewed in the previous section, the Forchheimer equation is the most widely used formulation for modeling steady inertial flows in porous media. This equation has been experimentally verified by many researchers. Representative samples of such confirmations are reviewed here to highlight the empirical approaches used, and some landmark results that were obtained.

The Forchheimer equation was verified by Blake (1922) using measurements of flow rates and pressure drops for porous media of glass beads of different shapes, dimensions, fillings and height. Ergun (1952) gave a further credence to the validity of the equation by using flow rate and pressure drop measurements from gas flow through a bed of crushed porous solids. It is instructive to note that in that paper, references were made to previous experimental data (*e.g.* Burke and Plummer 1928; Lindquist 1933) as justifications for the Forchheimer equation. Ergun (1952) also generalized the Forchheimer equation for packed beds in the form

$$-\frac{dP_f}{dx} = F\frac{(1-\varepsilon)^2}{\varepsilon}\frac{\mu}{d^2}U_d + G\frac{(1-\varepsilon)}{\varepsilon^3}\frac{\rho_f U_d^{\,2}}{d} \tag{2.5}$$

where F and G are constants determined through experimental data fitting. A similar form of this equation (for unidirectional flow) was derived by Irmay (1958). MacDonald *et al*. (1979) later expanded this work and provided values of the constants that would better fit much of the data. Ahmed (1967) also showed that the Forchheimer equation is correct, and reported values of a and b (in Equation 2.3) for sands. Bordier and Zimmer (2000) measured flow rates and pressure head differentials for various drainage materials like gravels, geonet and geocomposite materials. They were able to fit coefficients for the Forchheimer equations. Van Batenburg and Milton-Tayler (2005) also used results of flow rate and pressure differential measurements for high velocity gas and water flow tests on proppant packs to show that the Forchheimer equation is indeed valid. Forchheimer-like equations have been verified for Newtonian and non-Newtonian flow through various porous media such as packed beds of spheres, cylinders, polyhedrons and plates (Comiti and Renard 1989). These were achieved through pressure drop and flow rate measurements.

In evaluating this overwhelming amount of empirical support however, it should be pointed out that these experimental data mainly rest upon global measurements of flow rates and pressure differences across various porous media sample. This means that details (particularly of velocity) may have not been fully captured in those bulk measurements. Furthermore, there have also been a number of experiments that have been at variance with the Forchheimer equation. These include the notable experiments of Forchheimer (1930), Skjetne *et al*. (1995), and Barree and Conway (2004, 2005). In fact, after re-examining earlier reported data of Darcy (1856), Hazen (1895) and Chauveteau (1965), Firdaous *et al.* (1997) concluded that the data followed the cubic law given in Equation (1.4).

Further to this, there are some disputes about the value of the Forchheimer equation as a credible empirical tool that have arisen from the coefficients that are embedded in it. In conventional practise (Balhoff and Wheeler 2009) the inertial coefficient β of the Forchheimer equation, is determined by rearranging the equation (as given in Equation 1.3) into the following form

$$\frac{1}{k_{app}} = -\frac{1}{\mu U_d}\frac{dP_f}{dx} = \frac{1}{k_f} + \left(\frac{\beta \rho_f U_d^{\,2}}{\mu U_d}\right) \tag{2.6}$$

so that it is the value of the slope of the plot of the inverse of the apparent permeability $1/k_{app}$ against the dimensional Reynolds number $\beta\rho_f U_d/\mu$. This coefficient has been a subject of much research over the years, and many different correlations have evolved to define its value for various porous media (Li and Engler 2001). However, this parameter has also raised some suspicion about the universal application of the Forchheimer equation in the Forchheimer regime. In a recent study, for instance, van Barree and Conway (2005) published results that generated some discussion about the sufficiency of the linear correlation suggested in Equation (2.6) (Huang and Ayoub 2008, Balhoff and Wheeler 2009). Instead of the straight line expected from Equation (2.6), the experimental data of Barree and Conway (2004, 2005) yielded a downward concave curve. This assertion is supported theoretically and numerically by Edwards *et al.* (1990), Stanley and Andrade (2001) and Balhoff and Wheeler (2009). If this is anything to go by, then the implication is that the Forchheimer equation may not be an adequate model to describe the flow within the entire regime of viscous-inertial flow.

Apart from the inertial coefficient β, the permeability related to the Forchheimer equation, k_f has been another matter of varied interpretation in the literature. While some invariably equate this to the permeability obtained in the Darcy regime *k* (as given in reviews of Li and Engler 2001 and Huang and Ayoub 2008), others have been quick to emphasize the difference between the two permeabilities (Muskat 1937; Skjetne *et al.* 1937; Chauveteau 1965; Barree and Conway 2004). This confusion, though apparently subtle, raises a problem of interpretation, considering that some (*e.g.* review of Moutsopoulos and Tsihrintzis 2005) have interpreted the Forchheimer equation as a general case of the Darcy law, because at very low velocities, the second order terms of Equation (1.3) should be negligibly small. These coefficient-related issues have in part raised a cloud of doubt regarding the value of the Forchheimer equation in describing the flow in the Forchheimer regime.

2.2.4 Forchheimer Equation: Relevant Theoretical and Numerical Works

Just as for experiments, several successful proofs can be used as theoretical justifications for the Forchheimer Equation. Using various macro-scale approaches (*e.g.* volume averaging: Irmay 1958, Whitaker 1996; principle of variation: Knupp and Lage 1995; homogenization theory: Marušic-Paloka and Mikleic 2000; Chen *et al.* 2001; hybrid mixture theory: Hassanizadeh and Gray 1987); and micro-scale-based models (*e.g.* capillary orifice model: Blick 1966; non-linear drag models: Rumer 1969; capillary network mode: Comiti and Renaud 1989; hydraulic radius method: Eisfeld and Schitzlein 2001), there have been many analytical endeavours to this effect. Bear (1988) and Huang and Ayoub (2008) give comprehensive lists of these techniques in their reviews. It is important to point out that the derivation of the Forchheimer equation has been extended to cover compressible flows (Chen *et al.* 2001) and multiphase flows (Bennethum and Giorgi

1997). Numerical simulations have also admitted the use of the Forchheimer equation as an adequate model for the Forchheimer regime in both two-dimensional models (*e.g.* Wang *et al*. 1999) and three-dimensional models of porous media (Fourar *et al.* 2004), and particularly cases pertaining to the strong inertial regime (Wang *et al.* 1999; Balhoff and Wheeler 2009).

It should be noted that the techniques employed in many of these theoretical derivations have however been questioned. Ruth and Ma (1992) and Ma and Ruth (1993) for example, demonstrated that because microscopic inertial effects are not accounted for in the volume averaging technique, this technique cannot be a valid method to use in a conclusive derivation of the Forchheimer equation. They further showed the non-uniqueness of the equation that governs the steady non-linear flow, pointing out that any number of polynomials could have been used to describe the non-linear behaviour of the flow. This conclusion is in concurrence with Mei and Auriault (1991) and Woodié and Levy (1991) who had earlier shown that at low, finite velocities a homogenization technique yields a cubic law, not a quadratic law.

These latter findings are not surprising, given that other equations have been suggested in the past to describe inertial steady laminar flows in porous media (Basak 1977). Forchheimer (1901) himself suggested two other equations of the following forms, which are relatively less known

$$-\frac{dP_f}{dx} = aU_d + bU_d{}^g \tag{2.7a}$$

$$-\frac{dP_f}{dx} = aU_d + bU_d{}^2 + cU_d{}^3 \tag{2. 7b}$$

where g and c are empirical terms. Also, Izbash (1931) proposed an empirical power law of the form

$$-\frac{dP_f}{dx} = eU_d^{\ h} \tag{2.8}$$

where e is an empirical constant. The parameter h was specified to range from 1 to 2. Although this power law rivals the Forchheimer equation (as it is the preferred choice in modeling drainage systems; Bordier and Zimmer 2000), its physical soundness seems to be relatively less established. White (1935), after analyzing dry air flow through packed towers (Scheidegger 1960), also gave a correlation belonging to the family of equations of (2.8), but setting h equal to 1.8. There has been other less known empirical and semi-empirical power laws by Escande (1953), Wilkinson (1956) and Slepicka (1961) which are reviewed by Basak (1977), all demonstrating the non-uniqueness of the Forchheimer equation to describe the inertial flow. There are other formulations that may also be seen as extensions of the Forchheimer equation. These, such as those of Wooding (1957) have been passed over because they are mainly suited for unsteady flows.

In the recent past, many numerical studies (*e.g.* Couland *et al.* 1988; Rojas and Koplik 1988; Hill *et al.* 2001; Balhoff and Wheeler 2009), have given credence to the use of an alternative cubic equation, given in Equation (1.4). Although such numerical results were mostly simulations of simple two-dimensional periodic porous media (Barrére 1990; Firdaous and Guermond 1995; Amaral Souto and Moyne 1997), there has been at least one case in which the media was three-dimensional (*i.e.* a random pack of spheres; Balhoff and Wheeler 2009). It is also important to note that these results (whether two or three dimensional porous media models) are unanimous in support of a cubic law at relatively lower velocities of the Forchheimer regime, although they have not had experimental verification (apart from the confirmation provided by the re-examination of past data by Firdaous *et al* 1997).

2.2.5 Summary of Review of Pertinent Studies of Flow through Porous Media

The following, together with Tables 2.1 and 2.2 summarizes the review of studies of flow through porous media:

(a) Flow through porous media has been a matter of great research interest over the last 150 years (Table 2.1). Many useful formulations have been proposed to describe the flow phenomena (Table 2.2). These formulations have however been expressed mainly in terms of global parameters and they have been based on empirical observations of global streamwise measurements (as pointed out in Table 2.1).

(b) The regimes of flow through porous media have also been widely covered. However, the onset of inertia in the flow seems to be an area that needs further investigation. As pointed out in Table 2.1, apart from the work of Dybbs and Edwards (1984), there appears to be no detailed velocity measurements that cover the phenomena of inertia onset. The Forchheimer equation has been a matter of great controversy. As inferred from Table 2.2, its uniqueness has been in doubt, and there is yet more to be known about the governing equation of flow at the onset of inertia.

Table 2.1: Summary of selected studies on equation governing the Darcy-Forchheimer transition zone.

Focus of Research Study		Pertinent Studies Reviewed
Investigation Type	Experimental	Blake (1922) Ergun (1952) Burke and Plummer (1928), Lindquist 1933, and Morcom 1946) Ahmed (1967) Bordier and Zimmer (2000) Van Batenburg and Milton-Tayler (2005), Barree and Conway (2005), Balhoff and Wheeler (2009)
	Theoretical / Numerical	Irmay (1958), Blick (1966), Edwards *et al.* (1990), Ruth and Ma (1992), Ma and Ruth (1993), Knupp and Lage (1995), Whitaker (1996), Marušic-Paloka and Mikleic (2000), Chen *et al.* (2001), Stanley and Andrade (2001) and Balhoff and Wheeler (2009)
Velocity Measurement Technique (Experimental)	Global	Blake (1922), Ergun (1952), Burke and Plummer (1928), Lindquist (1933), and Morcom (1946), Ahmed (1967) Bordier and Zimmer (2000), Van Batenburg and Milton-Tayler (2005), Barree and Conway (2005), Balhoff and Wheeler (2009)
	Detailed	Dybbs and Edwards (1984)
Dimensionality of Porous Medium (Experimental)	Two Dimensions	none
	Three Dimensions	Blake (1922), Lindquist (1933), Morcom (1946), Ergun (1952), Ahmed (1967), Bordier and Zimmer (2000), Van Batenburg and Milton-Tayler (2005), Barree and Conway (2005), Balhoff and Wheeler (2009)
Dimensionality of Porous Medium (Theoretical / Numerical)	Two Dimensions	Barrére (1990), Firdaous and Guermond (1995), Amaral Souto and Moyne (1997), Wang *et al*. (1999),
	Three Dimensions	Fourar *et al.* (2004), Balhoff and Wheeler (2009)

Table 2.2: Summary of prominent formulations for the Darcy-Forchheimer transition zone.

Model	Mathematical Formulation	Comment
Forchheimer / quadratic equation; Forchheimer (1901)	$-\frac{dP_f}{dx}=\frac{\mu}{k}U_d+(\frac{\tau\rho_f{}^2}{\mu}U_d{}^3)$	Most widely used empirical equation for Forchheimer regime; However this has been found to be unsuitable for two dimensional flows, and the Darcy-Forchheimer transition zone (though not experimentally verified).
Empirical Cubic equation; Firdaous *et al.* 1997)	$-\frac{dP_f}{dx}=\frac{\mu}{k}U_d+(\frac{\tau\rho_f{}^2}{\mu}U_d{}^3)$	Appears to work well for two-dimensional flows in the Darcy-Forchheimer transition zone.
Ergun empirical equation Ergun (1952)	$-\frac{dP_f}{dx}=F\frac{(1-\varepsilon)^2}{\varepsilon}\frac{\mu}{d^2}U_d+G\frac{(1-\varepsilon)}{\varepsilon^3}\frac{\rho_f U_d{}^2}{d}$	Suitable for packed beds
Alternative empirical equations proposed by Forchheimer (1901)	$-\frac{dP_f}{dx}=aU_d+bU_d{}^g$ $-\frac{dP_f}{dx}=aU_d+bU_d{}^2+cU_d{}^3$	Not as well known as quadratic equation.
Power Law of Izbash (1931)	$-\frac{dP_f}{dx}=eU_d{}^h$	Empirical with no well established theoretical basis; works well for modeling drainage systems

2.3 Flow over Porous Media

Like flow through porous media, the problem of porous media flow coupled with a free flow has generated intense research interest. However, this review will consider only germane publications that highlight the main issues that have propelled research in this area of fluid mechanics. Although the methods under discussion are related in many ways, for the sake of clarity and order in presentation, the present evaluation will be made by dividing the pertinent studies into two main blocks, defined by the contributions of the researchers. The first block of contributions will hereafter be called the 'Brinkman related contributions', because it pertains to methods that are either based on Brinkman's equation, or utilizes a similar equation. The other contributions, denominated the 'boundary condition contributions', will enlist research findings that propose interfacial boundary conditions. Under the 'boundary condition contributions', studies that have been conducted to provide information about the boundary condition parameters (such as slip velocity and slip coefficient) are also reviewed.

2.3.1 The Brinkman Related Contributions

Brinkman (1947) studied the viscous flow past a dense swarm of spherical particles in a porous mass, and proposed an equation to calculate the viscous force that was exerted. This equation, called the Brinkman equation (presented in this work as equation 1.7), became a necessary hypothesis for the solution of the problem. This is because Darcy's law, devoid of a viscous stress component, was inadequate to use in cases of porous media of low particle densities ($k \rightarrow \infty$). Furthermore, obtaining consistent boundary conditions for coupled porous media and free flows was a particularly difficult task to under-take. Brinkman therefore used Equation (1.7) together with other logical boundary conditions to solve the whole flow domain problem. After comparing results with an empirical relation by Carman (1937), it was found that for particles of solid volume fraction $\phi <$ 0.6, there was satisfactory agreement with Carman's experimental relation when the apparent viscosity μ' in the Brinkman equation was equal to the fluid's dynamic viscosity μ. This choice of value of μ' is also known as the Brinkman model (Agelinchaab *et al.* 2006). The Brinkman equation has since been used for the study of coupled porous and free flows. The value of this Brinkman approach lies in its capacity to provide a velocity profile that accounts for the 'boundary layer' (*i.e.* the transition layer in the porous medium) that occurs between the interface and the Darcy region. There is further utility in the Brinkman approach, considering its adaptability for use for the whole coupled porous media- free flow as a single domain, if the variations of properties such as k, ϕ, and μ' are known. Perhaps, it is upon these bases that some have sought to establish its applicability, and to expand on this approach by defining particularly the value of the empirical coefficient μ'.

The Brinkman equation has therefore received rigorous verifications from numerous investigators, for low ϕ porous media (*e.g.* Tam 1969; Childress 1972; Howells 1974; Hinch 1977; Freed and Muthukumar 1978; Rubenstein 1986). However, many other studies using low ϕ porous media have shown that the Brinkman equation often fails to predict the flow field (*e.g.* Larson and Higdon 1986, 1987; James and Davis 2001; Davis and James 2004). Kaviany (1992) also showed that the Brinkman model gives an underestimation of the flow resistance at the interfacial boundary. The result is that the boundary effects persist further into the porous medium.

Experimental verifications of the Brinkman equation have furthermore, been largely sparse and indirect, and even some of these results have been in dispute. Some theoretical predictions of permeability of high ϕ porous media based on the Brinkman equation have been in agreement with experimental data (Brinkman 1947; Lungren 1972; Kim and Russel 1985). However, Dulorfski and Brady (1987) argued that because the permeability is a single scalar quantity, the permeabilities obtained do not represent the general flow, and thus, the empirical agreements in those experiments do not necessarily establish the validity of the Brinkman equation for media of high ϕ. To prove their point, they provided fundamental solutions of creeping flow through porous media, and upon comparing their results with solutions of the Brinkman equation, they concluded that for $\phi >$ 0.05, the Brinkman solution loses its 'detailed predictive value', though it remains a helpful qualitative tool. Givler and Altobelli (1994) matched velocity measurements with analytical data for $\phi = 0.028$, and came up with an apparent viscosity value, $\mu' = 7.5\mu$. Generally, the literature shows that at best, there is a non-uniform validity of the Brinkman equation even for low ϕ (Rubenstein 1986; Nield and Bejan 2006; Gerritsen *et al.* 2005).

Modelling of the apparent viscosity of the Brinkman equation has attracted some attention, but generated mixed results as well. Koplik *et al* (1983) analyzed the shear flow at a porous media – free-zone interface. They calculated the energy dissipated in a flow about an isolated sphere, and found the apparent viscosity to be less than the fluid viscosity (*i.e.* $\mu' < \mu$). This is in contrast with the findings of Lungren (1972), who concluded that this is not always the case. Kim and Russell (1985) later used dilution theory to solve the Stokes equation for flow through a random array of fixed spheres for ϕ ranging from 0.30 to 0.50. Their analytical prediction was that the value of the apparent viscosity is greater than the viscosity of the fluid (*i.e.* $\mu' > \mu$), in contrast to the result obtained by Koplik *et al.* (1983). Larson and Higdon (1986, 1987) also performed a numerical study of the shear flow near the surface of a porous media. Their model porous media were made up of square and hexagonal arrays of cylindrical inclusions. They concluded that $\mu < \mu'$ when the flow was parallel to the cylinders, and $\mu > \mu'$ when the flow was perpendicular to the cylinders. Ochoa-Tapia and Whitaker (1995a), also argued that μ' / μ is identically $1 / (1- \phi)$, a result which though strikingly similar, is yet different from the result of Bear and Bachmat (1991) who used a volume averaging process to show that μ' / μ is equal to $\tau / (1- \phi)$, where τ is the tortousity of the medium. In their derivation, Ochoa-Tapia and Whitaker (1995a) tried to clarify some ambiguities regarding the so-called apparent viscosity. According to them, this Brinkman viscosity concept is really a confusion of superficial and intrinsic properties. Due to the mixed results in the literature, there has been a proposal to use a variable apparent viscosity model (Kaviany 1992). However verification for this proposal remains to be provided. In spite of the apparent uncertainties in the Brinkman approach, it has been reported to give realistic accounts for the transport of momentum from the free flow to the porous medium, which is approximated to occur within thickness of $O(\sqrt{k})$ (Goyeau *et al.* 2003).

It must be pointed out that the Brinkman equation has also been extended for use in inertial flows. Hsu and Chang (1990) derived such an equation, after some modification of the earlier works of Vafai and Tien (1981, 1982). This equation can be written for incompressible steady flow in an isotropic porous media as follows

$$\rho_f \frac{1}{\phi}\left[\mathbf{U}_{fs}\cdot\nabla\left(\frac{\mathbf{U}_{fs}}{\phi}\right)\right] - \nabla\mathbf{P}_f = -\nabla\mathbf{P}_f + \frac{\mu}{\phi\rho_f}\nabla^2\mathbf{U}_{fs} - \frac{\mu}{k}\mathbf{U}_{fs} - \frac{c_f}{\sqrt{k}}\left|\mathbf{U}_{fs}\right|\mathbf{U}_{fs} \qquad (2.9)$$

More recently, Shavit *et al.* (2002) also investigated the average velocity profile around the interface between a shallow free surface and porous media flow. The porous region was modeled using the Cantor Taylor brush configuration (CTB) – similar to that studied by Taylor (1971) and Richardson (1971). A modified Brinkman equation (MBE) was developed by averaging the microscale Stokes equation. The MBE was found to provide an accurate prediction of the average velocity profile around the interface of the configuration, given a correct choice of the size of the REV, H_{rev}. The velocity profile and its first derivative were continuous and reproduced with high accuracy the results of the average microscale Stokes equation. In a succeeding numerical study, Shavit *et al.* (2004) generalized their MBE formulation, providing a complete macroscopic solution of the interface a 'brush configuration', given the fundamental properties of the porosity ε, and permeability k, the fluid dynamic viscosity μ, and the pressure gradient dP_f/dx. This general solution may only be applied to a laminar flow problem that involves an interface between a porous media that consists of a series of grooves, and a relatively fast moving flow region. The solution also provides an accurate description of the flow rate. The generalized MBE may be expressed as follows:

$$-\frac{dP_f}{dx} + \mu\left(\frac{\partial^2 U_f}{\partial y^2}\right) = 0 \text{ for } y \geq H_{rev}/2$$

$$-\frac{dP_f}{dx} + \mu\left(\left(\left(\frac{1-\varepsilon}{H_{rev}}\right)z + \frac{1+\varepsilon}{2}\right)\frac{\partial^2 U_f}{\partial y^2} + \frac{2(1-\varepsilon)}{H_{rev}}\left(\frac{\partial U_f}{\partial y}\right) - \alpha_R U_f\right) = 0$$

for $-H_{rev}/2 \leq y \leq H_{rev}/2$

$$-\frac{dP_f}{dx}+\mu\left(\varepsilon\frac{\partial^2 U_f}{\partial y^2}-\alpha_R U_f\right)=0 \; , y \leq -H_{rev}/2 \tag{2.10}$$

where U_f is the streamwise intrinsic velocity, and α_R is a conduction coefficient (= $(dP_f/d\mathrm{x})/(U_d\,\mu)$). They reported that the flow rate predicted by the MBE is accurate within a wide range of porosities (0.15 – 0.825). This equation has been verified in PIV measurements by Shavit *et al.* (2004) and Rosenzweig and Shavit (2007). The problem about the MBE is that it appears to be suited only for models of the Cantor Taylor brush configuration (CTB), and therefore provides only a limited solution to the problem of interfacial flow.

In another fresh look at the coupled porous medium-free flow problem, Nield and Kuznetsov (2009) modelled the problem by considering it as a flow in a three-layer channel, consisting of a transition layer sandwiched between a layer of free fluid and a porous medium layer. They assumed the permeability of the transition layer to vary linearly across the channel. They also assumed the permeability of the layers to be continuously matched. The Brinkman model was used in the porous medium and transition layer. Velocity profiles were obtained from closed form expressions for each layer, and the results were compared with models using the Beavers and Joseph (1967) boundary condition at the interface. It was observed that the results were satisfactory for thin transition layers and small Darcy numbers. Although this three-layer technique seems plausible in some respects and could be explored further, its utility in this study is largely limited because it involves a simplification of the transition layer that may only apply in theoretical cases.

2.3.2 Boundary Conditions Contributions

As pointed out in Chapter 1, an alternative approach to the solution of the problem of flow through and over porous media is that which requires boundary conditions at the interface. The boundary conditions that have been used in the literature range from empirically and analytically derived boundary conditions, to intuitive conditions such as continuity in shear stress and velocities.

For this block of studies, the contribution of Beavers and Joseph (1967) is very significant. They attempted one of the first experimental studies on the interfacial boundary conditions for a Poiseuille flow through and over a porous medium. In that work, various samples of two structurally different types of permeable materials - low density nickel foametal, and aloxite – were tested. The volume fraction ranged from 0.20 to 0.49 (Kim and Russel 1985). Based upon their measurements of the mass flow rates for demineralized water and Sinclair 100-Grade Duro oil, they detected a tangential slip velocity U_s at the nominal interfaces of the porous media. These investigators postulated that the difference between U_s, and the Darcian velocity $U_{d,}$ is proportional to the shear rate of the fluid at the interface, $du/dy\,|_{y=0-}$. The proportionality constant (*i.e.* slip coefficient, α) in the relation was speculated to depend linearly on $\sqrt{k}$, as well as the structure of the material at the interface. This postulation was expressed in a boundary condition presented as Equation (1.8) in Chapter 1, known as the Beavers and Joseph boundary condition. Values of α = 0.78, 1.45 and 4.0 for foametals and a value of 0.1 for aloxite were obtained based on the measured flow rates and known permeability values. Beavers and Joseph (1967) concluded that the rectilinear flow of a viscous fluid over the surface of a permeable material yields a boundary layer region within the material, whose effects could greatly change the nature of the tangential motion near the interface. It must be emphasized however that having noted this in their work, the boundary condition proposed did not truly account for a boundary layer region, and this has limited its utility.

Saffman (1971) theoretically verified the semi-empirical boundary condition of Beavers and Joseph (1967). He approached the derivation by modelling the problem as a case of flow through a non-homogenous porous medium with porosity and permeability changing discontinuously from the values of 1 and ∞ for the porous medium forming the boundary. By performing an ensemble averaging, a derivation of Equation (1.7) in the following form was made:

$$U_s = \frac{\sqrt{k}}{\alpha} \left.\frac{du}{dy}\right|_{y=0-} + O(k) \tag{2.11}$$

Saffman (1971) noted that Equation (2.11) is only sufficient to calculate the outer flow correct to $O(\sqrt{k})$. Furthermore, since U_d in the Darcy Law was much smaller than other quantities, that velocity could be neglected if the details of the boundary layer were not required. Saffman (1971) also noted that the actual location of the interfacial boundary will affect the value of the slip coefficient α, and may even take on negative values.

Following the findings of Beavers and Joseph (1967), Taylor (1971) performed experiments to verify whether the slip coefficient α, was dependent on any other features of the geometry of the media of flow apart from the porous material. In this respect, he conceived an ingenious means of designing an ideal porous material of solid volume fraction of about 0.5, for which the specific permeability k could be calculated using α. Shell Talpa oil was the working fluid. The permeability k was computed from a theoretical analysis by Richardson (1971), and a value of $\alpha \approx 2$ was obtained.

Jones (1973) made a generalization of the Beavers and Joseph condition, assuming it to be a relationship involving shear stress, and expressed it as:

$$\left.\frac{du}{dy}\right|_{y=0-} + \left.\frac{dv}{dx}\right|_{y=0-} = \frac{\alpha}{\sqrt{k}}\left(U_s \quad - U_d\right) \tag{2.12}$$

It is obvious from the foregoing equation that for cases where the transverse velocity gradient along the stream is negligible, the Beavers and Joseph boundary condition is readily obtained. This equation has however not yet been confirmed.

In another investigative study, Neale and Nader (1974) made attempts to solve the interfacial boundary condition problem. They however proposed continuity in both the velocity and the velocity gradient at the interface by introducing the Brinkman term in the momentum equation for the porous side. Nonetheless they also showed that the Beavers and Joseph boundary condition may be obtained from the solution of the Brinkman equation (*i.e*. Equation 1.7) valid in the region $y \leq 0$ of the parallel flow of Figure 1.1(a) if the slip coefficient $\alpha = \sqrt{(\mu/\mu')}$.

Beavers *et al.* (1974) also performed experiments to verify the Beavers and Joseph boundary condition for gas flows. They also sought to determine whether the fluid had any significant effect on α. Using a rectangular test section, a porous medium was placed at the bottom wall. The porous media were of two specimens of foametal of different dimensions and permeability, and each of $\phi \approx 0.05$. The experiments were performed in an open-loop air flow facility, and the airflow through the duct and the porous block were driven by the same axial pressure. The magnitude of the pressure gradient was chosen to fall within the range for which a coupled parallel flow was established with fully-developed laminar flow in the channel, and a Darcy flow in the porous material. Flow rate measurements of the laminar channel flow with a porous boundary were compared with that of a solid boundary. The results showed that slip velocity at a porous boundary could be detected even for a gaseous working fluid, flowing along the boundary. It was found that α was respectively, 0.27 and 0.19 for the two foametal specimens.

In a study that was the first of its kind, Larson and Higdon (1986, 1987) numerically analyzed the microscopic flow near the surface of a two-dimensional porous media made up of simple arrays of infinite and semi-infinite lattices of cylindrical inclusions. They used the boundary-integral method to solve the Stokes flow for cases of the idealized porous medium aligned with the flow (Larson and Higdon 1986), and across the flow (Larson and Higdon 1987). Their results indicated that penetration is greater in the aligned flow. They showed that the flow over the surface of a porous media is inherently surface-driven with extremely rapid velocity decay at even low porous media concentrations. They calculated the slip velocity based on the flux above and below the interface, and noted a considerable discrepancy between the two definitions, except for very low volume fractions. The slip velocities obtained from both methods decreased with increasing solid volume fraction as expected, however, negative values were also obtained – a result that has cast considerable doubt on the accuracy of their method. For both axial and transverse flows, it was observed that except for extremely low concentrations, the definition of the nominal interface was of considerable influence on the value of slip velocity obtained. They also noted that owing to slight protrusions of the medium above the nominal interface, the slip velocities may even take on negative values as suggested by Saffman (1971). Consequently, Larson and Higdon (1986, 1987) concluded that the use of slip coefficients for porous boundaries was not well justified, and that generally, the macroscopic models of Brinkman (1947), and Beavers and Joseph (1967) were inadequate to give a satisfactory descriptions of the detailed flow field at the porous surfaces.

Vafai and Thiyagaraja (1987) studied the flow field and heat transfer at the interface between two different porous media, the interface separating a porous medium from a fluid, and the interface between a porous medium and an impermeable medium. In the analysis, the velocity field in the porous medium was assumed to be independent of the flow direction. They used continuity of velocity, shear stress and heat flux at the interface, and the Forchheimer equation (to account for inertial effects within the porous medium). Vafai and Kim (1990) also considered the flow of fluid at the interface between a porous medium and a fluid layer with inertia and boundary effects. They gave an exact solution to a simplified problem by using an identical shear stress in the fluid and the porous medium at the interface region.

Ochoa-Tapia and Whitaker (1995a) on the other hand, proposed a jump momentum transfer condition at the boundary between a porous medium and a homogeneous fluid. The condition, based on the non-local form of the volume averaged momentum equation, was developed to join Darcy's law with the Brinkman equation in solving the coupled porous-free flow problem. The approach assumes a jump in the stress but not in the velocity, allowing the convective transport to be continuous at the boundary between a porous medium and a homogeneous fluid. However, it demands a specification of the Brinkman transition layer thickness of the interfacial region – something which needs experimental determination or verification. For a porous medium of porosity ε, the condition can be expressed as:

$$\frac{1}{\varepsilon}\frac{dU}{dy}\bigg|_{y=0+} - \frac{dU}{dy}\bigg|_{y=0-} = \frac{\beta_1}{\sqrt{k}}U_s \tag{2.13}$$

Empirical measurements are also required to determine the coefficient β_1 (which is a dimensionless parameter of a complex function) that appears in the condition. In Ochoa-Tapia and Whitaker (1995b), this coefficient was estimated to range from -1.0 to 1.5 for a good fit with experimental results of Beavers and Joseph (1967). In another study, Ochoa-Tapia and Whitaker (1998) proposed another shear stress jump boundary condition for situations where inertia effects play a key role in the flow. Here, for a porous medium of porosity ε, the condition requiring two empirical constants β_2, β_3 may be expressed as

$$\frac{\mu}{\varepsilon}\frac{dU}{dy}\bigg|_{y=0+} - \mu\frac{dU}{dy}\bigg|_{y=0-} = \beta_1\frac{\mu}{\sqrt{k}}U_s + \beta_2\rho U_s^{\,2} \tag{2.14}$$

Like Equation (2.13), this equation has empirical coefficients that need to be determined.

Unlike Equation (2.13), Equation (2.14), has been the subject of intense research. Kuznetsov (1996) gave analytical solutions for the steady fully developed laminar fluid flow in the parallel-plate and cylindrical channels filled in one part with a porous medium. The stress jump boundary condition suggested by Ochoa-Tapia and Whitaker (1995a) was used at the interface to match the Brinkman equation to the Stokes equation. Kuznetsov (1996) demonstrated that the stress jump boundary condition is not only of theoretical interest, but also important for solving practical fluid flow problems. Later, Goyeau *et al.* (2003) analyzed the forced flow parallel to the interface between the free flow and the porous medium by performing a momentum balance. They introduced a varying non-homogenous transition layer between the two domains and tried to provide insight into finding the jump coefficient in the model of Ochoa-Tapia and Whitaker (1995a). However, they were only able to provide a relationship dependent on velocity variations (which are unknown in the problem). According to the numerical computations of Deng and Martinez (2005), the jump coefficient β_1 is dependent on the Reynolds number (based on the seepage velocity U_d and the depth of the whole test section, H), and the Darcy number (the ratio k / H^2). This is yet to be confirmed experimentally.

Chandesris and Jamet (2006) analyzed a coupled homogenous porous media – free flow in order to determine the boundary condition that should hold at the interface. Using matched asymptotic expansions with a heterogeneous transition layer at the interfacial region, they were able to obtain a model in which the condition is based on fluid stress. Their jump interface condition was of the following form

$$\left.\frac{dU}{dy}\right|_{y=0+} - \left.\frac{dU}{dy}\right|_{y=0-} = \beta_3 \frac{\delta}{\sqrt{k}} U_s \tag{2.15}$$

where β_3 is an unknown jump coefficient, and δ is the thickness of the transition zone (which must be determined or verified experimentally). They reported the product $\beta_3\,\delta$ to range from -0.64 to 4.28, for a good fit to experimental results of Beavers and Joseph (1967). However, they also conceded that extra work would have to be done in order to define the value of this coefficient for various porous media.

In a bid to do away with the problem of an adjustable coefficient, Valdès-Parada *et al.* (2007) derived another jump condition similar to Equation (2.13). This condition however involves a mixed stress tensor at the right hand side of Equation (2.15) which combines the Brinkman and global stress at the interface. The Brinkman stress was determined using polynomial functions describing spatial changes in porosity, while the global stress was determined by deriving and solving the local closure problem. Although this work has been very helpful in dealing with related closure problems associated with interfacial boundary condition problems, it was nonetheless based on a rather convenient assumption that the interfacial velocity effects were negligible.

Chandesris and Jamet (2007, 2009) and Jamet and Chandesris (2009) have subsequently tried to account for the jump coefficients in Equations (2.13) to (2.15) using pressure surface-excess forces and the friction surface-excess forces. In the first of these papers, Chandesris and Jamet (2007) were able to obtain relationships between the structure of the transition region, and the value of the jump coefficients in Equations (2.13) and (2.15), provided the profiles of permeability and porosity at the transition region are known. In a succeeding paper, Jamet and Chandesris (2009) further demonstrated that the coefficients depend linearly on the position of the interface of the macroscopic discontinuous description. In Chandesris and Jamet (2009), a boundary condition similar to Equation (2.14), in which the right hand side parameters are expressed in terms of the pressure surface-excess force and the friction surface-excess force, was obtained. Nonetheless, these results are also subject to experimental verification, and are only an attempt to clarify an approximate solution to the problem.

2.3.3 Boundary Conditions Contributions: Supporting Works

There are a number of studies that provide further information about some of the boundary conditions that have been proposed in the literature, as well as the associated empirical coefficients.

One such numerical study of laminar flow across rod arrays was carried out by Sahraoui and Kaviany (1992) using a finite difference analysis to solve the momentum and continuity equations. A periodic structure of the rods for solid volume fractions between 0.2 and 0.5 was employed. The work revealed dependence of the slip coefficient on the solid volume fraction, Reynolds number, and flow type (whether shear- or pressure-driven). However, it was only focussed on flow through and over two dimensional porous media; neither did it suggest any alternative boundary condition.

Gupte and Advani (1997) later used an LDA technique to measure the fluid flow at the interface of a porous medium and a Hele-Shaw cell. They reported values of α for a random network of glass strand weaves of ϕ = 0.07, 0.14, and 0.21. The test channel was partially filled with the fibrous preform to create a free zone coupled with a Darcy flow. Saturated and steady flow through the cell was established by respectively injecting three different kinds of viscous fluids at a constant flow rate through the system. It was found that while the interface between the flow through the porous medium and the free zone is affected by ϕ, it was unaffected by either the fluid viscosity or the flow rates on either side of the permeable boundary. Furthermore, there was no specific trend in the variation of ϕ with the α. Gupte and Advane (1997) also reported that for fibrous mats, the transition layer within the porous medium was far larger than that predicted by the Brinkman solution. While their results provided significant insight, it was nonetheless limited to just one kind of porous medium, and the free flow was that of a simple Hele-Shaw flow.

James and Davis (2001) examined both shear-driven and pressure-driven flows in the interfacial region between an open and porous medium flow using models of porous medium consisting of arrays of circular cylinders of a maximum solid volume fraction, ϕ =

0.10. The porous medium was oriented across the flow, and filled the channel typically to half its width. Singularity methods were used in the analysis. They introduced a dimensionless slip velocity $U_s / (\dot{\gamma}\sqrt{k})$ (where $\dot{\gamma}$ is the shear rate of the fluid at the interface, $dU/dy\,|_{y=0+}$) which may be observed to be equal to $1/\alpha$ in Equation (1.8) in the case of shear flows. James and Davis (2001) found that for shear flow, $U_s / (\dot{\gamma}\sqrt{k})$ depends only on ϕ, and that the slip velocity was small even for arrays with $\phi < 0.01$ (*i.e.* open flows). For the case of pressure-driven flows, the dimensionless slip velocity was found to be affected by ϕ, filling fraction, and the ratio of the porous medium depth to pore. In another numerical work, Davis and James (2003) used singularity methods to investigate the slip velocity at the interface of a regular array of rods and the unfilled portion of the annulus for a shear-driven flow. Solid volume fractions ranging from 0.0001 to 0.10 were explored. The dimensionless slip velocity $U_s / (\dot{\gamma}\sqrt{k})$, was found to be nearly independent of the number of circles of rows behind the rods. However, with just a single row, the velocity increased by just about 10%. They therefore concluded that the velocity at the edge of a porous medium is nearly dependent only on the hydrodynamic resistance of the elements at the outer edge. Although the studies of James and Davis (2001) and Davis and James (2003) threw further light onto the interfacial flow phenomenon, they were also limited to low solid volume fraction two-dimensional porous media under non-inertial flow conditions.

In another experimental study, Shams *et al.* (2003) used particle image velocimetry (PIV) to make detailed measurements of the creeping shear flow field near the edge of a two-dimensional model porous medium. The model was an annular array of regularly spaced acrylic circular rods installed vertically onto a Plexiglass disk, to form a circular brush. Three annular arrays were made to cover solid volume fractions of 0.025, 0.052 and 0.10 respectively. Their results showed that secondary motion could arise in a porous medium. However, there was no quantification of shear rates at the interface.

Tachie *et al.* (2003) performed experiments using the PIV to study the simple creeping shear flow penetrating a model of a fibrous medium. They used an experimental set-up similar to that employed by Shams *et al.* (2003). The model porous media used were made up of transparent acrylic rods of circular, square, and equilateral triangular cross-sections. The rods were arranged in an annular array to provide a solid volume fraction range of 0.01 to 0.16. They observed that the minimum value of solid volume fraction for the onset of circulation depended on the rod geometry. Concurring with Shams *et al.* (2003), Tachie *et al.* (2003) suggested that circulation started at $0.04 < \phi < 0.052$. The dimensionless interfacial slip velocity $U_s / (\dot{\gamma}\sqrt{k})$ was found to be nearly independent of the rod shape, the number of circles of rods forming an array, as well as the solid volume fraction. The dimensionless slip velocity decayed from 0.30 to 0.24 as the solid volume fraction increased sixteen-fold. While the experiments of Shams *et al.* (2003) and Tachie *et al.* (2003) provided detailed experimental data, their results like James and Davis (2001) and Davis and James (2003), only apply to creeping shear flows over two-dimensional porous media of low solid volume fraction.

Tachie *et al.* (2004) consequently used PIV to measure velocities of slow shear flow over a three-dimensional model porous medium. The test facility and experimental technique employed were similar to that used by Tachie *et al* (2003). Here, however, the model porous medium used consisted of an array of uniformly–spaced rods oriented perpendicular to the axis of the cylinders, and mounted onto the inner cylinder to simulate a 'brush- flow' configuration of 81% filling fraction. The model brushes were of solid volume fractions 0.025, 0.05, and 0.10. The dimensionless slip velocity was found to be about 1, and nearly independent of the solid volume fraction. Their study like Tachie *et al.* (2003), was limited to simple shear flow, and the effects of filling fraction or inertial effects were neither covered.

With a combined refractive index matching method, Goharzadeh *et al.* (2005) used PIV to quantify the velocity field at the interfacial area between a pressure-driven laminar flow and a porous medium. The porous media was modelled by five different types of transparent borosilicate mono-disperse glass beads and polydisperse granulates. The porous media were of solid volume fraction 0.57, 0.59 and 0.62. In the test conditions, the porous media depth was kept constant, while the depth of the free zone was varied. Using averaged velocity data from their two-dimensional measurement, they observed that the transition layer in the porous medium was of the order of grain diameter and therefore much larger than the square root of permeability. They also concluded that the proper velocity scale for the interfacial flow is the slip velocity. It should however be noted that their results pertained only to flow in which the local Reynolds numbers in the porous media were much below 1, and therefore apply to cases where inertial effects were not apparent.

Agelinchaab *et al.* (2006) provided PIV measurements of flow driven by pressure, through and over a three-dimensional model porous media. The experiments were conducted in a channel of matched refractive index as the working fluid – mineral oil. The porous media models were made up of square arrays of circular rods installed on the bottom wall of the channel with the axes of the rods parallel to the wall-normal direction.

Solid volume fractions of $0.01 \leq \phi \leq 0.49$ and filling fractions of 0.28 and 0.56 were achieved. Reynolds number effects were also tested. The dimensionless parameter $U_s / (\dot{\gamma}\sqrt{k})$ for h / H = 28% and 56% filling fractions was found to be 1 and 2 respectively, and Reynolds number effects were negligible on the dimensionless velocity. The study also showed that penetration of the open flow into the porous medium is significantly higher than prior results obtained for the shear 'cross-flow' configuration. The transition layer within the porous medium was found to exceed the screening distance $\sqrt{k}$, and it decreased with increasing ϕ but increased with the depth of the porous medium. Some deficiencies of this work is that no interfacial boundary condition was suggested, nor was there any provision of substantive information about the slip coefficient, or of the empirical coefficients in the boundary conditions suggested in Equations (2.13) and (2.15).

In a more recent effort, Arthur *et al.* (2009) performed experiments using an experimental set-up similar to that used by Agelinchaab *et al.* (2006). Their models were also three dimensional, arrayed in the same way as Agelinchaab *et al.* (2006), so that the solid volume fraction ϕ, ranged from 0.01 to 0.49. However in this case, the models were installed so as to study three boundary conditions of porous media flow. In the first boundary condition, the model porous medium was mounted on the bottom wall so that there was a free flow over it. In other boundary conditions, model porous media were installed on both walls of the channel with and without an intervening space for free flow respectively. A planar PIV was used to obtain detailed velocity, using water as the working fluid. They reported that the slip velocity reduced with permeability, and that in the other boundary conditions in particular, flow communication between the porous media was affected by the combinations of ϕ used. Like Agelinchaab *et al.* (2006), Arthur *et al.*

(2009) did not propose any new interfacial boundary condition. Furthermore, they did not provide area averaged measurements to properly compare results with other boundary conditions proposed in the literature. However, their work provided further indications that the flow phenomenon at the interface of porous media and free flow are indeed complicated and need further research.

Using an experimental set-up similar to Goharzadeh *et al.* (2005), Morad and Khalili (2009) studied the transition layer flow inside a porous media of multi-sized spherical beds for which there is an overlying parallel pressure-driven free flow. The porous medium filled half of the total depth of the section. The range of permeability of porous media was 0.007 mm^2 to 0.038 mm^2. Morad and Khalili (2009) concluded that the ratio of the transition layer within the porous medium to the square root of the permeability is 29.3 and therefore of the order the characteristic diameter of the porous medium. Furthermore, by assuming a weak jump in the velocity gradient, they showed that their transition layer velocity data could be fitted to an exponential function with a depth-dependent coefficient. Although this work provided more information regarding the size of the transition layer, it is unclear as to whether conclusions were derived from a consideration of the average flow, which is the data of interest in porous media studies. Moreover, their results are limited to glass beads and inertial effects were not explored.

2.3.4 Summary of Reviewed Literature of Flow over Porous Media

From the foregoing, the following summarizes observations from the literature, as further demonstrated in Tables 2.3 – 2.5:

(a) Much work has been focussed on flow over porous media (Table 2.3). The contributions that have been made may be generally classified into the Brinkman (as summarized in Table 2.4), and the boundary condition groups (as summarized in Table 2.5). Nonetheless, the theoretical and numerical studies are larger (more than twice more) than the experimental works.

(b) There have been a number of experimental studies that provide velocity measurements of flow over porous media. However, as indicated in Table 2.3, these appear to be limited to flows in which inertia is not a factor. Indeed, there are few reports in the literature that cover flows through and over porous media where inertia is a factor, but these are numerical / theoretical works (Sahraoui and Kaviany 1992; Ochoa-Tapia and Whitaker 1998; Hsu and Chang 1990). There is therefore a clear requirement for experimental data that would cover this inertial range.

(c) While there have been some boundary conditions proposed based on empirical observations (as laid out in Table 2.5), many more are theoretical derivations. Generally, these boundary conditions are either drawn from analysis without firm experimental confirmation, or laden with coefficients that need experimental determination (which are lacking). As a result the flow at the interfacial region is not properly modeled.

(d) None of the experimental works using arrays of rods as model porous media utilized any other porous media rod arrangement. Neither did any provide any formulation to solve the boundary condition problem at the interface of porous media and free flow.

There is therefore need for work to be done to ascertain the proper boundary conditions that apply at the interface.

Table 2.3: Summary of flow over porous media studies.

Focus of Research Study		Pertinent Studies Reviewed
Investigation Type	Experimental	Beavers and Joseph (1967), Taylor (1971), Beavers *et al* (1974), Gupte and Advani (1997), Tachie *et al* (2003, 2004), Goharzadeh *et al.* (2005); Agelinchaab *et al*. (2006), Arthur *et al.* (2009); Morad and Khalili (2009)
	Theoretical / Numerical	Brinkman (1947), Richardson (1971), Saffman (1971), Koplik *et al.* (1983), Kim and Russel (1985), Larson and Higdon (1986, 1987) Vafai and Thiyagaraja (1987), Hsu and Chang (1990), Sahraoui and Kaviany (1992), Ochoa-Tapia and Whitaker (1995a,1995b, 1998), Kuznetsov (1996), James and Davis (2001), Deng and Martinez (2005); Davis and James (2003, 2004), Goyeau *et al.* (2003), Chandesris and Jamet (2006, 2007, 2009); Valdès-Parada *et al*. 2007); Jamet and Chandesris (2009); Nield and Kuznetsov (2009)
Velocity Measurements (Experimental)	Global	Beavers and Joseph (1967), Beavers *et al* (1974)
	Detailed	LDA: Gupte and Advani (1997) PIV: Shams *et al.* (2003), Tachie *et al.* (2003, 2004), Goharzadeh *et al.* (2005); Agelinchaab *et al*. (2006), Arthur *et al.* (2009); Morad and Khalili (2009)
Dimensionality of Porous Medium Flow	One Dimension	Pressure-Driven flow: Gupte and Advani (1997),
	Two Dimensions	Shear-Driven flow: Shams *et al*. 2003; Tachie *et al* (2003) Pressure-Driven flow: Shavit *et al.* (2004)
	Three Dimensions	Shear-Driven flow: Tachie *et al.* (2004), Pressure-Driven flow: Goharzadeh *et al.* (2005) Agelinchaab *et al*. (2006), Arthur *et al.* (2009); Morad and Khalili (2009)
Flow with inertial effects comprehensively considered	Detailed Experimental Work	None
	Theoretical / Numerical	Sahraoui and Kaviany (1992), Ochoa-Tapia and Whitaker (1998), Hsu and Chang (1990)

Table 2.4: Summary of formulations for solving flow over porous media: the Brinkman contributions.

Model	**Mathematical Formulation**	**Comments**
Brinkman Equation	$-\frac{dP_f}{dx} + \mu' \nabla^2 U_d = \frac{\mu}{k} U_d$ Brinkman (1947)	Generally acceptable for dilute solutions only ($\phi <$ 0.60); Has little experimental support. Disputable value of μ'
Extended Brinkman Equation	$\rho_f \frac{1}{\phi}\left[\mathbf{U}_{fs} \cdot \nabla\left(\frac{\mathbf{U}_{fs}}{\phi}\right)\right] - \nabla \mathbf{P}_f = -\nabla \mathbf{P}_f + \frac{\mu}{\phi \rho_f} \nabla^2 \mathbf{U}_{fs} - \frac{\mu}{k} \mathbf{U}_{fs} - \frac{c_f}{\sqrt{k}} \left\|\mathbf{U}_{fs}\right\| \mathbf{U}_{fs}$ Hsu and Chang (1990)	Consideration of inertial effects
Generalised Modified Brinkman Equation	$-\frac{dP_f}{dx} + \mu\left(\frac{\partial^2 U_f}{\partial y^2}\right) = 0$ for $y \geq H_{rev}/2$ $-\frac{dP_f}{dx} + \mu\left(\left(\left(\frac{1-\varepsilon}{H_{rev}}\right)z + \frac{1+\varepsilon}{2}\right)\frac{\partial^2 U_f}{\partial y^2} + \frac{2(1-\varepsilon)}{H_{rev}}\left(\frac{\partial U_f}{\partial y}\right) - \alpha_R U_f\right) = 0$ for $-H_{rev}/2 \leq y \leq H_{rev}/2$ $-\frac{dP_f}{dx} + \mu\left(\varepsilon \frac{\partial^2 U_f}{\partial y^2} - \alpha_R U_f\right) = 0$, for $y \leq -H_{rev}/2$ Shavit *et al.* (2002, 2004)	Applicable only for CTB configuration. This has some experimental support Shavit *et al.* (2004) and Rosenzweig and Shavit (2007).

Table 2.5: Summary of formulations used for solving flow over porous media: the boundary condition contributions.

References	Velocity	Velocity gradient	Comments
Beavers and Joseph (1967)		$\left.\frac{du}{dy}\right\|_{y=0-} = \frac{\alpha}{\sqrt{k}}\left(U_s - U_d\right)$	Does not account well for boundary layer at interfacial region; for simple flows; need to determine coefficient
Jones (1973)		$\left.\frac{du}{dy}\right\|_{y=0-} + \left.\frac{dv}{dx}\right\|_{y=0-} = \frac{\alpha}{\sqrt{k}}\left(U_s - U_d\right)$	Not verified; ; need to determine coefficient
Neale and Nader (1974); Vafai and Kim (1990)	$U_+ = U\_$	$\left.\frac{dU}{dy}\right\|_{y=0+} = \left.\frac{dU}{dy}\right\|_{y=0-}$	Simple and intuitive; needs empirical evidence
Vafai and Thiyagaraja (1987)	$U_+ = U\_$	$\mu\left.\frac{dU}{dy}\right\|_{y=0+} = \mu'\left.\frac{dU}{dy}\right\|_{y=0-}$	Simple and intuitive; not grounded on empirical evidence; need to determine coefficient
Ochoa-Tapia and Whitaker (1995a)	$U_+ = U\_$	$\frac{1}{\varepsilon}\left.\frac{dU}{dy}\right\|_{y=0+} - \left.\frac{dU}{dy}\right\|_{y=0-} = \frac{\beta_1}{\sqrt{k}}U_s$	Requires determination of coefficient, and interfacial region (or transition layer) thickness
Ochoa-Tapia and Whitaker (1998)	$U_+ = U\_$	$\frac{\mu}{\boldsymbol{\varepsilon}}\left.\frac{dU}{dy}\right\|_{y=0+} - \mu\left.\frac{dU}{dy}\right\|_{y=0-} = \beta_1\frac{\mu}{\sqrt{k}}U_s + \beta_2\rho U_s{}^2$	Considers case where inertia plays a role; but there is a need to determine coefficients and interfacial region (or transition layer) thickness
Chandesris and Jamet (2003)	$U_+ = \mu U\_$	$\left.\frac{dU}{dy}\right\|_{y=0+} - \left.\frac{dU}{dy}\right\|_{y=0-} = \beta_3\frac{\delta}{\sqrt{k}}U_s$	Requires determination of coefficient and interfacial region (or transition layer) thickness

2.4 Objectives and Methodology

2.4.1 Objectives

The present research program seeks to experimentally investigate pressure-driven laminar flows through and over porous media. Due to a pressing need to study the onset of inertia in porous media flow, and to determine the requisite interfacial boundary conditions between porous media and an adjoining free flow, the following are the specific objectives of the present work:

a) To conduct comprehensive experiments to characterize the effects of solid volume fraction, porous media rod shape, porous media rod arrangement, filling fraction (separate and combined with the depth to porous medium pore ratio) porous medium dimensionality, and Reynolds number on laminar flows through and over porous media flow. This should form a fundamental basis for further experimental, theoretical or numerical studies of more complicated cases of real porous media.

b) To apply the benchmark experimental data to establish the governing equation that best describes the porous media flow when inertia sets in, and the conditions under which they hold.

c) To employ averaged velocity measurements at the interface to verify or propose formulations that may be used to describe the interfacial boundary conditions between a porous medium and a free flow, and consequently, the flow at the interfacial transition layer.

2.4.2 Research Methodology and Measurement Techniques

The above-mentioned goals are achieved by experimentation. Regular arrays of rods are used to model real porous media. Using such models is very helpful because of their relative simplicity and adaptability in theoretical, numerical, and experimental studies. Such models are also practical, as they simulate real cases such as banks of heat exchanger tubes, and provide valuable information of flow that may be applied in reservoir simulation.

The effect of inertia will be studied by varying the Reynolds number so as to cover up to the Darcy regime and the transitional regime between the Darcy and Forchheimer regimes. Other flow factors to be varied are those identified through dimensional reasoning and observations made in the literature. In this vein, other parameters considered in the experimental study include:

i. The solid volume fraction of the model porous media. In the present case, the solid volume fractions considered are 0.03, 0.06, 0.12, 0.22 and 0.49. This range practically covers loosely packed and compact media for the experimental techniques to be used;

ii. The porous media rod shape, *i.e.*, rods of circular and square cross-sections;

iii. The mode of arrangement of porous media rods, *i.e.*, in-line and staggered arrays;

iv. The separate and combined effects of the filling fraction (h / H) and the test section depth to porous medium pore ratio (H / l). The fraction h / H ranged from 0.34 to 1, and H / l from 5.75 to 18.25.

v. The porous media dimensionality, determined in this case by the axial orientation of the rods used in the arrays;

With the development of technology, there has been an increasing demand to conduct more porous media experiments which capture multi-dimensional flow quantities, as opposed to mere global quantities. Accordingly, there have been many advances in measuring velocity in multi-dimensions. As pointed out by Arthur *et al.* (2009), several pore-scaled experimental studies of flow through porous media have been conducted in the past using various non-intrusive measurement techniques. Amongst the available techniques, the particle image velocimetry (PIV) technique stands out as one of the most appropriate. The PIV allows for the instantaneous whole flow-field measurement of pore-scale two- and three-dimensional velocities from which averages of flow quantities can be obtained.

Using a high resolution PIV technique, detailed velocity measurements are conducted both within the porous medium and the plain medium, as well as at the porous – free media interface. To capture the variations of velocities in all directions various planes are measured along various sections along the span of the test section. The velocities are averaged spatially. In addition to the velocity measurements, differential pressure measurements are obtained using pressure-measurement gauges and transducers where possible, as also used in previous works (*e.g.* Zhong, Currie and James 2006). The refined pressure and velocity datasets are then analysed and presented to provide a complete set of experimental data to characterize the flow through the model porous media, and to describe the interfacial boundary conditions.

Chapter 3

Experimental Apparatus and Measurement Procedure

3.1 Overview

This chapter describes the test channel, porous media models, velocity and pressure measurement set-ups, as well as the general experimental rig. This is followed by an account of how certain preliminary measurement concerns were resolved, quantification of measurement uncertainty, general measurement procedures, and test conditions.

3.2 Experimental Apparatus

3.2.1 Test Channel and Accessories

The experiments were conducted in a transparent acrylic channel of length L = 500 mm, span W = 115.5 mm and a variable depth H, as shown in Figure 3.1. The channel [Figure 3.1(a)] was constructed from a transparent 25 mm thick acrylic sheet of refractive index (RI) 1.47, so as to allow optical access. It was designed so as to allow flow to pass into it through a central entry hole at the upstream end, then through a 200 mm section reserved for flow conditioning, and finally through a 300 mm test section, before exiting through another central hole at the downstream end. As shown in Figure 3.1(b), the flow conditioning section was made up of a square cross-sectioned insert assembly in which half of the assembly was packed with rods and separated from the other unfilled half by a perforated acrylic sheet. The purpose of the flow conditioning section was to ensure that the flow that entered the measurement section was reasonably uniform. Both entry and exit holes are of 25 mm diameter, and each of the 300 mm × H faces of the channel at the test section were reserved for either velocity or pressure measurements. The pressure test side of the test section (shown in Figure 3.1c) was arrayed with pressure tap holes of 3.18 mm diameter.

3.2.2 Porous Media Models

Three types of model porous media were used in the experiments. For clarity and convenience, these model types will hereafter be referred to as 'horizontal', 'vertical' and 'mesh' models. They are schematized in Figures 3.2 and 3.3. The horizontal models were composed either of circular (round) or square rods arrayed in a staggered or non-staggered fashion. All other models (i.e. vertical and mesh models) were composed only of circular rods in non-staggered arrays. For clarity and simplicity, the horizontal models in particular are hereafter referred to as 'round non-staggered horizontal', 'round staggered horizontal', or 'square non-staggered horizontal' models, depending on the particular type of rods or arrays used. All other models are simply called 'vertical' or 'mesh' models because all of them are of circular rods in non-staggered arrays. A summary of the porous media models used in the experiments is presented in Tables 3.1 and 3.2.

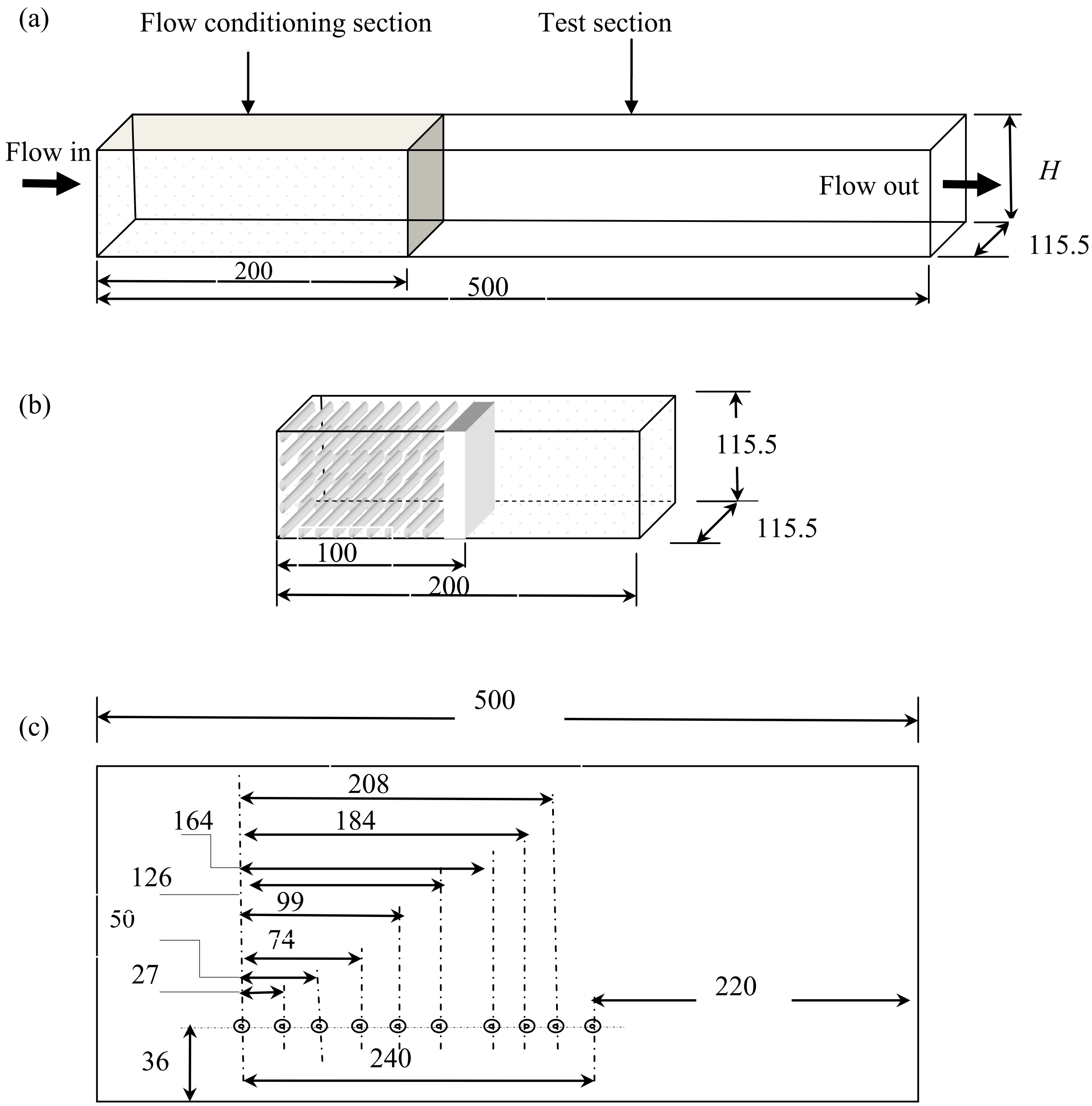

Figure 3.1: (a) A schematic of the test channel; (b) the flow conditioner; (c) the pressure measurement face of the test channel; The shaded section is to distinguish the flow conditioning section from the measurement section. All numeric dimensions are internal and are in millimetres. These are not drawn to scale.

(a)

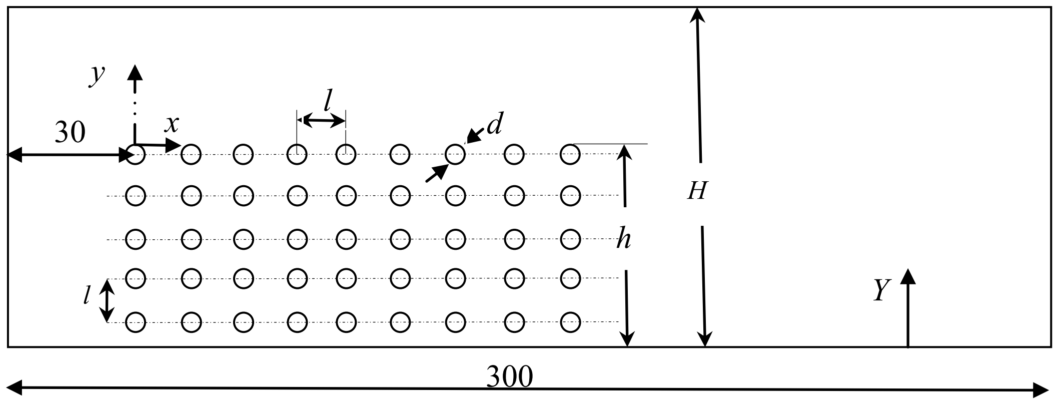

(b)

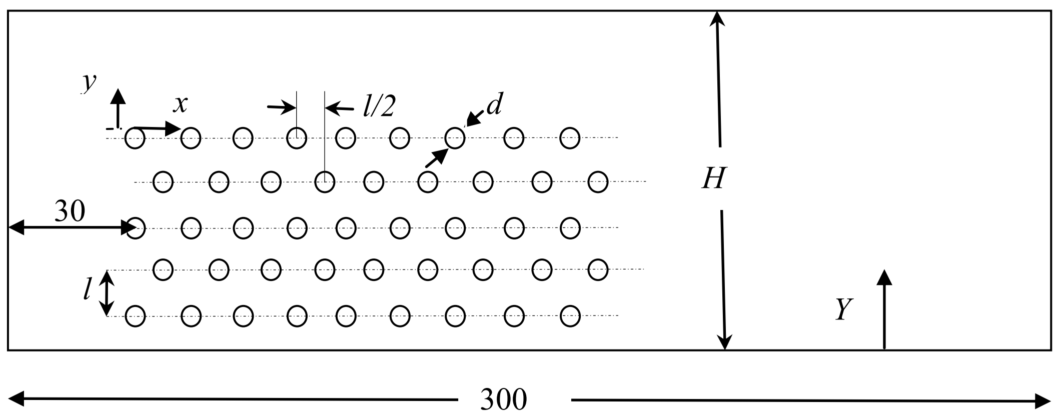

Figure 3.2: Horizontal models in: (a) front section showing non-staggered array (b) front section showing staggered array.

Each of the porous media models was constructed from acrylic rods of RI 1.47, as well as two side plates and one lower acrylic plate of RI, 1.47. As shown in Figure 3.2(a), for the non-staggered horizontal model, corresponding holes were drilled through the side plates in a square array, so that when installed, the axes of the circular or square rods were aligned along the span of the test channel. On the other hand, the staggered horizontal models were constructed with holes arrayed as shown in Figure 3.2(b) so that alternate rows of rods were staggered by a distance of $l/2$ along the stream.

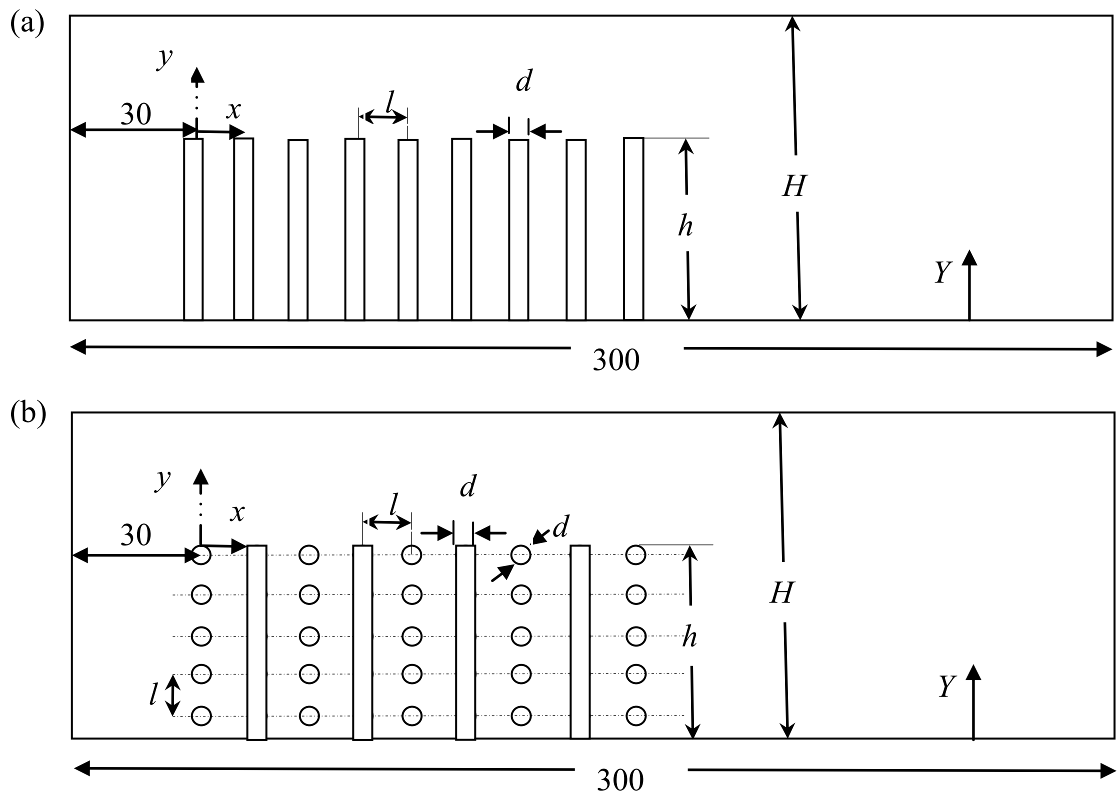

Figure 3.3: Front section of (a) vertical model, and (b) mesh model. The coordinate directions used in the experiments are shown. In this drawing, all numeric dimensions are in millimetres.

Table 3.1: Summary of geometrical dimensions of horizontal model.

Model	ϕ	***s* or *d* (mm)**	***l* (mm)**	***h* (mm)**	***H* (mm)**	h/H	H/l
Round non-staggered horizontal	0.06	3.18	12	83.0	83.0	1.00	6.92
	0.12	3.18	8	83.0	83.0	1.00	10.38
	0.22	3.18	6	83.0	83.0	1.00	13.83
	0.06	3.18	12	82.1	109.5	0.75	9.13
	0.12	3.18	8	82.1	109.5	0.75	13.69
	0.22	3.18	6	82.1	109.5	0.75	18.25
	0.49	4.76	6	82.1	109.5	0.75	18.25
	0.12	3.18	8	34.0	46.0	0.74	5.75
	0.22	3.18	6	34.0	46.0	0.74	7.67
	0.49	4.76	6	34.0	46.0	0.74	7.67
	0.12	3.18	8	54.8	109.5	0.50	13.69
	0.06	3.18	12	27.2	54.6	0.50	4.55
	0.12	3.18	8	27.2	54.6	0.50	6.83
	0.22	3.18	6	27.2	54.6	0.50	9.10
	0.12	3.18	8	13.9	41.3	0.34	5.16
Round staggered horizontal	0.12	3.18	8	82.1	109.5	0.75	13.69
	0.12	3.18	8	54.8	109.5	0.50	13.69
Square non-staggered horizontal	0.12	3.18	8	82.1	109.5	0.75	13.69
	0.12	3.18	8	27.2	54.6	0.50	6.83

Table 3.2: Summary of geometrical dimensions of vertical and mesh models

Model	ϕ	***s* or *d* (mm)**	***l* (mm)**	***h* (mm)**	***H* (mm)**	h/H	H/l
Vertical	0.03	3.18	16	34.0	46.0	0.74	2.88
	0.06	3.18	12	34.0	46.0	0.74	3.83
	0.12	3.18	8	34.0	46.0	0.74	5.75
	0.12	3.18	8	54.2	73.0	0.74	13.83
	0.12	3.18	8	34.0	61.0	0.56	13.83
	0.12	3.18	8	34.0	73.0	0.47	10.38
Mesh	0.06	3.18	12	83.0	83.0	1.00	6.92
	0.12	3.18	8	83.0	83.0	1.00	10.38
	0.22	3.18	6	83.0	83.0	1.00	13.83
	0.12	3.18	8	34.0	46.0	0.74	5.75
	0.22	3.18	6	34.0	46.0	0.74	7.67
	0.49	4.76	6	34.0	46.0	0.74	7.67

For the vertical model, holes were drilled through the lower plate of the model in a square array, so that the axes of installed circular rods were aligned in the transverse direction, as shown in Figure 3.3(a). The mesh model is schematically shown in Figure 3.3(b). This may be seen as a hybrid of the horizontal and vertical models. Here, some of the circular rods were held by the two side plates (as in the horizontal models), and some were inserted into the lower plate (as in the vertical models) in a regularly alternating manner, but in a cubic array.

For models of circular rod of diameter d or square rods of side s, and solid volume fraction ϕ, rods were spaced at a distance l determined from the relations:

$$l = d/2\sqrt{(\pi/\phi)} \tag{3.1}$$

$$l = s/\sqrt{\phi} \tag{3.2}$$

Circular rods used were of diameter d = 3.18 mm and 4.76 mm and inter-rod spacing of l = 6 mm, 8 mm, 12 mm and 16 mm, while square rods of side 3.18 mm and inter-rod spacing l = 9 mm were used. The rods were arrayed so as to cover solid volume fractions within the range $0.03 \leq \phi \leq 0.49$. The vertical models were of solid volume fraction ϕ = 0.03, 0.06, and 0.12, whereas each of the horizontal and mesh models were of the range $0.06 < \phi \leq 0.49$. These values were selected because they cover the entire range of solid volume of fibrous and porous media for which the models and the measurement technique could be practically utilized.

In a complete assembly, each porous medium model consisted of three plates screwed together to form a box of length 300 mm, and span 109.5 mm. Each model was designed to hold a minimum of 10 rows of rods. Each of the models consisted of rods that cover the entire span of the models. Filling fractions were obtained by varying the depth of the porous medium h, and the channel depth H. Variation of H was made possible by filling the bottom wall of the models with acrylic sheets. The depth of the porous medium was also varied by filling the porous media to required depths (in the case of horizontal models and mesh models), or using various lengths of the rods (as in the vertical and mesh models). The maximum relative standard deviation of the rod heights is estimated to be 1%. As indicated in Table 3.1, in one set of models, horizontal porous media were made to fill the test section of depth H = 83.0 mm. Four filling fractions, h / H = 0.75, 0.74, 0.50 and 0.34 were also obtained in the horizontal models by respective combinations of H = 109.5 mm and h = 82.1 mm; H = 46.0 mm and h = 34.0 mm; H = 109.5 mm and h = 54.8 mm; and H = 41.3 mm and h = 13.9 mm. Furthermore, with H = 54.6 mm and h = 27.2 mm, an additional model of filling fractions of h / H = 0.50 was achieved. As summarized in Table 3.2, for the vertical models, with mean depths of H = 46.0 mm and h = 34.0 mm, H = 61.0 and h = 34.0 mm, and H =73.0 mm and h = 34.0 mm, filling fractions, h / H of 0.74, 0.56 and 0.47 were respectively attained. An additional vertical model of h / H = 0.74 was obtained from mean depths of H =73.0 mm and h = 54.2 mm. For the mesh models, one set of models was made to fill the test section of mean depth H = 83.0 mm. Furthermore, with mean depths of H = 46.0 mm and h = 34.0 mm a filling fraction, h/H of 0.74 was achieved for another set of models. Each of the porous media models was tested by placing them into the section of the test channel reserved for measurement as typified in Figure 3.4.

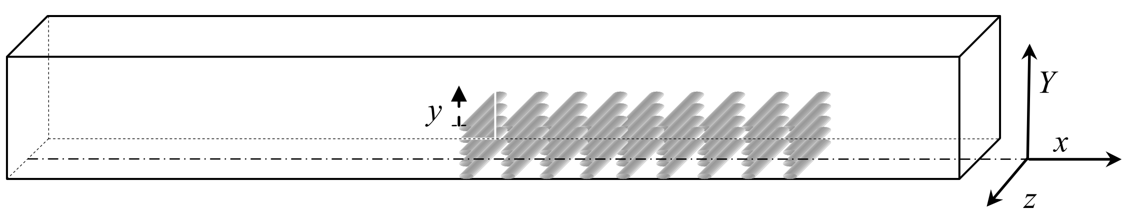

Figure 3.4: A schematic three dimensional view of the test channel with a test round non-staggered horizontal model installed in the channel. The coordinate directions used in the experiments are shown.

3.2.3 The PIV System and Arrangement

A planar particle image velocimetry (PIV) system was used in the velocity data acquisition. The reader is referred to Appendix A for a more detailed description of the PIV system and technique. The typical hardware for the PIV system is schematized in Figure 3.5. In general, the components of the system used are as follows:

a) A laser generator providing a Nd-YAG, 120 mJ / pulse laser at 532 nm wavelength of light to illuminate the flow. Connected to this generator was a set of cylindrical lens used to convert the laser light into a thin sheet.

b) A C–mount 58 mm – 62 mm diameter EX *Sigma* lens, and a *Nikon* lens, equipped with a band-pass filter. These lenses were fitted to a Dantec Dynamic HiSense 4M digital camera that used a charge coupled device (CCD) of 2048 pixel × 2048 pixel chip and pitch 7.4 μm. The camera was used to capture images of the flow section.

c) A hub provided an interconnection and synchronization for the laser, camera, and the computer. This hub also served as a medium for transferring captured images onto the computer.

d) Dantec Dynamic DynamicStudio v.2.30 commercial software was installed on the hard-drive of a 3.0 GHz Pentium 4 computer. This software was used to operate the PIV system, and to process the data that was acquired.

The working fluid was a *Cargille* Immersion liquid (Code 5040) of kinematic viscosity $\nu = 20 \times 10^{-6}$ m^2/s (at 25^{o}C), density $\rho = 848$ kg/m^3 and RI = 1.47. This fluid was specially synthesized in order to match the refractive indices of the acrylic materials of the test channel and porous media models. The fluid was seeded with silver-coated hollow glass spheres of mean diameter 10μm and specific gravity 1.4. These particles were chosen because they are sufficiently large to scatter light detectable by the recording medium. Based on the working fluid and seeding particles, the particle settling velocity and response time were estimated to be 1.77μm/s and 7.98 ps, respectively (The formulas for calculating the particle settling velocity and response time are provided in Appendix A). As these values are very small compared with the typical velocity and time scales used in the experiment, the particles were considered to follow the fluid faithfully.

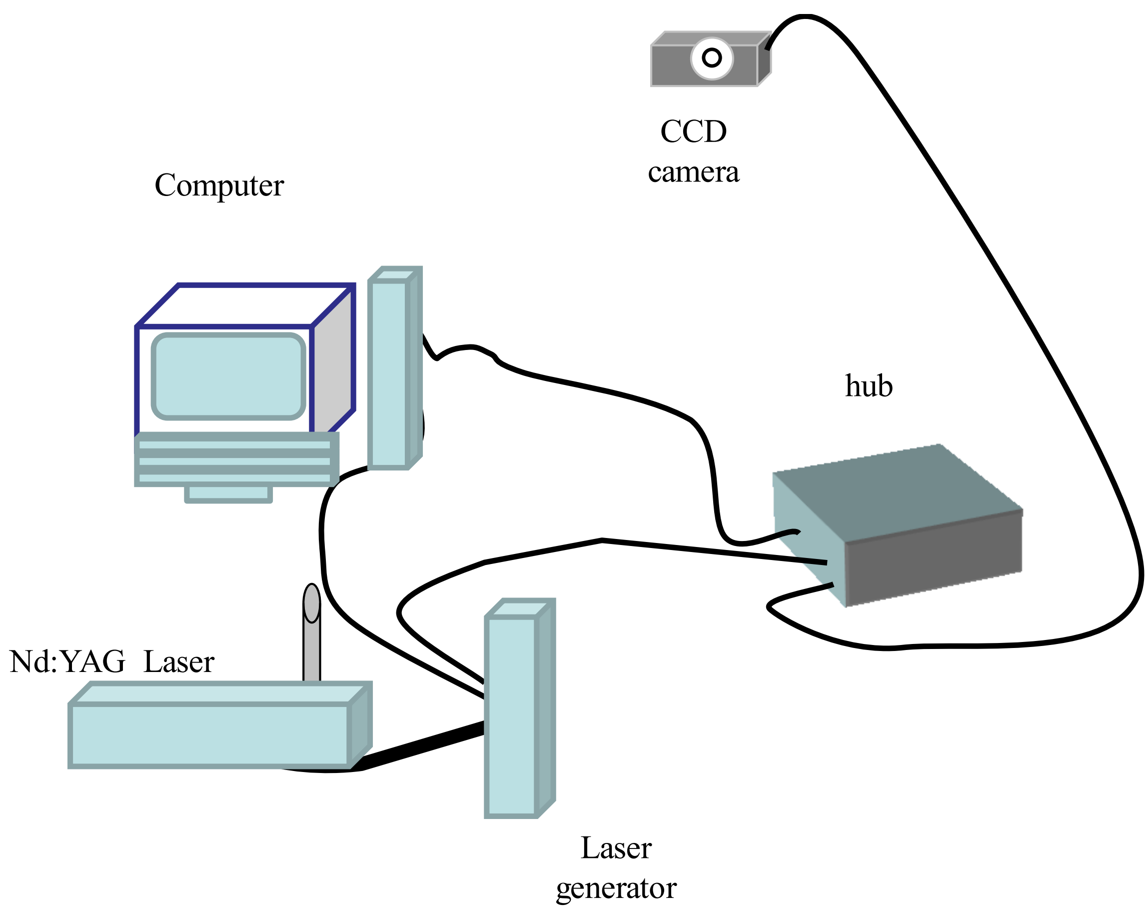

Figure 3.5: Schematic of hardware components of a typical PIV system.

3.2.4 The Pressure System

Differential pressure measurements were made consecutively using two 4000 Series Capsuhelic pressure gauges, rated to measure pressures ranging from 0 to 0.5 and 0 to 1 inches of water respectively. These measurement devices were connected to the pressure ports on one side of the test channel by a system of tubes, brass quick disconnect fixtures, and other accessory connectors. A DTD+ electronic transducer rated to measure 0 to 1 inches of water was also used. This transducer was connected to a digital *Model Pax* read-out meter and a personal computer to display the measurements.

3.2.5 Arrangement of Test Facility

Figures 3.6 and 3.7 show the arrangement and connections of the porous media test facility. As indicated, the test facility was made up of the test channel, a 1 L acrylic reservoir, a single speed centrifugal pump, two piston–spring loaded flow meters (so as to cover the wide range of flow rates to be tested), interconnecting hoses, tubing, and valves. Other important components of the facility are sets of acrylic models (which were placed inside the tank to simulate various flow conditions), collecting trays (placed at various points to collect any leakages), and miscellaneous containers to store drained or dripping fluid. The test channel was seated in a set of metered acrylic plates so that the tank could be moved in the streamwise and lateral directions. The channel and the metered plates were both placed on a black PVC panel, and supported on a structural frame at about 1 meter height from the ground. The laser and the camera were arranged so that they could be traversed along the frame mechanism in a parallel plane. The camera in particular was fixed onto an *x-y* translation stage having a least count of 0.5 mm, while the test channel was also held in an *x-z* stage also with a least count of 0.5 mm.

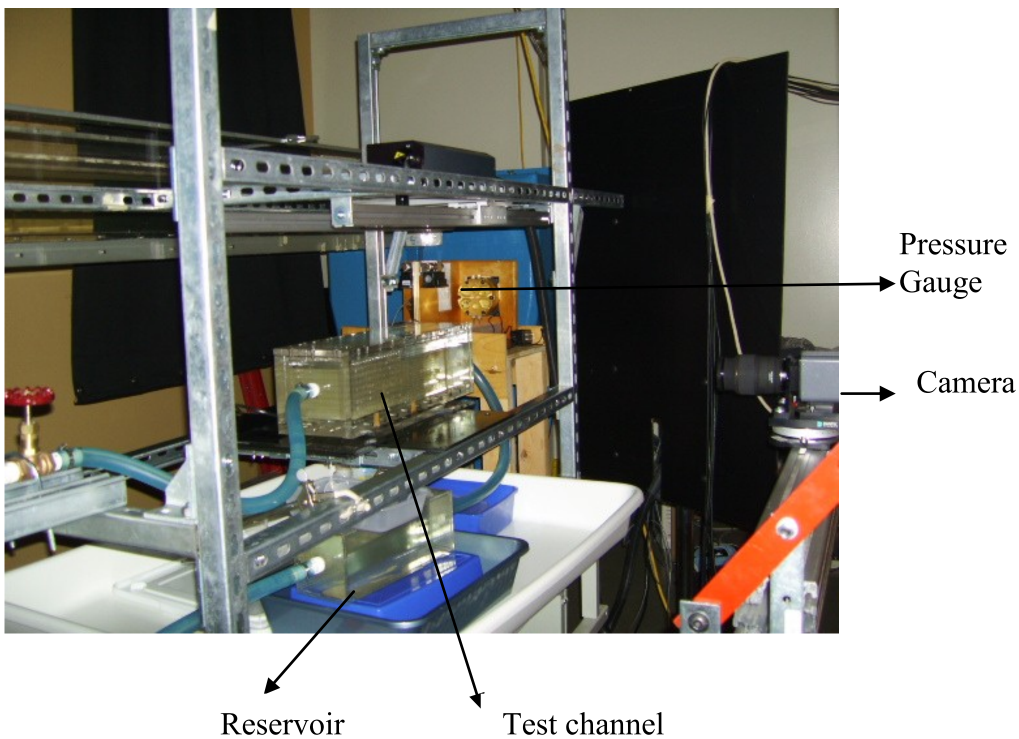

Figure 3.6: Porous media test facility.

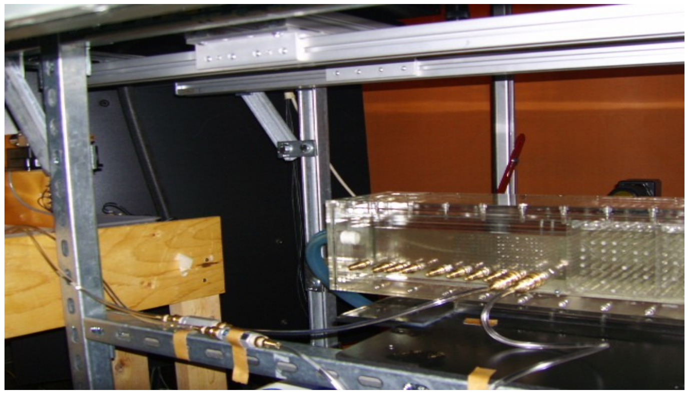

Figure 3.7: A picture showing the rear end of the test channel fitted with pressure port connectors.

3.3 Measurement Procedure

The *Cargille* immersion fluid, seeded with silver-coated hollow glass spheres, was conducted through the flow system as indicated in the circuit in Figure 3.8. The seeded fluid was pumped from the reservoir through a needle valve located downstream of a bypass. It was then passed through the piston flow meter(s), then through needle valve(s) into the test channel, and recirculated back to the reservoir. The needle valves served to regulate various flow rate levels required for specific test conditions. Different test conditions were achieved by inserting models into the measurement section of the test channel.

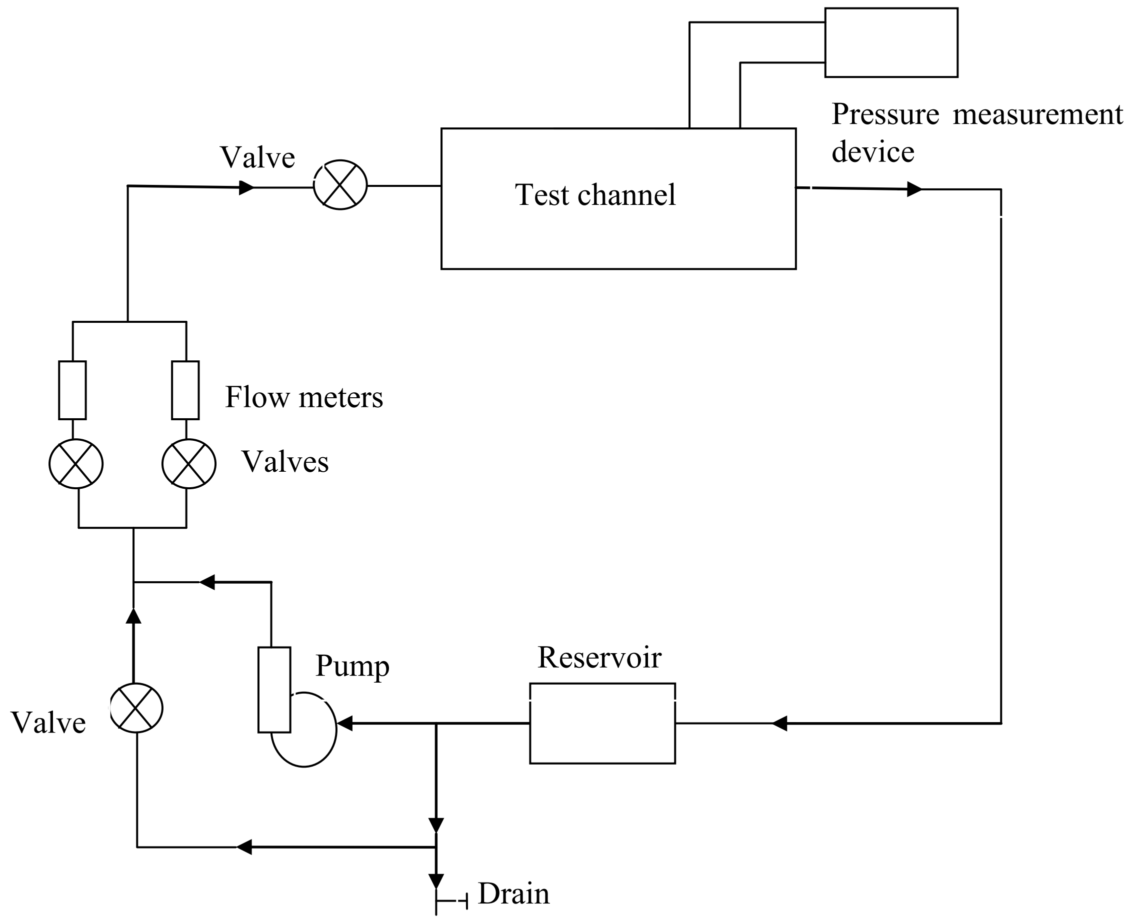

Figure 3.8: Schematic diagram of the flow circuit.

3.3.1 Velocity Measurements

As schematized in Figure 3.9, the PIV measurements were performed in the streamwise –transverse plane along the test channel. Before these velocity measurements were made, the PIV system was calibrated to establish a scale factor between the real-time displacement of the flow displacements (in physical units) and the pixel displacements (in pixel units). This was done by the use of a metallic rule fixed onto a try-square at the measurement section of the channel within the still fluid. A fine focus of the graduations of the ruler was reached by careful adjustments of the camera lens. The required scale factor was then obtained through the use of the Dantec Dynamic DynamicStudio v.2.30 software.

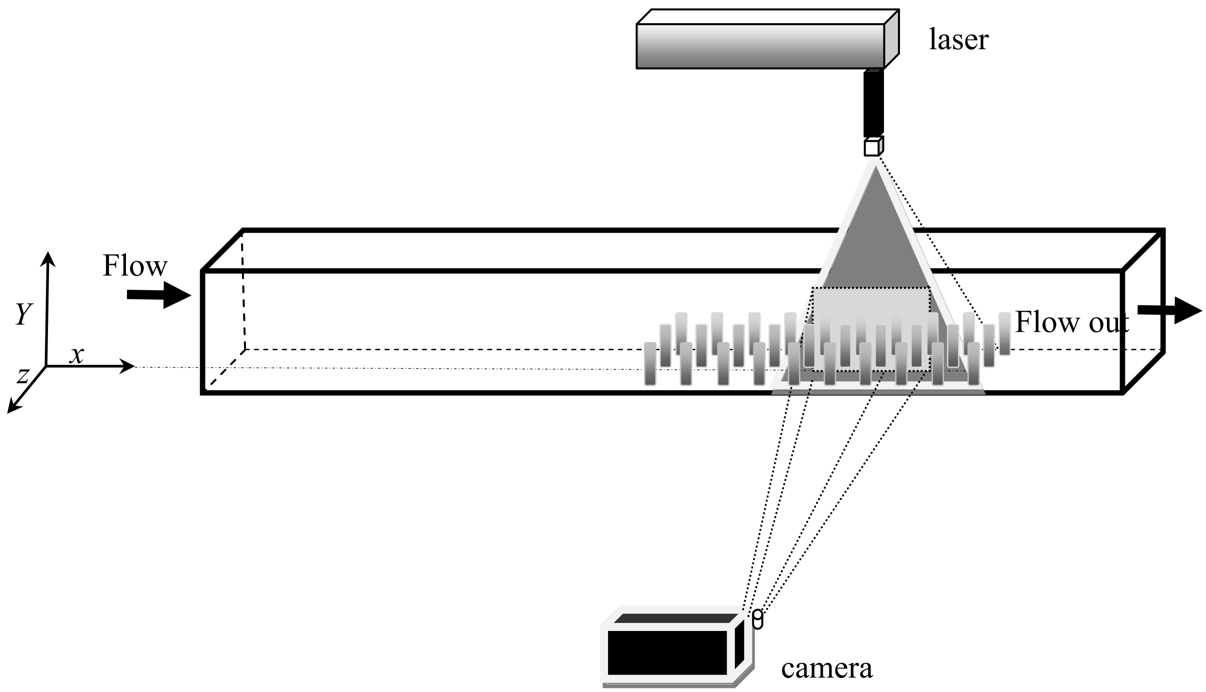

Figure 3.9 A schematic diagram of a typical PIV arrangement with test channel and a porous medium model.

A number of precautions were taken to optimize the PIV measurements. Optimum background contrast and resolution were kept by using requisite camera focal lengths. By ensuring that particle image diameters were of 2.3 pixels (which is close to 2 pixels as recommended by Raffel *et al*. 2007), errors due to peak-locking were kept minimal. Histograms of the typical instantaneous images (provided in Appendix A) confirm this. In order to ensure a good signal to noise ratio, images were acquired using laser pulses, timed in such a way that the particle displacement in an interrogation area (IA) was less than a quarter of the side of the IA (Prasad 2000). In the present experiments, using a typical interrogation window of 32 pixels by 32 pixels, and a sub-pixel accuracy of 0.1 (Scarano and Riethmuller 1999), the dynamic range is estimated to be 80. It is further noted that by choosing requisite time pulses between laser illuminations, the ratio of the displacement field variation to the root mean square of the pixel size and particle image diameter was kept far less than 1. This was done to keep velocity gradient bias errors associated with the potentially large mean velocity gradients near the porous medium–free zone interface, negligible.

The best vector correlations of images were obtained by post-processing captured images using the adaptive-correlation option of Dantec's Dynamic DynamicStudio v.2.30 software. It is important to note that the adaptive-correlation option utilizes a multi-pass fast Fourier transform cross-correlation algorithm to compute the mean displacements of particles within an IA for a period of laser exposure. In connection with this, a Gaussian window function of width 0.1 pixels, and a low-pass Gaussian output filter of width 1.8 pixels were respectively used as an input filter and as a filter on the correlation plane prior to peak detection. Furthermore, two steps of correlation processes were used to ensure that ample valid vectors were obtained. Two iterations were performed at the first step, and then one more followed at the final step. In all of these iterations, the acceptance factor used was 0.05.

Extensive velocity measurements were conducted at various sections of the *x*-*y* plane for various test conditions. Because the thickness of the sheet of laser light illuminating the flow section was approximately 1.5 mm, channel movements along the streamwise-spanwise plane were done in intervals of 2 mm in order to capture the spanwise variations in velocity typically over 2 unit cells of the model porous media.

As mentioned in Chapter 1, in this work, all microscopic quantities are denominated by italicized lower case letters, and their corresponding averaged quantities by italicized upper case letters. For the Cartesian frame of reference used, the components of the microscopic velocity in the streamwise (x), transverse (y) and spanwise (z) directions are designated respectively by u, v, and w. Similarly, averaged velocities in the x, y and z directions are signified respectively by U, V, and W.

To study the variation of the averaged streamwise velocities between rod centers along the transverse direction of horizontal models in particular, a line averaging scheme was used. In this scheme, averages were computed along line $y = c$ at a particular z plane. Thus, the line averaged streamwise velocity was typically calculated as,

$$U_l = \frac{1}{l}\int_0^l u(x, y = c)\, dx \tag{3.3}$$

and the line averaged transverse velocity, similarly as,

$$V_l = \frac{1}{l}\int_0^l v(x, y = c)\, dx \tag{3.4}$$

Additionally, area averaged streamwise and transverse velocities were respectively obtained from averaging microscopic velocities between adjacent rods of spacing l in the following manner

$$U = U_a = \frac{1}{l^2}\int_0^l \int_0^l u(x,z)\, dxdy \tag{3.5}$$

$$V = V_a = \frac{1}{l^2}\int_0^l \int_0^l v(x,z)\, dxdy \tag{3.6}$$

Volume averaged streamwise and transverse velocities were also computed as follows

$$U = U_v = \frac{1}{l^3}\int_0^l \int_0^l \int_0^l u(x,y,z)\, dxdydz \tag{3.7}$$

$$V = V_v = \frac{1}{l^3}\int_0^l \int_0^l \int_0^l v(x,y,z)\, dxdydz \tag{3.8}$$

3.3.2 Differential Pressure Measurement

Differential pressure measurements were obtained concurrently with the velocity measurements. This was done using pressure gauges or an electronic transducer connected to the flow at the time of testing, and recording the two measurements at the same condition. Each of these differential pressure measuring instruments was calibrated under standard conditions prior to measurements. Due to the high sensitivity of these instruments, they were connected and installed so that the potential for any clogging of the unit by seeding particles was kept minimal. To do this, filters were installed between the connections at the channel, and those at the instruments. The pressure measurement instruments were also located at areas isolated from vibrations. Further precautions were taken to ensure that bubbles in the tapping lines were bled off. To optimise the dynamic response of the instruments, the pressure lines were generally short, and of internal diameters of the order of 3 mm.

The differential pressure values measured by the gauges were read off in such a way that errors due to parallax were minimal. The least count of the gauges were respectively 0.05 and 0.1 inches of water, for the 0 – 0.5 and 0 – 1 inches of water ranged 4000 Series Capsuhelic gauges. The least count of the DTD+ electronic transducer was 0.0002 inches of water. Measurements with this transducer were recorded from the digital displays on a meter receiving signals transmitted from the transducer. By connecting the meter to a personal computer, differential pressure data could be obtained as a function of time. The differential pressure measurements were therefore computed from an average of the pressure differences recorded for each round of measurement. Most of the pressure measurements were done with the electronic transducer. This is because its precision was better, compared with the gauges.

3.4 Preliminary Checks

A number of experiments were carried out to: determine the sample size required to attain statistical convergence of velocity data, ascertain the accuracy of the velocity data, optimise the resolution of velocity measurements, verify the dimensionality of the horizontal porous media models, verify the pressure accuracy of pressure measurements, check the entrance effects and the development of flow through models, and to estimate measurement uncertainties.

3.4.1 Sample Size Determination of PIV Measurements

To assess the sample size N, necessary to achieve statistical convergence, measurements of u and v were made for flow through and over various porous media models.

In Figure 3.10, the flow through horizontal model of $\phi = 0.22$ is shown, because that gives a representative view of the statistical convergence in a test section where velocity scatter is expected to be high. Various sample sizes were used. From Figure 3.10, it is clear that the u profiles were indeed independent of the sample size. A minimum sample size of $N = 30$ images was used in subsequent measurements.

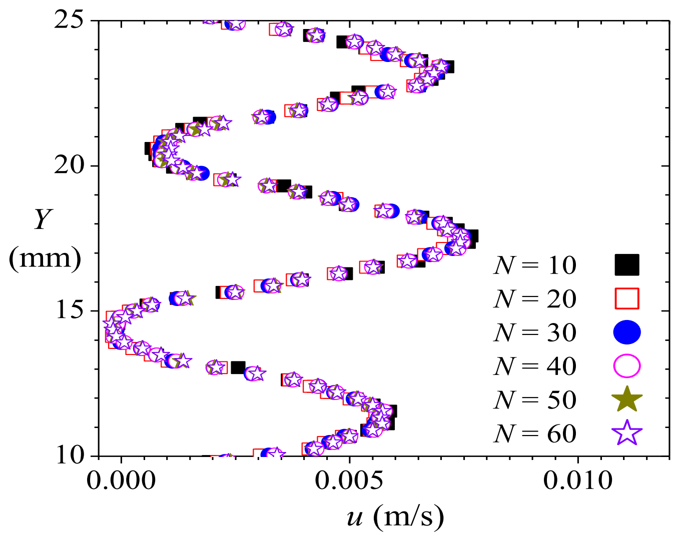

Figure 3. 10: Convergence test using ensemble-averaged streamwise (u) measurements of flow through 0.22 solid volume fraction horizontal model, and at $z = 0$. This result was extracted at $x/l = 6.5$.

3.4.2 Accuracy of Velocity Data

To establish the accuracy of the PIV velocities, fully developed velocity profiles obtained for a plane laminar channel flow in the test section were compared with analytically derived results. In the plots, the velocity u was normalized by the corresponding local maximum velocity, u_{max} whilst the transverse distance was normalized by the depth of the channel flow, *H*. As observed in Figure 3.11 the measured profiles are in good agreement with the analytical profile.

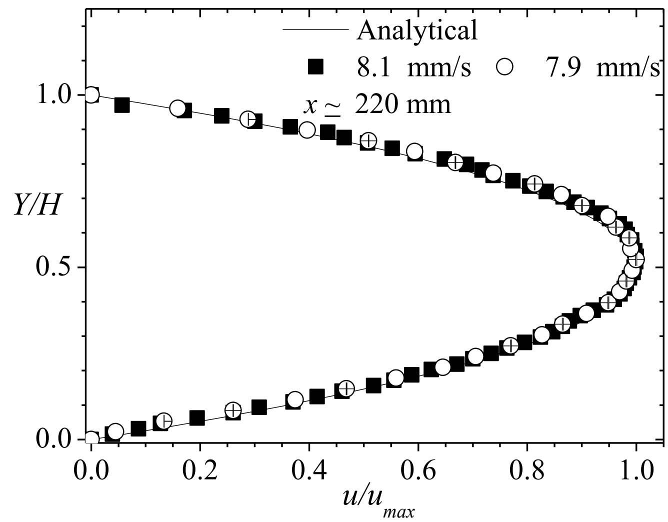

Figure 3. 11: Verifying velocity measurements using fully developed channel flow *u* profiles taken at $z = 0$.

3.4.3 Optimisation of PIV Measurements

PIV provides velocity over a finite IA. Previous works (*e.g.* Agelinchaab *et al.* 2006; Morad and Khalili 2009) shows that the transition layer thickness between the interface and the region further into the porous medium could range from a fraction to about two times the square root of the specific permeability of the porous medium. This thickness spans over the size of typical interrogation windows used in previous works (*e.g.* Shams *et al.* 2003; Goharzadeh *et al.* 2005). Thus, it was necessary to determine the best spatial resolution that could be used to optimize the quality of interfacial velocity and shear rate data obtained with the PIV measurement technique. To this end, an exploratory preliminary experiment was undertaken for this purpose.

As summarized in Table 3.3, various fields of view, IAs, and overlaps of PIV measurements were tested (following precautions that ensured reduced peak-locking, and a good signal to noise ratio as discussed in section 3.3.1) in order to determine that which would produce a highly resolved velocity field while capturing a substantial range of depth of flow. Averaged values of the slip velocity and shear rate at the interface were subsequently compared.

Table 3.3: Summary of fields of view and IA sizes explored in preliminary experiments.

Camera Lens	**Field of View (mm)**	**Interrogation Window for 32 × 32 pixels (mm)**
Nikon	55.65	0.84
	39.84	0.62
EX-Sigma	102.23	1.60
	56.58	0.88
	27.60	0.42
	22.58	0.35
	For IAs ≤ 0.42mm × 0.42 mm using field of view = 27.60 mm	
IA in pixels: pixels × pixels × overlap	**IA in mm ($l_x \times l_y$)**	**IA in pixels: pixels × pixels × overlap**
16 × 16 × 50	0.11 × 0.11	16 × 16 × 50
16 × 16 × 75	0.05 × 0.05	16 × 16 × 75
32 × 16 × 50	0.21 × 0.11	32 × 16 × 50
32 × 32 × 50	0.21 × 0.21	32 × 32 × 50
32 × 32 × 75	0.11 × 0.11	32 × 32 × 75
64 × 64 × 50	0.42 × 0.42	64 × 64 × 50
64 × 64 × 75	0.21 × 0.21	64 × 64 × 75

In a typical first test run on a round non-staggered horizontal model sample, PIV IAs of 0.84 mm × 0.84 mm, 0.62 mm × 0.62 mm, and 0.35 mm × 0.35 mm, obtained from processing data with 32 pixels × 32 pixels IA with 50% overlap were explored. Averaged values of the slip velocity and shear rate at the interface were subsequently compared. In a typical test run on a horizontal model sample, it was observed that slip velocities decreased with increasing sizes of the IA sides such that the slip velocity of the 0.84 mm × 0.84 mm and 0.62 mm × 0.62 mm IAs were respectively ~50% and 10% less that of the 0.35 mm × 0.35 mm measurement. The interfacial shear rate values also decreased with increasing size of the IA side, such that the value obtained for the 0.84 mm × 0.84 mm and 0.62 mm × 0.62 mm IAs were respectively ~85% and 12% less than that of the 0.35 mm × 0.35mm measurements. While the deviations in measurement between the 0.62 mm × 0.62 mm and 0.35 mm × 0.35 mm IAs are well within those that may be attained within the IA sides of the respective measurement, the deviations between 0.84 mm × 0.84 mm and 0.35 mm × 0.35 mm are significantly higher. Subsequently, further tests were run to investigate the effect of IAs and overlaps focussing on the range 0.05 $mm^2 \leq$ IAs $\leq$ 0.42 mm^2 measurements only. Velocity measurements were thus made following precautions (as discussed in section 3.3.1) that ensured reduced peak-locking, and a good signal to noise ratio. Regarding seeding density, the average number of particles ranged from 6 (in 16 pixels × 16 pixels) to 60 (in 64 pixels × 64 pixels). The data were then processed with three kinds of IA pixel sizes (that is, 16, 32 and 64 pixels) and two different IA overlaps (that is 50% and 75%. It should be noted that overlapping IA does not improve spatial resolution). By doing this, the effects of IA and overlaps on velocity measurements were investigated for IA sides ranging from 0.05 mm to 0.42 mm as summarized in Table 3.3. In the table, l_x represents the length of the IA in the streamwise direction, while l_y stands for the length of the IA in the transverse direction.

Sample results of velocity measurements are presented in Figure 3.12 using a round non-staggered horizontal model of solid volume fraction 0.12 and filling fraction 0.50 as a typical case study to show the effect of varying PIV interrogation area sizes and overlaps on the flow measurements, for 0.05 mm^2 $\leq$ IAs $\leq$ 0.42 mm^2. As shown in Figure 3.12, for 0.05 mm^2 $\leq$ IAs $\leq$ 0.42 mm^2 all the results collapse, and the interfacial quantities are equivalent. It may be observed that there is little scatter from measurements within the porous medium. This scatter may be partly due to the relatively low velocities measured. This scatter however does not affect the interfacial flow.

Based on the above-mentioned results, subsequent tests were done with a 58 mm – 62 mm diameter EX *Sigma* lens on the camera using a field of view of 27 mm per side so that the scale factor was typically 1.8. The resultant spatial resolution was about 0.42 mm when the velocity data was processed using an interrogation window of size 32 pixels by 32 pixels. By maintaining an overlap of 50% between neighbouring interrogation areas during the processing of data, additional vectors were provided so that the distance between neighbouring vectors was ~ 0.21 mm.

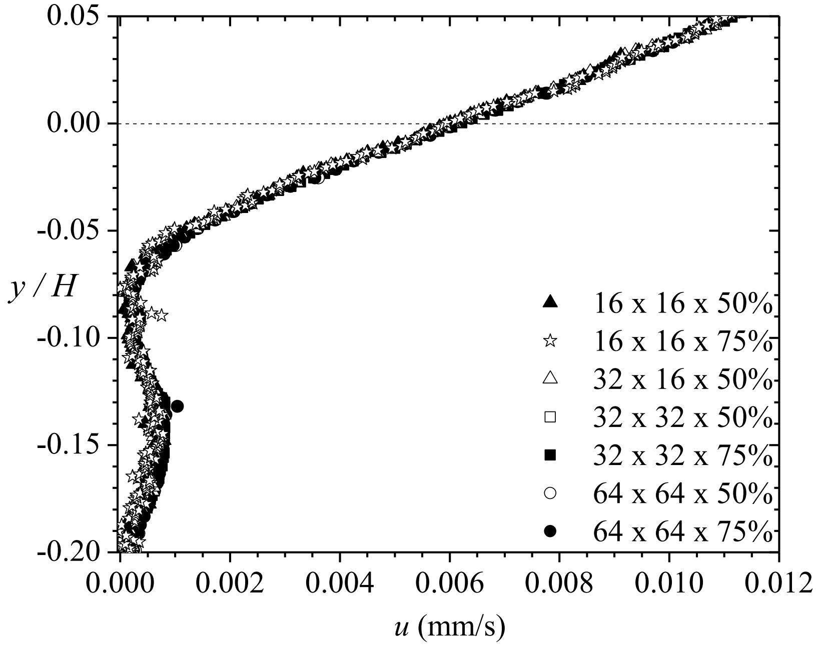

Figure 3. 12: Ensemble-average streamwise velocity distributions of a flow through and over round non-staggered horizontal model sample extracted at $x / l \sim 4.5$ to study the effects of IA sizes and overlaps. The interface is marked by the dashed line.

3.4.4 Dimensionality of Horizontal Porous Media Models

Various porous media models were extensively tested to determine the variation of flow along the span. It was observed that at least within -15 mm < z < 15 mm (which is greater than twice the size of a unit cell for the smallest solid volume fraction, ϕ), the flow variation along the span was negligible. Figure 3.13 shows typical results in which measurements made at various z planes for microscopic flow through and over horizontal porous media non-staggered and staggered models of $\phi = 0.06$, and 0.12 respectively are compared. The results demonstrate that within limits of uncertainty, this two dimensional flow assumption holds within the range of spanwise distance covered. Due to the two-dimensional nature of the horizontal porous medium and interfacial microscopic flows, it was not necessary to take velocity measurements along multiple sections in the spanwise direction. Succeeding measurements were therefore mainly conducted in the $z = 0$ plane.

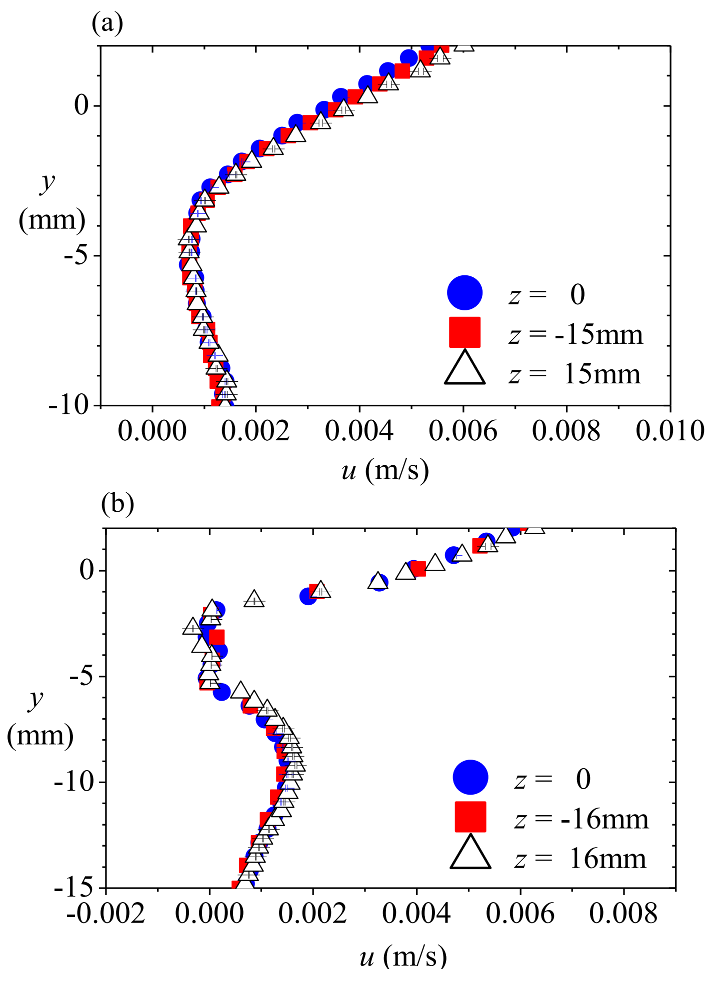

Figure 3.13: (a) Measurements in non-staggered test model of $\phi = 0.06$ at $x/l = 4.5$ are shown; and in (b) are measurements in test model of staggered array of rods of $\phi = 0.12$ at $x/l = 7$ showing that at least within -15 mm< z < 15 mm, the flow variation was negligible for flow within the porous medium and near the interface.

3.4.5 Flow Development in Porous Media and Entrance Effects

Previous works in the literature have demonstrated that after a number of rows of rods, the flow through the porous medium becomes periodic or fully developed (Agelinchaab *et al.* 2006; Arthur 2008). To determine this region of periodicity, measurements were made in the *x-y* plane at $z = 0$, and line averaged velocity measurement were extracted. Figure 3.14 (a) shows a sample result, using profiles of 0.06 solid volume fraction non-staggered horizontal models of 0.75 filling fraction. The results indicate that the flow generally became periodic at $x / l \geq 3$ (that is, from the 4th row onwards). All subsequent measurements were taken at $x / l > 3$ in order to ensure that results were within the region of periodicity.

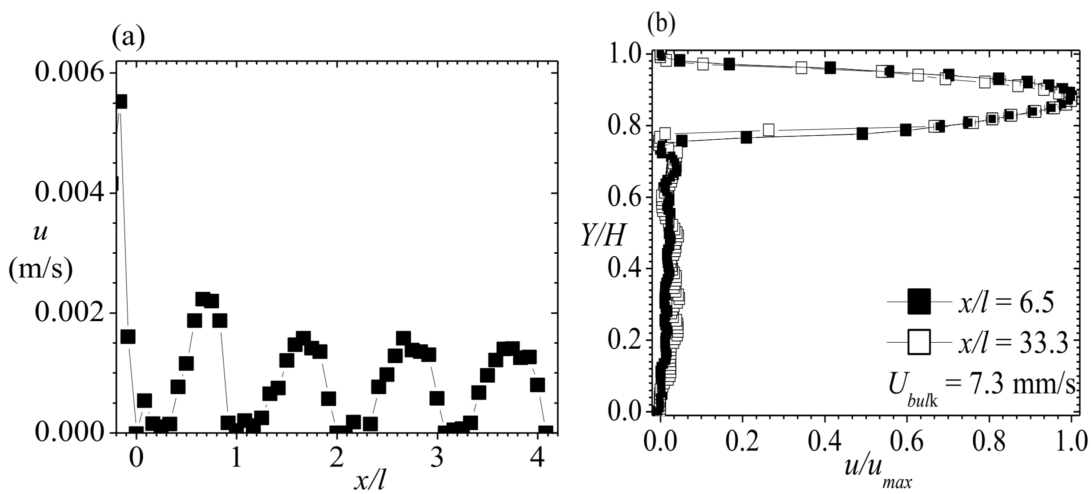

Figure 3. 14: Sample results of data measurements of tests with non-staggered horizontal test model of $\phi = 0.06$ taken at $z = 0$ and extracted at $y / l = -1.6$ to show flow periodicity at $x / l > 3$.; (b) Corresponding points of flow are compared when the most upstream rods are located at $x = 0$ mm (*i.e.* results for $x / l = 6.5$) and $x = 214$ mm (*i.e.* results for $x / l = 33.3$) to determine the entrance effects on flow.

As pointed out in Section 3.2, the flow at $x = 0$ was expected to be reasonably uniform, but not necessarily fully developed. However, previous measurements of flow through and over porous media have been mainly done at locations where the corresponding empty channel flow was fully developed. It was therefore necessary to check whether the state of the flow at the entrance will have any significant effect on the flow within and over the porous media. To do this, measurements were made for flow through and over vertical porous media models of $\phi = 0.12$ when the models were consecutively placed at points in the measurement section for which the most upstream rods were respectively $x = 0$ and 214 mm. Results presented in Figure 3.14(b) show that entrance effects do not have significant effect on the flow through and over the porous medium at the periodic region. The velocity U_{bulk} is the streamwise bulk velocity, and it was calculated as follows:

$$U_{bulk} = \frac{1}{H}\int_0^H U_l\,(Y)dY \tag{3.9}$$

3.4.6 Accuracy of Differential Pressure Data

Further tests were carried out to ascertain the accuracy of the differential pressure measurements. In this case, velocity measurements were made through a horizontal porous medium of solid volume fraction 0.05, and of 100% filling fraction. A 0.05 solid volume fraction horizontal porous medium model was used for this test because for such a low solid volume fraction, there are known results for the value of specific permeability k. For a porous medium of long circular cylinders with uniform radius r (= d / 2), k is given by (Sangani and Acrivos 1982; Jackson and James 1986):

$$\frac{k}{r^2} = \frac{1}{8\phi}\left[-\ln\phi - 1.476 + 2\phi - 1.774\phi^2 + 4.076\phi^3\right] \tag{3.10}$$

This value can then be used to predict pressure drops for measured streamwise seepage velocities, U_d using Equation (1.2). Velocity and pressure measurements were made, focussing the PIV measurements within the core of the porous medium. For the horizontal model used, the seepage velocity U_d was obtained from an area averaging of u in a unit cell of 4 rods. Equation (3.3) was used to compute this average of various velocity measurements in the $z = 0$ plane for a given flow rate. Differential pressure measurements obtained were compared with predictions for the measured U_d using Equations (1.2) and (3.10) for characteristic Reynolds number $Re_{part} = U_d\, d/\nu << 1$ (*i.e.* in the Darcy regime). As shown in Figure 3.15, the agreement between experiments and the previous results is reasonable within experimental uncertainty limits (These limits are given in the next section).

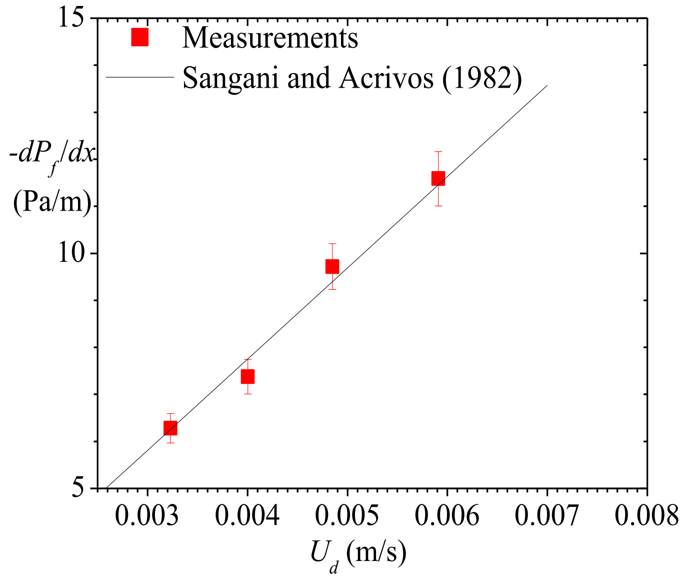

Figure 3. 15: Verifying accuracy pressure measurements. Agreement between present experiment and previous results by Sangani and Acrivos (1982) is reasonable within measurement uncertainties.

3.4.7 Measurement Uncertainties

A formal assessment of the measurement uncertainties was undertaken for velocity and pressure measurements, based on the methodology outlined by Coleman and Steele (1995) and Stern *et al*. (1999). This assessment is detailed in Appendix B. The uncertainty in streamwise velocity u in the free zone is approximately 1% of the local maximum velocity, u_{max}. Within the porous medium, the uncertainty in u within porous media of $\phi = 0.03$ and 0.06 is estimated to be 1.5% of u_{max}. For model porous media of $\phi =$ 0.12, 0.22 and 0.49, the uncertainties of u measured for flows through them are approximately 2.5%, 4% and 5% respectively of u_{max} within the medium due to relatively low optical access and lower velocities measured through these models. For the transverse velocities v, total uncertainties are also estimated to be 1% of u_{max} in the free zone and in porous media of $\phi = 0.03$ and 0.06; and 2%, 3% and 3.5% of u_{max} in model porous media of $\phi = 0.12$, 0.22 and 0.49 respectively. The total uncertainty in the differential pressure measurement is also estimated to be 3% of the average pressure drop. All error estimates are at 95% confidence level, and are signified by error bars in pertinent plots in this work.

3.5 Test Conditions of Experiments

Following preliminary checks, further tests were performed in four series of experiments. These are summarized in Tables 3.4 to 3.8. In this work, test conditions are typically denoted by special names for the sake of convenience. In cases where the models are to be distinguished the horizontal, vertical and mesh models are respectively signified as M_h, M_v and M_m. Similarly, for cases where the kinds of horizontal models are distinguished, the staggered, round and square features of the model are respectively signified by *St*, *Rd*, and *Sq*. Additionally, the particular solid volume fraction, test section depth to porous medium pore ratio (DPR), filling fraction, and bulk Reynolds number Re_{bulk} (= $U_{bulk}\, d/\nu$ or $U_{bulk}\, s/\nu$) are respectively denoted by ϕ, *ff*, *Dp* and *Re* with subscript numbers indicating their respective values. These special denotations are also provided in Tables 3.4 to 3.8.

Table 3.4: Summary of test conditions in 1st series of experiments

Model	ϕ	**Range of U_d (mm/s)**	**Range of Re_d**	**Name**
Horizontal	0.06	2.2 to 79.7	0.4 to 12.7	$M_h\ \phi_6$
Horizontal	0.12	2.6 to 25.0	0.4 to 4.0	$M_h\ \phi_{12}$
Horizontal	0.22	2.2 to 28.1	0.3 to 4.5	$M_h\ \phi_{22}$
Mesh	0.06	2.3 to 37.5	0.8 to 6.0	$M_m\ \phi_6$
Mesh	0.12	1.5 to 17.7	0.2 to 2.8	$M_m\phi_{12}$
Mesh	0.22	0.3 to 4.1	0.1 to 0.7	$M_m\ \phi_{22}$

In the first series of experiments, the focus was on flow through round non-staggered horizontal and mesh model porous media only. This was done to provide velocity and differential pressure measurements of flow through these models in order to determine the equation that best governs porous media flow up to the regime of the onset of inertia effects. The test conditions are summarized in Table 3.4. For further clarity, the geometrical descriptions of the models used in this specific series of experiments are also summarized. The Reynolds number Re_d (= $U_d\, d/\nu$) was used in each case. Here, the seepage velocity U_d was obtained by averaging the velocities within the core of the porous media model. The test conditions are denominated as shown in the last column of the table. It is to be noted that for these experiments, the goal was to obtain measurements to cover the range of Re_d numbers where inertia is expected to be just apparent (*i.e.* $2 < Re_d < 4$ as prescribed by Fourar *et al.* 2004). However, this was not always possible (particularly for M_m ϕ_{22}) because pressure values for $Re_d > 1$ exceeded the range that could be measured by the instruments that were used in this work.

In the second series of experiments, the focus was on providing a comprehensive characterization of the effects of solid volume fraction, rod shape and arrangement, filling fraction and Reynolds number on laminar flow through and over two-dimensional porous media. The pertinent test conditions are summarized in Table 3.5 and 3.6. As shown, only horizontal models were tested. The geometrical characteristics of the respective test models per condition are repeated for further clarity in reference. Table 3.5 gives a summary of test conditions for models of $h / H = 0.75$, while Table 3.6 shows test conditions for $h / H = 0.50$ and 0.34. The range of Re_{bulk} covered was $0.1 < Re_{bulk} < 3$. Each of the test conditions is named as shown in the tables.

In the third series of experiments, tests were performed on all three types of porous media models of the same filling fraction (*i.e.* $ff = 0.74$). The focus was on the comparison of flow through and over two- and three-dimensional models of a wider range of solid volume fraction ($0.03 \leq \phi \leq 0.49$) and Reynolds number ($0.8 < Re_{bulk} < 10.3$). One type of two-dimensional porous medium (*i.e.* horizontal porous medium), and two types of three-dimensional porous media (*i.e.* vertical and mesh models) were tested. The pertinent test conditions are summarized in Table 3.7. The names of the test conditions are shown in the last column of the table.

Table 3.5: Summary of test conditions in 2nd series of experiments for h / H = 0.75.

Rod Shape / Arrangement	ϕ	U_{bulk} **(mm/s)**	Re_{bulk}	h / H	**Name**
Round / Non-staggered	0.06	1.0	0.2	0.75	$Rd\phi_6Re_{0.2}ff_{75}$
Round / Non-staggered	0.06	1.6	0.3	0.75	$Rd\phi_6Re_{0.3}ff_{75}$
Round / Non-staggered	0.06	3.3	0.5	0.75	$Rd\phi_6Re_{0.5}ff_{75}$
Round / Non-staggered	0.06	6.4	1.0	0.75	$Rd\phi_6Re_{1.0}ff_{75}$
Round / Non-staggered	0.06	15.5	2.5	0.75	$Rd\phi_6Re_{2.5}ff_{75}$
Round / Non-staggered	0.12	0.9	0.1	0.75	$Rd\phi_{12}Re_{0.1}ff_{75}$
Round / Non-staggered	0.12	6.1	1.0	0.75	$Rd\phi_{12}Re_{1.0}ff_{75}$
Round / Non-staggered	0.12	1.9	0.3	0.75	$Rd\phi_{12}Re_{0.3}ff_{75}$
Round / Non-staggered	0.12	15.8	2.5	0.75	$Rd\phi_{12}Re_{2.5}ff_{75}$
Round / Non-staggered	0.12	1.6	0.3	0.75	$Sq\phi_{12}Re_{0.3}ff_{75}$
Square / Non-staggered	0.12	4.5	0.7	0.75	$Sq\phi_{12}Re_{0.7}ff_{75}$
Square / Non-staggered	0.12	6.7	1.1	0.75	$Sq\phi_{12}Re_{1.1}ff_{75}$
Square / Non-staggered	0.12	14.6	2.3	0.75	$Sq\phi_{12}Re_{2.3}ff_{75}$
Round / Staggered	0.12	1.9	0.3	0.75	$St\phi_{12}Re_{0.3}ff_{75}$
Round / Staggered	0.12	5.1	0.8	0.75	$St\phi_{12}Re_{0.8}ff_{75}$
Round / Staggered	0.12	6.5	1.0	0.75	$St\phi_{12}Re_{1.0}ff_{75}$
Round / Non-staggered	0.22	0.7	0.1	0.75	$Rd\phi_{22}Re_{0.1}ff_{75}$
Round / Non-staggered	0.22	1.7	0.3	0.75	$Rd\phi_{22}Re_{0.3}ff_{75}$
Round / Non-staggered	0.22	7.0	1.1	0.75	$Rd\phi_{22}Re_{1.1}ff_{75}$
Round / Non-staggered	0.22	14.5	2.3	0.75	$Rd\phi_{22}Re_{2.3}ff_{75}$
Round / Non-staggered	0.49	1.1	0.3	0.75	$Rd\phi_{49}Re_{0.3}ff_{75}$
Round / Non-staggered	0.49	5.3	1.3	0.75	$Rd\phi_{49}Re_{1.3}ff_{75}$
Round / Non-staggered	0.49	10.7	2.5	0.75	$Rd\phi_{49}Re_{2.5}ff_{75}$

Table 3.6: Summary of test conditions in 2nd series of experiments for h / H = 0.50 and 0.34.

Rod shape / Arrangement	$\boldsymbol{\phi}$	$\boldsymbol{U_{bulk}}$ **(mm/s)**	$\boldsymbol{Re_{bulk}}$	$\boldsymbol{h / H}$	**Name**
Round / Non-staggered	0.06	1.8	0.3	0.50	$Rd\phi_6Re_{0.3}ff_{50}$
Round / Non-staggered	0.06	3.3	0.5	0.50	$Rd\phi_6Re_{0.5}ff_{50}$
Round / Non-staggered	0.06	4.6	0.7	0.50	$Rd\phi_6Re_{0.7}ff_{50}$
Round / Non-staggered	0.06	8.6	1.4	0.50	$Rd\phi_6Re_{1.4}ff_{50}$
Round / Non-staggered	0.12	2.6	0.4	0.50	$Rd\phi_{12}Re_{0.4}ff_5$
Round / Non-staggered	0.12	9.1	1.5	0.50	$Rd\phi_{12}Re_{1.5}ff_5$
Square / Non-staggered	0.12	1.1	0.2	0.50	$Sq\phi_{12}Re_{0.2}ff_{50}$
Square / Non-staggered	0.12	9.0	1.4	0.50	$Sq\phi_{12}Re_{1.4}ff_{50}$
Round / Staggered	0.12	1.4	0.2	0.50	$St\phi_{12}Re_{0.2}ff_{50}$
Round / Staggered	0.12	9.4	1.5	0.50	$St\phi_{12}Re_{1.5}ff_{50}$
Round / Non-staggered	0.22	2.7	0.4	0.50	$Rd\phi_{22}Re_{0.4}ff_5$
Round / Non-staggered	0.22	6.0	1.0	0.50	$Rd\phi_{22}Re_{1.0}ff_5$
Round / Non-staggered	0.22	10.7	1.7	0.50	$Rd\phi_{22}Re_{1.7}ff_5$
Round / Non-staggered	0.12	3.0	0.5	0.34	$Rd\phi_{12}Re_{0.5}ff_5$
Round / Non-staggered	0.12	4.7	0.7	0.34	$Rd\phi_{12}Re_{0.7}ff_5$
Round / Non-staggered	0.12	12.6	2.0	0.34	$Rd\phi_{12}Re_{2.0}ff_{50}$

Table 3.7: Summary of test conditions in 3rd series of experiments.

Model	ϕ	U_{bulk} **(mm/s)**	Re_{bulk}	**Name**
Vertical	0.03	5.1	0.8	$M_v\phi_3Re_{0.8}$
Vertical	0.03	51.5	8.2	$M_v\phi_3Re_{8.2}$
Vertical	0.06	7.7	1.2	$M_v\phi_6Re_{1.2}$
Vertical	0.06	48.7	7.7	$M_v\phi_6Re_{7.7}$
Vertical	0.12	6.6	1.1	$M_v\phi_{12}Re_{1.1}$
Vertical	0.12	42.1	6.7	$M_v\phi_{12}Re_{6.7}$
Horizontal	0.12	6.9	1.1	$M_h\phi_{12}Re_{1.1}$
Horizontal	0.12	46.0	7.3	$M_h\phi_{12}Re_{7.3}$
Mesh	0.12	5.0	0.8	$M_m\phi_{12}Re_{0.8}$
Mesh	0.12	41.5	6.6	$M_m\phi_{12}Re_{6.6}$
Horizontal	0.22	5.9	0.9	$M_h\phi_{22}Re_{0.9}$
Horizontal	0.22	38.4	6.1	$M_h\phi_{22}Re_{6.1}$
Horizontal	0.22	41.7	6.6	$M_h\phi_{22}Re_{6.6}$
Mesh	0.22	4.9	0.8	$M_m\phi_{22}Re_{0.8}$
Mesh	0.22	8.5	1.3	$M_m\phi_{22}Re_{1.3}$
Mesh	0.22	43.2	6.9	$M_m\phi_{22}Re_{6.9}$
Horizontal	0.49	3.8	0.9	$M_h\phi_{49}Re_{0.9}$
Horizontal	0.49	22.5	5.4	$M_h\phi_{49}Re_{5.4}$
Horizontal	0.49	30.1	7.2	$M_h\phi_{49}Re_{7.2}$
Horizontal	0.49	41.5	9.9	$M_h\phi_{49}Re_{9.9}$
Mesh	0.49	3.9	0.9	$M_m\phi_{49}Re_{0.9}$
Mesh	0.49	43.3	10.3	$M_m\phi_{49}Re_{10.3}$

A supplementary series of experiments was undertaken to further assess the separate and combined effects of filling fraction and test channel depth-to-porous medium pore ratio on the flow through and over porous media at similar bulk Reynolds numbers. This was done for two-dimensional porous media (*i.e.* horizontal model) and three-dimensional porous media (*i.e.* vertical model). A summary of general test conditions is presented in Table 3.8. For the horizontal models, tests were performed only on round non-staggered models. The test conditions were also kept at a similar Reynolds number (*i.e.* $Re_{bulk} \sim 1$). As for previous experiments, the test conditions are denominated as shown in the last column of the table.

Table 3.8: Summary of test conditions in 4th series of experiments

Model	$\boldsymbol{\phi}$	***h*** **(mm)**	***H*** **(mm)**	***H / l***	***h / H***	$\boldsymbol{U_{bulk}}$ **(mm/s)**	$\boldsymbol{Re_{bulk}}$	**Name**
Vertical	0.12	34.0	46.0	5.75	0.74	6.6	1.1	$M_v\ \phi_{12}Dp_{5.75}ff_{74}$
Vertical	0.12	34.0	61.0	7.63	0.56	7.0	1.1	$M_v\ \phi_{12}Dp_{7.63}ff_{56}$
Vertical	0.12	54.2	73.0	9.13	0.74	7.0	1.1	$M_v\ \phi_{12}Dp_{9.13}ff_{74}$
Vertical	0.12	34.0	73.0	9.13	0.47	6.7	1.1	$M_v\ \phi_{12}Dp_{9.13}ff_{47}$
Horizontal	0.12	27.2	46.0	5.75	0.74	6.9	1.1	$M_h\ \phi_{12}Dp_{5.75}ff_{74}$
Horizontal	0.12	27.2	54.6	6.83	0.50	6.9	1.1	$M_h\ \phi_{12}Dp_{6.83}ff_{50}$
Horizontal	0.12	54.8	109.5	13.69	0.50	7.6	1.2	$M_h\ \phi_{12}Dp_{13.69}ff_{50}$
Horizontal	0.12	82.1	109.5	13.69	0.75	6.1	1.0	$M_h\ \phi_{12}Dp_{13.69}ff_{75}$

Chapter 4

Results and Discussions

4.1 Overview

In this chapter, results of experiments are presented and discussed in order of the series of experiments conducted (as stated in section 3.5). In section 4.2, the discussion is focussed on the study of flow through two- and three-dimensional porous media up to the regime of the onset of inertia, to determine the equation that best applies at that condition. In section 4.3.1, attention is then focussed on laminar flow through and over two-dimensional porous media to characterize the bulk and interfacial flow conditions when various parameters are varied, and to determine the requisite interfacial boundary conditions. Following this in section 4.3.2 is a discussion of results obtained from the comparison of flow through and over two- and three-dimensional models, while extending the range of Reynolds number to cover inertial flows through porous media. In section 4.3.3, results of supplementary series of experiments are discussed to assess the separate and combined effects of filling fraction and test section depth to porous medium pore ratio (DPR) on the flow through and over porous media at similar bulk Reynolds numbers.

Although planar PIV provides a whole flow field of two-dimensional velocity measurements (of which typical vector map is shown in Appendix C), the flow phenomena under consideration were mainly that of spatially averaged distributions, and are presented as profiles of averaged velocity measurements. As all the porous media and porous media-open flow interfacial velocity quantities reported in this chapter were averaged superficially, they are hereafter simply represented by upper case letters of the respective microscopic (pore-level) quantities, without any specification of superficial or intrinsic averaging. Furthermore, velocity measurements were either averaged over lines, areas, or volumes. For clarity, where necessary, all averaged measurements (*e.g.* U, V) and derived quantities (*e.g.* $\dot{\gamma} = dU/dy|_{y=0}$) are distinguished in terms of the mode of averaging by subscripting the quantity by 'l' (*e.g.* U_l, V_l, γ_l) for the case of line averages, 'a' for area averages (*e.g.* U_a, V_a, γ_a), or 'v' for volume averages (*e.g.* U_v, V_v, γ_v).

4.2 Flow through a Porous Medium

The section begins by drawing attention to some important observations from the results of measurements obtained from the first series of experiments. In Figure 4.1, the superficial velocities normalized by the maximum superficial streamwise velocity $U_{d,max}$ measured for the model, are plotted against the normalized pressure drop gradients (*i.e.* friction factor f_{f2}) for the test conditions tested (presented in Table 3.4). This is done for the streamwise components [Figure 4.1(a)] and transverse components [Figure 4.1(b)] of the superficial velocity (respectively U_d and V_d) in a log-linear plot. This is an important depiction of the flow because the presentation of the transverse components in particular in such an experiment is virtually non-existent in the literature. The figure shows that while the streamwise components are in a nearly linear relationship with the pressure drop measurements, the transverse components and the pressure-drop gradients are independent of each other. The transverse velocities are also generally insignificant compared with the corresponding streamwise components. The exception to this is for the horizontal mesh models of 0.22 solid volume fraction (i.*e.* M_m ϕ_{22}), where the streamwise velocities measured are very small ($U_{d,max}$ is 4.1 mm/s).

The log-log plot of the friction factor f_{f2} [= $(-dP_f/dx)$ $(d/\rho_f U_d^2)$] against the characteristic particle Reynolds number Re_d (= $U_d d/\nu$) in Figure 4.2 shows that the friction factor f_{f2} reduces with increasing Re_d. If f_{f2} is interpreted as the ratio of the pressure drag to the most dominant inertial forces along the stream, then inertia appears to be a parameter of interest as Re_d increases.

It is also important to point out from Figure 4.2 that f_{f2} increases with increasing solid volume fraction of the porous medium for a given Reynolds number. Furthermore, at a given Reynolds number, f_{f2} of the mesh models is significantly higher than that of horizontal media. The f_{f2} values of mesh models of solid volume fraction 0.12 and 0.22 (*i.e.* M_m ϕ_{12} and M_m ϕ_{22} respectively) in particular are about ten times the value of the corresponding horizontal porous media (*i.e.* M_h ϕ_{12} and M_h ϕ_{22} respectively). These results indicate then that the pressure drag increases as the porous medium becomes more compact and complex in arrangement, as expected.

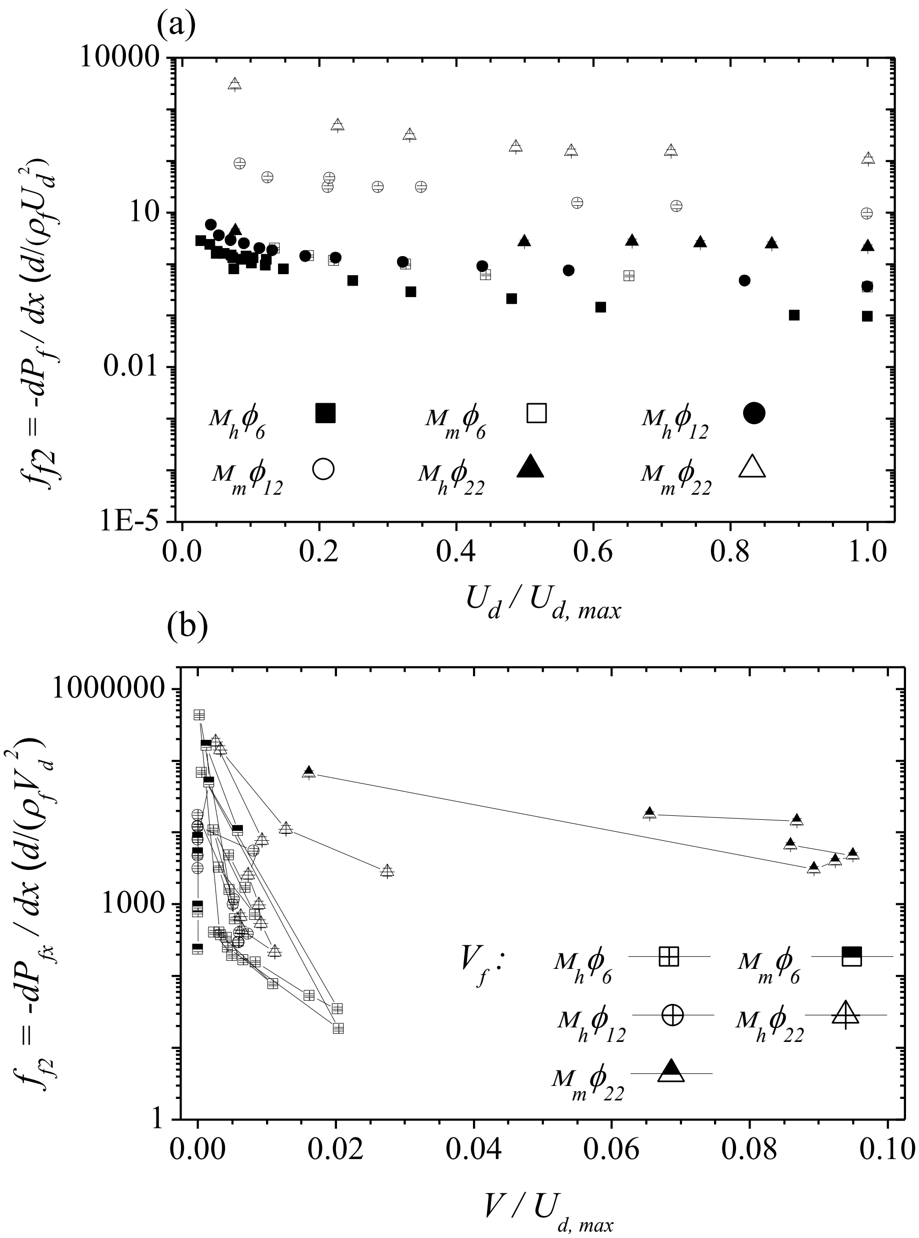

Figure 4.1: Streamwise (U_d) and transverse (V_d) superficial velocities normalized by the maximum streamwise superficial velocity ($U_{d,\,max}$) plotted against the friction factor for various test conditions.

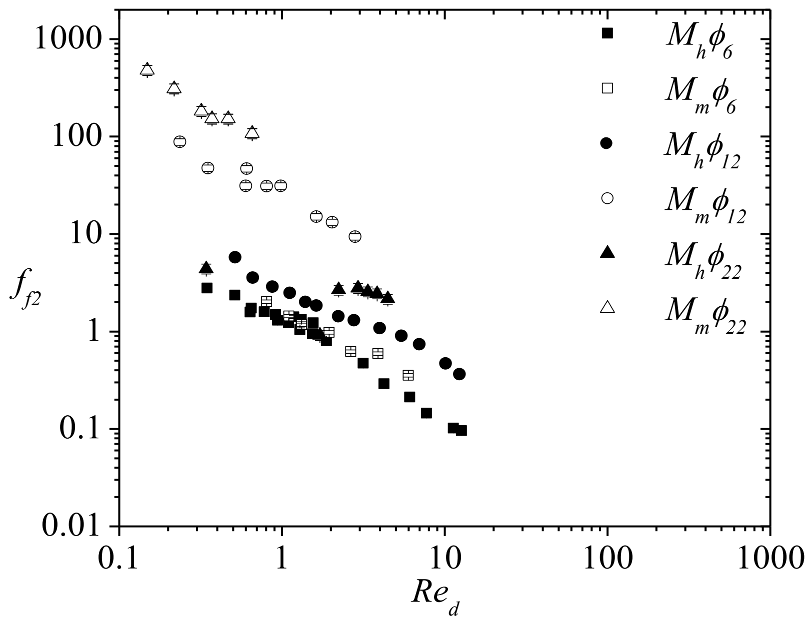

Figure 4.2: The Reynolds number against the friction factor for the test conditions.

To explore the empirical equation that best applies to the flow for the conditions tested, each of the superficial streamwise velocity – streamwise pressure-drop gradient plots was fitted with polynomial (*i.e.* quadratic and cubic) and power (allometric) curves. The forms of the equations fitted to the data are the following

$$-\frac{dP_f}{dx} = a_1 U_d + b_1 {U_d}^2 \tag{4.1}$$

$$-\frac{dP_f}{dx} = c_1 U_d + d_1 {U_d}^3 \tag{4.2}$$

$$-\frac{dP_f}{dx} = e_1 U_d + g_1 {U_d}^2 + h_1 {U_d}^3 \tag{4.3}$$

$$-\frac{dP_f}{dx} = i_1 {U_d}^j \tag{4.4}$$

It may be noted that Equation (4.1) is of the form of the 'Forchheimer quadratic' (F-Q) equation, while Equation (4.2) is of the form of the cubic equation supported by recent works (*e.g.* Couland *et al.* 1988; Rojas and Koplik 1988, Hill *et al.* 2001, Balhoff and Wheeler 2009). This form would be referred to as the 'cubic' equation. Equation (4.3) is of the form suggested by Forchheimer (1901), and it will hereafter be referred to as the 'Forchheimer cubic' (F-C) equation. The Equation (4.4) is of the form of the power law proposed by Izbash (1931). This form would henceforth be referred to as 'Izbash', for convenience. Fitting data to such dimensional equations has been found to be a useful method of providing a preliminary assessment of constitutive equations in porous media studies (Skjetne and Auriault 1999). The results of the present curve fits are summarized in Figures 4.3, and in Tables 4.1and 4.2. The tables provide magnitudes of the curve fitting parameters as well as the adjusted coefficient of determination R^2 of each curve.

Table 4.1 indicates that the adjusted coefficient of determination is highest for the F-C curve. However, this equation has the highest number of empirical parameters, and therefore complicating its practical application. The Izbash equation is a simpler formulation, and it is comparably proficient with the F-Q equation. However, the F-Q equation is preferred because of a higher R^2 it yields when fitted to the experimental data.

It is worth noting however, that the high R^2 of the Izbash equation with the $M_h\phi_6$ and $M_h\phi_{12}$ data in particular indicates that for horizontal models of such low solid volume fraction, the flow at $Re_{part} > 1$, though not strictly Darcian in character, has pressure drops in a quasi-linear relationship with the seepage velocities. This is similar to the flow through pipe at such Reynolds numbers. It therefore indicates that for horizontal media of similar conditions, the porous medium flow behaves like a channel flow.

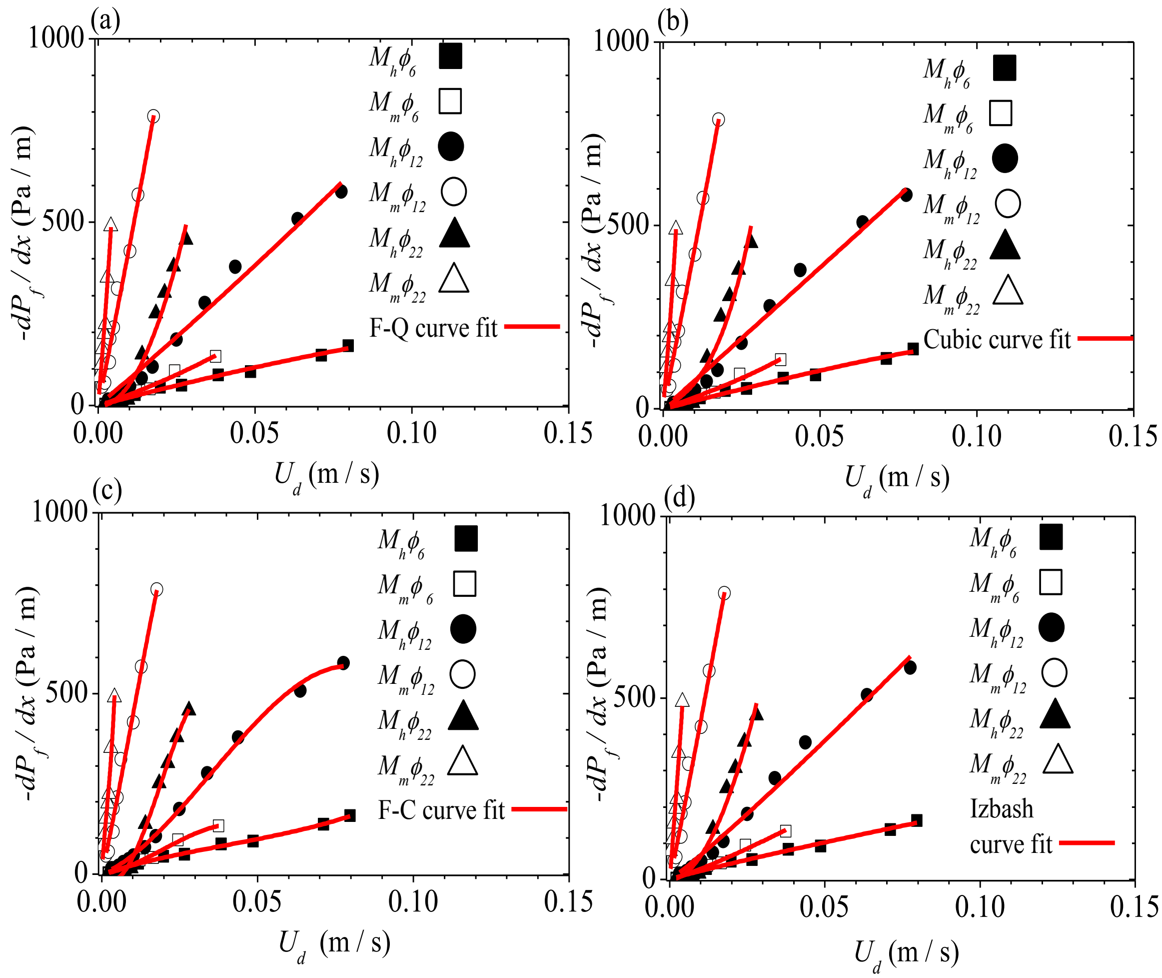

Figure 4.3: Curves of the equations fitted to the experimental results.

Table 4.2 shows that for the mesh (three-dimensional) models, the adjusted coefficient of determination is lowest for the cubic equation, but highest for the F-C equation, followed by the F-Q equation. However the F-C equation is marked by multiple fitting parameters. It is clear then that for that model, the F-Q may be recommended for accuracy and simplicity based on this preliminary assessment.

Table 4.1: Magnitudes (modulos) of curve fitting parameter, and adjusted coefficients of determination for two-dimensional test model cases.

Equations of Fitted Curves, and parameters		**Test Conditions** $M_h\phi_6$	$M_h\phi_{12}$	$M_h\phi_{22}$
F-Q	a_1	2280	7300	682
	b_1	4024	6890	650971
	R^2	0.994	0.991	0.980
	$R^2{}_d$	0	0.647	0.161
Cubic	c_1	2159	7677	5489
	d_1	30378	9269	1865
	R^2	0.988	0.984	0.943
	$R^2{}_d$	0	0.388	0.753
F-C	e_1	2723	3634	11187
	g_1	26563	184280	1927520
	h_1	222200	1747120	33812300
	R^2	0.996	0.999	0.992
	$R^2{}_d$	-9.367	-0.189	0.998
Izbash	i_1	1552	9703	521155
	j_1	0.91	1.08	1.95
	R^2	0.991	0.987	0.968
	$R^2{}_d$	0	0.810	0.980

Table 4.2: Magnitudes (modulos) of curve fitting parameters and coefficients of determination for three-dimensional test model cases.

Equations of Fitted Curves, and parameters		**Test Condition** $M_m\phi_6$	$M_m\phi_{12}$	$M_m\phi_{22}$
F-Q	a_1	2812	41825	97435
	b_1	22368	157059	4972290
	R^2	0.988	0.993	0.987
	R^2_d	0.550	0.103	0.946
Cubic	c_1	3118	42806	102758
	d_1	361875	5605490	949747000
	R^2	0.975	0.984	0.959
	R^2_d	0.419	0.002	-0.057
F-C	e_1	1387	38944	138099
	g_1	160749	743733	26428500
	h_1	273590	24774700	5351890000
	R^2	0.993	0.992	0.987
	R^2_d	-1.536	-1.757	-2.705
Izbash	i_1	6248	53579	178891
	j_1	1.16	1.05	1.08
	R^2	0.982	0.985	0.952
	R^2_d	0.581	0.233	0.750

For a more complete assessment of the flow, Equations (4.1) to (4.4) were non-dimensionalized. The following are the resulting equations:

$$f_{f2}\,Re_d = \frac{a_1 d^2}{\mu} + b_1 \frac{d}{\rho_f} Re_d \tag{4.5}$$

$$f_{f2}\,Re_d = \frac{c_1 d^2}{\mu} + \frac{\nu d_1}{\rho_f} Re_d \tag{4.6}$$

$$f_{f2}\,Re_d = d\,Re_d\,(e_1 + g_1 + 1) + \frac{h_1 \nu}{\rho_f} {Re_d}^2 \tag{4.7}$$

$$f_{f2}\,Re_d = i_1 {U_d}^{j-1} \left(\frac{d}{\rho_f} Re_d\right) \tag{4.8}$$

Equations (4.5), (4.6), (4.7) and (4.8) are respectively the non-dimensionalized forms of Equations (4.1), (4.2), (4.3) and (4.4). The equations are fitted to the data, and presented in plots of the dimensionless resistance (*i.e.* the product of f_{f2} and Re_d) against Re_d, in Figure 4.4. The adjusted coefficients of determination of the fitted curves are also presented as R^2_d in Tables 4.1 and 4.2.

Results show that although the cubic equation has a relatively high R^2_d for two-dimensional porous media, the F-Q and the Izbash equations are better fits when both two- and three-dimensional porous media are considered. Of the F-Q and the Izbash equations, the F-Q equation appears to be the better fit for three-dimensional porous media, whereas the Izbash equation is better in the case of two-dimensional porous media.

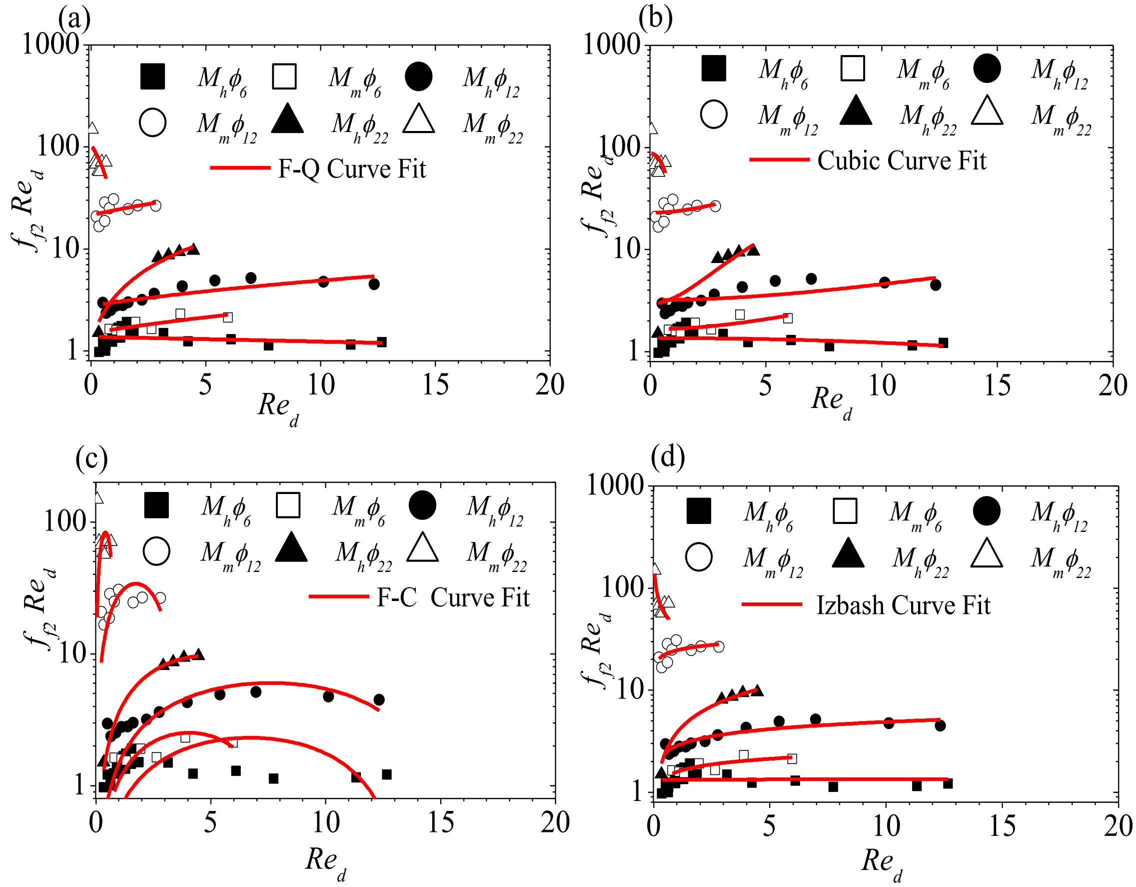

Figure 4.4: Curves of equation fitted to the dimensionless experimental results.

4.3 Flow through and over Porous Media

4.3.1 General Comments

In this section, results obtained from series 2 to 4 (of experiments) are the subjects of attention. For each of these experiments, pertinent results are presented and discussed by first examining the bulk flow through the whole test section, and then focusing on the flow at the interface of the porous medium. In each of these considerations, the bulk Reynolds number effects, solid volume fraction effects, filling fraction effects, as well as the effects of the porous medium structure (such as the staggered or non-staggered arrangements, and the shape of the rod cross-sectional area) on the flow are studied. All discussions are based on averaged streamwise and transverse components of velocity measurements made within the region of periodic flow. These results are presented in Figures 4.5 – 4.32, and in Tables 4.3 – 4.10.

As reviewed in Chapter 2, previous studies have shown the dependence of the interfacial flow on certain key empirical quantities such as the specific permeability k, seepage velocity U_d, slip velocity U_s, shear rate at the interface $\dot{\gamma}$ ($= dU/dy\,|_{y=0}$), the slip coefficient α, and the channel's local maximum velocity U_{max}.

The specific permeability, k of each test model was quantified using empirical values in the literature. This was done because permeability values obtained in the first series of experiments could not be assured to be values pertaining the Darcy regime. Accordingly, for non-staggered models of $\phi < 0.12$, Equation (3.10) was used. For models of $\phi \geq 0.12$

and distance between rod centers l, the following equation due to Sahraoui and Kaviany (1992), and proposed for a similar range of porous medium and arrangement was used:

$$k = 0.062(1-\phi)^{5.1} l^2 \tag{4.9}$$

Specific permeabilities for staggered models of rod radius r and solid volume fraction ϕ were calculated using the following equation by Hellou, Martinez and El Yazidi (2004):

$$k = \frac{\pi r^2}{\phi}(0.0406(1-\phi)^{2.5} - 0.2356(1-\phi)^{3.5} + 0.3422(1-\phi)^{4.5} + \\ 0.5960(1-\phi)^{5.5} - 1.5601(1-\phi)^{6.5} + 0.9092(1-\phi)^{2.5}) \tag{4.10}$$

The specific permeability for each mesh model was also calculated using the following empirical equation by Tamayol and Bahrami (2011):

$$k = 0.032 r^2 (1-\phi)^{0.5}\left[\left(\frac{\pi}{4\phi}\right)^2 - \frac{\pi}{2\phi} + 1\right] \tag{4.11}$$

For each test condition, U_d was also obtained by averaging the streamwise velocities only over a distance depending on the solid volume fraction and filling fractions of the models. This limitation was put in place so as to shield the U_d values from any error emanating from the incorporation of velocities close to the interface and the lower wall boundary layer.

Following Sahraoui and Kaviany (1992) and James and Davis (2001) who performed studies on similar porous media arrays, U_s in this work is defined as the average streamwise velocity "at the plane tangent to the outer edges of the cylinders in the first row" (James and Davis 2001). In the present measurements, it was not always possible to provide the averaged slip velocities at the interface. This is because PIV provides velocities measured over a finite interrogation area, whose center was not always located exactly at the interface. Thus, the uncertainty in the interfacial location for the present experiments is expected to fall within ±0.11 mm which is half the size of an interrogation window.

To determine the shear rate at the interface $\dot{\gamma}$ (= $dU/dy\,|_{y=0}$), a curve of minimum adjusted coefficient of determination of 0.99, was always fitted to six or more U data points located at the region close to the interface. Differentiation of the curve was then performed in the direction of the free flow to obtain the shear rate at the interface. For some of the line averaged data however, following this procedure using measurement data points could not be done without incurring errors. Therefore, there was the need to first utilize a polynomial curve fit using a least square method, and then differentiate the curve smoothly over data points covering a distance of about 0.11mm.

The interfacial flow was investigated using the dimensionless groupings U_s / U_{max}, U_s $/(\dot{\gamma}\sqrt{k}\,)$ and the slip coefficient α. The value of the dimensionless slip velocities U_s / U_{max}, and U_s $/(\dot{\gamma}\sqrt{k}\,)$ is that the former shows the relative effect of the overlying free zone flow conditions on the slip velocity, whereas the latter provides information about the dependence of the slip velocities on the porous medium conditions. The slip coefficient was also obtained using Equation (1.8), relating U_s with U_d.

A location sensitivity test was also undertaken for the slip parameters U_s / U_{max}, U_s $/(\dot{\gamma}\sqrt{k}\,)$ and α. All models typically showed higher sensitivity of α to location, compared with U_s / U_{max} and U_s $/(\dot{\gamma}\,k^{0.5})$. The deviations due to location of line averaged slip parameters were about 30% more than that of volume averages within ±0.11 mm. Taking into consideration these sensitivities, the total uncertainties associated with the volume averaged dimensionless U_s / U_{max} are estimated to be 3% for $\phi = 0.03$, 0.06, and 5%, 8% and 10% for $\phi = 0.12$, 0.22 and 0.49, respectively. The total uncertainties of $U_s / (\dot{\gamma}\, k^{0.5})$ are approximately 5% for $\phi = 0.03$, 0.06, and 8%, 12% and 14% for $\phi = 0.12$, 0.22 and 0.49 respectively. The uncertainties of α are also estimated to be 8% for $\phi = 0.03$, 0.06, and 11%, 13% and 15% for $\phi = 0.12$, 0.22 and 0.49, respectively. All of these uncertainties are at a confidence level of 95%.

4.3.2 Flow through and Over Two-Dimensional Porous Media

The section presents and discusses results of the second series of experiments. Here, the focus is to characterize the effects of solid volume fraction (ranging from 0.06 to 0.49), porous medium rod shape (*i.e.* circular and square rods), porous medium arrangement (*i.e.* staggered and non-staggered arrays), filling fraction (ranging from 0.34 to 0.75), and bulk Reynolds number (ranging from 0.1 to 2.5) on flows through and over two-dimensional porous media.

4.3.2.1. Bulk Flow Characterization

The bulk flow is characterized using the relative magnitudes of the streamwise and transverse velocities, the position of the maximum velocity, percentage flow rate distributions and the ratio of the maximum to bulk velocities (U_{max} / U_{bulk}).

In Figure 4.5, results are presented to show the relative magnitudes of the line averaged streamwise (U_l) and transverse (V_l) velocity data for cases in which the bulk Reynolds number Re_{bulk} is 0.3 and h / H = 0.75. Similar plots are also shown for the corresponding volume averaged streamwise (U_v) and transverse (V_v) velocity data in the same test condition. For $Re_{bulk} \lesssim 1$, the transverse velocities are no more than 3.5% of the local maximum streamwise velocity in the free zone. Indeed, V measurements were for the most part within the bounds of error, and could therefore be neglected. This observation is independent of the solid volume fraction, the mode of arrangement, and the shape of the rod cross-section. Further assessment of data (as presented in Appendix C) indicates that the transverse velocities are at most 7% when $1 \lesssim Re_{bulk} \lesssim 2.5$.

To show the effects of solid volume fraction ϕ on the bulk flow, plots of test results are presented in Figure 4.6 for cases in which Re_{bulk} is 0.3 and $h / H = 0.75$. Figure 4.6(a) in particular, shows the solid volume fraction effects using the percentage of the total mass flow through the test section that is channelled through the free zone. The results, (as further presented in Table 4.3 for other test conditions) show that there is an increase in the proportion of flow channelled into the free zone from 76% to 100% as ϕ is increased from 0.06 to 0.49. A similar trend is also found in the cases of filling fraction $h / H = 0.50$ (shown in Table 4.4), where the average percentage distributions increase from 84% to 95% as ϕ increases from 0.06 to 0.22. This trend (not necessarily the values) also follows that observed by Arthur *et al.* (2009) in their vertical porous media configurations. It follows then that the increase in percentage flow through the free zone when the solid volume fraction increases occurs independent of the filling fraction, or the type of porous medium. In fact, further checks from Tables 4.3 and 4.4 indicate that this effect is not only apparent at $Re_{bulk} = 0.3$, but at higher Reynolds numbers (such as $Re_{bulk} \sim 2$ in Table 4.3, and $Re_{bulk} \sim 1$ in Table 4.4). Thus, the increase in percentage flow into the free zone with an increase in ϕ, is a result of an increase in the resistance to the path of flow within the porous medium.

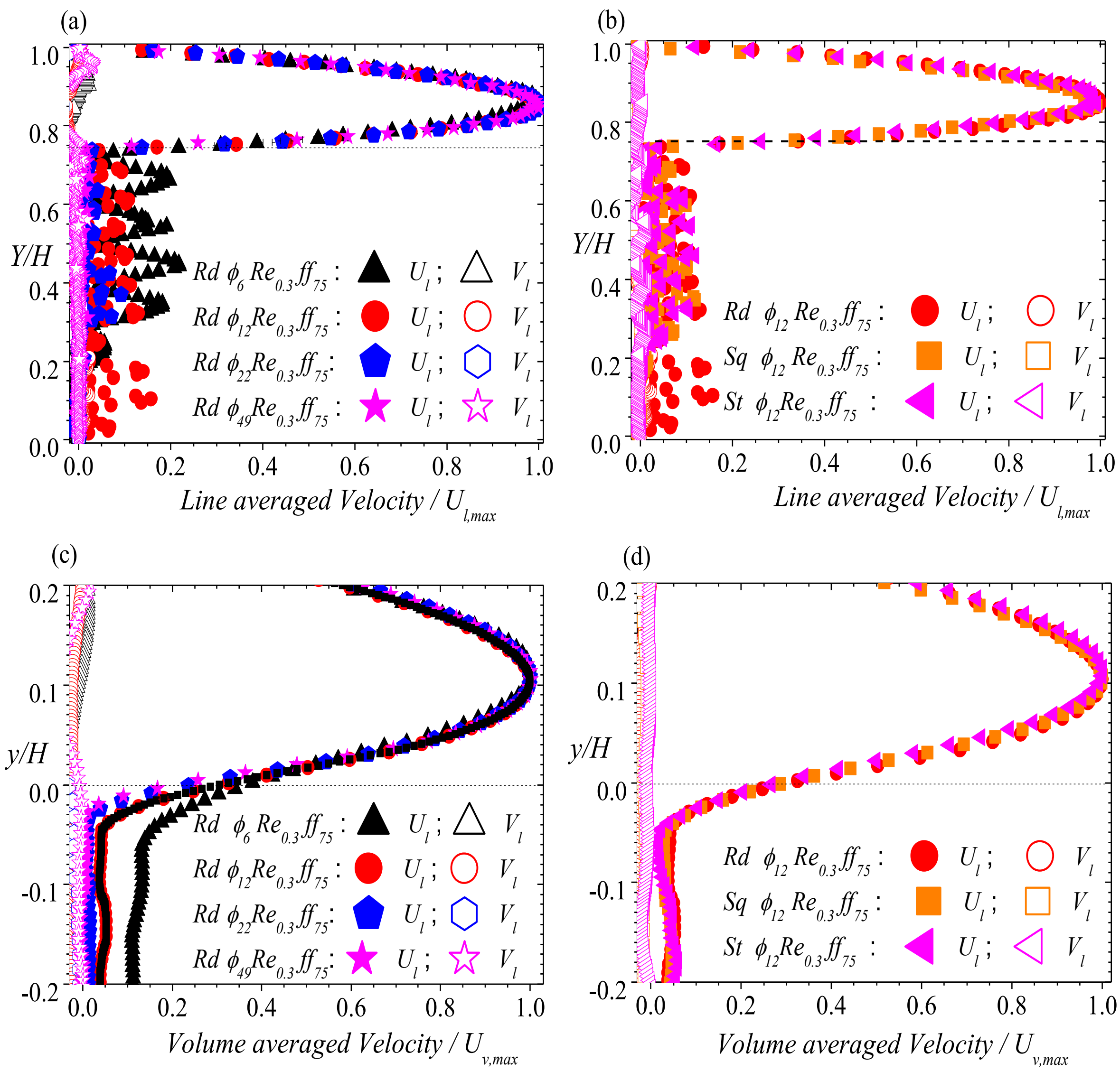

Figure 4.5: The relative magnitudes of streamwise (U) and transverse (V) average velocities. Plots in (a) and (b) show the line averaged plots, while (c) and (d) show volume averaged plots. Plots in (a) and (c) are results of models using round rods, while plots in (b) and (d) compare results obtained for round, and square rods, as well as in-line and staggered arrangements. The dashed line shows the interface.

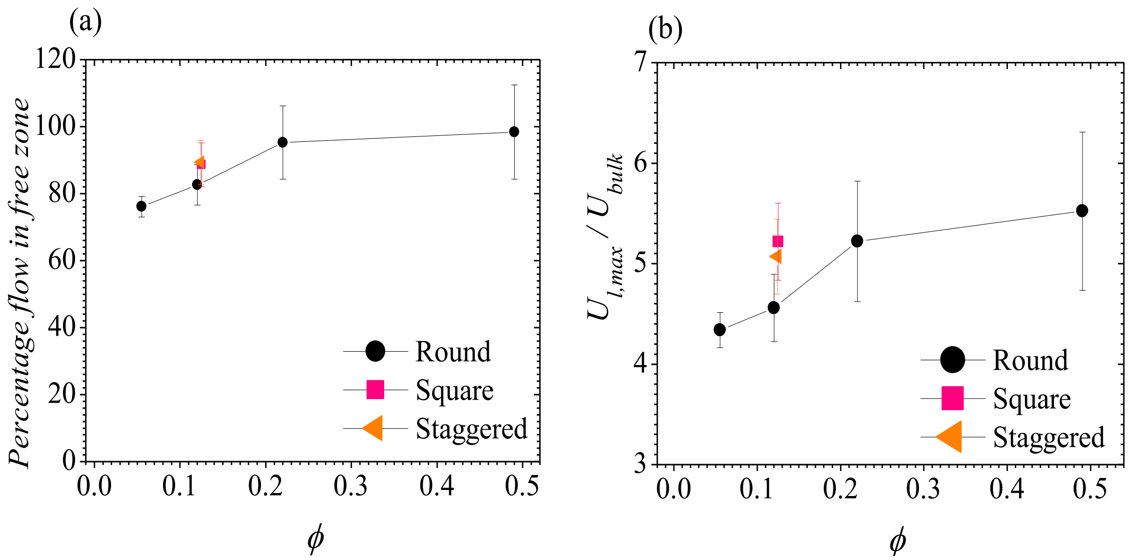

Figure 4. 6: (a) Percentage flow channelled in the free zone; and (b) $U_{l,max}$ / U_{bulk} ratios for the test conditions for which Re_{bulk} = 0.3.

Further effects of the variation of ϕ are also depicted in Figure 4.6(b) using $U_{l,max}$ / U_{bulk} ratios for the same conditions as in Figure 4.6(a). (Only line averaged results of U_{max} / U_{bulk} are shown in the figure because the corresponding volume averaged results are equivalent when experimental uncertainties are considered, as may be verified from Tables 4.3 to 4.6). It may be observed that as ϕ increases from 0.06 to 0.49, $U_{l,max}$ / U_{bulk} increases from 4.6 to ~6, which is the limiting value expected for the case where the porous media is replaced by a solid block. This trend is similarly observed for a filling fraction h / H = 0.50. From Table 4.4, $U_{l,max}$ / U_{bulk} increases from about 2.3 to 2.8, as ϕ increases from 0.06 to 0.22. These values tend towards the limiting value of $U_{l,max}$ / U_{bulk} = 3, for a solid block filling 0.50 of the depth of the test section. It should be noted that Tables 4.3 and 4.4 also show that the increase in $U_{l,max}$ / U_{bulk} with ϕ occurs at Reynolds numbers greater than 0.3. These $U_{l,max} / U_{bulk}$ trends of variation in ϕ are similar to results obtained for vertical models in the literature (Agelinchaab *et al.* 2006).

The effects of porous media rod shape (that is, circular and square rods) and arrangements (that is, non-staggered and staggered arrays) on the bulk flow may be demonstrated using Figure 4.6, and Tables 4.3 and 4.4. As shown, the bulk flow appears to be independent of the porous media rod or shape. At $Re_{bulk} \sim 0.3$ for example, the mean percentage flow channelled into the free zone remains at 87% for non-staggered and staggered arrays of circular rods, and models of square rods of $h / H = 0.75$ and $\phi = 0.12$. The ratios $U_{l,max} / U_{bulk}$ are also unaffected by the porous media structure when experimental errors are considered. The same trend is observed for a filling fraction of 0.50 where the percentage flow remains the same at about 97% when $Re_{bulk} \sim 1.5$ for non-staggered and staggered arrays of circular rods, and models of square rods, so long as ϕ is 0.12. The $U_{l,max} / U_{bulk}$ ratios are also nearly unaffected by the porous media rod shape or arrangement.

Table 4.3: Summary of pertinent results of line averaged data for $h / H = 0.75$.

Name	% of flow through free zone	y / H of $U_{l,max}$	$U_{l,max}$ / U_{bulk}	$k^{0.5}$ (mm)	$U_{l,s}$ (mm/s)	$U_{l,s}$ / $U_{l,max}$	$\dot{\gamma}_l$ (/s)	$U_{l,s}$ / ($\dot{\gamma}_l \sqrt{k}$)
$Rd\phi_6 Re_{0.2} ff_{75}$	73	0.12	4.03	3.0	1.3	0.33	0.47	0.94
$Rd\phi_6 Re_{0.3} ff_{75}$	76	0.11	4.34	3.0	2.1	0.30	0.90	0.78
$Rd\phi_6 Re_{0.5} ff_{75}$	79	0.13	4.61	3.0	4.1	0.27	1.40	0.99
$Rd\phi_6 Re_{1.0} ff_{75}$	63	0.14	3.73	3.0	5.3	0.22	2.24	0.80
$Rd\phi_6 Re_{2.5} ff_{75}$	50	0.16	2.79	3.0	8.3	0.19	4.16	0.68
$Rd\phi_{12} Re_{0.1} ff_{75}$	85	0.10	4.67	1.4	1.3	0.30	0.78	1.21
$Rd\phi_{12} Re_{0.3} ff_{75}$	83	0.10	4.56	1.4	2.6	0.30	1.49	1.25
$Rd\phi_{12} Re_{1.0} ff_{75}$	89	0.17	5.39	1.4	3.0	0.09	2.98	0.73
$Rd\phi_{12} Re_{2.5} ff_{75}$	76	0.15	4.42	1.4	5.1	0.07	7.02	0.52
$Sq\phi_{12} Re_{0.3} ff_{75}$	89	0.10	5.22	1.5	2.3	0.27	1.27	1.23
$Sq\phi_{12} Re_{0.7} ff_{75}$	94	0.14	5.43	1.5	3.3	5.43	3.56	0.65
$Sq\phi_{12} Re_{1.1} ff_{75}$	89	0.16	5.31	1.5	3.8	5.31	3.46	0.75
$Sq\phi_{12} Re_{2.3} ff_{75}$	75	0.16	4.34	1.5	8.4	4.34	5.55	1.04
$St\phi_{12} Re_{0.3} ff_{75}$	89	0.10	5.07	0.9	2.4	0.25	0.85	3.03
$St\phi_{12} Re_{0.8} ff_{75}$	95	0.14	5.36	0.9	3.9	0.14	3.76	1.11
$St\phi_{12} Re_{1.0} ff_{75}$	95	0.15	5.42	0.9	4.9	0.14	1.86	2.87
$Rd\phi_{22} Re_{0.1} ff_{75}$	94	0.09	5.13	0.8	1.0	0.28	0.98	1.33
$Rd\phi_{22} Re_{0.3} ff_{75}$	95	0.10	5.22	0.8	2.3	0.26	1.72	1.74
$Rd\phi_{22} Re_{1.1} ff_{75}$	97	0.14	5.85	0.8	4.9	0.12	2.50	2.51
$Rd\phi_{22} Re_{2.3} ff_{75}$	94	0.13	5.52	0.8	7.4	0.09	4.93	1.94
$Rd\phi_{49} Re_{0.3} ff_{75}$	98	0.10	5.52	0.3	0.8	0.13	0.63	4.92
$Rd\phi_{49} Re_{1.3} ff_{75}$	100	0.14	6.05	0.3	2.3	0.07	0.68	13.14
$Rd\phi_{49} Re_{2.5} ff_{75}$	100	0.14	6.52	0.3	0.9	0.01	1.16	2.94

Table 4.4: Summary of pertinent results of line averaged data for h / H = 0.50 and 0.34.

Name	% of flow through free zone	y / H of $U_{l,max}$	$U_{l,max}$ / U_{bulk}	$\sqrt{k}$ (mm)	$U_{l,s}$ (mm/s)	$U_{l,s}$/ $U_{l,max}$	$\dot{\gamma}_l$ (/s)	$U_{l,s}$/ ($\dot{\gamma}_l \sqrt{k}$)
$Rd\phi_6Re_{0.3}ff_{50}$	84	0.25	2.29	3.0	1.4	0.33	0.36	1.26
$Rd\phi_6Re_{0.5}ff_{50}$	87	0.23	2.40	3.0	2.6	0.32	0.87	1.01
$Rd\phi_6Re_{0.7}ff_{50}$	88	0.25	2.42	3.0	3.7	0.33	1.21	1.03
$Rd\phi_6Re_{1.4}ff_{50}$	91	0.27	2.52	3.0	5.3	0.25	1.90	0.95
$Rd\phi_{12}Re_{0.4}ff_{50}$	93	0.24	2.55	1.4	2.0	0.29	0.80	1.75
$Rd\phi_{12}Re_{1.5}ff_{50}$	97	0.28	2.80	1.4	4.6	0.18	1.95	1.68
$Sq\phi_{12}Re_{0.2}ff_{50}$	91	0.25	2.45	1.5	0.6	0.23	0.23	1.82
$Sq\phi_{12}Re_{1.4}ff_{50}$	97	0.25	2.67	1.5	4.1	0.17	2.00	1.40
$St\phi_{12}Re_{0.2}ff_{50}$	89	0.22	2.38	0.9	0.9	0.27	0.43	2.28
$St\phi_{12}Re_{1.5}ff_{50}$	97	0.27	2.73	0.9	4.7	0.18	2.35	2.16
$Rd\phi_{22}Re_{0.4}ff_{50}$	95	0.22	2.65	0.8	1.9	0.26	1.28	1.86
$Rd\phi_{22}Re_{1.0}ff_{50}$	98	0.27	2.80	0.8	3.5	0.21	2.27	1.96
$Rd\phi_{22}Re_{1.7}ff_{50}$	98	0.30	2.83	0.8	4.4	0.14	3.00	1.87
$Rd\phi_{12}Re_{0.5}ff_{34}$	98	0.34	2.07	1.4	1.3	0.21	0.76	1.25
$Rd\phi_{12}Re_{0.7}ff_{34}$	98	0.33	2.07	1.4	1.8	0.18	1.22	1.03
$Rd\phi_{12}Re_{2.0}ff_{34}$	99	0.35	2.10	1.4	4.1	0.15	2.49	1.17

Figures 4.7 and 4.8, and Tables 4.3 to 4.6, show the effects of filling fraction on the flow using the percentage flow distribution, the position of U_{max}, and the ratio U_{max} / U_{bulk} It may be observed from Tables 4.3 and 4.4 that for ϕ = 0.06 of a non-staggered model of round rods for example, about 76% of the bulk flow is channelled through the free zone when h / H = 0.75 and Re_{bulk} is maintained at 0.3. This value increases marginally to 84% at h / H = 0.50 for the same Re_{bulk}. However, for ϕ = 22% the percentage flow rate

through the free zone remains constant at 95% when filling fraction is changed from 0.75 to 0.50. These results indicate that a reduction in filling fraction generally results in little or no increase in the percentage flow channelled.

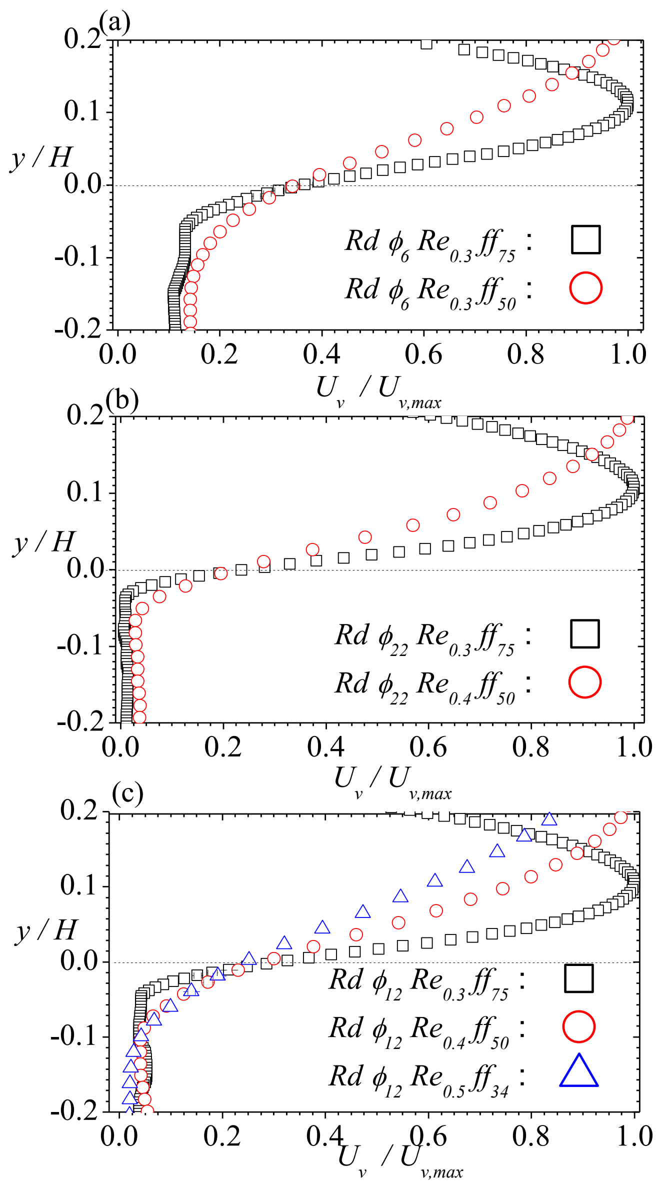

Figure 4.7: The filling fraction effects shown, comparing selected conditions for which Reynolds numbers are nearly the same, and the ϕ = 0.12. Dashed line shows the interface.

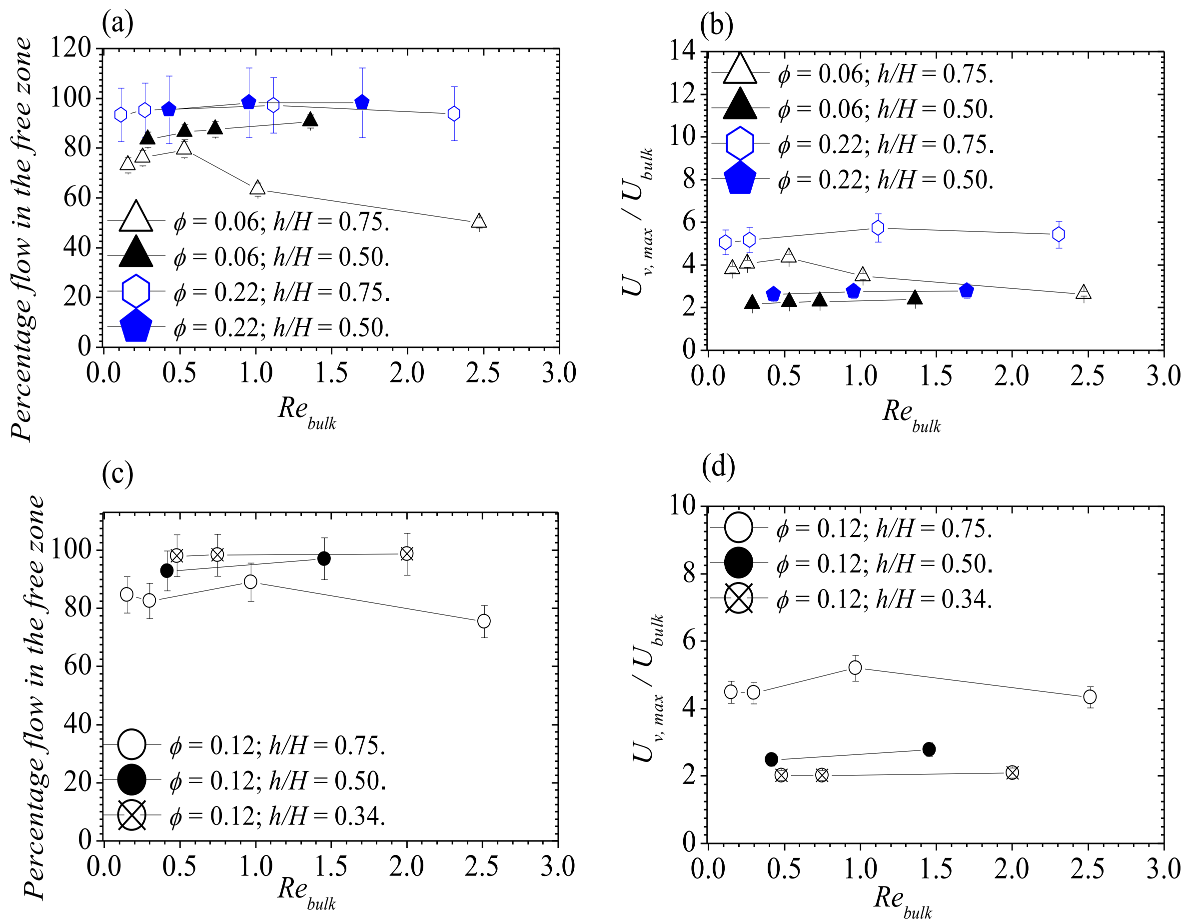

Figure 4.8: The effects of filling fraction using percentage flow rate distributions and $U_{v,max} / U_{bulk}$ ratios for selected test conditions using non-staggered models.

Table 4.5: Summary of pertinent results of volume averaged data for *h/H* = 0.75.

Name	$U_{v,s}$ (mm/s)	$U_{v,max}$ / U_{bulk}	$U_{v,s}$/ $U_{v,max}$	$\dot{\gamma}_v$ (/s)	$U_{v,s}$/ ($\dot{\gamma}_v\sqrt{k}$)	$U_{v,s}$/ ($\dot{\gamma}_v$) (mm)	R^2	U_d (mm/s)	α_v
$Rd\phi_6Re_{0.2}ff_{75}$	1.4	3.80	0.37	0.22	2.14	6.33	0.997	0.6	0.79
$Rd\phi_6Re_{0.3}ff_{75}$	2.4	4.07	0.36	0.40	1.98	5.87	0.998	0.8	0.75
$Rd\phi_6Re_{0.5}ff_{75}$	4.4	4.35	0.30	0.83	1.77	5.23	0.999	1.2	0.78
$Rd\phi_6Re_{1.0}ff_{75}$	6.0	3.48	0.27	1.09	1.87	5.54	0.992	4.0	1.59
$Rd\phi_6Re_{2.5}ff_{75}$	11.3	2.65	0.27	1.60	2.39	7.07	0.950	11.3	157.90
$Rd\phi_{12}Re_{0.1}ff_{75}$	1.3	4.49	0.32	0.39	2.40	3.36	0.993	0.4	0.58
$Rd\phi_{12}Re_{0.3}ff_{75}$	2.6	4.47	0.31	0.79	2.38	3.33	0.997	0.5	0.51
$Rd\phi_{12}Re_{1.0}ff_{75}$	4.7	5.20	0.15	1.54	2.20	3.08	0.985	1.3	0.63
$Rd\phi_{12}Re_{2.5}ff_{75}$	10.5	4.34	0.15	3.44	2.18	3.06	0.984	4.8	0.84
$Sq\phi_{12}Re_{0.3}ff_{75}$	2.4	4.96	0.30	0.68	2.45	3.56	0.996	0.4	0.48
$Sq\phi_{12}Re_{0.7}ff_{75}$	4.8	5.22	0.20	1.45	2.26	3.28	0.997	0.5	0.49
$Sq\phi_{12}Re_{1.1}ff_{75}$	5.4	5.10	0.16	1.63	2.28	3.31	0.998	1.3	0.58
$Sq\phi_{12}Re_{2.3}ff_{75}$	10.2	4.23	0.17	2.84	2.48	3.61	0.997	4.2	0.68
$St\phi_{12}Re_{0.3}ff_{75}$	2.5	4.92	0.27	0.80	3.40	2.81	0.990	0.4	0.36
$St\phi_{12}Re_{0.8}ff_{75}$	5.5	5.24	0.20	1.88	3.16	2.92	0.996	0.4	0.34
$St\phi_{12}Re_{1.0}ff_{75}$	6.0	5.29	0.17	2.01	3.24	2.99	0.997	0.7	0.35
$Rd\phi_{22}Re_{0.1}ff_{75}$	1.0	5.06	0.29	0.43	3.02	2.36	0.998	0.1	0.42
$Rd\phi_{22}Re_{0.3}ff_{75}$	2.2	5.18	0.24	0.92	3.00	2.34	0.998	0.2	0.36
$Rd\phi_{22}Re_{1.1}ff_{75}$	5.1	5.75	0.13	2.11	3.09	2.41	0.999	0.2	0.34
$Rd\phi_{22}Re_{2.3}ff_{75}$	7.0	5.44	0.09	3.22	2.80	2.18	0.994	1.2	0.43
$Rd\phi_{49}Re_{0.3}ff_{75}$	1.2	5.43	0.21	0.60	7.74	2.00	0.998	0.1	0.14
$Rd\phi_{49}Re_{1.3}ff_{75}$	3.4	5.93	0.11	1.79	7.41	1.92	0.998	0.0	0.14
$Rd\phi_{49}Re_{2.5}ff_{75}$	2.9	6.35	0.04	1.8	6.07	1.57	0.998	0.0	0.17

Table 4.6: Summary of pertinent results of volume averaged data for 0.50 and 0.34.

Name	$U_{v,s}$ (mm/s)	$U_{v,max}$ / U_{bulk}	$U_{v,s}$/ $U_{v,max}$	$\dot{\gamma}_v$ (/s)	$U_{v,s}$/ ($\dot{\gamma}_v \sqrt{k}$)	$U_{v,s}$/ ($\dot{\gamma}_v$) (mm)	R^2	U_d (mm/s)	α_v
$Rd\phi_6Re_{0.3}ff_{50}$	1.4	2.17	0.36	0.24	2.02	5.99	0.998	0.6	0.83
$Rd\phi_6Re_{0.5}ff_{50}$	2.8	2.28	0.36	0.48	1.94	5.74	0.999	0.9	0.76
$Rd\phi_6Re_{0.7}ff_{50}$	3.8	2.30	0.35	0.64	1.99	5.87	0.999	1.1	0.72
$Rd\phi_6Re_{1.4}ff_{50}$	5.9	2.39	0.29	1.13	1.77	5.25	0.999	1.8	0.81
$Rd\phi_{12}Re_{0.4}ff_{50}$	2.0	2.49	0.30	0.55	2.53	3.54	0.994	0.4	0.49
$Rd\phi_{12}Re_{1.5}ff_{50}$	4.9	2.79	0.19	1.50	2.35	3.29	0.998	0.4	0.47
$Sq\phi_{12}Re_{0.2}ff_{50}$	0.8	2.38	0.32	0.21	2.72	3.96	0.990	0.2	0.52
$Sq\phi_{12}Re_{1.4}ff_{50}$	5.9	2.60	0.25	1.69	2.38	3.47	0.998	0.5	0.46
$St\phi_{12}Re_{0.2}ff_{50}$	1.1	2.34	0.32	0.31	3.80	3.51	0.985	0.3	0.37
$St\phi_{12}Re_{1.5}ff_{50}$	5.4	2.63	0.22	1.72	3.43	3.16	0.998	0.4	0.32
$Rd\phi_{22}Re_{0.4}ff_{50}$	1.7	2.61	0.25	0.70	3.18	2.48	0.998	0.2	0.36
$Rd\phi_{22}Re_{1.0}ff_{50}$	3.3	2.76	0.20	1.35	3.10	2.42	0.998	0.1	0.33
$Rd\phi_{22}Re_{1.7}ff_{50}$	4.6	2.79	0.15	1.84	3.21	2.51	0.998	0.2	0.33
$Rd\phi_{12}Re_{0.5}ff_{34}$	0.1	2.02	0.23	0.44	0.19	3.22	0.999	0.1	0.48
$Rd\phi_{12}Re_{0.7}ff_{34}$	0.2	2.02	0.22	0.70	0.19	3.01	0.999	0.2	0.52
$Rd\phi_{12}Re_{2.0}ff_{34}$	0.3	2.10	0.18	1.59	0.20	3.00	0.999	0.3	0.50

Tables 4.3 and 4.4 however show that a reduction in filling fraction results in significant shifts in the position of U_{max} towards the top wall. For example, in the case of $Rd\phi_6Re_{0.3}ff_{75}$, the position of U_{max} is y / H = 0.11 while that of $Rd\phi_6Re_{0.3}ff_{50}$ is 0.25. Comparing U_{max} / U_{bulk} values for various filling fractions of ϕ = 0.12, it may be deduced from Figure 4.8(d), and Tables 4.3 to 4.6 that a reduction in the filling fraction from 0.75

to 0.34 leads to a reduction of the ratio from ~5 to ~2. This tends closer towards the 1.5 mark expected for a fully developed channel flow with no porous media in the test section.

To explain these phenomena pertaining filling fraction effects, it should be noted that as the filling fraction reduces, the effective flow path for flow through the porous media is reduced. This reduction is prominent in cases where the pores of the porous medium and the difference in filling fraction are relatively large (such as the case of a change in h / H from 0.75 to 0.34 in non-staggered models of $\phi \leq 0.12$). With such models, a reduction in filling fraction results in an increased or sustained percentage flow distribution through the free zone, and a consequent shift in the position of U_{max} towards the top wall. The ratio U_{max} / U_{bulk} reduces when h / H reduces from 0.75 to 0.34 due to U_{max} increasing at a higher proportion compared with U_{bulk}.

To investigate the Reynolds number effects on the bulk flow, test cases run on the same model but at different Re_{bulk} may be compared. Percentage flow rate distributions in Figure 4.9, and Tables 4.3 and 4.4 show that Re_{bulk} actually plays a significant role in the distribution of flow. However the role of Re_{bulk} is apparently not similar in trend for all the solid volume fractions. For example, as Re_{bulk} increases from 0.1 to ~ 2.5, the percentage flow through the free zone decreases by 32% and 11% for $\phi = 0.06$ and 0.12 non-staggered models respectively. However the deviations in percentage distributions are insignificant for Re_{bulk} changes in other models.

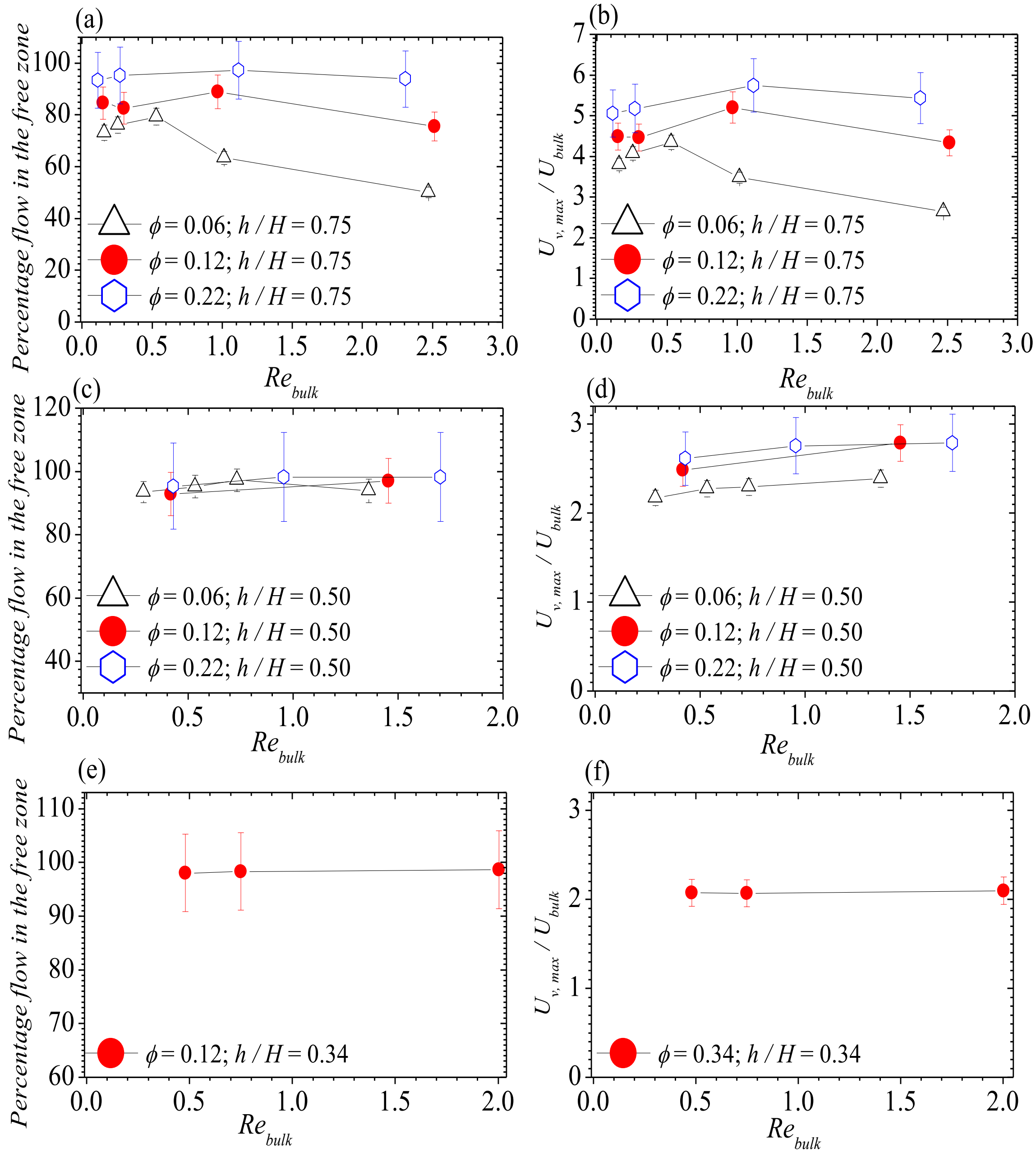

Figure 4.9: The Reynolds number effects shown by percentage flow rate distributions and $U_{v,max}$ / U_{bulk} ratios for selected test conditions of non-staggered models.

Furthermore, the results of the ratio U_{max} / U_{bulk} presented in Figure 4.9 and Tables 4.3 to 4.6 also show that within error limits, $U_{v,max} / U_{bulk}$ ratios of non-staggered models decrease by at most 40% and 9% for $\phi = 0.06$ and 0.12 respectively as Re_{bulk} increases from 0.1 to ~2.5. All other models are relatively unaffected by a change in Reynolds number. Additionally, it is clear from Tables 4.3 and 4.4 that as Re_{bulk} increases from 0.1 to 2.5, the position of $U_{l,max}$ tends to shift towards the top channel wall. The shift is by an average of 34% as Re_{bulk} increases from 0.1 to ~ 2.5 in $h / H = 0.75$, an average of 18% as Re_{bulk} increases from 0.2 to ~1.7 in $h / H = 0.50$, and about 8% as Re_{bulk} increases from 0.5 to 2.0 in $h / H = 0.34$.

To explain the trends observed with changes in Re_{bulk}, it is noted that as Re_{bulk} increases, more flow is expected to be channelled through the free zone until the flow distribution remains constant. A shift in the maximum velocity towards the region where there is least resistance to flow is also expected. However, it should be noted that an increase in flow through the free zone occurs only when the resistance to flow in the free zone is less than that through the porous medium. For more flow to be channelled through the porous medium, the effective drag due to the walls of the rods must be overcome; and this is not easily accomplished under conditions of a low bulk flow, compact non-fibrous porous media (such as $\phi \geq 0.12$, and $h / H = 0.50, 0.34$). When there is a combination of characteristics such as $\phi \leq 0.12$, $h / H = 0.75$ and $h / l \leq 10.27$ in non-staggered arrays however, the resistance to flow by the medium may be overcome even at a low Re_{bulk}. Consequently, with further increase in Re_{bulk}, the large porous medium pores provide a pathway of flow for more bulk flow as Re_{bulk} increases. The result of this is a reduction in the relative percentage flow through the free zone and a reduction in the U_{max} / U_{bulk} ratio as observed in $\phi = 0.06$ and 0.12 non-staggered models.

4.3.2.2. Interfacial Flow Characterization

For each varying factor (*i.e.* solid volume fraction, rod shape, rod arrangement, filling fraction, and Reynolds number), the discussion on dimensionless slip velocities begins by considering first of all, the ratio U_s / U_{max}, followed by the dimensionless slip velocity U_s / ($\dot{\gamma}\sqrt{k}$). It should be noted that both line averaged and volume averaged equivalents of U_s / U_{max} (shown in Tables 4.3 and 4.4, and 4.5 and 4.6 respectively), indicate similar trends of variation, although their values may be different. For U_s / ($\dot{\gamma}\sqrt{k}$) on the other hand, results of the two modes of averaging are typically different in trends. This may be largely attributed to sensitivity of line averaged shear rate to the location.

Regarding ϕ, it is clear from representative test results of Figures 4.10(a) and 4.10(b) that for line and volume averages, U_s / U_{max} decreases with increasing solid volume fraction. Comparing the two averaged ratios of the present results, it is observed that the reduction in the volume averaged ratio as ϕ is increased from 0.06 to 0.49 is over 50%, while that of line averages is just about 16%. Agelinchaab *et al.* (2006) also reported a decreasing trend of U_s / U_{max} with increasing ϕ, even though the porous medium model and filling fractions were different. This shows that the decreasing trend of U_s / U_{max} with ϕ is essentially the result of large increments in the maximum velocity coupled with a reduction in the slip velocities as the resistance in flow through the porous medium section increases.

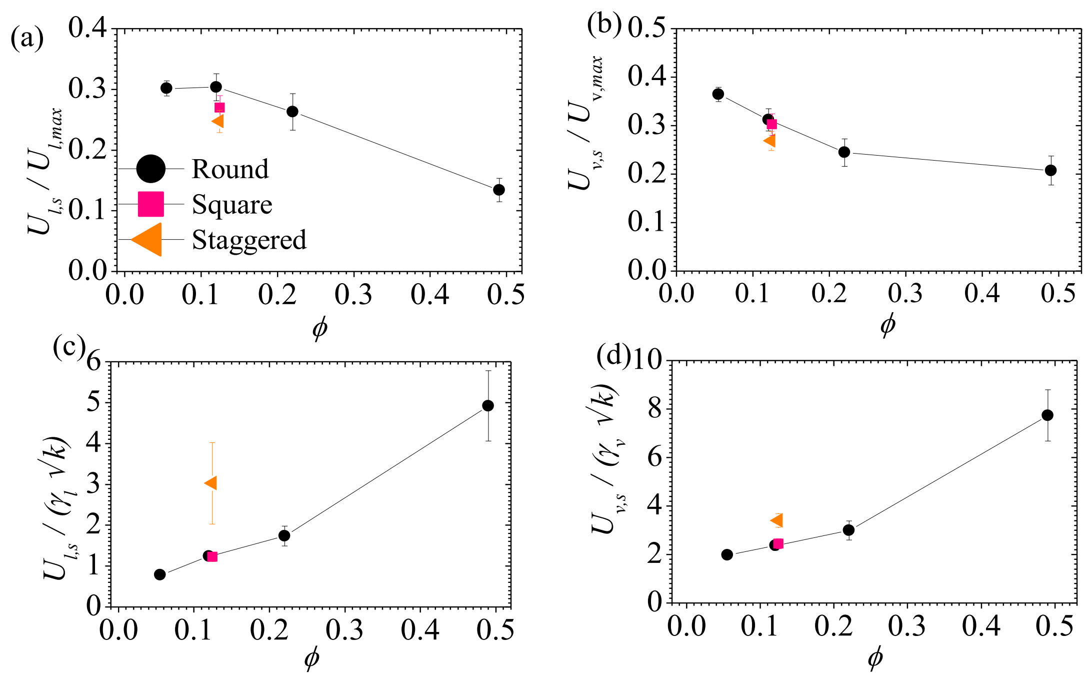

Figure 4.10: Profiles of (a) line averages of U_s / U_{max} (b) volume averages of U_s / U_{max} (c)line averages of U_s / ($\dot{\gamma}$ $\sqrt{k}$) (d) volume averages of U_s / ($\dot{\gamma}$ $\sqrt{k}$) for which Re_{bulk} = 0.3 and h/H = 0.75. The same legend used in (a) applies to all the plots.

The dependence of U_s / ($\dot{\gamma}$ $\sqrt{k}$) on ϕ is also shown in Figure 4.10(b), using test cases at Re_{bulk} = 0.3, and h / H = 0.75. The parameter U_s / ($\dot{\gamma}$ $\sqrt{k}$) generally increases with ϕ. It should be noted that similar trends were also observed for Re_{bulk} ~ 1 and 2. The strong dependence of U_s / ($\dot{\gamma}$ $\sqrt{k}$) on ϕ illustrates the strong influence of local conditions of the porous medium conditions on this dimensionless slip. This observation is however in contrast with previous results (Agelinchaab *et al.* 2006; Arthur *et al.* 2009) where this dimensionless velocity was found to be independent of ϕ in vertical models. This difference in trends of the two results indicates that the type of porous medium has a strong bearing on U_s / ($\dot{\gamma}$ $\sqrt{k}$), as expected. To better understand the trend of this dimensionless slip velocity however, the ratio U_s / $\dot{\gamma}$ (as summarized in Table 4.6) should be examined. This ratio may be interpreted as a measure of the screening length (James and Davis 2001). A comparison of the ratio indicates that as expected, the depth of penetration decreases with increasing ϕ. Thus, the increase in U_s / ($\dot{\gamma}$ $\sqrt{k}$) with ϕ suggests that using $\sqrt{k}$ to approximate the screening length (as done in the past) for such a flow becomes less meaningful as the ϕ increases.

The variation of the rod shape and arrangements are also shown in the U_s / U_{max} ratios in Figures 10(a) and (b), and Tables 4.3 to 4.6. Results show that the staggered circular arrays are about 15% less than non-staggered arrays. However, U_s / U_{max} ratios of square and circular rods are essentially the same. This implies that for a porous medium of ϕ = 0.12, and filling fraction 0.75, the arrangement of the models (whether staggered or non-staggered) is of greater consequence at the slip, than the shape of the rods. Staggered arrays will record smaller slip velocities than the non-staggered arrays. This seems reasonable as staggered models may offer greater resistance to flow at the region close to the interface, compared with the non-staggered models.

As shown in Figures. 4.10(c) and 4.10(d), the arrangement of the rods affects the value of the dimensionless U_s /($\dot{\gamma}$ $\sqrt{k}$). The dimensionless slips for the staggered models are more than 40% higher than that of non-staggered arrays. The relatively high deviation in the case of $U_{l,s}$ / ($\dot{\gamma}_l$ $\sqrt{k}$) is due to the relatively low line averaged shear rates which are highly sensitive to location. This sensitivity is somewhat dampened for volume average results. Comparing the ratios U_s / $\dot{\gamma}$ to give a better explanation of the trends in terms of penetration depth, it may be observed that that of the staggered model is about 22% of the depth of penetration of the non-staggered model when line averages are considered. For the rod shapes, results of Figure 4.10 and Tables 4.3 to 4.6 show that the depths of penetration of the free zone flow into the porous medium are similar in both circular and square.

Regarding filling fraction, the variation of U_s / U_{max}, for various filling fractions are compared for selected test models in Figure 4.11. Figure 4.11(a) and (b) in particular show that the trend is inconsistent. This inconsistency may be due to the varied H / l ratio used in each filling fraction, as indicated in the previous work of James and Davis (2001). The line averaged values of U_s / ($\dot{\gamma}$ $\sqrt{k}$) also do not seem to follow any systematic trend, as shown in Figure 4.11(c). As mentioned earlier, this may be the result of the sensitivity of shear rates when line averages are used. However, Tables 4.5 and 4.6 and Figure 4.11(d) indicate that volume averaged values $U_{v,s}$ / ($\dot{\gamma}_v$ $\sqrt{k}$) are independent of filling fraction. This is expected because the free zone remained unchanged at 27.4 mm in all the filling fractions used in the present work.

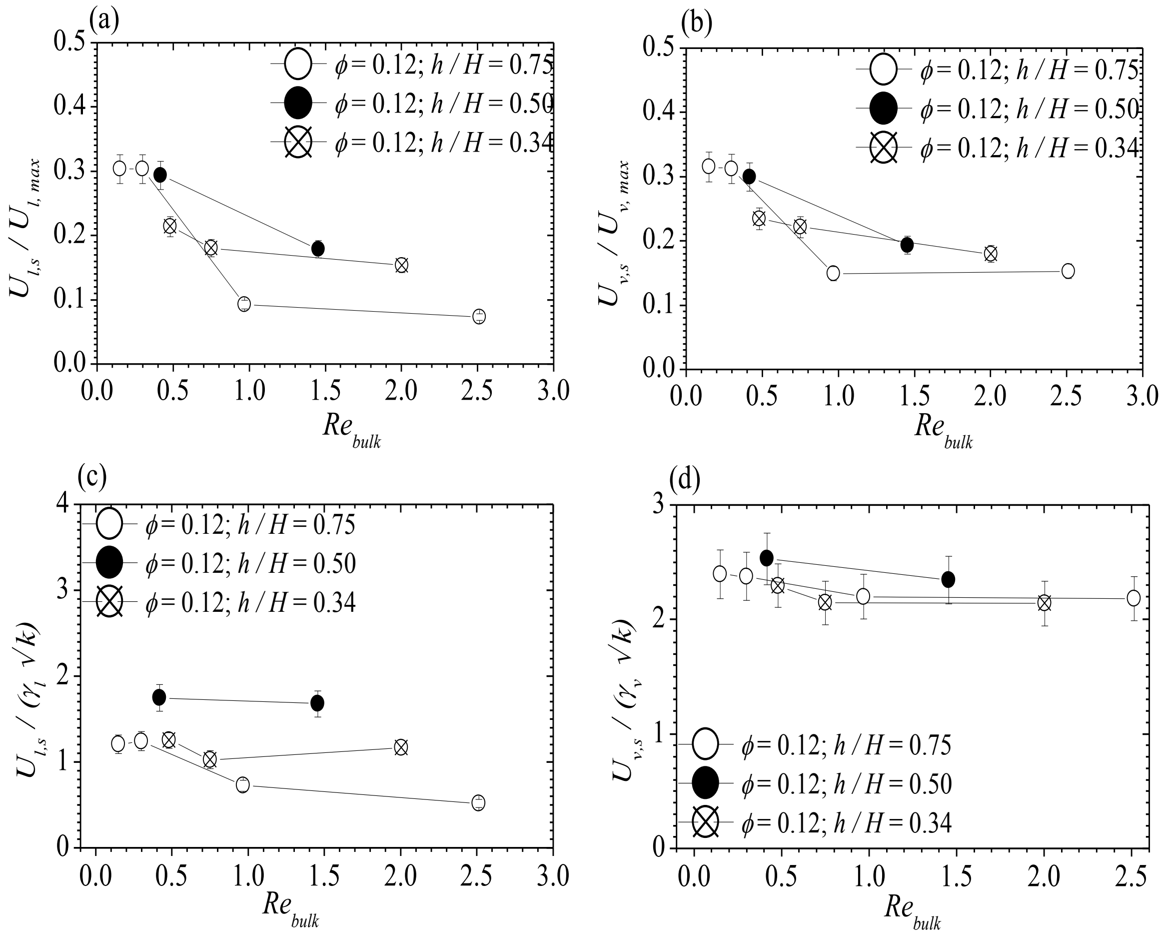

Figure 4.11: Profiles of selected test conditions line averages of U_s / U_{max} in (a) and volume averages of U_s / U_{max} in (b), to show the effect of *h* / *H* on the slip velocity. Profiles of selected test conditions line averages of U_s / ($\dot{\gamma}$ $\sqrt{k}$) in (c) and volume averages U_s / ($\dot{\gamma}$ $\sqrt{k}$) in (d), to show the effect of *h* / *H* on the slip velocity.

The variation of the dimensionless slip velocities with Reynolds may also be drawn from Figures 4.12 and 4.13, and Tables 4.3 to 4.6. It should be noted that both line averaged and volume averaged equivalents of this ratio show similar trends of variation, although their values may be different. Figure 4.12 shows the trend of Re_{bulk} effects for U_s /

U_{max}, using representative cases for which the filling fraction is 0.75 and 0.50. Generally, as Re_{bulk} increases from 0.1 to ~1, $U_{l,s}$ / $U_{l,max}$ and $U_{v,s}$ / $U_{v,max}$ decrease sharply, and then gradually for $Re_{bulk} > 1$. In h / H = 0.75, the decline is at least 40%, and in h / H = 0.50, it is at least 27%. The decline is due to the maximum velocity increasing at a rate much higher than that of the slip velocity.

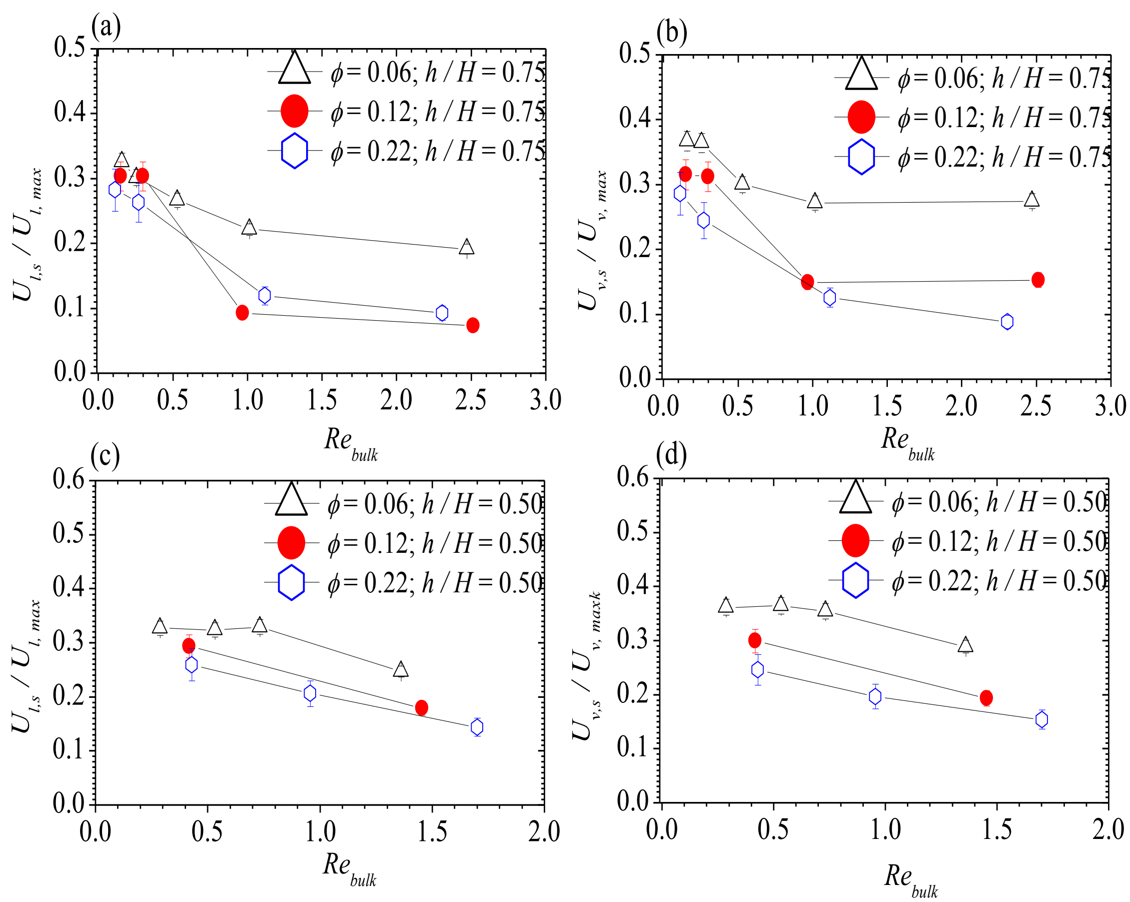

Figure 4.12: Profiles of selected test conditions line averages of U_s / U_{max} in (a) and (c); and volume averages of U_s / U_{max} in (b), and (d), to show the effects Re_{bulk} on the interfacial flow.

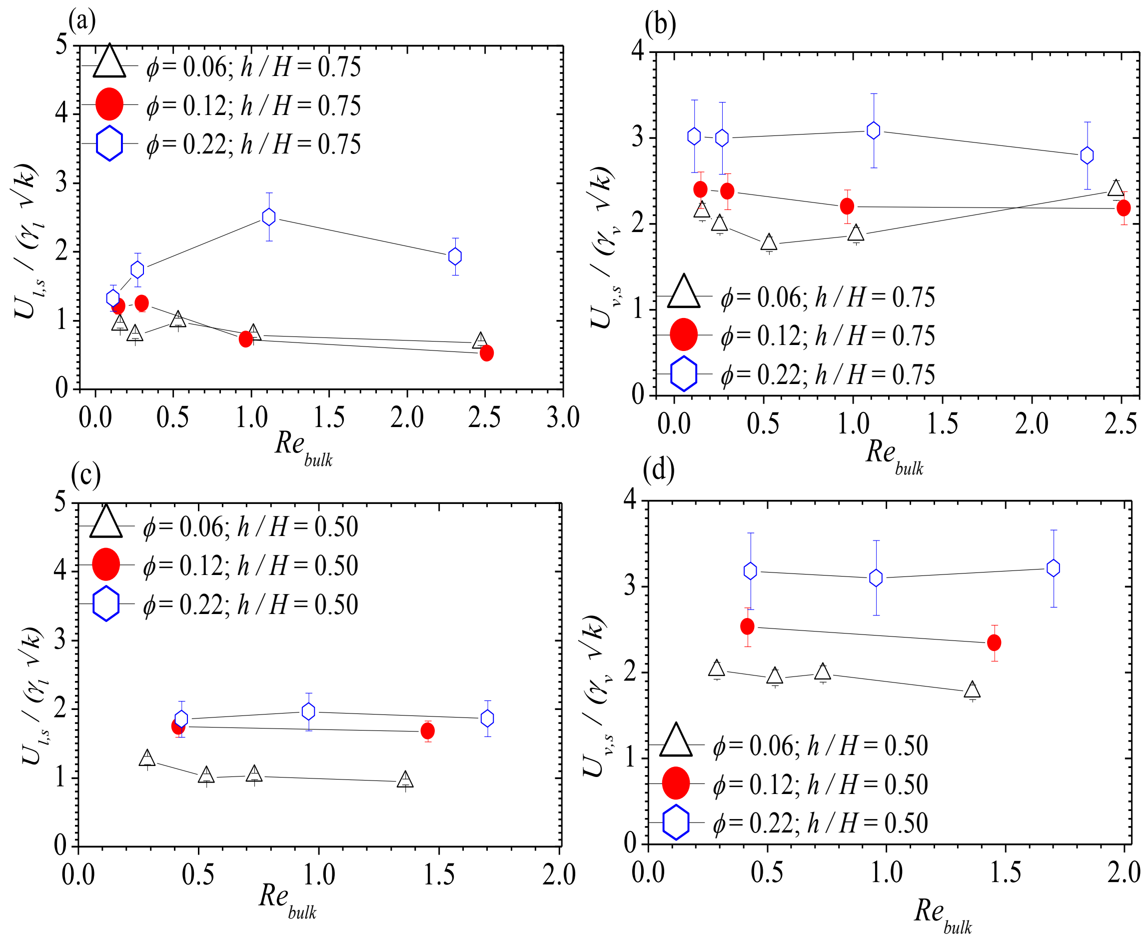

Figure 4.13: Profiles of selected test conditions line averages of $U_s / (\dot{\gamma} \sqrt{k})$ in (a) and (c); and volume averages of $U_s / (\dot{\gamma} \sqrt{k})$ in (b), and (d), to show the effects of Re_{bulk} on the interfacial flow.

Figure 4.13 shows the relationship between the dimensionless $U_s / (\dot{\gamma} \sqrt{k})$ and Re_{bulk}. It should be noted that some of the line averaged values do not seem to follow any systematic trend for models of 0.75 filling fraction [Figures 4.13(a), (c), and Table 4.3]. The volume averaged results [Figures 4.13(b), (d), and Tables 4.5 and 4.6] however, show that taking into consideration measurement uncertainties, there is no dependence of $U_{v,s}$ /

($\dot{\gamma}_v \sqrt{k}$) on Re_{bulk}. This apparent independence between U_s / ($\dot{\gamma} \sqrt{k}$) and Re_{bulk} observed is expected as the bulk flow within the porous medium section of the test cases are generally not affected by inertia. Hence the normalization of the slip velocity by these local parameters associated with the porous medium would yield a dimensionless grouping that is relatively unaffected by Reynolds number. This is unlike the dimensionless U_s / U_{max} whose direct relationship with the free zone (with larger inertial effects) makes it susceptible to greater Reynolds number dependence.

James and Davis (2001) also analyzed slow flow through and over two-dimensional model porous media of comparable filling fractions. Although the solid volume fractions of their model porous media were only up to 0.10, their study is the most comprehensive in the literature available for some form of comparison. Thus, their results for filling fraction 0.75 are plotted with the present results in Figure 4.14 for circular rods of non-staggered arrangements. It may be observed however that the deviations between the dimensionless slip velocity defects $(U_{l,s} - U_d)/\dot{\gamma}_l \sqrt{k}$ of the present results and those of James and Davis (2001) are more than 200% even at ϕ = 0.06, where the solid volume fractions of the two studies coincide. Further comparisons were made with corresponding results of James and Davis (2001; shown in Figure 8 of that publication) and the present work for the case of h / H = 0.50. It was also observed that the deviations between those analytical results and present results are over 300% for cases of comparable solid volume fractions. These deviations are noteworthy given that Tachie *et al.* (2003) also measured dimensionless slip velocity defects for shear flow over porous media, and obtained values which were within 10% of comparable analytical results of James and Davis (2001).

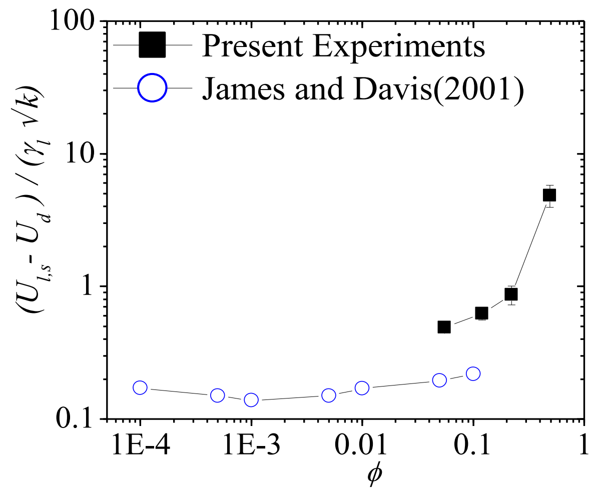

Figure 4.14: The effects of the variation of solid volume fraction on the dimensionless slip velocity studied using line-averaged dimensionless slip velocity defect $(U_{l,s} - U_d) / \dot{\gamma}_l \sqrt{k}$ values to compare with results of James and Davis (2001) wherein h / H is also 0.75.

These apparent discrepancies may be explained by considering the contrasting roles of depth ratios (such as h / H, H / l, and the ratio of the channel depth to the porous medium pore h_f / l) on pressure- and shear-driven flows through and over porous media. As James and Davis (2001) point out in their work, depth ratios are of no consequence in shear flows. On the contrary, in pressure-driven flows, depth ratios play an important role in the flow dynamics, and should be factored in if complete similarity is to be assured between corresponding models. Thus, it is noted that for the case compared in Figure 4.14, the depth ratios h / H, H / l and h_f / l for the present work are respectively 0.75, 9.1 and 2.3, while that of James and Davis (2001) were respectively 0.75, 20 and 5. In another comparable case, the present depth ratios h / H, H / l and h_f / l are respectively 0.50, 4.6 and 2.3 while that of James and Davis (2001) were respectively 0.50, 10 and 5. Although cases compared are of the same h / H, due to significant differences in H / l and h_f / H in all these cases, complete similarities between the present cases and that of James and Davis (2001) were not attained. Therefore, the results of the two studies are not expected to be equivalent, and are thus over 200% in deviation.

It is also pointed out that although the two-dimensional porous media results of Sahraoui and Kaviany (1992) may not be appropriately compared with the present work due to differences in filling fraction, they also reported that the slip coefficient increases with porosity. This interpreted in the present case, means $(U_{l,s} - U_d)/ \dot{\gamma}_l \sqrt{k}$ increases with ϕ, which agrees with the present results as shown in Figure 4.14.

4.3.2.3. Interfacial Flow: Comparison with Literature, and Prediction

The present section on interfacial flow closes by attempting to predict the flow at the interface in light of previous approaches of Brinkman (1947), Beavers and Joseph (1967), and Ochoa-Tapia and Whitaker (1995a) as provided in the literature. As these previous approaches were primarily derived for flows in flow regimes where inertia is not a factor, the comparisons made here are first limited to cases in which Re_{bulk} is far less than 1 (*i.e.* $Re_{bulk} = 0.3$). Only volume averaged data are used in this section. It may also be noted that due to the periodic nature of the flow, the streamwise gradient of the volume averaged transverse velocity is zero, so that this gradient represented in the Equation (2.12) proposed by Jones (1973) is of no value here.

In Chapter 2, the application of the Brinkman equation to describe the flow near the interface was briefly reviewed. Due to the difficulty in modelling the apparent viscosity in this equation, two models of this viscosity are usually utilized. The models are $\mu / \mu' = 1$, which Brinkman (1947) used; as well as $\mu / \mu' = \alpha^2$, advanced by Neale and Nader (1974). To verify the applicability of these models in the present work, volume averaged data from the present experiments are compared with the models. The comparisons are made in Figure 4.15. Predictions from the use of the Brinkman equation are based on the following volume averaged form of the solution of the Brinkman equation valid in the porous medium (Neale and Nader 1974; Gupte and Advani 1997)

$$U_v(y) = U_d + (U_{v,s} - U_d)\mathbf{exp}\left[\frac{y}{(\sqrt{k\mu' / \mu})}\right] \tag{4.12}$$

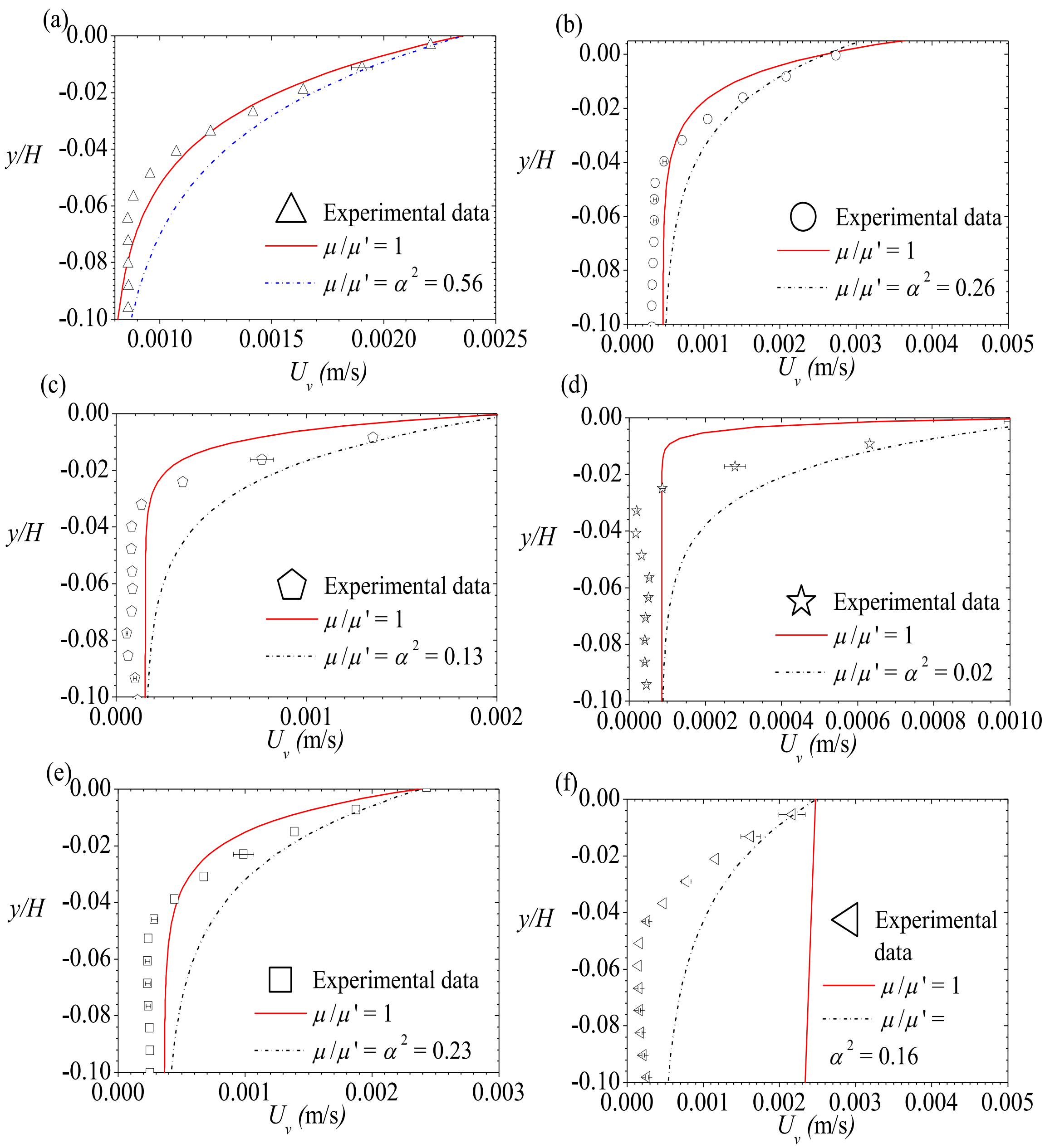

Figure 4. 15: Verifying the Brinkman equation using experimental data at the interfacial zone of (a) $Rd\phi_{6}Re_{0.3}ff_{75}$ (b) $Rd\phi_{12}Re_{0.3}ff_{75}$ (c) $Sq\phi_{12}Re_{0.3}ff_{75}$ and (d) $St\phi_{12}Re_{0.3}ff_{75}$ (e) $Rd\phi_{22}Re_{0.3}ff_{75}$ (f) $Rd\phi_{49}Re_{0.3}ff_{75}$.

It should be noted that if $\mu \,/\, \mu' = \alpha_v^2$, differentiating Equation (4.12) once with respect to y, and evaluating it at $y = 0$ should give

$$\frac{dU_v}{dy} = \frac{\alpha_v}{\sqrt{k}}(U_{v,s} - U_d) \tag{4.13}$$

Equation (4.13) is a modified form of the Beaver and Joseph (1967) boundary condition, accounting for continuity in velocity and shear at the interface. Thus using $\mu \,/\, \mu' = \alpha_v^2$, Equation (4.12) should predict the velocity distribution if the model or the Brinkman equation is valid. For the specific cases of $\mu \,/\, \mu' = \alpha_v^2$ used in Figure 4.15, the slip coefficient α_v was derived from Equation (4.13) using experimental results obtained for the respective test cases. Figure 4.15 shows that apart from the singular case of agreement between experiments and the Brinkman model (*i.e.* $\mu \,/\, \mu' = 1$) for $Rd\phi_6Rd_{0.3}ff_{75}$ (resulting in an adjusted coefficient of determination of 0.97) the two models of the Brinkman equation give incorrect predictions of the velocity profile within the porous medium.

In order to compare selected results with the jump conditions of Ochoa-Tapia and Whitaker (1995a) and to provide some data regarding its empirical coefficient β_1, an additional up-scaling was performed at the interfacial region of the volume averaged data. This was done using a transverse length equal to two times the value of the transition layer thickness δ_I within the porous medium. It should be noted that the transition layer thickness δ_I is defined in this work as the transverse distance taken for the streamwise velocity within the porous medium to decay to $1.01U_d$ with reference to the interfacial location (Nield and Nader 1974; Morad and Khalili 2009). The values are summarized in Table 4.7. Included in Table 4.7 are the values of β_1. The values of this coefficient are derived from Equation (2.13), and their uncertainties are estimated to range from 10% to 18% as solid volume fraction increases from 0.06 to 0.49.

Table 4.7: Summary of values pertaining to the interfacial flow and its prediction for selected test conditions.

Name	δ_1 **(mm)**	β_1	R^2	α_v
$Rd\phi_6Re_{0.3}ff_{75}$	14.0	7.35	0.998	0.75
$Rd\phi_{12}Re_{0.3}ff_{75}$	4.2	0.57	0.997	0.51
$Sq\phi_{12}Re_{0.3}ff_{75}$	4.1	0.59	0.996	0.48
$St\phi_{12}Re_{0.3}ff_{75}$	4.2	0.43	0.990	0.36
$Rd\phi_{22}Re_{0.3}ff_{75}$	3.4	0.44	0.998	0.36
$Rd\phi_{49}Re_{0.3}ff_{75}$	2.8	0.76	0.998	0.14

From the results, it may be observed that β_1 ranges over more than one order of magnitude as ϕ is varied from 0.06 to 0.49. While the dependence of the coefficient with ϕ is unclear, it is independent of the shape of the rods. However, β_1 reduces significantly (by about 30% for $\phi = 0.12$) when arrays are changed from non-staggered to staggered array. One clear limitation of the Ochoa-Tapia and Whitaker (1995a) boundary condition in this work is that it results in a jump in shear at the interface, which is clearly not the case in the present results. Nonetheless the Ochoa-Tapia and Whitaker (1995a) boundary condition is an improvement of the Beavers and Joseph boundary condition, which results in jumps in both velocity and shear.

To provide an alternative to predict the interfacial flow, curve-fitting techniques were applied to the experimental data at the interfacial region. For the present results, the interfacial flow was found to be well described by the following dose response curve, with an adjusted coefficient of determination of 0.99 and above (as shown in Figure 4.16 and shown in Table 4.7; a fuller report for all the test conditions is given in Tables 4.5 and 4.6):

$$U_v(y) = A + \frac{B-A}{1+10^{(D-y)p}} \tag{4.14}$$

Here, A, B, D, and p are respectively the asymptote as $y \to -\infty$, the asymptote as $y \to \infty$, the transverse component of the center of the curve, and the hill slope of the curve. The curve fits are shown for selected test conditions in Figure 4.16 where $Re_{bulk} = 0.3$. The shear rate of the flow at the interface yields

$$\left.\frac{dU_v}{dy}\right|_{y=0+} = \frac{(B-A)10^{Dp}}{(1+10^{Dp})^2}\left[p\ln 10\right] \tag{4.15}$$

This equation is the boundary condition at the interface between the porous medium and free zone flow of the configuration studied. As mentioned earlier, as $y \to -\infty$ in Equation (4.14), $U = A$ which is equivalent to the seepage velocity U_d. Furthermore, at $y = 0$ (*i.e.* at the interface),

$$U_v(0) = U_{v,s} = A + \frac{B-A}{1+10^{Dp}} \tag{4.16}$$

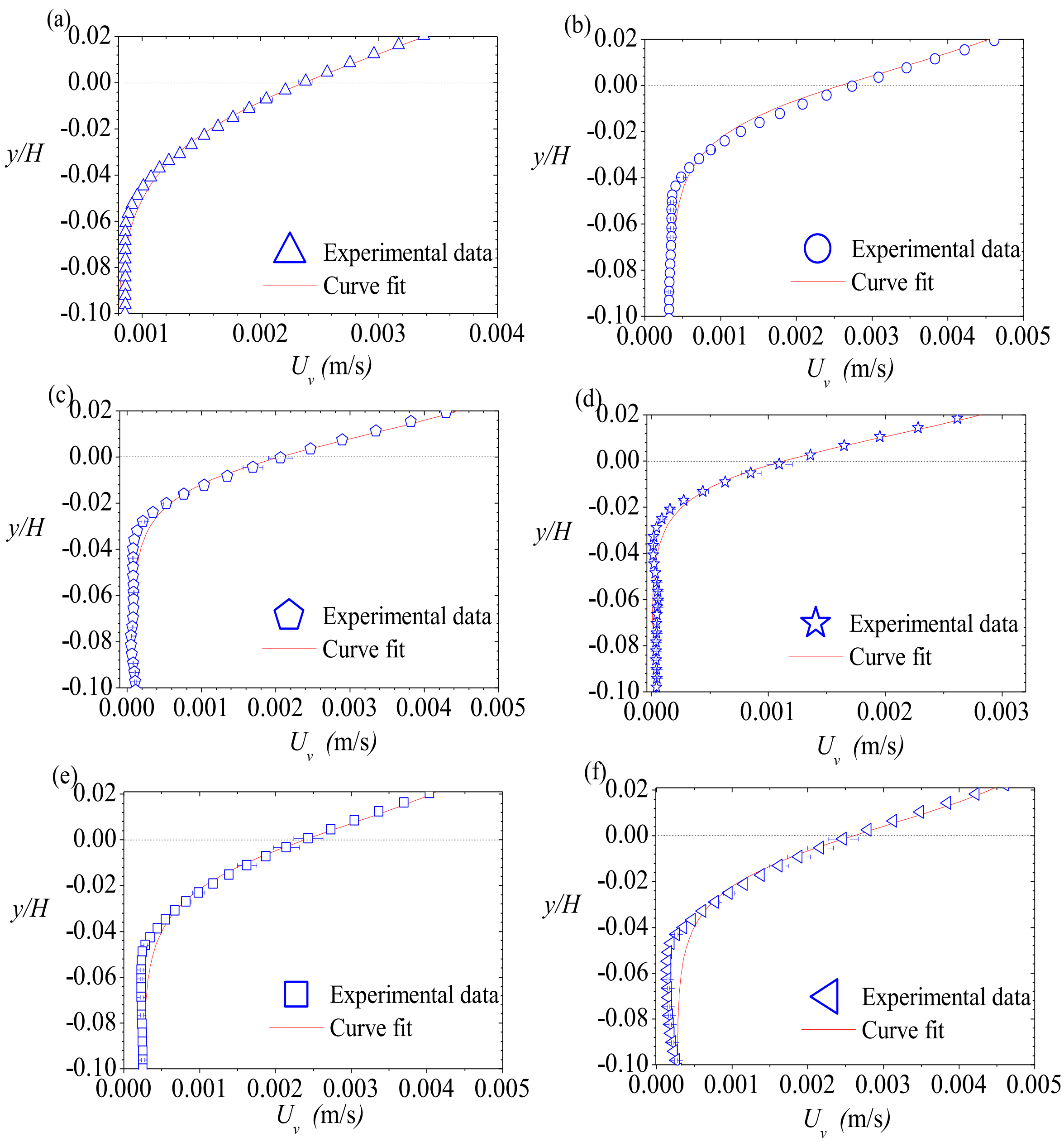

Figure 4.16: Experimental data at the interfacial zone fitted to data points of (a) $Rd\phi_{6}Re_{0.3}ff_{75}$ (b) $Rd\phi_{12}Re_{0.3}ff_{75}$ (c) $Rd\phi_{22}Re_{0.3}ff_{75}$ (d) $Rd\phi_{49}Re_{0.3}ff_{75}$ (e) $Sq\phi_{12}Re_{0.3}ff_{75}$ and (f) $St\phi_{12}Re_{0.3}ff_{75}$. Dashed line indicates the interfacial location.

The boundary condition in Equation (4.15) may therefore be interpreted as a form of the Beavers and Joseph (1967) boundary condition as the velocity defect is

$$U_{v,s} - U_d = \frac{(B - A)}{1 + 10^{Dp}} \tag{4.17}$$

Thus rearranging Equation (4.15) in the form of the Beavers and Joseph (1967) boundary condition, it may be shown that

$$\left.\frac{dU_v}{dy}\right|_{y=0+} = \left[\frac{10^{Dp}}{(1+10^{Dp})} p \ln 10\right](U_{v,s} - U_d) = \frac{\alpha_v}{\sqrt{k}}(U_{v,s} - U_d) \tag{4.18}$$

The coefficient α_v is a dimensionless empirical coefficient, equivalent to the slip coefficient of the Beavers and Joseph (1967) boundary condition, and the values are provided in Figures 4.17 and 4.18, and Tables 4.5 to 4.7. The results show that the equivalent slip coefficient decreases with increasing solid volume fraction (Figure 17). While this coefficient is independent of the shape of the rods, there is a strong dependency of this coefficient with the arrangement of the porous medium. Indeed, the slip coefficient of the staggered model of $\phi = 0.12$ is equivalent to the non-staggered model of $\phi = 0.22$. Unlike the coefficients β_1 earlier discussed, α_v ranges over less than one order of magnitude (Table 4.7) when $Re_{bulk} = 0.3$.

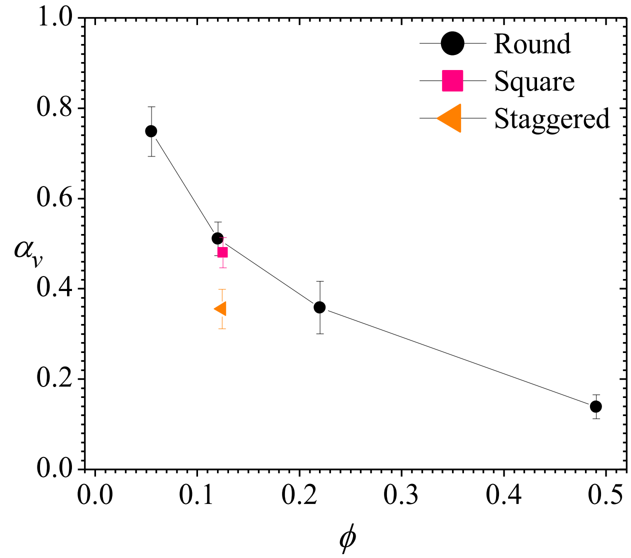

Figure 4.17: The effects of the variation of solid volume fraction, shape and arrangements of rods on the equivalent dimensionless slip coefficient for $Re_{bulk} = 0.3$, $h / H = 0.75$.

The results presented in Figure 4.18(a) and Tables 4.5 and 4.6 indicate that filling fraction effects may only be significant for $1 \leq Re_{bulk} \leq 2.5$, in which case, increasing h / H from 0.50 to 0.75 increases α_v substantially by ~34%. It may also be deduced from Tables 4.5 and 4.6 that, α_v is unaffected by Re_{bulk} in all other models apart from the non-staggered models of filling fraction, 0.75 and $\phi \leq 0.12$. It may be recalled that in the assessment of the bulk flow, this group of models also showed inertial effects on the bulk flow. As shown in Figure 4.18, for $1 \leq Re_{bulk} \leq 2.5$, α_v could increase by over 100 fold in non-staggered model of $\phi = 0.06$.

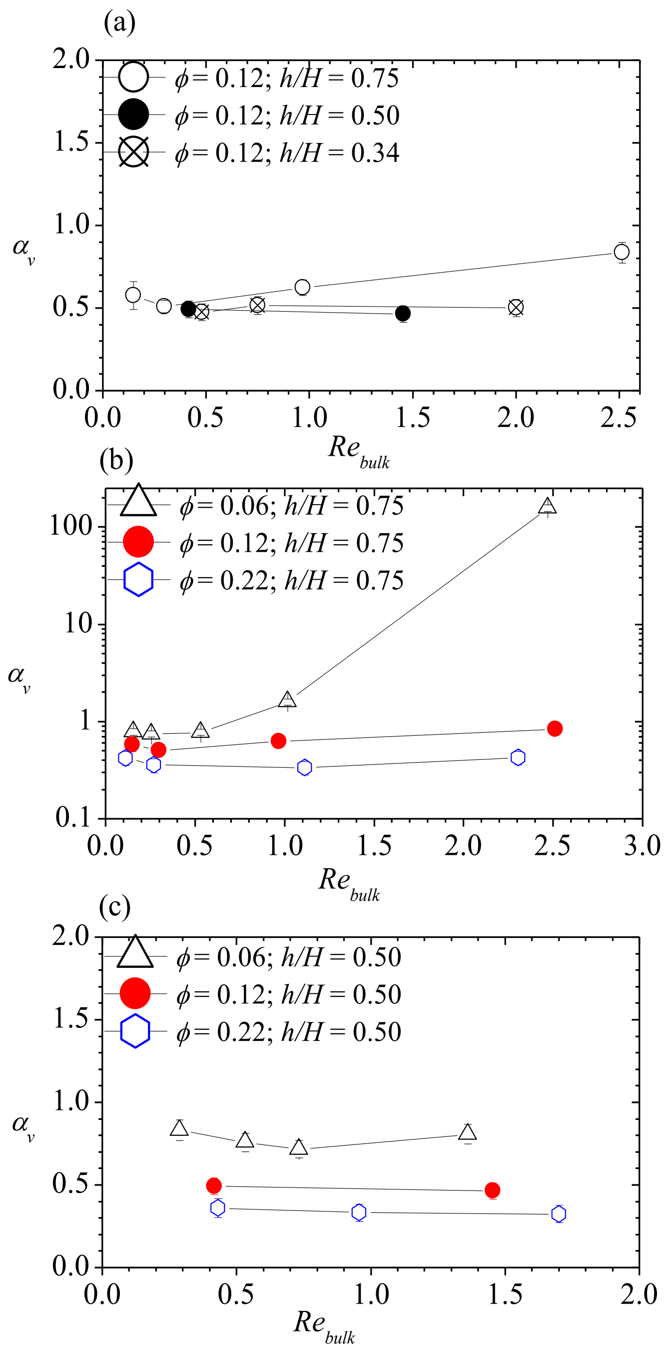

Figure 4.18: The effects of the variation of Re_{bulk} and h / H on the equivalent dimensionless slip coefficient.

While likening Equation (4.18) to the Beavers and Joseph (1967) boundary condition, it is important to remark that the Beavers and Joseph (1967) boundary condition was originally based on a simplified porous medium–free zone flow model in which the shear rate within the porous medium was not considered. This therefore resulted in a description of the flow with a discontinuity in velocity, and a jump in the shear at the interface. Equation (4.18) corrects these deficiencies by accounting for continuities in velocity and stress at the interface. The form of this boundary condition indicates the complex nature of the interfacial flow.

It should also be added that unlike the formulations of Ochoa-Tapia and Whitaker (1995a, 1998) which need modification with the onset of inertia, the same boundary condition as given in Equation (4.18) is sufficient for cases of porous medium–free zone interfacial flow with or without inertial effects. This may be verified in Figure 4.19, for selected curve fits. As shown, in all cases, the plots are in reasonable agreement with the prediction. Apart from $Rd\phi_6Re_{2.5}ff_{75}$ [*e.g.* Figure 4.24(b)], all other fits were found with adjusted coefficient of determinations R^2 of above 0.98, as summarized in Tables 4.5 and 4.6.

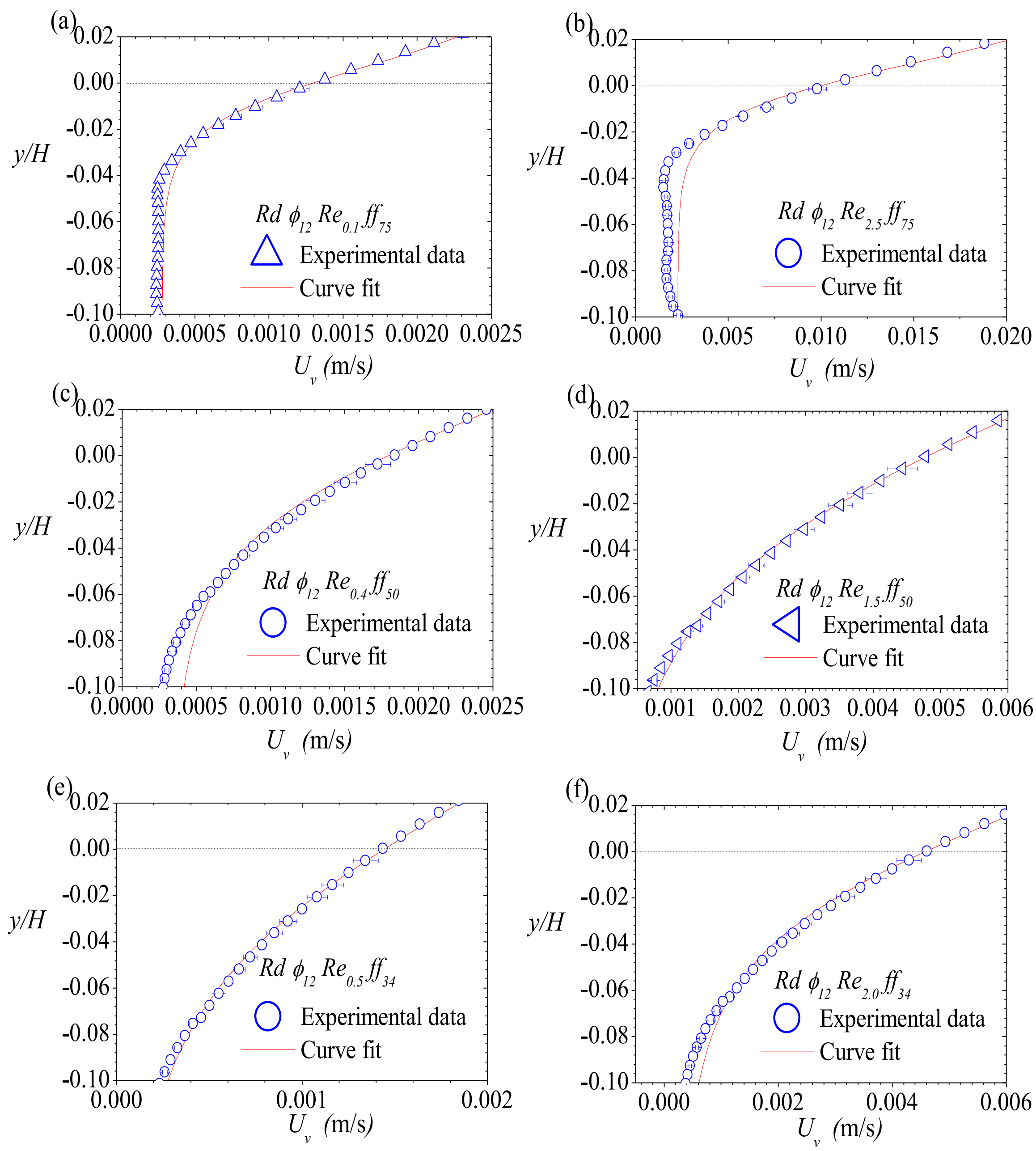

Figure 4.19: Experimental data at the interfacial zone fitted to data points of selected test conditions. Dashed line indicates the interfacial location.

4.3.3 Flow Phenomena in two- and three-dimensional Porous Media

This section presents and discusses results of the 3rd series of experiments. The aim is to compare flows through and over two- and three-dimensional porous media, focussing only on inertial and solid volume fraction effects. To avoid unnecessary repetitive descriptions of trends, the discussion is limited to only area and volume averaged velocities. In the first part of this section, averaged velocities are used to examine the bulk flow. The averaged velocities are subsequently used to study the flow at the interface of the porous medium in the following part of the section. In each of these considerations, flow through and over one type of two-dimensional porous media model (*i.e.* horizontal model) and two types of three-dimensional (*i.e.* vertical and mesh model) porous media are examined and compared. This section extends the scope of study in the previous section to cover a wider range of solid volume fraction (*i.e.* $0.03 \leq \phi \leq 0.49$) and Reynolds number (*i.e.* $0.8 < Re_{bulk} < 10.3$).

4.3.3.1. Bulk Flow Characterization

Sample results plotted in Figure 4.20, show how area averaged streamwise velocities (U_a) and transverse velocities (V_a) compare for flow through and over horizontal, vertical, and mesh models. In the plots, corresponding volume averaged streamwise velocities (U_v) and transverse velocities (V_v) are also shown. Results show that transverse velocities are no more than 3.4% of the maximum local streamwise velocity U_{max} when $Re_{bulk} \sim 1$. The transverse velocities increase to a maximum of 8.7% of U_{max} in high Reynolds number test conditions (as in $M_h\phi_{22}Re_{6.6}$). However, in cases where the flow through the porous media is virtually a plug flow (*e.g.* $M_m\phi_{49}Re_{10.3}$), transverse velocities are typically comparable with the streamwise velocities. These descriptions are common with each type of porous medium model tested.

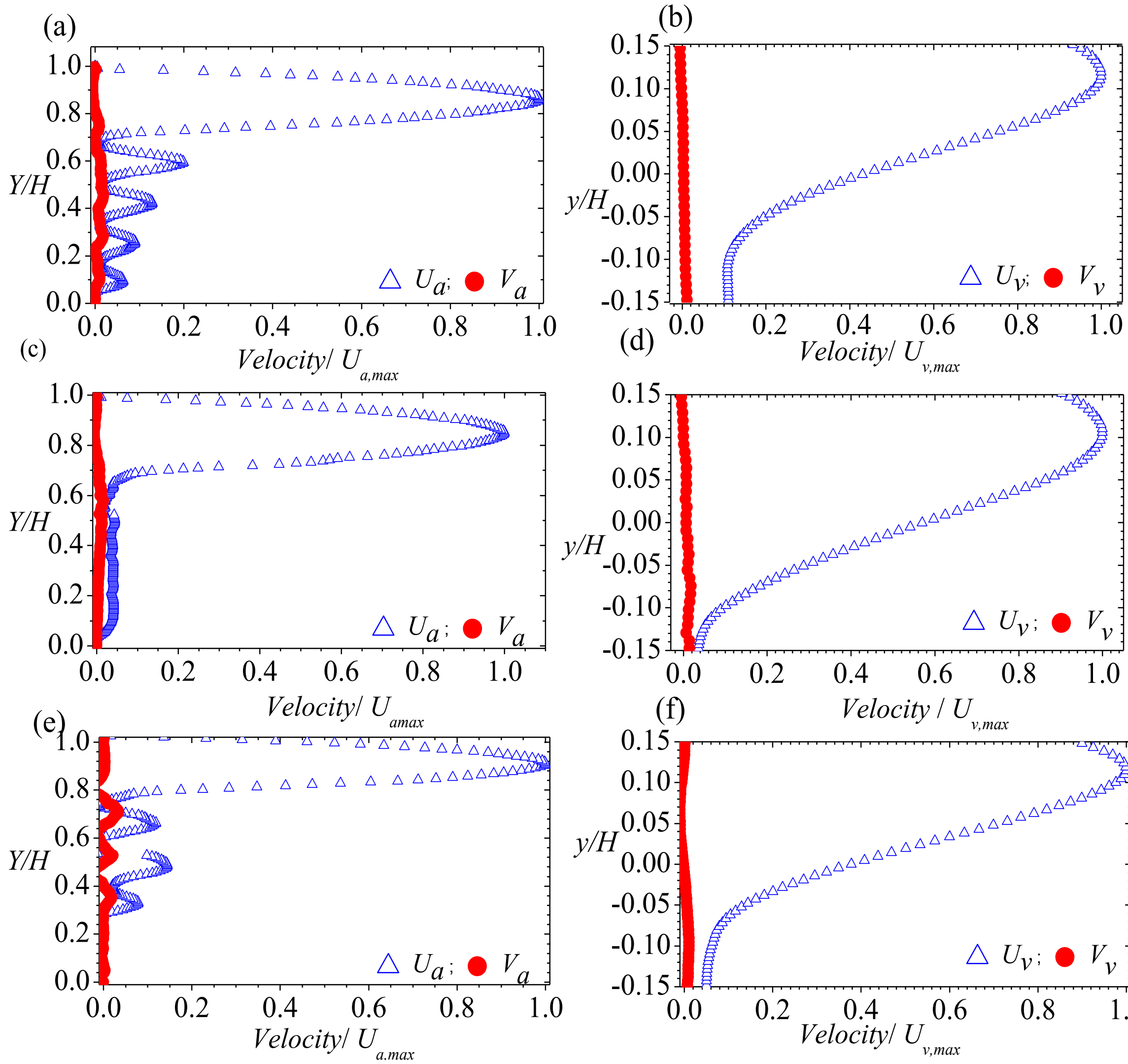

Figure 4.20: The relative magnitudes of area averaged streamwise (U_a) and transverse (V_a) velocities are compared for the following sample test cases - (a) and (b): $M_h\phi_{12}Re_{1.1}$; (c) and (d): $M_v\phi_{12}Re_{1.1}$; (e) and (f): $M_m\phi_{12}Re_{0.8}$.

To compare the effects of inertia on the bulk flow for all the three types of porous media, the position of the maximum velocity, the percentage flow rates per unit width of test section channelled through the free zone, and $U_{a,max}$ / U_{bulk} (together with the volume average equivalent $U_{v,max}$ / U_{bulk}) may be assessed, as done in previous cases. Results presented in Table 4.8 for all the types of model porous media show that the increase in Re_{bulk} from 1 to ~7 is attended with up to a 36% shift in the position of U_{max}. Figure 4.21 (a) shows percentage flow rate distributions obtained for models of $\phi = 0.12$, while Figure 4.21(b) shows that for models of $\phi = 0.22$. These results also show that increasing Re_{bulk} within the range of Reynolds number for the model types tested, leads to as much as 20% more of the fractional flow being diverted into the porous medium as long as $\phi <$ 0.22. It is only at $\phi \geq 0.22$ that the effective drag due to the walls of the porous medium is high enough to resist significant increases in relative bulk flow through them.

To further study the inertial effects in the models, the $U_{v,max}$ / U_{bulk} ratios at the same test conditions of Figures 4.21(a) and (b) are respectively plotted for Figures 4.21 (c) and (d) (It should be noted that similar trends may be observed for $U_{a,max}$ / U_{bulk} as shown in Table 4.8). The plots show that the bulk distribution of flow and the $U_{v,max}$ / U_{bulk} ratios decreases by about 22% as Re_{bulk} increases from ~1 to ~7. This reduction however tends to become less significant as $\phi \geq 0.22$, and insignificant at $\phi = 0.49$. The results also indicate that for all the models tested, as Re_{bulk} increases, the rate of increase in $U_{v,max}$ is relatively lower than U_{bulk}, and this remains the case even at $\phi = 0.49$.

Table 4.8: Summary of area averaged test results

Name	**y/H at $U_{a,max}$**	**% of flow through free zone**	**U_{bulk} $/U_{a,max}$**	**$\sqrt{k}$ (mm)**	**$U_{a,s}$ (mm/s)**	**$U_{a,s}$ $/U_{a,max}$**	**$\dot{\gamma}_a$ (/s)**	**$U_{a,s}/$ $(\dot{\gamma}_a \sqrt{k})$**
$M_v\phi_3Re_{0.8}$	0.06	39	2.05	4.6	9.6	0.91	0.91	2.30
$M_v\phi_3Re_{8.2}$	0.08	37	1.86	4.6	80.7	0.84	9.50	1.86
$M_v\phi_6Re_{1.2}$	0.10	56	2.87	3.0	13.6	0.62	4.13	1.11
$M_v\phi_6Re_{7.7}$	0.11	48	2.30	3.0	78.4	0.70	17.59	1.51
$M_v\phi_{12}Re_{1.1}$	0.11	82	4.30	1.4	16.0	0.56	2.54	4.49
$M_v\phi_{12}Re_{6.7}$	0.15	67	3.28	1.4	69.4	0.50	9.25	5.36
$M_h\phi_{12}Re_{1.1}$	0.12	80	4.30	1.4	9.6	0.32	6.89	1.00
$M_h\phi_{12}Re_{7.3}$	0.14	61	3.42	1.4	48.1	0.31	31.50	1.09
$M_m\phi_{12}Re_{0.8}$	0.12	90	5.47	1.5	3.0	0.11	4.42	0.45
$M_m\phi_{12}Re_{6.6}$	0.13	70	4.42	1.5	24.7	0.13	41.70	0.40
$M_h\phi_{22}Re_{0.9}$	0.12	90	4.77	0.8	12.7	0.45	6.74	2.42
$M_h\phi_{22}Re_{6.1}$	0.15	70	3.57	0.8	45.2	0.33	26.19	2.21
$M_h\phi_{22}Re_{6.6}$	0.15	83	4.39	0.8	58.2	0.32	29.26	2.55
$M_m\phi_{22}Re_{0.8}$	0.13	96	5.52	0.7	6.4	0.24	7.21	1.29
$M_m\phi_{22}Re_{1.3}$	0.13	96	5.56	0.7	9.8	0.21	11.89	1.20
$M_m\phi_{22}Re_{6.9}$	0.15	88	5.19	0.7	42.3	0.19	39.10	1.58
$M_h\phi_{49}Re_{0.9}$	0.13	99	5.74	0.3	1.6	0.07	4.30	1.43
$M_h\phi_{49}Re_{5.4}$	0.13	98	5.26	0.3	16.0	0.14	34.07	1.81
$M_h\phi_{49}Re_{7.2}$	0.11	98	5.15	0.3	30.3	0.20	48.27	2.42
$M_h\phi_{49}Re_{9.9}$	0.10	99	4.99	0.3	30.3	0.15	60.56	1.93
$M_m\phi_{49}Re_{0.9}$	0.15	99	6.47	0.2	1.7	0.07	2.78	2.80
$M_m\phi_{49}Re_{10.3}$	0.15	99	5.57	0.2	18.6	0.08	47.54	1.84

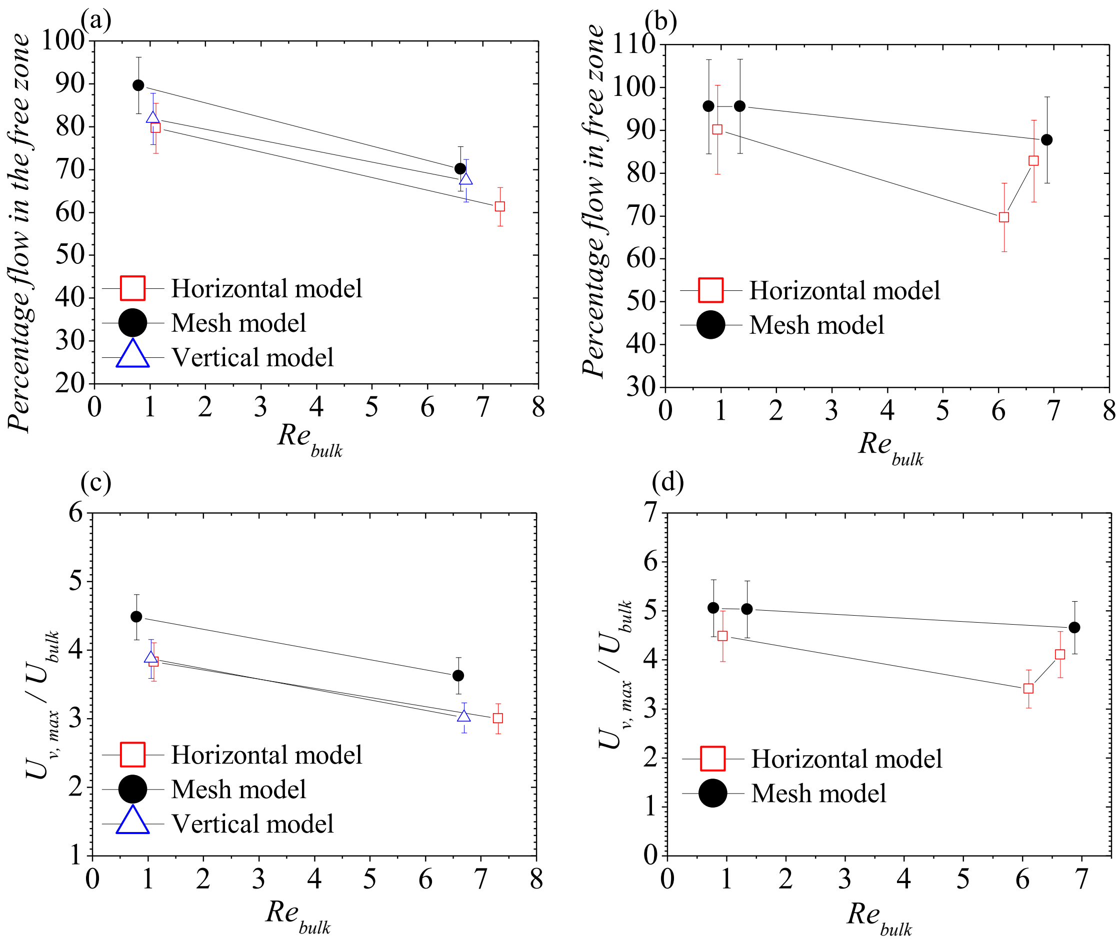

Figure 4.21: The effects of Reynolds number on flow through and over the porous medium studied using: percentage of bulk flow that is channelled through the free zone of test models of (a) $\phi = 0.12$, (b) $\phi = 0.22$; $U_{v,max} / U_{bulk}$ of test models of (c) $\phi = 0.12$; and (d) $\phi = 0.22$. The lines are not meant to imply a linear trend.

In Figure 4.22, plots of selected test conditions are used to compare the solid volume fraction effects. As shown, there is an increase in the proportion of flow channelled into the free zone, as ϕ is increased from 0.03 to 0.49. This increasing trend is independent of the type of model porous media, or the Reynolds number. However, three-dimensional mesh models channel about 10% more flow through the free zone, compared with the three-dimensional vertical and two-dimensional horizontal models at $\phi = 0.12$. The vertical and horizontal models on the other hand, record fairly equal levels of flow distribution. The variation in $U_{v,max}$ / U_{bulk} ratios for different solid volume fraction of porous media are also respectively shown in Figures 4.22(c) and (d) for the same conditions as Figures 4.22(a) and (b) to study solid volume fraction effects in all model types. The figures show that $U_{v,max}$ / U_{bulk} ratios increase with solid volume fraction irrespective of the Reynolds number or the type of porous medium. As expected, $U_{v,max}$ / U_{bulk} increases to the limiting value of ~6 expected for the case where the porous medium is replaced by a solid block. As the observed increases in percentage flow distribution and $U_{v,max}$ / U_{bulk} with solid volume fraction is independent of the model porous medium type or the Re_{bulk}, it is confirmed that the increases are a direct result of an increase in the solid volume fraction of the porous medium. As the solid volume fraction increases, it leads to an increase in percentage flow through the free zone and thus the position of $U_{a,max}$ for each U_{bulk} tested. Table 4.8 also shows that the position of $U_{a,max}$ shifts towards the top wall by about 80% .

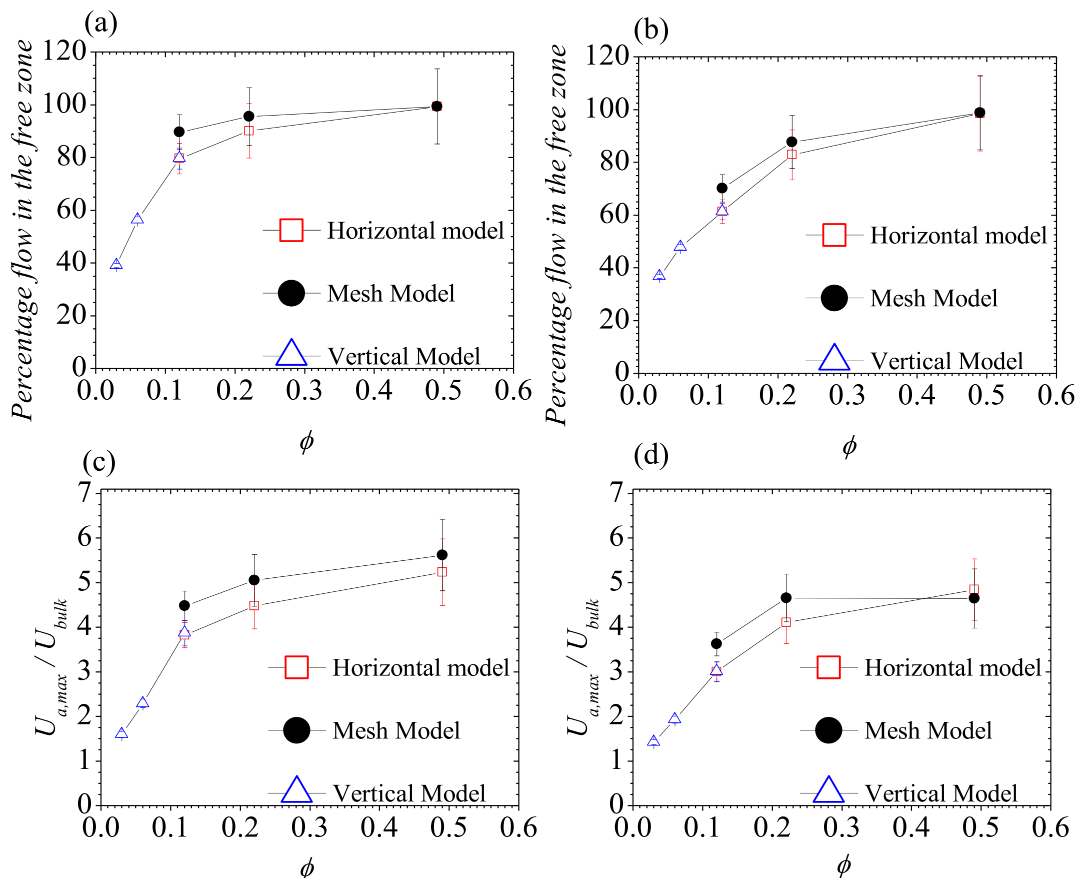

Figure 4.22: The effects of the variation of solid volume fraction ϕ on the bulk flow demonstrated using (a) percentage of bulk flow channelled through the free zone for cases of Re_{bulk} ~1, (b) percentage of bulk flow that is channelled through the free zone for cases of Re_{bulk} ~ 7; (c) ratio of the volume averaged maximum to the bulk velocities for cases of Re_{bulk} ~1; and (d) ratio of the volume averaged maximum to the bulk velocities for cases of Re_{bulk} ~ 7.

These phenomena may be understood by considering that the mesh models (by virtue of their arrangement) induce blockage of flow in two orthogonal directions, compared with the blockage in one direction in the vertical and horizontal models. The blockage in two directions (in mesh models) leads to an enhanced channelling of flow through the free zone, compared with the horizontal or the vertical models, which have rods arrayed in only one direction. It is important to note however that the foregoing observations may only apply when the solid volume fractions are less than 0.22. Figures 4.21(b), 4.22(a) and 4.22(b) and Table 4.8 indicate that the blockage levels of horizontal and mesh models tend to converge as the solid volume fraction increases from $\phi = 0.22$ onwards, so that there are ultimately equal levels of flow distribution at $\phi = 0.49$. For similar reasons as given for the flow distribution, the $U_{v,max} / U_{bulk}$ values for the mesh models are more than 15% higher than the horizontal or vertical models for $\phi \leq 0.12$. As $\phi \geq 0.22$, the $U_{v,max}/U_{bulk}$ values of horizontal and mesh models also tend to converge.

In closing, the effects of varying Re_{bulk} and solid volume fraction in the bulk flow for the types of porous media studied are summarized using the velocity distributions plotted in Figure 4.23. Though mesh models tend to channel more flow through the free zone, generally [as shown in Figure 4.23 (a)], all models of $\phi < 0.22$ decrease in the percentage flow channelled in the free zone, as Re_{bulk} increases [*e.g.* Figure 4.23 (b)]. This decrease however becomes insignificant by $\phi = 0.49$ [*e.g.* Figure 4.23 (c)]. As solid volume fraction increases, more flow is channelled through the free zone [as exemplified in the vertical model case studies in Figure 4.23 (d)]. Furthermore, the position of $U_{a,max}$ shifts towards the upper wall of the test section as Re_{bulk} and ϕ increases.

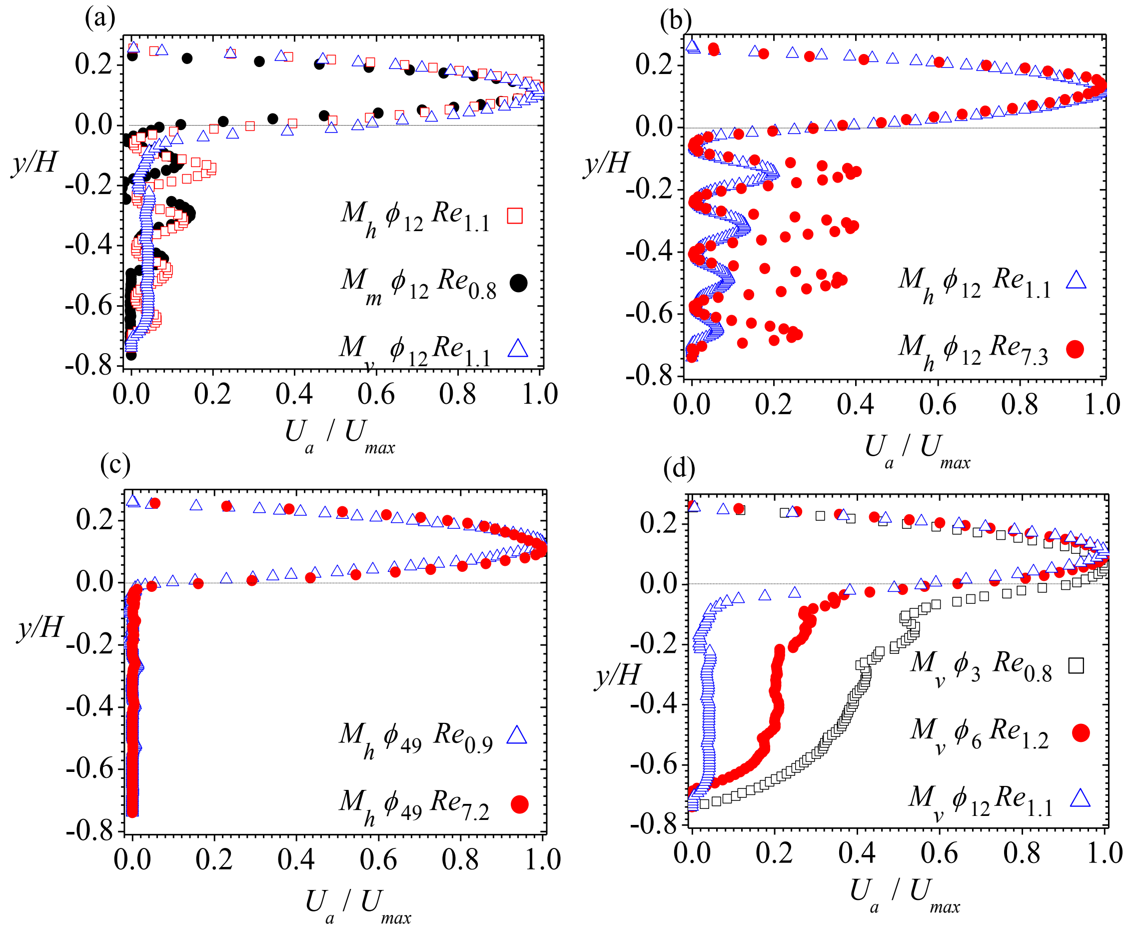

Figure 4.23: Summary of effects of bulk variations using velocity distributions of flow through and over porous media as (a) porous media arrangements are varied, using horizontal, vertical and mesh models of $\phi = 0.12$ and $Re_{bulk} \sim 1$; (b) Reynolds number is increased (this typifies observations in models of $\phi < 0.49$); (c) Reynolds number is increased in a typical model of $\phi = 0.49$; and (d) Solid volume fraction is varied, using vertical models of $Re_{bulk} \sim 1$;. Dashed line indicates the interfacial location.

4.3.3.2. Interfacial Flow Characterization

As done in previous study of the two-dimensional porous medium (*i.e.* § 4.3.2.2), attention will be limited to the dependence of the interfacial flow on the specific permeability k, the average slip velocity U_s at the interface between the porous medium and overlying free flow, the average shear rate at the interface $\dot{\gamma}$ (= $dU/dy|_{y=0+}$), and the channel's maximum average velocity U_{max}. It is re-iterated that the specific permeability, k of the test models were quantified using correlations in the literature expressed in Equations (3.10), (4.9) and (4.11). Values of $\sqrt{k}$ are provided in Table 4.8. The specific permeability k is expected to be inversely related to the proportion of flow channelled through the open section. Thus from the percentage flow distribution results obtained, $\sqrt{k}$ for the mesh models are to be significantly less than that of the horizontal and vertical models. However, this is not the case when $\sqrt{k}$ for mesh models of $\phi = 0.12$ are compared with that of vertical and horizontal models of the same solid volume fraction. The reason for this deviation may be the presence of inertial effects in the measurements. Nonetheless it is important to stress that this does not in any way affect the conclusions of the trends observed for slip velocities.

It is important to note that because this section deals with local interfacial conditions, the values of the slip velocity and interfacial shear rates are expected to be highly sensitive to the method of averaging, especially when shear rates are considered. Therefore, the trends of corresponding dimensionless groupings may not necessarily be the same for area and volume averages. However, to properly compare the results obtained in the three types of model porous media, only trends of volume averaged values will be discussed. Occasional references to area averaged results are made where necessary (the area averaged results are summarized in Table 4.8). The volume averaged interfacial flows are investigated using the dimensionless groupings $U_{v,s}$ / $U_{v,max}$ and $U_{v,s}$ / ($\dot{\gamma}_v \sqrt{k}$), summarized in Table 4.9.

The discussion on dimensionless slip velocities begins by first considering the ratio U_s / U_{max}. Figures 4.24(a) and (b) show the relationship between Re_{bulk} and U_s / U_{max}, using volume averaged measurements for selected test cases of ϕ = 0.12 [in Figure 4.24 (a)], and ϕ = 0.22 [in Figure 4.24(b)]. These selected cases are representative of the entire experimental data set, as may be verified from the experimental data summarized in Table 4.9. It may be readily observed that although there appears to be a decrease in U_s / U_{max} with increasing Re_{bulk}, the dependence is very weak in all models.

Table 4.9: Summary of volume averaged test results

Name	$U_{v,max}$ (mm/s)	U_{bulk} $/U_{v,max}$	$U_{v,s}$ (mm/s)	$U_{v,s}$ $/U_{v,max}$	$\dot{\gamma}_v$ (/s)	$U_{v,s}/$ $(\dot{\gamma}_v \sqrt{k})$	R^2	α_v
$M_v\phi_3Re_{0.8}$	8.2	1.60	8.1	0.99	0.12	14.98	0.997	0.14
$M_v\phi_3Re_{8.2}$	73.5	1.43	71.5	0.97	1.76	8.87	0.999	0.31
$M_v\phi_6Re_{1.2}$	17.6	2.30	14.0	0.79	1.25	3.79	0.999	0.39
$M_v\phi_6Re_{7.7}$	94.1	1.93	74.4	0.79	6.05	4.15	0.998	0.45
$M_v\phi_{12}Re_{1.1}$	25.7	3.88	14.6	0.57	3.35	3.11	0.998	0.35
$M_v\phi_{12}Re_{6.7}$	127.0	3.02	66.4	0.52	14.30	3.32	0.994	0.43
$M_h\phi_{12}Re_{1.1}$	26.6	3.83	11.4	0.43	3.41	2.40	0.999	0.49
$M_h\phi_{12}Re_{7.3}$	138.1	3.00	55.4	0.40	16.53	2.40	0.999	0.80
$M_m\phi_{12}Re_{0.8}$	22.3	4.48	8.5	0.38	3.06	1.89	0.993	0.63
$M_m\phi_{12}Re_{6.6}$	150.5	3.63	53.8	0.36	18.91	1.90	0.997	0.81
$M_h\phi_{22}Re_{0.9}$	26.4	4.48	13.0	0.49	4.21	3.96	0.999	0.26
$M_h\phi_{22}Re_{6.1}$	130.9	3.41	50.0	0.38	18.13	3.54	0.999	0.34
$M_h\phi_{22}Re_{6.6}$	171.7	4.11	65.1	0.38	22.84	3.66	0.999	0.33
$M_m\phi_{22}Re_{0.8}$	24.7	5.06	9.3	0.38	3.74	3.62	0.999	0.28
$M_m\phi_{22}Re_{1.3}$	42.6	5.03	14.3	0.34	6.01	3.47	0.999	0.30
$M_m\phi_{22}Re_{6.9}$	201.5	4.66	53.9	0.27	22.68	3.47	0.993	0.34
$M_h\phi_{49}Re_{0.9}$	19.9	5.24	5.7	0.28	2.95	7.40	0.999	0.14
$M_h\phi_{49}Re_{5.4}$	111.6	4.96	36.7	0.33	17.10	8.29	0.998	0.12
$M_h\phi_{49}Re_{7.2}$	145.8	4.85	52.6	0.36	23.31	8.72	0.999	0.12
$M_h\phi_{49}Re_{9.9}$	195.1	4.70	67.3	0.34	31.21	8.33	0.999	0.12
$M_m\phi_{49}Re_{0.9}$	22.0	5.62	4.5	0.20	2.57	8.24	0.998	0.12
$M_m\phi_{49}Re_{10.3}$	201.1	4.65	62.3	0.31	29.62	9.94	0.988	0.10

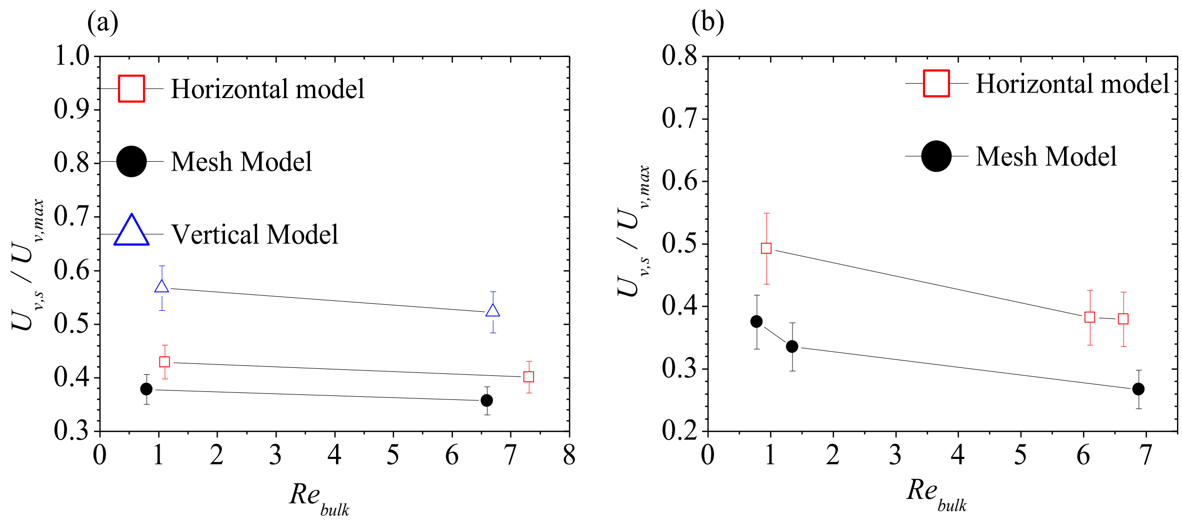

Figure 4.24: The effects of Reynolds number on the slip velocities using the ratio of: (a) volume-averaged slip velocity to maximum velocity for $\phi = 0.12$, and (b) volume averaged slip velocity to maximum velocity for $\phi = 0.22$.

To demonstrate how U_s / U_{max} generally varies with ϕ, results of selected cases for which $\phi = 0.12$ have been plotted in Figure 4.25. Volume averaged values at $Re_{bulk} \sim 1$ are shown in Figure 4.25(a), whereas in Figure 4.25(b), volume averaged results at Re_{bulk} ~7 are shown. From these plots, it is clear all models decrease in U_s / U_{max} with increasing ϕ. Three-dimensional vertical models decrease by about 42% as ϕ increases from 0.03 to 0.12. Area averaged results of vertical models in Table 4.8 are similar in trend, as reported by Agelinchaab *et al.*(2006) and Arthur *et al.* (2009) who also performed tests on vertical models. Indeed, present values are ~30% higher, and that is anticipated, given that the filling fraction of the present models (that is, 0.74) is higher than those previous studies (which had a maximum filling fraction of 0.56). For two-dimensional horizontal models, U_s / U_{max} decreases by ~10% when solid fraction varies from $\phi = 0.22$ to 0.49. In the case of mesh models also, U_s / U_{max} decreases by at least 14% when ϕ increases from 0.22 to 0.49. The decreasing trends observed in all models (as shown in Figure 4.25) may be understood by considering that there will be large increments in the maximum velocity compared with slip velocities, as the ϕ in the porous medium section increases.

To summarize the relative values of U_s / U_{max} data of the three models, reference is made to Figures 4.24 and 4.25 again. It is observed that the U_{vs} / $U_{v,max}$ ratio of the vertical model is more than 30% that of the horizontal and mesh models. The two-dimensional horizontal models also record ratios of U_{vs} / $U_{v,max}$ that are at least 10% more than the mesh models. These results therefore indicate that penetration of the free flow through porous media of $\phi \leq$ 22 is largest for three-dimensional vertical models, followed by horizontal models, and then the mesh models. This is intuitive. The vertical models are expected to be the highest considering that they offer the least surface area resistance of the models in the *x*-*z* plane at the interfacial region. Mesh models on the other hand, would offer the greatest resistance to the penetration of flow penetration through the porous medium, compared with the other models.

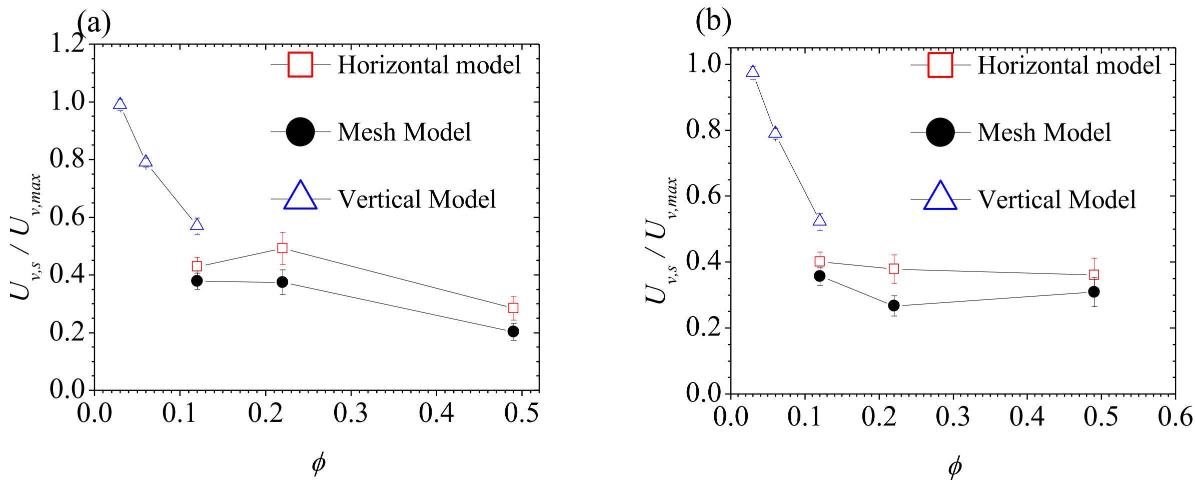

Figure 4.25: The effects of the variation of solid volume fraction on the slip velocities using the ratio of the (a) volume averaged slip velocity to maximum velocity for cases of Re_{bulk} ~1; and (b) volume averaged slip velocity to maximum velocity for cases of Re_{bulk} ~ 7.

Having considered U_s / U_{max}, attention is now turned to $U_s /(\dot{\gamma} \sqrt{k})$. Figure 4.26 shows the relationship between the dimensionless grouping $U_{v,s} /(\dot{\gamma}_v \sqrt{k})$ and Re_{bulk} for test cases of $\phi = 0.12$ [in Figure 4.26(a)], and $\phi = 0.22$ [in Figure 4.26(b)]. The reader may refer to Tables 4.8 and 4.9 for a fuller version of the $U_s /(\dot{\gamma} \sqrt{k})$ results. The overall observation of the dimensionless slip variation is that taking into account experimental errors, $U_{v,s} /(\dot{\gamma}_v \sqrt{k})$ is nearly independent of Re_{bulk} in all models when $\phi \geq 0.12$. Inertial effects are most prevalent in vertical models of $\phi \leq 0.12$ where the $U_{v,s} /(\dot{\gamma}_v \sqrt{k})$ values at Re_{bulk} ~7 are at least five times the value at Re_{bulk} ~ 1.

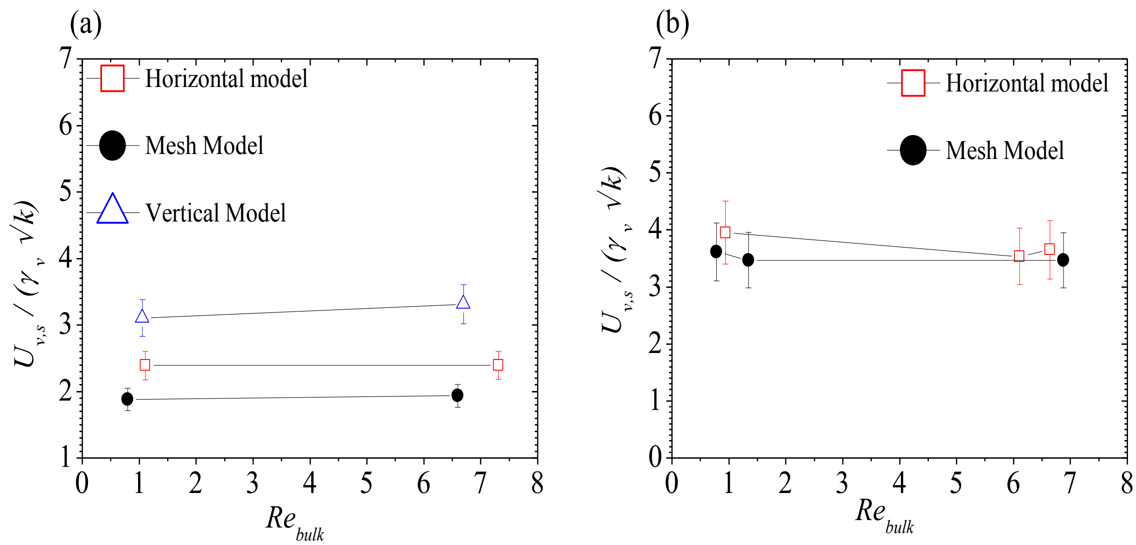

Figure 4.26: The effects of varying Re_{bulk} on $U_{v,s} /(\dot{\gamma}_v \sqrt{k})$ for: (a) $\phi = 0.12$, and (b) $\phi = 0.22$.

In Figure 4.27, the variation of $U_s /(\dot{\gamma} \sqrt{k})$ with ϕ is presented using selected volume averaged results for models at $Re_{bulk} \sim 1$ [in Figure 4.27 (a)], and $Re_{bulk} \sim 7$ [in Figure 4.27 (b)]. The figures clearly indicate that while vertical models decrease with increasing ϕ, the horizontal and mesh models rather increase with increasing ϕ. It is important also to note that the trend of $U_s /(\dot{\gamma} \sqrt{k})$ variation with ϕ obtained in the present vertical models at $Re_{bulk} \sim 1$, is different from that obtained by Agelinchaab *et al.*(2006). Agelinchaab *et al.*(2006) observed that $U_{a,s} /(\dot{\gamma}_a \sqrt{k})$ remained approximately constant at ~1 and ~2 for 0.28 and 0.56 filling fractions respectively, despite changes in ϕ. However, present results (as in Table 4.8) show that the dimensionless slip is not constant. Although the cause of this discrepancy between the present observations and that of Agelinchaab *et al.*

(2006) is uncertain, it may be speculated that it may be mainly due to the differences in resolution of the area averaged velocity measurements used in obtaining the interfacial shear rate. Present velocities are spaced at 0.11 mm intervals while theirs is about 1 mm. Furthermore, the H / l and h / H ratios for comparable test conditions in the experiments are different.

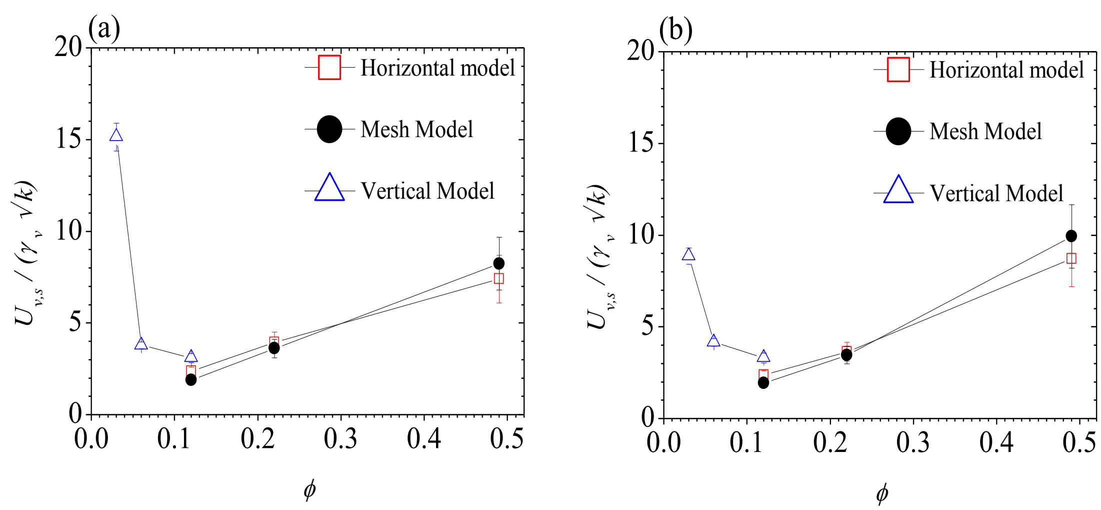

Figure 4.27: The effects of varying ϕ on $U_{v,s} /(\dot{\gamma}_v \sqrt{k})$ for: (a) Re_{bulk} ~1; and (b) Re_{bulk} ~ 7.

To summarize the relative values of $U_s /(\dot{\gamma} \sqrt{k})$ for the three porous media types, the volume averaged results presented in Figures 4.26 and 4.27 may be used. At $\phi = 12$, results show that three-dimensional vertical models record $U_s /(\dot{\gamma} \sqrt{k})$ which are at least 65% higher than those of the mesh and horizontal models. The results also indicate that although $U_s /(\dot{\gamma} \sqrt{k})$ of mesh models are somewhat lower than the horizontal models, the trends of variation with solid volume fraction are similar (see Figures 4.26 and 4.27). An examination of the screening length $U_s / \dot{\gamma}$ provides a clearer insight to the value of the trends in $U_s /(\dot{\gamma}\sqrt{k})$. The screening lengths show that the vertical models allow free flow to penetrate the porous medium ~4.5 times the penetration depth of horizontal models, and ~9.4 times the penetration depth of mesh models. These conclusions are intuitive, considering that the vertical models are expected to provide a surface area resistance to flow in the *x-z* plane that is least compared with that of the horizontal and the mesh models. However, because of the value of *k* used, within experimental errors, $U_{v,s} /(\dot{\gamma}_v \sqrt{k})$ for the horizontal and mesh models of $\phi = 0.12$, 0.22 and 0.49 are equivalent.

4.3.3.3. Interfacial Flow Prediction

An attempt is now made to predict the flow at the interface and its immediate regions for all the models investigated in the 3rd series of experiments.

After applying curve-fitting techniques to the volume averaged experimental data, the interfacial flow was found to be well described by the dose response curve of Equation (4.14), with an adjusted coefficient of determination of 0.98 and above (as shown in Table 4.9). In Figure 4.28, the applicability of this curve in vertical and mesh model porous media is also demonstrated. Given that Equation (4.14) agrees well with the experimental data, it may be concluded that this form of flow equation applies at the interface between two- or three-dimensional isotropic porous media and an overlying free flow.

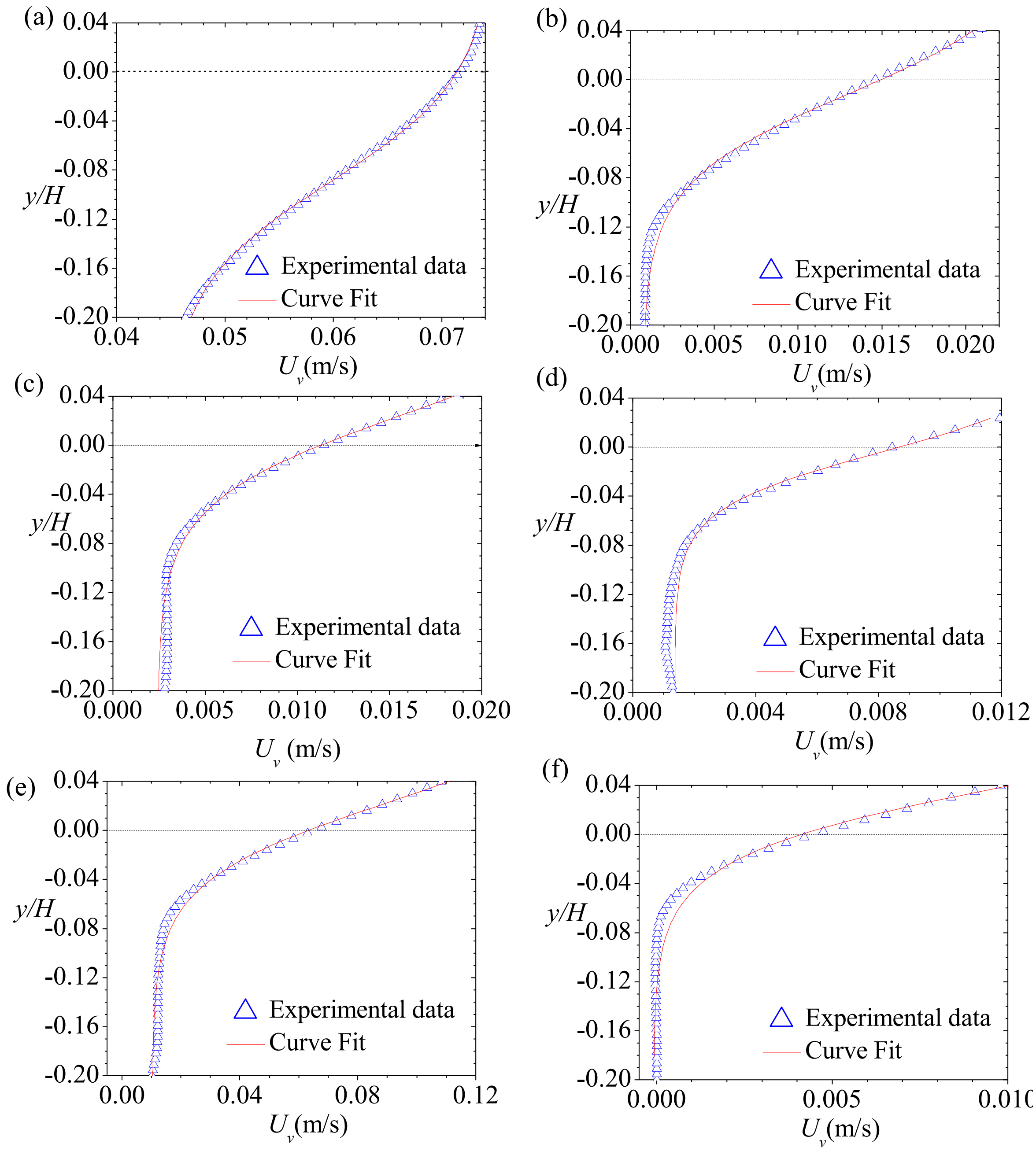

Figure 4.28: Experimental data at the interfacial zone fitted to curves, and shown for selected cases of: (a) $M_v\phi_{12}Re_{8.2}$ (b) $M_v\phi_{12}Re_{1.1}$ (c) $M_h\phi_{12}Re_{1.1}$ (d) $M_m\phi_{12}Re_{0.8}$ (e) $M_h\phi_{22}Re_{6.6}$ and (f) $M_m\phi_{49}Re_{0.9}$. Dashed line indicates the interfacial location.

The coefficient α_v is the dimensionless empirical coefficient. This is provided for all test conditions in Table 4.9. As shown in Table 4.9 and Figure 4.29, α_v is dependent on Re_{bulk} for all models of $\phi = 0.12$ for Re_{bulk} up to ~ 7. In these cases, as Re_{bulk} increases, α_v increases by a range of 15% to 120%. However at $\phi > 0.12$, inertial effects are non-existent. It should also be pointed out that the trend of change in α_v with ϕ for vertical model is distinctly different from that of the mesh and horizontal models which are equivalent at $\phi \geq 0.12$. This further shows that the slip parameters are dependent on the direction in which the axes of the rods are arrayed.

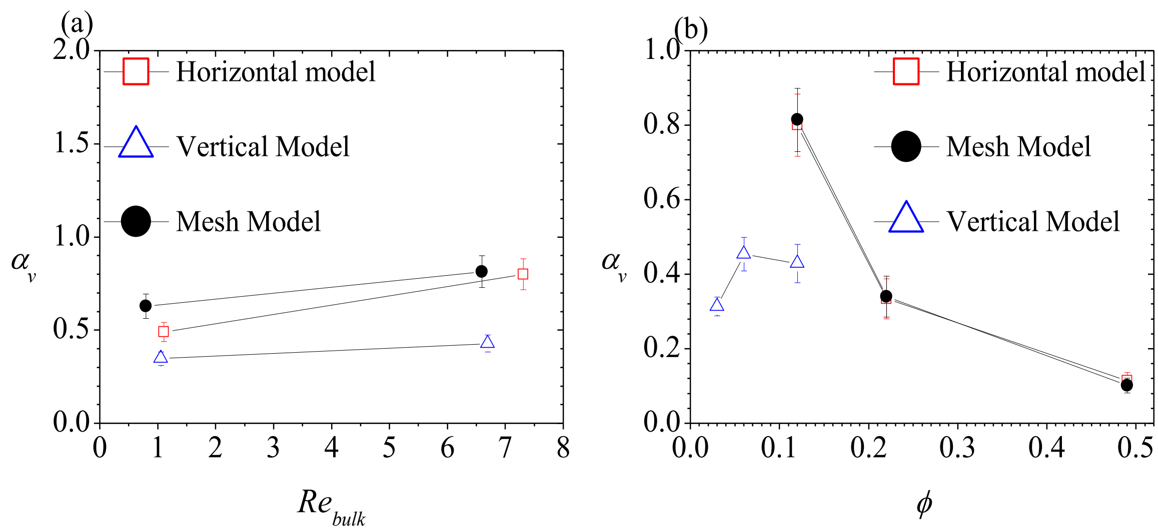

Figure 4.29: (a) Inertial effects on α_v for three types of model porous media of $\phi = 0.12$; (b) Solid volume fraction effects on α_v for three types of model porous media at Re_{bulk} ~ 7.

Additionally, as shown in Figure 4.30, $U_{v,s}/(\dot{\gamma}_v\sqrt{k})$ and α_v obtained for horizontal and mesh porous media models $\phi \geq 0.12$ bear the following allometric correlation

$$\alpha_v = 1.731\left(\frac{U_{v,s}}{\dot{\gamma}_v\sqrt{k}}\right)^{-1.284} \tag{4.19}$$

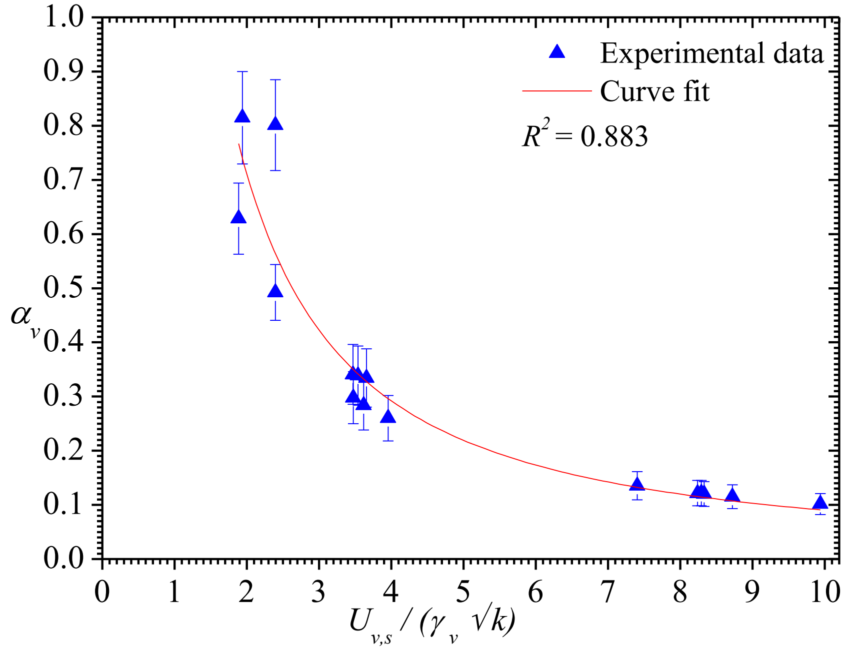

Figure 4.30: Plot for predicting α_v from $U_{v,s}/(\dot{\gamma}_v\sqrt{k})$ for present horizontal and mesh models of $\phi \geq 0.12$ and bulk Reynolds number up to $Re_{bulk} \sim 10$.

4.3.4 Investigating the Separate and Combined Effects of Filling Fraction and Test Section Depth-to-Porous Medium Pore Ratio (DPR)

This section presents and discusses results of the 4th series of experiments. The study was conducted to further investigate the separate and combined effects of filling fraction (h / H) and DPR (H / l) on flows through and over two- and three-dimensional porous media. For the bulk flow, the percentage of the total flow rates per unit width of test section channelled through the free zone were calculated for each of the test conditions. Results are presented in Table 4.10. Corresponding results may also be seen in the area averaged streamwise velocity distributions normalized by the local maximum ($U_{a,max}$) in Figure 4.31.

Table 4.10: Results of volumetric averages

Name	**% of flow through free zone**	U_d **(mm/s)**	$U_{v,s}$ **(mm/s)**	$\dot{\gamma}_v$ **(/s)**	$U_{v,s}$ / $U_{v,max}$	$U_{v,s}$ / ($\dot{\gamma}_v \sqrt{k}$)	α_v
$M_v\ \phi_{12}Dp_{5.75}ff_{74}$	82	1.1	14.6	3.35	0.57	3.11	0.35
$M_v\ \phi_{12}Dp_{7.63}ff_{56}$	97	0.1	5.9	1.60	0.28	2.62	0.39
$M_v\ \phi_{12}Dp_{9.13}ff_{74}$	87	1.8	8.2	2.54	0.26	2.34	0.55
$M_v\ \phi_{12}Dp_{9.13}ff_{47}$	98	0.4	3.4	0.99	0.20	2.43	0.47
$M_h\ \phi_{12}Dp_{5.75}ff_{74}$	80	1.8	11.4	3.41	0.43	2.39	0.49
$M_h\ \phi_{12}Dp_{6.83}ff_{50}$	95	0.8	5.2	1.64	0.29	2.28	0.48
$M_h\ \phi_{12}Dp_{13.69}ff_{50}$	97	0.5	2.5	0.81	0.11	2.24	0.57
$M_h\ \phi_{12}Dp_{13.69}ff_{75}$	89	1.3	4.7	1.54	0.15	2.20	0.63

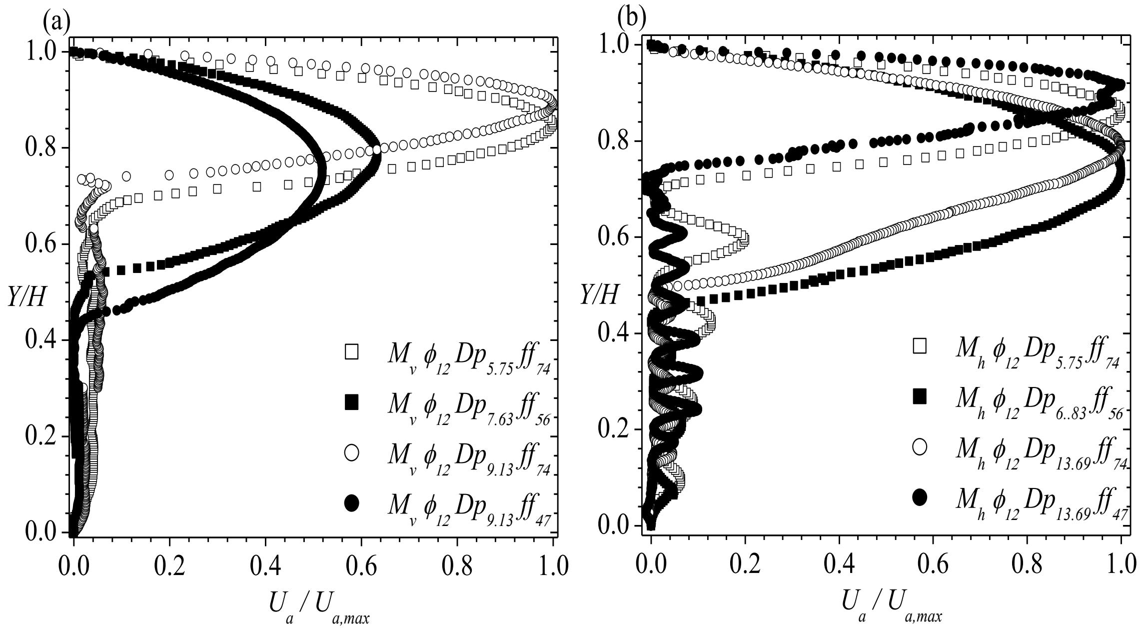

Figure 4.31: Area averaged velocity distributions for (a) vertical models and (b) horizontal models.

It may be observed from results of $M_v\ \phi_{12}Dp_{9.13}ff_{74}$ and $M_v\ \phi_{12}Dp_{9.13}ff_{47}$ that for the three-dimensional vertical porous media, the percentage flow channelled through the free zone increases by 11% as h / H decreases from 0.74 to 0.47. This is expected because as h / H decreases for a given depth of flow, the proportion of flow passing through the porous medium reduces. As a consequence, more flow is conducted through the free zone. The results of $M_v\ \phi_{12}Dp_{5.75}ff_{74}$ and $M_v\ \phi_{12}Dp_{9.13}ff_{74}$ also suggest that increasing H / l from 5.75 to 9.13 increases the percentage flow channelled through the free zone by 5%. This is also expected because as H / l increases, there is a decrease in distance between rods relative to the depth, and therefore an increase in the proportion of flow that is blocked by the porous medium.

A relative comparison of the effects of filling fraction and DPR on the flow distribution shows that filling fraction effects may be more prominent than DPR effects. This is evident by the fact that an increase in filling fraction by a factor of 1.6, decreases the fractional free zone flow by up to 12%, while an increase in depth-to-pore ratio by a factor of 1.6 increases the percentage free zone flow by only 5%.

For the two-dimensional horizontal porous media, the percentage flow channelled through the free zone increases by 9% as h / H decreases from 0.75 to 0.50 for a constant H / l of 13.69. This is different from what was observed in the three-dimensional vertical porous media, and it is due to the increase in the depth of the free zone. It should also be noted that for the horizontal model, doubling H / l at h / H of 0.50 increases the percentage of flow channelled through the free zone from 95% to 97% only. This change is small (and insignificant considering error limits), compared with the 9% increase recorded when the filling fraction was reduced by half. This further demonstrates that the H / l effect on the flow is relatively less pronounced than the filling fraction, when the flow rate distributions are considered.

To study the slip velocities in the experiments, $U_{v,s} / U_{v,max}$ ratios for the different test conditions are compared. As shown in Table 4.10 and Figure 4.32, the filling fraction and the DPR affect the value of $U_{v,s} / U_{v,max}$. For the vertical models, the effects of these two factors are counteractive. As the filling fraction is increased from 0.47 to 0.74 for example, the $U_{v,s} / U_{v,max}$ ratio increases marginally from 20% to 26%; but as the DPR is increased from 5.75 to 9.13, the $U_{v,s} / U_{v,max}$ ratio reduces from 57% to 26%. A comparison of the results however indicates that in a dual play of the two depth ratios, the DPR is the more important factor. The contribution of the DPR may seem more significant here because that is a more direct indication of the flow penetration of the open flow into the porous medium. As l is increased for a given H, flow penetration is expected to increase. Conversely, as l is decreased for a given H, flow penetration is expected to decline. Similar observations in trend may also be deduced for the horizontal models.

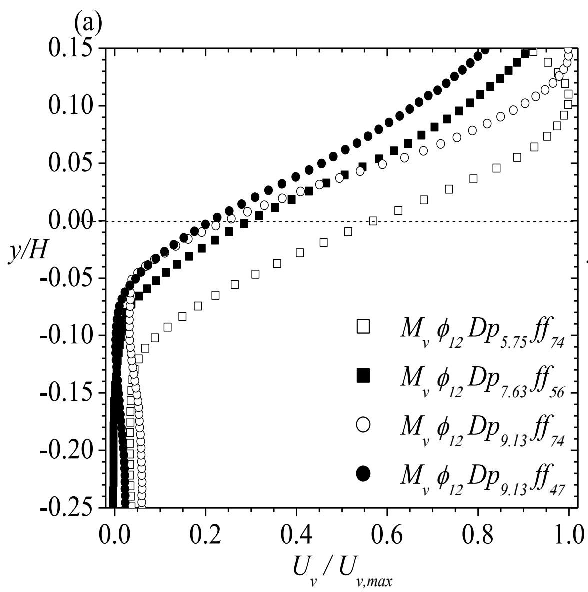

Figure 4.32: Volume averaged velocity distributions at the interfacial region for (a) vertical models and (b) horizontal models. The interface is marked by the dashed line.

For the dimensionless slip $U_{v,s} /(\dot{\gamma}_v \sqrt{k})$, the present results indicate that for a given DPR, the filling fraction is not a significant factor. Thus as shown in Table 4.10, $U_{v,s} /(\dot{\gamma}_v \sqrt{k})$ obtained remained at an average value of ~2.39 when H / l was kept constant at 9.13 for the vertical models of filling fraction change from 0.74 to 0.47, and ~2.22 when H / l for horizontal models was kept constant 13.69 for filling fraction change from 0.50

to 0.75. On the other hand, the DPR appears to have a more pronounced influence. As for the $U_{v,s}$ / $U_{v,max}$ ratio, in both horizontal and vertical models as H / l increases, the dimensionless $U_{v,s}$ /($\dot{\gamma}_v$ $\sqrt{k}$) decreases appreciably. This is a clear indication of the marked effect of pore size on the penetration of flow from the free zone into the porous medium. Agelinchaab *et al.* (2006) used vertical models of $\phi = 0.12$, $h / H = 0.56$, and at $H / l = 2.08$. For that test condition, they obtained $U_{a,s}$ /($\dot{\gamma}_a$ $\sqrt{k}$) = 1.97. At $\phi = 0.12$ and $h / H = 0.56$, the present results of $U_{a,s}$ /($\dot{\gamma}_a$ $\sqrt{k}$) = 1.74 which shows some weak but significant effect of H / l (even when measurement uncertainty limits are taken into account). This further corroborates the fact that increasing H / l leads to a significant decrease in dimensionless slip velocity as observed earlier.

In closing, the effect of h / H and H / l on the slip coefficient α_v is considered. Present results indicate that for both vertical and horizontal models, an increase in either parameter by a factor of 1.5 leads to an increase in the slip coefficient α_v by at ~10% or more.

Chapter 5

Summary of Results and Future Work

In this final chapter, a summary of results and conclusions are provided. The implications of these findings for theoretical and numerical work are also briefly pointed out, followed by an outline of recommendations for future work that can be considered.

5.1 Summary and Conclusions

In this experimental research, laminar flows through and over porous media with or without inertial effects were investigated with three main objectives in view. The first objective was to provide comprehensive data to characterize the effects of solid volume fraction, porous media rod shape and arrangement, porous medium dimensionality, Reynolds number and filling fraction (separate and combined with the depth to porous medium pore ratio) on laminar flows through and over porous media flow. The second objective was to use the measurements to verify which governing equation best applies in two- and three-dimensional porous media flow conditions at the onset of inertia. The third objective of this research was to seek a better formulation for predicting interfacial flow and the interfacial boundary conditions.

To achieve the above-mentioned objectives, detailed experiments were undertaken for flow through and over porous media of solid volume fraction ranging from 0.03 to 0.49. Various porous media were modelled using circular and square rods, in non-staggered and staggered array, and with the rod axes aligned exclusively parallel to the spanwise direction (to simulate a two-dimensional porous medium, called 'horizontal' model), and exclusively parallel to the spanwise direction (to simulate a three-dimensional porous medium, called 'vertical' model). Another model was constructed so that the rods were arranged in a combination of spanwise and transverse directions (to simulate a more complicated version of the three-dimensional porous medium, called 'mesh' model). The filling fractions of the porous media were also varied from 0.34 to 1. By varying the flow rate of the pressure-driven flow through the test section, bulk Reynolds numbers ranging from 0.1 to 10.3 were studied. A two-dimensional particle image velocimetry technique was used to conduct detailed velocity measurements. Electronic transducers were used to obtain differential pressure measurements in some of the experiments.

Experiments were conducted in four series. In the first series of experiments, the focus was on flow through round non-staggered horizontal and mesh model porous media only. This was done to provide velocity and pressure measurements of flow through these models in order to determine the equation that best describes the flow that governs porous media flow up to the regime of the onset of inertia effects. In the second and third series, flows through two-dimensional porous media, and two- and three-dimensional porous media were respectively studied to study the effects of solid volume fraction, filling fraction, arrangement and shape of the porous medium rods, inertia, and porous medium dimensionality on the flow. In the last series of experiments, flow through and over porous media was investigated to particularly study the independent and combined effects of filling fraction and depth to porous medium pore ratio on the flow.

5.1.1 Flow through a Porous Medium

Results of the first series of experiments indicate that for flows through porous medium, transverse velocities are generally insignificant compared with the corresponding maximum streamwise velocities. Furthermore, these transverse velocities are independent of the pressure drops. The friction factor also increases with solid volume fraction of porous medium, and it is also affected by the dimensionality of the models. The three dimensional mesh porous media models of solid volume fraction 0.12 and 0.22 (*i.e.* $M_m\ \phi_{12}$ and $M_m\ \phi_{22}$ respectively) in particular were found to be about ten times the value of the corresponding horizontal porous media. Notwithstanding the dimensionality of the porous media model, the relationship between the pressure drops and seepage velocities was found to be well described by the quadratic Forchheimer equation. The quasi-linear relationship of the two-dimensional porous media of low solid volume fraction (*i.e.* $\phi \leq 0.12$) in particular was indicative of channel-like flow results which were best described by the Izbash Equation.

5.1.2 Flow Through and Over Porous Media

For flows through and over porous media, the following summarizes the effects of the solid volume fraction, rod shape and arrangements, filling fraction (separate and combined with and depth to porous medium pore ratio), porous media dimensionality and inertia.

(a) For the bulk flow, the percentage flow channelled through the free zone increases from ~40% to 98% as ϕ is increased from 0.03 to 0.49. The percentage flow distributions of models of $\phi \geq 0.22$ are independent of the solid volume fraction. At the interface, the ratio of slip velocity to the corresponding maximum velocity (U_s / U_{max}) decreases from ~0.91 to 0.05 as ϕ increases from 0.03 to 0.49. The dimensionless velocities related to the interfacial shear rate [*i.e.* $U_s / (\dot{\gamma} \sqrt{k})$] show that penetration is reduced by at least half when ϕ increases from 0.06 to 0.49.

(b) The bulk flow is nearly independent of the shape and arrangement of rods (*i.e.* staggered or non-staggered arrangements). At the interface however, U_s / U_{max} of staggered arrays are about 15% less than that of non-staggered arrays, while square and circular rods are similar. The penetration of the free flow into the staggered porous medium is at least 15% less that of the non-staggered arrays. The penetrations are independent of the shape of the rods. It must be noted however, that for the staggered arrays in particular, the value of the shear rate is significantly affected by the mode of averaging.

(c) A reduction in filling fraction from 0.75 to 0.34 (while maintaining a constant depth of free flow) results in about 18% increase in the percentage flow channelled through the free zone. The depth to porous medium pore ratio effect on the flow is relatively less pronounced than the filling fraction, when the flow rate distributions are considered. In the case of the interfacial flow, the two effects are counteractive, and the depth to porous medium pore ratio effects are more pronounced. Present results also show that the effect of modifying the filling fraction on $U_{v,s} /(\dot{\gamma}_v \sqrt{k})$ is insignificant when the depth of the free zone remains unchanged.

(d) With respect to porous media dimensionality, it is noted that for the same solid volume fraction (*i.e.* $\phi = 0.12$), three-dimensional mesh models channel about 10% more flow through the free zone, compared with the vertical and horizontal models. Inertial effects are most prevalent in three-dimensional vertical models of $\phi < 0.12$ where the $U_{v,s} /(\dot{\gamma}_v \sqrt{k})$ values at Re_{bulk} ~7 are at least five times the value at Re_{bulk} ~ 1. Three-dimensional vertical models allow free flow to penetrate the porous medium ~4.5 times the penetration depth of horizontal models, and ~9.4 times the penetration depth of mesh models.

(e) As the bulk Reynolds increases, the transverse velocities compared with U_{max}, increase from insignificant levels when $Re_{bulk} < 1$ to about 8.7% when $Re_{bulk} = 6.6$. The bulk flows are also more susceptible to inertial effects when $\phi \leq 0.12$, $h / H = 0.75$ and $h / l \leq 10.26$, and arrays are non-staggered. Increasing Re_{bulk} within the range of Reynolds number for the model types tested, leads to more of the fractional flow being diverted into the porous medium as long as $\phi < 0.22$. For the interfacial flow, as Re_{bulk} increases from 0.1 to ~2.5, the ratios of the slip velocity to the corresponding maximum velocity $U_{l,s} / U_{l,max}$ and $U_{v,s} / U_{v,max}$ decreases sharply by at least 27%. Beyond this range of

Reynolds number, the decrease in ratio is weak. There is no dependence of the volume averaged dimensionless slip velocity $U_{v,s}/(\dot{\gamma}_v \sqrt{k})$ on Re_{bulk}.

By using curve-fitting techniques, a dose response equation was proposed as an adequate model for flow distribution near the interface. The derivative of this equation at the interface yields a boundary condition at the interface akin to that of the Beavers and Joseph (1967). This formulation is to be preferred to those of Brinkman (1947), the original Beavers and Joseph (1967), Ochoa-Tapia and Whitaker (1995) and other related models in the literature, because it provides a more realistic description of the interfacial flow, and it applies to both non-inertial and inertial laminar flows. Its related slip coefficient varies from 0.75 to 0.36 as ϕ increases from 0.06 to 0.49. The coefficient is strongly dependent on the mode of arrangement of the rods, but independent of the shape of the rods. Furthermore, α_v appears to be unaffected by Re_{bulk} and filling fraction in all other models apart from non-staggered models of filling fraction, 0.75 and $\phi \leq 0.12$. Indeed, the slip coefficient may be predicted for given values of $U_{v,s}/(\dot{\gamma}_v \sqrt{k})$ for two-dimensional horizontal and three-dimensional mesh models of $\phi = 0.12$, 0.22 and 0.49, and Re_{bulk} up to 10.3.

The same form of the interfacial formulation prescribed in this work applies to two- and three-dimensional porous media of ϕ ranging from 0.03 to 0.49, filling fraction ranging from 0.34 to 0.75, porous media of square or circular rods, or staggered or non-staggered arrays. The formulation is also applicable for a flow regime of Re_{bulk} ranging from 0.1 to 10.3.

5.2 Implications of Results for Theoretical and Numerical Studies

The experimental data presented in this work provides great insight into porous medium flows as well as interfacial flow phenomena for porous medium-free non-inertial flows. This information may be used to calibrate and to validate theoretical models (as has been demonstrated in this work).

This study provides other particular benefits in the theoretical and numerical modelling of laminar flows through and over model porous media, and the following is a sample of such benefits:

(a) The use of the quadratic form of the Forchheimer equation has been verified to be adequate for the analysis and simulation of flows through two- and three-dimensional porous media at the onset of inertia. A cubic equation may not be necessary to improve accuracy. However, the Izbash equation should be preferred when only two-dimensional porous media are used.

(b) The characterization of the interfacial flow has shown that the use of non-local average flow distribution to study the local interfacial flow quantities is not accurate, as these average distributions are not always sensitive to specific flow conditions (such as staggered or non-staggered arrangement of the porous media) compared with the local interfacial flows. This is an important point to note giving that much of the present theoretical work in the literature (*e.g.* Ochoa-Tapia and Whitaker 1995b, Goyeau *et al.* 2003; Chandesris and Jamet 2006, 2009) are heavily dependent on the average measurements of Beavers and Joseph (1996) in support of their theoretical analysis.

(c) Coupled porous-free flows may now be theoretically analyzed and numerically solved using a more realistic boundary condition at the interface, given explicitly in this work. Furthermore, a realistic formulation by which the interfacial flows over porous media over a wide range of solid volume fraction can be modeled, has been provided. Its utility has been proven for cases with or without inertia effects, and it is expected to help deduce effective properties of the flow at the interfacial region.

(d) The interfacial flow data presented in this thesis provides accurate information about the thickness of the interfacial region, which is not known *a priori* in theoretical studies. It should be noted that although this length scale is critical in the up-scaling of averaged velocity data to obtain a macroscopic description, it is often generalized, leading to an under-estimation or an over-estimation. This work provides accurate information for this purpose.

(e) The provision of extensive data on the dimensionless slip velocity $U_{v,s}/(\dot{\gamma}_v \sqrt{k})$ will be a valuable tool to help assess the penetration of flow at the interface for various conditions of free-porous media coupled flows in theoretical analysis. Present results show $U_{v,s}/(\dot{\gamma}_v \sqrt{k})$ is not equal to $1/\sqrt{\varepsilon}$ as claimed by Chandesris and Jamet (2009) in their theoretical work. It shows that the value of this is not only dependent on the solid volume, but also on the structure of the porous medium particles, and this must be taken into consideration when modeling.

(f) This work shows that flow over porous media can be modeled without incorporating any stress or velocity jump at the interface, as previous theoretical works and boundary conditions suggest (*e.g.* Beavers and Joseph 1967, Ochoa-Tapia and Whitaker 1995b, Goyeau *et al.* 2003; Chandesris and Jamet 2006, 2009).

5.3 Recommendations for Future Studies

To extend the characterization the effect of the depth to porous medium pore ratio on porous media interfacial flow, further work is recommended for a wider range of ratios (*e.g.* covering $20 \leq H/l \leq 40$).

Furthermore, having shown the form of equation that applies at the interfacial boundary for models of porous media made up of regularly repeated units, perhaps what remains is to test whether this formulation also pertains to porous media made up of irregularly arranged units. For a more complete study, it will also be necessary to explore the theoretical basis of this equation, as well as its practical applications in future studies.

One other natural extension of this work will be to consider turbulent flows over porous media. That is of important bearing to many engineering areas such as canopy flows, currents over river beds, grain and storage drying, and turbulent atmospheric boundary layers over forests under fire (De Lemos 2009). Given the enormous engineering value of such flows, the inadequacy of pertinent experimental work as well as the limitations of numerical studies, cutting-edge experimental studies are critically required to characterize the flow, and to provide further understanding into the underlying transport mechanisms of such turbulent interfacial flows.

Bibliography

Adeyinka, O. B. and Naterer, G. F. (2005) ‘Experimental uncertainty of measured entropy production with pulsed laser PIV and planar laser induced fluorescence,’ Int. J. Heat Mass Transfer, Vol. **48**, pp. 1450 – 1461.

Agelinchaab, M. (2005) ‘Velocity measurements of flow through model three-dimensional porous media using particle image velocimetry,’ M.Sc. Thesis, University of Manitoba, Winnipeg, Manitoba.

Agelin-Chaab, M. (2010) ‘Experimental study of three-dimensional offset jets and wall jets,’ Ph.D. Thesis, University of Manitoba, Winnipeg, Manitoba.

Agelinchaab, M., Tachie, M. F. and Ruth, D. W. (2006) 'Velocity measurement of flow through a model three-dimensional porous medium,' Phys. Fluids, Vol**. 18**, pp. 017105-1 – 11.

Ahmed, N. (1967) 'Physical properties of porous media affecting laminar and turbulent flow,' Ph.D. Thesis, Colorado State University at Fort Collins, Fort Collins, Colorado.

Amaral Souto, H. and Moyne, C. (1997) ‘Dispersion in two-dimensional periodic porous media. Part I. Hydrodynamics,’ Phys. Fluids, Vol. **9** (8), pp. 2243 – 2252.

Stanley, H. E. and Andrade, J. S. (2001) ‘Physics of the cigarette filter: fluid flow through structures of randomly-packed obstacles,’ Physica A., Vol. **295**, pp. 17 – 30.

Arthur, J. K. (2008) ‘Velocity measurements of flow through model three-dimensional porous media with varying boundary conditions,’ Master of Science Thesis, University of Manitoba, Winnipeg, Manitoba.

Arthur, J. K., Ruth, D. W. and Tachie, M. F. (2009) ‘PIV measurements of flow through a model porous medium with varying boundary conditions,’ J. Fluid Mech., Vol. **629**(1), pp. 343 - 374.

Balhoff, M. T. and Wheeler, M.F. (2009) 'A Predictive Pore-Scale Model for Non-Darcy Flow in Porous Media,' SPE J., Vol.**14** (4), pp. 579-587 SPE-110838-PA.

Barree, R. D. and Conway, M.W. (2004) ‘Beyond beta factors: A complete model for Darcy, Forchheimer and Trans-Forccheimer flow in porous media,’ Paper SPE 89325, presented at the SPE Annual Technical Conference and Exhibition held in Houston, Texas, USA, 26–29 September 2004.

Barree, R.D. and Conway, M.W. (2005) ‘Reply to discussion of ‘Beyond beta factors: a complete model for Darcy, Forchheimer, and Trans-Forchheimer flow in porous media,’ J. Pet. Tech., pp. 73 – 74.

Barrère, J. (1990) 'Modélisation des écoulements de Stokes et Navier-Stokes en milieu poreux,' Ph.D. Thesis, University of Bordeaux I.

Basak, P. (1977) 'Non-Darcy flow and its implications to seepage problems,' J. Irrig. Drain. Div., Vol. **103** (IR4), pp.459 – 473.

Basu, A. J. and Khalili, A. (1999) 'Computation of flow through a fluid-sediment interface in a Benthic chamber', Phys. Fluids, Vol. **11**, pp.1395 - 1405.

Bear, J. (1988) 'Dynamics of fluids in porous media,' Dover Pub. Inc., New York.

Bear, J. and Bachmat, Y. (1991) 'Introduction to modeling of transport phenomena in porous media,' Kluwer Academic Publishers, Dordrecht.

Beavers, G. S. and Joseph D. D. (1967) 'Boundary conditions at a naturally permeable wall,' J. Fluid Mech., Vol. **30**, pp 197 - 207.

Beavers, G. S., Sparrow, E. M. and Masha B.A. (1974) 'Boundary conditions at a porous surface which bounds a flow,' AICH. E. J., Vol. **20**, pp. 596 - 597.

Bennethum, L. S. and T. Giorgi, T (1997) 'Generalized Forchheimer law for two-phase flow based on hybrid mixture theory,' Transp. Porous Med., Vol **26**(3), pp. 261 - 275.

Blake, F. C. (1922) 'The resistance of packing to fluid flow,' Trans. Am. Inst. Chem. Engrs., **14**, pp. 415 – 421.

Blick, E. F. (1966) 'Capillary orifice model for high speed flow through porous media,' I. & EC, Process Design and Development, Vol.**1** (5), pp. 90 - 94.

Bordier, C. and Zimmer, D. (2000) 'Drainage equations and non-Darcian modeling in coarse porous media or geosynthetic materials,' Journal of Hydrology, Vol. **228**, pp. 174 – 187.

Breugem, W. P. (2004) 'The influence of wall permeability on laminar and turbulent flows,' Ph.D. Thesis, Delft University of Technology, Delft, The Netherlands.

Brinkman, H. C. (1947) 'A calculation of the viscous force exerted by a flowing fluid on a dense swarm of particle,' Appl. Sci. Res., Sect. A, Vol. **1**, pp. 27 – 34.

Burke, S. P. and Plummer, W. B. (1928) 'Gas flow through packed columns,' Industrial Engineering Chemistry, Vol. **20** (1928), pp. 1196 – 1200.

Carman, P. C. (1937) 'Fluid flow through a granular bed,' Trans. Inst. Chem. Engrs., Vol. **15**, pp. 150 - 156.

Chandesris, M. and Jamet, D. (2006) 'Boundary conditions at a planar fluid–porous interface for a Poiseuille flow,' Int. J. Heat and Mass Transfer, Vol. **49,** pp. 2137 – 2150.

Chandesris, M. and Jamet, D. (2007) 'Boundary conditions at a fluid-porous interface: an a priori estimation of the stress jump coefficients,' Int. J. Heat and Mass Transfer, Vol. **50,** pp. 3422 – 3436.

Chandesris, M. and Jamet, D. (2009) ‘Boundary conditions at a planar fluid–porous interface for a Poiseuille flow,’ Transp. Porous Med., Vol. **78,** pp. 419 – 438.

Chauveteau G. (1965) ‘Essai sur la loi de Darcy,’ Ph.D. Thesis, University of Toulouse, Toulouse.

Chen, Z., Lyons, S. L. and Qin, G. (2001) ‘Derivation of the Forchheimer law via homogenization,’ Transp Porous Med., Vol. **44**, pp. 325 – 335.

Childress, S. (1972) ‘Viscous flow past a random array of spheres,’ J. Chem. Phys., Vol. **56**(6), pp.2527 – 2539.

Coleman, W. H. and Steele, W. G. (1995) ‘Engineering application of experimental uncertainty analysis,’ AIAA J., Vol. **33**, pp.1888 – 1896.

Comiti, J. and Renaud, M. (1989) ‘A new model for determining mean structure parameters of fixed beds from pressure drop measurements—application to beds packed with parallelepipedal particles,’ Chem. Eng. Sci., Vol. **44**, pp. 1539 – 1545.

Couland, O., Morel, P. and Caltagirone, J. P. (1988) ‘Numerical modelling of nonlinear effects in laminar flow through a porous medium,’ J. Fluid Mech., Vol. **190**, pp. 393 - 407.

Darcy, H. P.G. (1856) ‘Les fontaines publiques de la ville de Dijon,’ Paris: Victor Dalmont.

Davis, A. M. J. and James, D. F. (2003) ‘The slip velocity at the edge of a porous medium: effects of interior resistance and interface,’ Transp. Porous Med., Vol. **53**, pp. 175 – 196.

Davis, A. M. J. and James, D. F. (2004) ‘Penetration of shear flow into an array of rods aligned with the flow,’ Can. J. Chem. Eng., Vol. **82**, pp. 1169 – 1174.

De Lemos, M. J. S. (2009) ‘Turbulent flow around fluid–porous interfaces computed with a diffusion-jump model for k and ε transport equations,’ Transp. Porous Med., Vol. **78** pp. 331–346.

Deng, C. and Martinez, D. M. (2003) ‘Viscous flow in a channel partically filled with a porous medium and with wall suction,’ Chem. Eng. Sci., Vol. **60**, pp. 329 – 336.

Dullien, F.A.L. (1992) 'Porous media: fluid transport and pore structure,' Academic Press, San Diego.

Durlovsky, L. and Brady, J.F. (1987) ‘Analysis of the Brinkman equation as a model for flow in porous media,’ Phys. Fluids, Vol. **30**(11), pp. 3329 – 3341.

Dupuit, J. (1863) ‘Etudes theoretiques et practiques sur le mouvement des eaux,’ Dunond, Paris.

Dybbs, A. and Edwards, R. V. (1984) ‘A new look at porous media fluid mechanics—Darcy to turbulent,’ fundamentals of transport phenomena in porous media flow, pp. 199 - 256 Martinus Nishoff, Dordrecht.

Edwards, D. A., Shapiro, M., Bar-Yoseph, P. and Shapira, M. (1990) ‘The influence of Reynolds number upon the apparent permeability of spatially periodic arrays of cylinders,’ Phys. Fluids A., Vol. **2**(1), pp. 45 – 55.

Eisfeld, B. and Schnitzlein, K. (2001) ‘The influence of confining walls on the pressure drop in packed beds,’ Chem. Eng. Sci., Vol. **56**, pp. 4321–4329.

Ergun, S. (1952). ‘Fluid flow through packed columns,’ Chemical and Engineering Progress, Vol. **48**, pp. 89 - 94.

Escande, L (1953) ‘Experiments concerning the filtration of water through rockmass,’ Proc. Minnesota Int. Hydraul. Conv.

Firdaous, M. and Guermond, J. L. (1995) ‘Sur l'homogénéisation des équations de Navier-Stokes à faible nombre de Raeynolds,’ C. R. Acad. Sci. Paris, Vol. **I320**, pp. 245–251.

Firdaous, M. Guermond, J. L. and P. Le Quéré, P. (1997) ‘Nonlinear corrections to Darcy's law at low Reynolds numbers,’ J. Fluid Mech., Vol **343**, pp. 331 – 350.

Forchheimer, P. (1901) ‘Wasserberwegung durch Boden,’ Z. Vereines deutscher Ing. Vol.**45** (50), pp. 1782 – 1788.

Forchheimer, P. (1930) ‘Hydraulik,’ 3rd edn. Teubner, Leipzig.

Forliti, D. J., Strykowski, P. J. and Debatin, K. (2000) ‘Bias and precision errors of digital particle image velocimetry,’ Exp. Fluids, Vol. 28(5), pp. 436 - 447.

Fox, R. W., McDonald, A. T. and Pritchard, P. J. (2004) ‘Introduction to fluid mechanics,’ 6th edn. Wiley, New Jersey.

Fourar, M. Lenormand, R. and Larachi, F. (2001) ‘Extending the F-function concept to two-phase flow in trickle beds,’ Chem. Eng. Sci., Vol. **56**, pp. 5987 – 5994.

Fourar, M., Radilla, G., Lenormand, R. and Moyne, C. (2004) ‘On the non-linear behaviour of a laminar single-phase flow through two and three-dimensional porous media,’ Advances in Water Research Vol. **27**, pp. 669 – 677.

Freed, K. F. and Muthukumar, M (1978) ‘On the Stokes problem for a suspension of spheres at finite concentration,’ J. Chem. Phys., Vol. **68**(5), pp. 2088 – 2096.

Geertsma, J. (1974) ‘Estimating the coefficient of inertial resistance in fluid flow through porous media,’ Soc. Petrol. Eng. J., pp. 445 - 450.

Garrouch, A. A. and Ali, L. (2001) ‘Predicting the onset of inertial effects in sandstone rocks,’ Transp Porous Med., Vol. **44**, pp. 487 – 505.

Gerritsen, M., Jessen, K., Mallison, B. and Lambers, J. (2005) 'A fully adaptive streamline framework for the challenging simulation of gas-injection processes,' SPE 97270, in SPE ATCE.

Givler, R.C. and Altobelli, S. A. (1994) 'A determination of the effective viscosity for Brinkman-Forchheimer flow model,' J. Fluid Mech., Vol. **258**, pp. 355 – 370.

Goharzadeh, A., Khalili, A. and Jörgensen, B. B. (2005) 'Transition layer thickness at a fluid-porous interface,' Phys. Fluids, Vol. 17, pp. 057102/1-057102/10.

Gui, J., Longo, L. and Stern, F. (2001) 'Towing tank PIV measurement system, data and uncertainty assessment for DTMB Model 5512,' Exp. Fluids, Vol. **31**(3), pp. 336 – 346.

Goyeau, B., Lhuillier D., Gobin, D. and Velarde, M. G. (2003) 'Momentum transport at a fluid-porous interface,' Int. J. Heat Mass Transfer, Vol. **46**, pp. 4071 – 4081.

Gui, J., Longo, L. and Stern, F. (2001) 'Towing tank PIV measurement system, data and uncertainty assessment for DTMB Model 5512,' Exp. Fluids, Vol. **31**(3), pp. 336 – 346.

Gupte, S. K. and Advani, S. G. (1997) 'Flow near the impermeable boundary of a porous medium: an experimental investigation using LDA,' Exp. Fluids, Vol. **22**, pp. 408 – 422.

Hassanizadeh, S.M. and Gray,W.G. (1987) 'High velocity flow in porous media,' Transp. Porous Med., Vol. **2**, pp. 521–531.

Hayes, R. E., Afacan, A. and Boulanger, B. (1995) 'An equation of motion for an in-compressible Newtonian fluid in a packed bed,' Transp. Porous Med., Vol. **18,** pp. 185 – 198.

Hazen, A. (1895) 'The filtration of public water-supplies,' Wiley, New York.

Hellou, M., Martinez, J. and El Yazidi, M. (2004) 'Stokes flow through microsctructural model of fibrous media,' Mech Res Commun., Vol **31**(1), pp. 97 – 103.

Howells, I. D. (1974) 'Drag due to the motion of a Newtonian fluid through a sparse random array of small fixed rigid objects,' J. Fluid Mech., Vol. **64**, pp. 449 – 475.

Hsu, C.T. and Cheng, P. (1990) 'Thermal Dispersion in a porous medium', Int. J. Heat Mass Transfer, Vol. **33**, pp. 1587 - 1597.

Huang, A. Y. L., Huang, M. Y. F., Carpart, H. and Chen, R. H. (2008) 'Optical measurements of pore geometry and fluid velocity in a bed of irregularly packed spheres,' Exp. Fluids, Vol. **45**, pp. 309 – 321.

Huang, H. and Ayoub, J. (2008) 'Applicability of the Forcheimer equation for non-Darcy flow in porous media,' SPE Journal, Vol. **13**(1), pp. 112 – 122.

Hill, R. J., Koch, D. L. and Ladd, A. J. C. (2001) ‘Moderate-reynolds-number flows in ordered and random arrays of spheres,’ J. Fluid Mech., Vol. **448**, pp. 243 – 278.

Hinch, E. J. (1977) ‘An averaged-equation approach to particle interactions in a fluid suspension,’ J. Fluid Mech., Vol. **83**, pp. 695 – 720.

Hlushkou, D. and Tallarek, U. (2006) ‘Transition from creeping via viscous-inertial to turbulent flow in Fixed beds,’ Journal of Chromatography A., Vol.**1126**, pp. 70 – 85.

Irmay, S. (1958) ‘On the theoretical derivation of Darcy and Forchheimer formulas,’ Trans. Am. Geophys. Union, Vol. **39**, pp. 702–707.

Izbash, S. V. (1931) ‘O fitracii v krupnozernstom materiale, Izr. Nauchno-isoled, Qust. Gidrotechniki,’ (NIIG), Leningrad.

Jackson, G. W. and James, D. F. (1986) ‘The permeability of fibrous porous media,’ Can. J. Chem. Eng., Vol. **64**, pp. 364 -374.

James, D. F. and Davis, A. M. J. (2001) ‘Flow at the interface of a model fibrous medium,’ J. Fluid Mech., Vol. **426**, pp. 47 – 71.

Jamet, D. and Chandesris, M. (2009) ‘On the intrinsic nature of jump coeffecients at the interface between a porous medium and a free fluid region,’ Int. J. Heat Mass Transfer, Vol. **52**, pp. 289 – 300.

Jamet, D., Chandesris, M. and Goyeau, B. (2009) ‘On the equivalence of the discontinuous one- and two-domain approaches for the modelling of transport phenomena at a fluid/porous interface,’ Transp. Porous Med., Vol. **78,** pp. 403 – 418.

Jones, I. P. (1973) ‘Low Reynolds number flow past spherical shell,’ Proc. Camb. Phil. Soc. Vol. **73**, pp. 231-238.

Joseph, D. D., Nield, D. A. and Papanicolaou, G. (1982). ‘Nonlinear equation governing flow in a saturated porous mdium,’ Water Resources Research, Vol **18**(4), 1049 – 1052.

Kaviany, M. (1992) ‘Principles of heat transfer in porous media,’ NewYork: Springer.

Keane, R.D. and Adrian, R.J. (1990) ‘Optimization of particle image velocimeters Part I. Double pulsed systems,’ Measurement Science and Technology, Vol. **1**, pp. 1202 – 1215.

Keane, R.D. and Adrian, R.J. (1992) ‘Optimization of particle image velocimeters II. multiple pulse systems,’ Engineering Optics, Vol. **5**, pp. 47.

Khalili, A., Basu, A. J., Pietrzyk, U., and Raffel, M. (1999) ‘An experimental study of recirculating flow through fluid-sediment interfaces,’ J. Fluid Mech., Vol. **383**, pp. 229 – 247.

Kim, S. and Russel, W. B. (1985) ‘Modeling of porous media by renormalization of the Stokes equation,’ J. Fluid Mech., Vol. **154**, pp. 269 – 286.

Knupp, P. M. and Lage, J. L. (1995), ‘Generalization of the Forchheimer-extended Darcy model to the tensor permeability case via a variational principle,’ J. Fluid Mech., Vol. **299**, pp. 97 – 104

Koplik, J., Levine, H. and Zee, A. (1983) ‘Viscosity renormalization in the Brinkman equation,’ Phys. Fluids, Vol. **26**, pp. 2864 – 2870.

Kozeny, J. (1927) ‘Uber kapillare leitung des wassers in boden. sitzungsber akad,’ Wiss.Wien Math.Naturwiss.Kl., Abt.2a, Vol. **136**, pp. 271 - 306.

Kuznetsov, A. V. (1996) ‘Analytical investigation of the fluid flow in the interface region between a porous medium and a clear fluid in channels partially filled with a porous medium,’ Applied Scientific Research, Vol. **56,** pp. 53 – 67.

Larson, R. E. and Higdon, J. J. L. (1986) ‘Microscopic flow near the surface of two-dimensional porous media Part 1. Axial flow,’ J. Fluid Mech., Vol. **166**, pp. 449 – 472.

Larson, R. E. and Higdon, J. J. L. (1987) ‘Microscopic flow near the surface of two-dimensional porous media Part 2. Transverse flow,’ J. Fluid Mech., Vol. **178**, pp. 119 – 136.

Li, D. and Engler, T. W. (2001) ‘Literature review on correlations of the non-Darcy coefficient,’ paper SPE 70015, Proc., the 2001 SPE Permian Basin Oil and Gas Recovery Conference, Midland, TX, May 15-17, 2001.

Lindquist E. (1933) ‘On the flow of water through porous soil,’ Premier Congrès des Grands barrages, Stockholm, Vol. **5**, pp. 81 – 101

Lundgren, T. S. (1972) ‘Slow flow through stationary random beds and suspensions of spheres,’ J. Fluid Mech., Vol 51, pp. 273 – 299.

Ma, H. and Ruth, D. W. (1993) ‘The microscopic analysis of high Forchheimer number flow in porous media,’ Transp. Porous Med., Vol. **13**, pp. 139 – 160.

MacDonald, I. F., EL-Sayed, M. S., Mow, K. and Dullien, F. A. L. (1979) ‘Flow through porous media - the Ergun equation revisited,’ Industrial and Engineering Chemistry Fundamentals, Vol. **18**(3), pp. 199 - 208.

Marušic–Paloka, E., Mikelic, A. (2000) ‘The derivation of a non-linear filtration law including the inertia effects via homogenization,’ Nonlinear Anal. Theory Methods Appl. Vol. **42**, pp. 97 – 137.

Mei, C. C. and Auriault, J. L. (1991) ‘The effect of weak inertia on flow through a porous medium,’ J. Fluid Mech., Vol. **222**, pp. 647 – 663.

Mei, R., Adrian, R.J. and Hanratty, T.J. (1991) 'Particle dispersion in isotropic turbulence under stokes drag and Basset force with gravitational settling,' J Fluid Mech., Vol. **225**, pp. 481 – 495.

Minsky E.M. (1951) 'On the turbulent flow through porous media,' Dokl Acad Nauk SSSR, Vol. **58**(3), pp. 409– 412.

Morad, R. Z. and Khalili, A. (2009) 'Transition layer thickness in a fluid-porous spherical beads,' Exp. Fluids, Vol. 46, pp. 323 – 330.

Moroni, M. and Cushman, J. H. (2001) 'Statistical mechanics with three-dimensional particle tracking velocimetry experiments in the study of anomalous dispersion. II. Experiments,' Phys. Fluids, Vol. **13**, p. 81.

Moutsopoulos, K. N. and Tsihrintzis, V. A. (2005) 'Approximate analytical solutions of the Forchheimer equation,' Journal of Hydrology, Vol. **309**, pp. 93 – 103.

Muskat, M. (1937) 'The flow of homogeneous fluids through porous media,' International Human Resources Development Corporation.

Nield, D. A. and Bejan, A. (2006) 'Convection in porous media,' 3rd edn. Springer, New York.

Neale G. and Nader W. (1974) ‘Practical significance of Brinkman’s extension of Darcy’s law—coupled parallel flows within a channel and a bounding porous-medium,’ Can. J. Chem. Eng., Vol. **52**, pp. 475 – 478.

Northrup, M. A., Kulp, T. J., Angel, S. M. and Pinder, G. F. (1993) ‘Direct measurement of interstitial velocity field variations in a porous medium using fluorescent-particle image velocimetry,’ Chem. Eng. Sci., Vol. **48**, pp. 13 – 21.

Ochoa-Tapia, J. A. and Whitaker, S. (1995a) ‘Momentum-transfer boundary between a porous medium and a homogenous fluid – I. Theoretical development,’ Int. J. Heat Mass Transfer, Vol. **38**, pp. 2635 – 2646.

Ochoa-Tapia, J. A. and Whitaker, S. (1995b) ‘Momentum-transfer boundary between a porous medium and a homogenous fluid –II. Comparison with experiment,’ Int. J. Heat Mass Transfer, Vol. **14**, pp. 2647 – 2655.

Ochoa-Tapia, J. A. and Whitaker, S. (1998) ‘Momentum jump condition at the boundary between a porous medium and a homogenous fluid: inertial effects,’ J. Porous Media, Vol. **1**, pp. 201 – 217.

Ogawa, K., Matsuka, T., Hirai, S. and Okazaki, K. (2001) ‘Three-dimensional velocity measurement of complex interstitial flows through water-saturated porous media by the tagging method in the MRI technique,’ Meas Sci Technol., Vol. **12**, pp. 172 – 180.

Panfilov, M., Oltean, C., Panfilova, I. and Bues, M. (2003) ‘Singular nature of nonlinear macroscale effects in high-rate flow through porous media,’ Comtes Rendus Mecanique, Vol. **331**, pp. 41 – 48.

Peurrung, L. M., Rashidi, M. and Kulp, T. J. (1995) ‘Measurement of porous medium velocity fields and their volumetric averaging characteristics using particle tracking velocimetry,’ Chemical Engineering Science, Vol. **50 (14)**, pp. 2243 – 2253.

Prasad, A. K., (2000) ‘Particle image velocimetry,’ Current Science, Vol. **79** (1), pp. 51- 60.

Raffel, M., Willert, C., Wereley, S. and Kompenhans, J. (2007) ‘Particle image velocimetry. A practical guide,’ 2nd edn. Springer.

Rashidi, M. Peurrung, L., Tompson, A. F. B. and Kulp, T. J. (1996) ‘Experimental analysis of pore-scale flow and transport in porous media,’ Adv Water Resour., Vol. **19**, pp. 163 – 180

Richardson, S. (1971) ‘A model for the boundary condition of a porous material Part 2,’ J Fluid Mech., Vol. **49**, pp. 327 – 336.

Rosenzweig, R. and Shavit, U. (2007) ‘The laminar flow field at the interface of a Sierpinski carpet configuration,’ Water Resources Research, Vol. **43**, W10402.

Rojas, S. and Koplik, J. (1988) ‘Nonlinear flow in porous media,’ Phys. Rev. E., Vol. **58**(4), pp. 4776–4782.

Rubinstein, J. and Torquato, S. (1989) ‘Flow in random porous media: mathematical formulation, variational principles, and rigorous bounds,’ J. Fluid Mech., Vol. 206, pp. 5 – 46.

Rumer Jr., R. R. (1969) ‘Resistance to flow through porous media,’ In: R.J.M. De Wiest, Editor, Porous Media, pp. 91–108.

Ruth, D. W. and Ma, H. (1992) ‘On the derivation of the Forchheimer equation by means of the averaging theorem,’ Transp. Porous Med. Vol. **7**, pp. 255 – 264.

Saffman, P. G. (1971) ‘On the boundary condition at the surface of a porous medium’, Studies in Applied Math, Vol. **50**, pp. 93 - 101.

Sahraoui, M. and Kaviany, M. (1992) ‘Slip and no-slip conditions at interface of porous, open media,’ ASME / JSME Thermal Engineering Proceedings, Vol. **4**, pp 273 – 286.

Saleh, S., Thovert J.F. and Adler, P.M. (1993) ‘Flow along porous-media by partial image velocimetry,’ AIChE J., Vol. **39**, 1765 – 1776.

Sangani, A. S. and Acrivos, A. (1982) ‘Slow flow past periodic arrays of cylinders with application to heat transfer,’ Int. J. Multiphase flow, Vol. **8**, pp. 193 – 206.

Scheidegger, A. E. (1960) ‘The physics of flow through porous media,’ University of Toronto Press.

Scarano F. and Riethmuller M. L. (1999) ‘Iterative multigrid approach in PIV image processing with discrete window offset,’ Exp. Fluids, Vol. 26(6), pp. 513 - 523.

Shams, M., James, D. F. and Currie, I. G. (2003) ‘The velocity field near the edge of a model porous medium,’ Exp. Fluids, Vol. **35**, pp. 193 – 198.

Shavit U., Bar-Yosef, G., Rosenzweig, R. and Assouline S. (2002) ‘Modified Brinkman equation for a free flow problem at the interface of porous surfaces: the Cantor–Taylor brush configuration case,’ Water Resour. Res. Vol. **38**(12), pp. 1320 – 1334.

Shavit U., Bar-Yosef, G., Rosenzweig, R. and Assouline S. (2004) ‘Free flow at the interface of porous surfaces: A generalization of the Taylor brush configuration,’ Transp Porous Med., Vol. **54**(3), pp. 345 - 360.

Skjetne, E. and Auriault, J. L. (1999) ‘New insights on steady non-linear flow in porous media,’ Eur. J. Mech. B/Fluids., Vol. **18**(1), pp. 131 – 145.

Skjetne, E., Hansen, A. and Gudmundsson, J. S. (1999) ‘High-velocity flow in a rough fracture,’ J. Fluid Mech., Vol. **383**, pp. 1 – 28.

Slepicka, F. (1961) 'Hydraulic function of cylindrical well in an artesian aquifer with regard to new research on flow through porous media,' IAHR, 9th Congr. Dubrovnik, p. 395.

Spena, F. R. and Vacca, A. (2001). 'A potential formulation of non-linear models of flow through anisotropic porous media,' Transp. Porous Med., Vol. **45**, pp. 405 – 421.

Stanley, H. E. and Andrade Jr., J. S. (2001) 'Physics of the cigarette filter: fluid flow through structures with randomly-placed obstacles,' Physica A., Vol., **295**, pp. 17 – 30.

Stephenson, J. L. and Stewart, W.E. (1986) 'Optical measurements of porosity and fluid motion in packed beds,' Chem. Eng. Sci., Vol. **41**, pp. 2161 - 2170.

Stern, F., Muste, M., Beninati, M, Eichinger, W.E. (1999) 'Summary of experimental uncertainty assessment methodology with example,' IIHR Technical Report No. 406.

Tachie, M. F., James, D. F. and Currie, I. G. (2003) 'Velocity measurements of the shear flow penetrating a porous medium,' J. Fluid Mech., Vol. **493**, pp. 319 – 343.

Tachie, M. F., James, D. F. and Currie, I. G. (2004) 'Slow flow through a brush,' Phys. Fluids, Vol. **16**, pp. 2 – 7.

Tam, C. K. W. (1969) 'The drag on a cloud of spherical particles in low Reynolds number flow,' J. Fluid Mech., **38**, pp. 537–546.

Tamayol, A. and Bahrami, M. (2011) ‘Transverse permeability of fibrous porous media,’ Physical Review E **83**, pp. 046314-1 – 046314-9.

Taylor, G. I. (1971) ‘A model for the boundary condition of a porous material. Part 1,’ Fluid Mech., Vol. **49**, pp. 319 – 326.

Vafai P. C. and Tien (1981) ‘Boundary and inertia effects on flow and heat transfer in porous media,’ Int. J. Heat Mass Transfer, Vol. **24**, pp. 195 - 203.

Vafai, K. and Kim, S. (1990) ‘Fluid mechanics of the interface region between a porous medium and a fluid Layer- an exact solution,’ Int. J. Heat Mass Transfer, Vol. **11**, pp. 254 - 256.

Vafai, K. and Thyagaraja, R. (1987) ‘Analysis of flow and heat transfer at the interface region of a porous medium,’ Int. J. Heat Mass Transfer Vol. **30**, pp. 1391 – 1405.

Van Batenburg, D. and Milton-Taylor, D. (2005) ‘Discussion of SPE 89325, ‘Beyond beta factors: a complete model for Darcy, Forchheimer, and Trans-Forchheimer flow in porous media,’ J. Pet. Tech., pp. 72 – 73.

Vafai, K. and Tien, C. L. (1981) ‘Boundary and Inertia Effects on Flow and Heat Transfer in Porous Media,’ Int. J. Heat Mass Transfer, Vol. **24**, pp. 195 - 203.

Vafai, K. and Tien, C. L. (1982) ‘Boundary and inertia effects on convective mass transfer in porous media,’ Int. J. Heat Mass Transfer, Vol. **25**, pp. 1183 - 1190.

Valdés-Parada, F. J., Alvarez-Ramírez, J., Goyeau, B. and J. A. Ochoa-Tapia, 'Computation of jump coefficients for momentum transfer between a porous medium and a fluid using a closed generalized transfer equation,' Transp. Porous Med.,Vol. **78**, pp. 439 - 457.

Wang, P., Balay, S., Spernhoori, K., Wheeler, M., Abate, J., Smith, B. and Pope, G. (1999) 'A fully implicit parallel EOS compositional simulator for large scale reservoir simulation,' In: Proceedings of 15th SPE Symposium on Reservoir Simulation, Houston, TX, SPE, pp. 63-71.

Westerweel, J. (1996) 'Measurement of fully developed turbulent pipe flow with digital particle image velocimetry,' Exp. Fluids, Vol..**20**, pp.165 – 177.

Whitaker, S. (1986) 'Flow in porous media I: a theoretical derivation of Darcy's law,' Transp. Porous Med., Vol. **1**, pp. 3–25.

Whitaker, S. (1996) 'The Forchheimer equation: a theoretical development,' Transp. Porous Med., Vol. **25**, pp. 27 – 62.

Whitaker, S. (1999) 'The method of volume averaging,' Dordrecht: Kluwer Academic Publishers.

White, A. M. (1935). Transactions of the American Institute of Chemical Engineers, Vol. **31**, 390 in: J. Bear, Dynamics of fluid flow through porous media. New York: Dover.

Wilkinson, J. K. (1956) ‘The flow of water through rockfill and application to the design of dams,’ Proc. 2nd Australia-New Zealand Conf. on Soil Mechanics and Foundation Engineering p. 141.

Willert, C. E. and Gharib, M. (1991) ‘Digital particle image velocimetry,’ Exp. Fluids. Vol. **10**, pp. 181 – 193.

Woodié , J. C. and T. Levy, T. (1991) ‘Correction non linéaire de la loi de Darcy,’ C. R. Acad. Sci. Paris II312, pp. 157–161.

Wooding, R. A. (1957) ‘Steady-state free thermal convection of liquid in a saturated permeable medium,’ J. Fluid Mech., Vol. **2**, pp. 273 – 285.

Yarlagadda, A. P. and Yoganathan, A. P. (1989) ‘Experimental studies of model porous media fluid dynamics,’ Exp. Fluids, Vol. **8**, pp. 59 – 71.

Zhong, W. H., Currie, E. I. G. and James, D. F. (2006) ‘Creeping flow through a model fibrous porous medium,’ Exp. Fluids, Vol. **40**, pp. 119 – 126.

Appendix A

Principles and Implementation of Particle Image Velocimetry

A.1 Introduction

This is an overview of the particle image velocimetry (PIV) technique is given. While this overview provides information particularly related to the PIV system used in the research program readers may refer to the manual provided by Dantec Dynamics for a more comprehensive layout of the system. This outline (adapted from Arthur 2008) presents aspects such as the tracer particles, light sources, image recording media, image analysis methods, and some precautions taken to ensure optimization of measurements.

A.2 The PIV Technique

PIV is an optical technique that allows for the quantitative measurement of whole flow fields instantaneously in two or three dimensions. Figure A.1 shows a schematic diagram of a typical experimental arrangement of a PIV system for the two-dimensional velocity measurement of a flow field. The set-up is made up of a number of components. The components are: tracer particles in a flow, a light source (*e.g.* a laser) and an image recording medium (*i.e.* a camera). As shown, there are other systems used for the synchronisation of the camera and laser pulses (*e.g.* synchronising hub), the evaluation the data images, and post-processing of the data acquired (*e.g.* a computer with image acquisition software). The specific components of the PIV technique used in this work are described in Chapter 3.

The PIV technique is premised on the assumption that the tracer particles in the flow whose velocity is really being measured, faithfully follows the fluid flow. In a typical PIV system, a plane of flow seeded with tracer particles is illuminated twice within a short interval of time by means of a laser. The particles scatter the light, and this is in turn recorded on frames of a camera. The displacements of the particle images between the intervals of light pulses are calculated from the positions at the two instances of time by statistical methods. The velocity is then computed using the time delay between the two illuminations, and the imaging magnification.

Unlike other techniques of measurements where probes such as pressure tubes and hotwires are required to complete measurement, PIV allows for the study of flows in a relatively non-intrusive manner. The tracer particles have properties such as to enable the flow measurements without any disturbance. Furthermore, current developments of PIV technique make it possible for large portions of flow fields to be measured instantaneously and yet with optimum temporal and spatial resolution. For a more detailed overview of the technique, the reader is directed to a practical guide by Raffel *et al.* (2007).

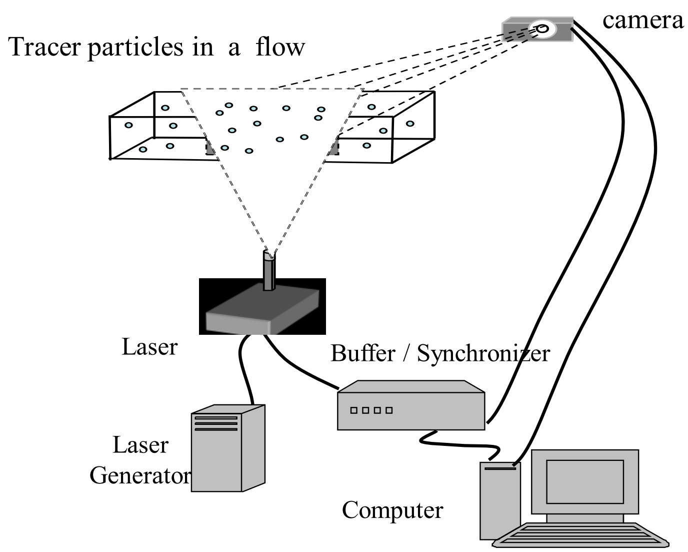

Figure A. 1: A typical PIV experimental set-up for the two-dimensional velocity measurement of a flow field.

A.3 Tracer Particles

In PIV, the hydrodynamic and optical properties of the tracer particles are critical to ensure high accuracy in measurement. This is because the fluid flow is measured indirectly by measuring the velocity of tracer particles themselves within the flow.

Using Stokes' drag law to model the behaviour of a particle under acceleration, for a spherical particle in a viscous fluid at a Reynolds number less than unity, the settling velocity v_s induced due to the difference in the tracer particle density, ρ_p, and the fluid density, ρ_f. is given by (Mei *et al* 1991):

$$v_s = \frac{(\rho_p - \rho_f) g d_p^2}{18\mu} \tag{A.1}$$

The parameter g is the gravitational acceleration, d_p is the particle diameter, and μ is the dynamic viscosity of the fluid. As this velocity is undesirable (being a result of the influence of gravitational force when ρ_p and ρ_f are mismatched.), one important precaution to be taken is that the particles are neutrally buoyant in the fluid. The ability of the particle to follow the flow is measured in terms of a response time parameter, τ_R This is governed by Stokes law, and also expressed as (Westerweel *et al*. 1996):

$$\tau_R = \frac{\rho_p v_s g d_p^2}{18\mu} \tag{A.2}$$

From this equation, it is readily observed that to ensure that, τ_R is small enough to faithfully follow the flow, the particles must be sufficiently small. However, it must also be large enough to scatter light sufficiently to be detected by the camera.

These light scattering properties of a tracer particle are on the other hand subject to the particle size, shape, and orientation, the refractive index of the particles to that of the surrounding medium, and the wavelength of radiation.

Some of the seeding particles available commercially are silver-coated hollow glass spheres, hollow glass spheres, polyamide seeding particles, and fluorescent polymer particles.

A.4 Light Source

In PIV, the flow field needs to be illuminated with light of sufficient intensity to scatter light which can be recorded by the camera. This is done using a suitable light source that is pulsed so that the seeding particles and flow field do not move significantly during the light-pulse exposure.

Lasers are widely used in PIV techniques to illuminate the flow region. They find ready application in this technique because they are able to emit monochromatic light at high intensity, which is converted into a thin sheet of light without chromatic aberrations. A laser system basically consists of a laser material, a pump source, and a mirror arrangement. The laser material is excited by the pump source by the introduction of electro-magnetic or chemical energy to generate a sheet of light. The mirror arrangement allows the thickness and orientation of the light sheet to be adjusted. Lasers can be classified as gas lasers (*e.g.* Helium-neon lasers, Copper-vapour lasers, Argon-ion lasers), or semiconductor / solid-state lasers (*e.g.* Ruby lasers, Neodymium: yttrium-aluminium-garnet *i.e.* Nd:YAG lasers) based on the type of laser material. These lasers have atomic or molecular gas laser materials, and are continuous wave types, suitable for applications in low-speed water flows. The semiconductor / solid-state lasers in particular are able to produce high quality beams, have high power efficiency and high amplification.

A.5 Image Recording Media

The initial and final positions of tracer particles scattering light in the field of flow are recorded with a camera. Recording is either captured altogether by a single frame method, or by a multi-exposure means (in which there is an illuminated image per illumination pulse).

For the single frame method, because the particle images are recorded onto one frame, there is no retention of information regarding the temporal order of the illumination pulse. This leaves the displacement vector with directional ambiguity which must be accounted for by the use of additional schemes (such as image shifting), and necessitates a time-consuming iteration procedure for image optimization and processing.

The multi-frame exposure PIV recording method however results in the retention of the temporal order of the particle images. The evaluation procedure associated with this method is also much easier to handle. That explains why it is currently the preferred method for image recording. Modern technological developments in electronic imaging in multi-frame recording now allow for immediate feedback and optimization of image quality during the experiment. The most widely used PIV multi-frame recording device is the charge-coupled device (CCD) camera. This type of camera is particularly noted for its production of highly spatially resolved images, its capacity to enable PIV recordings do be done in a way that the recordings are temporarily spaced by microseconds, and its ability to give instantaneous digital signals of the image map of the particle positions for possible online analysis.

Perhaps, the most important component of a CCD based camera is the sensor. There are two types of CCD sensors, namely: full-frame-transfer CCD and interline transfer CCD sensors. In either of these types however, the sensors typically consist of a two-dimensional array of light sensitive picture detectors called pixels. Each pixel is a capacitor, charged by the photons of light converted into electric charge as light is incident on it. The electric charge is proportional to the photon flux incident on the pixel, and the time interval of flux exposure. This charge is transformed to a read-out voltage observed on the PIV image map as a distribution in grey scale.

CCD sensors have another set of cells called storage cells that is quite different from the pixels. Unlike pixels, these storage cells are not exposed to light. However, the storage cells work in close relation with the pixels. Laser pulse and the camera frames are synchronised in such a way that the first laser pulse is timed to expose the first frame. The charge of the light-sensitive cells of the frame is then transferred to the storage cells after the laser pulse. At the second laser pulse the second frame is exposed. The first and the second frames are then transferred in a sequential manner to the camera outputs within a time interval of ~ 0.5 to 1 milliseconds (Agelinchaab 2005) or even less than 1 microsecond (Agelin-Chaab 2010).

A.6 Image Analysis

Each camera frame bears image of particles that is sub-divided into rectangular regions called interrogation areas (IA). The images that are recorded sequentially per impulse of laser radiation are correlated within each IA. This correlation involves a statistical evaluation of the average spatial shift in corresponding images, as described in Figure A.2.

In the linear signal processing model of Figure A.2, the functions a and d of pixel coordinates (x, y) represent the known functions of light intensities within an IA recorded at times t and $t + \Delta t$. What needs to be determined is the spatial shift (displacement) function b(x, y) that exists in the presence of a noise function c(x, y). To do this efficiently, fast Fourier transformation (FFT) processes are used in the correlation evaluation, so that the two-dimensional field of the camera image is made analogous to a time series in one dimension. It should be noted that in the figure, Fourier transforms are represented by upper case functions of the corresponding lower case functions in the spatial frequency domain coordinates (u, v). The transforms A(u, v) and D(u, v) reduce the summation of elements of the sampled region to something of a complex conjugate multiplication of each corresponding pair of Fourier coefficients. The resultant coefficient function, Φ_{ad} is then transformed to obtain the correlation function ϕ_{ad}. Using the location of the displacement peak on the correlation plane and the time between laser pulses, the velocity vector in the IA is then evaluated. For an array of IAs, a velocity map is generated by processing images similarly over that array. This numerical processing of images is typically done using commercially developed softwares such as DynamicStudio v.2.30 (by Dantec Dynamics).

There are two basic correlation methods are commonly used in estimating the spatial shift function. These are auto-correlation and cross-correlation methods. The auto-correlation method is not able to support the separation of particle positions on distinct frames of camera. Thus an image recorded on a camera frame is correlated with a spatially shifted version of itself, resulting in a large central peak in the correlation plane and two displacement peaks. The average particle displacement in the IA is obtained from the distance from the self-correlated central peak to either of the displacement peaks. As auto-correlation is a result of a self-correlation of particle images, particle displacements less than 2 – 3 pixels are not detected, and this reduces the range of a particle displacement over sub-pixel resolution (*i.e.*, the dynamic range). Furthermore, because of the nature of this method of correlation process, there is directional ambiguity in the particle images. This makes it difficult to apply this correlation to flow applications in which eddies are expected. The problems of dynamic range and directional ambiguity may however be resolved using special cameras that have the capacity to shift the image of the particles on the CCD-chip in the interval between the first and second exposure. Nonetheless, a better option for the correlation of images that ensures complete separation of consecutive camera images with high resolution is the cross-correlation technique.

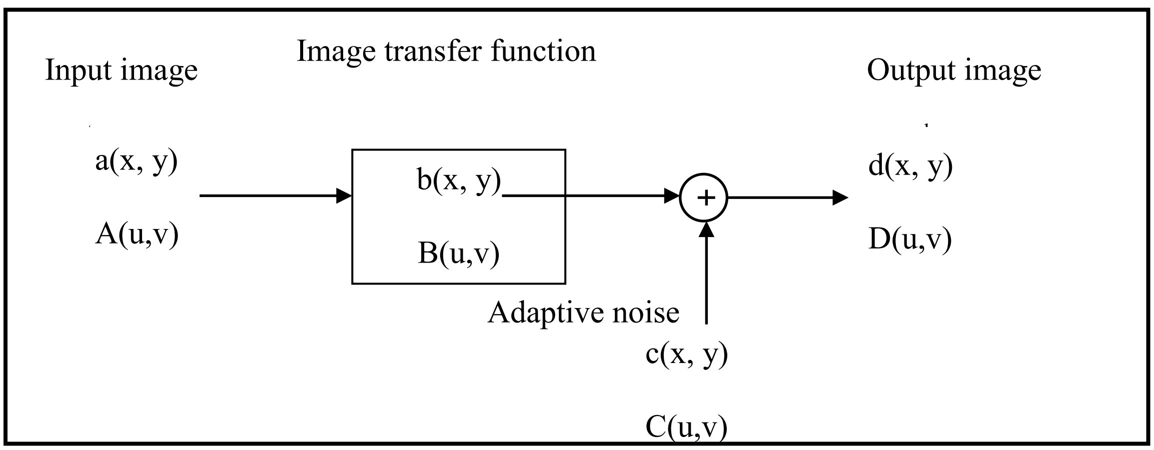

Figure A. 2: This is a linear model of an image displacement function (Raffel *et al*. 2007). The denominations x and y are respectively used to describe coordinates in the streamwise and transverse directions.

While the cross-correlation technique is applied to a single exposure / multiple (double) frames by sampling two interrogation windows from the image recordings, the auto-correlation technique is applied to single frame / double exposure recordings by using interrogation windows of different sizes and / or slightly displaced from each other. In either case however, at time $t = t_0$ and at $t = t_0 + \Delta t$ the input signals of first and the second images are recorded. The spatial shift functions are obtained by the use of FFT algorithms. As the calculation of correlations by means of FFT results in a cyclic noise at the edges of an IA, particle images at the edges have no corresponding pair. To reduce this, functions as overlapping of interrogation areas are employed to make use of all the information near the edges of the IA. In PIV, it is also recommended that particle image displacements be less than a quarter of the IA (Prasad 2000) because large relative displacements results in a reduction in the signal to noise ratio.

When many particle images in the first frame match with corresponding spatially shifted images in the next frame, high correlation values (called true correlations) result. Likewise small correlation values (or random correlations) are present when only individual particles match with other particles in a second frame. The correlations in the latter case occur because of seeding particles leaving an IA between the first and second image recordings. This phenomenon is called ‘loss-of-pairs’. Random correlations lead to a decrease in signal-to-noise ratio. In applying the cross-correlation method, a sufficiently large match of particle pairs is required to provide a satisfactory peak in the correlation plane. The position of the peak gives the average displacement of the particle within the IA.

Comparing the two basic methods of correlation, the following remarks may be made (Further details may be seen in Raffel *et al* 2007 and Willert and Gharib 1991). As already mentioned, the cross-correlation technique is superior to the autocorrelation technique. It is typically characterised by a higher dynamic range and no directional ambiguity. Furthermore, the cross-correlation technique places less demands on the number of particles required per IA. While autocorrelation techniques may require 10 particles per IA to obtain satisfactory results, cross-correlation requires only 6 (Keane and Adrian, 1992). It should be added that although calculations in the cross-correlation technique are more complex and time-consuming, those computational challenges are usually overcome by using computers of high speed and memory.

Another preferred method of correlation is the adaptive correlation. It is a special iterative type of cross-correlation, and it depends on the use of a guessed velocity spatial distribution. This initial guess is used to introduce an offset from the first IA. (*i.e.,* the IA in the image frame from the first laser pulse) to the second IA (*i.e.* the IA in the image frame from the second laser pulse). The resultant vector is validated, and then used as an input to estimate another IA offset. The process is thus repeated, but with a subsequently smaller window. The iteration continues until a convergence criterion is reached. As the iterative process associated with the adaptive correlation leads to an increase in signal strength, this correlation technique has some characteristics superior to other conventional correlation methods. More vectors are successfully recovered (and not lost through loss of pairs) for a given seed density of the flow. Furthermore, there is consequential decrease in the size of the IA, improving the spatial resolution of the IA. To obtain a high valid detection probability for an adaptive correlation technique, the number of particle images per IA is to be only 3 or more (Keane and Adrian 1992).

A.7 Post-Processing of Data from PIV Measurements

The data obtained from PIV measurements is usually huge, and requires fast reliable and fully automated post-processing to facilitate interpretation. This post-processing is usually accomplished by data validation, replacement of incorrect data, data reduction, further data analysis and presentation of results.

Upon evaluation of correlations, wrongly determined vectors (or outliers – vectors which have a signal to noise ratio is less than unity) are usually apparent by a visual inspection of the raw data. While outliers may be treated interactively for a small number of PIV recordings, for a large number of PIV recordings, this interactive treatment is not realistic. Such cases are therefore treated by means of an automatic algorithm with a high level of confidence, so that no questionable data is stored in the final data set. For cases of less than 5% outliers (under extremely challenging experimental conditions; Raffel *et al*, 2007), it is acceptable to recover erroneous data by using a replacement scheme, such as bilinear interpolation of valid neighbouring vectors. To facilitate the thorough inspection of vectors, techniques such as averaging, conditional sampling and vector field operators are usually applied. The PIV data may then be further analysed, and then presented in the form of plots which are easily appreciable. Post-processing of PIV data can be done using commercially available software such as DynamicStudio, MATLAB (technical computing software developed and supplied by the MathWorks) and OriginPro (data analysis and graphing software by OriginLab).

A.8 Optimizing PIV Measurements

As the best of experimental conditions are still subject to outliers in its PIV vector map, optimization of PIV measurements is necessary so as to reduce outliers. To do this, such parameters as measurement of the particle diameter, laser energy, light sheet dimensions, intervals between images, camera magnification and focal ratio ought to be carefully controlled. To ensure optimal optical assess, the flow section must be refractive index-matched with the working fluid. Further to this, to optimise hydrodynamic and optical properties, the particle to be chosen must with density similar to the fluid density but large and polished enough to scatter light.

It is recommended that to improve signal to noise ratio of vectors from a PIV measurement, an IA should be large enough to accommodate enough particles, but small enough so that a vector describes the flow (Keane and Adrian 1990). Furthermore, to make corresponding particle image pairs separable, it has also be prescribed that the particles be allowed to travel more than one particle image diameter $d_{\tau,}$ given by (Keane and Adrian 1990)

$$d_\tau = \left[\frac{d_p^2}{S^2} + \left(2.44 \left(1 + \frac{1}{S} \right) f_{\#} \lambda \right)^2 \right]^{1/2} \tag{A.3}$$

where d_p is particle diameter, S is the object to image scale factor (also defined as the inverse of the magnification factor of the lens arrangement of the camera). The focal ratio of the camera, denoted by $f_{\#}$, is the diaphragm aperture. The aperture controls the light per unit area that is admitted into the image plane of the system. Light per unit area reaching the image plane of the system reduces as $f_{\#}$ increases. The laser light wavelength is denoted by λ.

The particle image diameter should be appropriately small. According to Raffel *et al.* (1998) it becomes too small there will be insufficient information to utilize in sub pixel interpolation (sub pixel interpolation is a phase in data correlation intended to increase accuracy in detecting the location of the correlation peak by fractions of a pixel). This is because there is a tendency for the data to be biased towards integer pixel values. One notable error caused by a wrong estimate of the sub-pixel interpolation is called peak locking. It has a periodic pattern on pixel intervals. To minimize this, the particle image diameter is recommended to be 2.0 pixels (Raffel *et al*. 2007) for minimizing peak locking. Figure A3 shows typical histograms that show cases of minimized peak locking, as maintained in the present experiments.

(a)

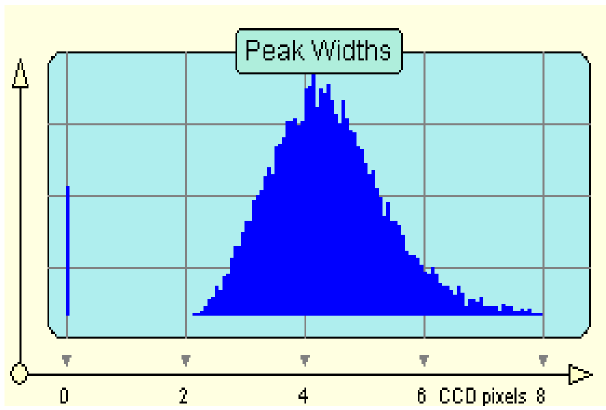

(b)

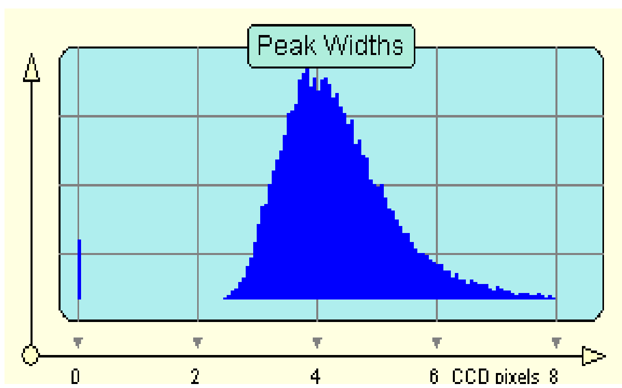

Figure A. 3: Typical histogram of peak widths for flow (a) through a free zone, and (b) through and over a $\phi = 0.12$ vertical model porous media to demonstrate lack of peak locking. This is captured for flow through a mesh mode.

For an image magnification M, and a minimum velocity, u_{min}, the minimum time interval between images is given by:

$$\Delta T \geq \frac{d_\tau}{M u_{\min}} \tag{A.4}$$

Using Equation (A.4), appropriate time intervals can therefore be carefully controlled to ensure that particle displacements are less than a quarter of IA.

The average number of particle images within a square IA of window size I and for a light sheet thickness of Δz is given as

$$N_I = \frac{CI^2 \Delta z}{M^2} \tag{A.5}$$

where C is the number of particles per unit fluid volume.

Appendix B

Uncertainty Analysis

B.1 Overview

As this report focuses on measurements of the streamwise velocity u, transverse velocity v, and average differential pressure measurements ΔP, it was needful that the uncertainties regarding these quantities be evaluated. To assess the uncertainty in u (*i.e.* E_u), v (*i.e.* E_v), and in ΔP measurements (*i.e.* $E_{\Delta P}$), the bias and precision errors were identified and then quantified. This was done by evaluating the measurement chain based on the methodologies outlined by Coleman and Steele (1995), Stern *et al*. (1999), Forliti *et al.* (2000), Gui *et al.* (2001) and Adeyinka and Naterer (2005).

B.2 Velocity Measurements

The bias component of E_u was first estimated, taking into consideration that the limitations on the accuracy of velocity measurements brought about by such factors as the particle response to fluid motion, light sheet positioning, velocity gradient, light pulse timing, the size of IA, the sub-pixel interpolation of the displacement correlation peak and insufficient sample size (Arthur 2008; Agelin-Chaab 2010). Many of these limitations were however expected to be minimized by the precautionary measures outlined in section 3.3.1. The elements of the velocity bias limits were identified as the resolutions of the image, the CCD camera chip, time interval between laser pulses, and the particle displacement (Agelinchaab 2005). These have been respectively denoted by Lo, L_I, Δt, and Δs. Using the following equation, the bias limit of the measured velocity, B_u was then determined

$$B_u{}^2 = \theta_L{}^2 B_L{}^2 + \theta_{L^I}{}^2 B_{L^I}{}^2 + \theta_{\Delta s}{}^2 B_{\Delta s}{}^2 + \theta_{\Delta t}{}^2 B_{\Delta t}{}^2 \tag{B.1}$$

where the sensitivity coefficients, $\theta_X = \partial u_i/\partial X$, for $X = Lo$, L_I, Δt, Δs. Typical assessments for bias limits of u have been outlined in Tables B.1 and B.2.

The precision limit of the measured time-averaged streamwise velocity, P_u was statistically evaluated from

$$P_u = \frac{K}{n^{0.5}}\sigma = \frac{K}{n^{0.5}}\left[\frac{1}{n-1}\sum_{k=1}^{n}\left(u_k - \left(\frac{1}{n}\sum_{k=1}^{n}u_k\right)\right)^2\right]^{0.5} \tag{B.2}$$

where K is the confidence coefficient, and σ the standard deviation of the measurements. The coefficient K has a value of 2 for a 95% confidence level for n = 15 experiments to measure of velocity at the same location (Adeyinka and Naterer 2005).

The value of the total uncertainty E_u was computed from the square root of the sum of the squared bias and precision errors, *i.e.*,

$$E_u = \sqrt{(B^2{}_u + P^2{}_u)} \tag{B.3}$$

They were estimated to be 1% of the maximum velocity, u_{max} in the free zone, and 1.5% of u_{max} within porous media of $\phi = 0.03$ and 0.06. Due to the presence of etches on the rod surfaces, the increase in solid volume fraction of the porous media was attended with a reduction in optical assess. This, together with the record of low velocities within the porous medium contributed to considerable increments in precision errors of the measured velocities as the solid volume fraction increased. Therefore, for the streamwise velocities of flow through model porous media of $\phi = 0.12$, 0.22 and 0.49, the total uncertainties are approximately 2.5%, 4% and 5% respectively of u_{max}.

The total uncertainties of the transverse velocities E_v, were also similarly determined (as discussed above) and found to be approximately 1% of u_{max} in the free zone and in porous medium of $\phi = 0.03$ and 0.06; and 2%, 3% and 3.5% of u_{max} in model porous media of $\phi = 0.12$, 0.22 and 0.49 respectively.

Table B.1: A typical assessment of the bias limit of u in free zone flow.

Variable	Magnitude	B_X	θ_X	$B_X\theta_X$	$(B_X\theta_X)^2$
Lo (m)	2.72 E-02	5.00 E-04	8.63 E -01	4.32 E -04	1.86 E-07
L_I (pix)	2.05 E+03	5.00 E-01	-1.14 E -05	5.72 E -06	3.28 E-11
Δt (s)	2.30 E -03	1.00 E-07	-1.02 E 01	1.02 E -06	1.04 E-12
Δs (pix)	4.07 E 00	1.27 E-02	5.77 E-03	7.32 E-05	5.36 E-09
u (m/s)	2.34 E -02				
					$\sum(B_X\theta_X)^2$ = 1.92 E-07
					B_u = 4.38 E -04

Table B.2: A typical assessment of the uncertainties of u in porous medium for flow through and over $\phi = 0.22$ horizontal sample.

Variable	Magnitude	B_X	θ_X	$B_X\theta_X$	$(B_X\theta_X)^2$
Lo (m)	2.72 E-02	5.00 E-04	4.40 E -02	2.20 E -05	4.83 E-10
L_I (pix)	2.05 E+03	5.00 E-01	-5.83 E -06	2.92 E -07	8.50 E-14
Δt (s)	4.20 E -03	1.00 E-07	-2.84 E -01	2.84 E -08	8.08 E-16
Δs (pix)	3.78 E -01	1.27 E-02	3.16 E -03	4.01 E-05	1.61 E-09
u (m/s)	1.19 E -03				
					$\sum(B_X\theta_X)^2$ = 5.56 E-09
					B_u = 7.46 E -05

B.3 Differential Pressure Measurements

The bias component of the pressure measurement was assessed using a methodology similar to that used for the velocity uncertainties. As the measurement of the differential pressure was only limited by the pressure transducer, the relative bias error, as provided by the manufacturer was used. The relative bias error due to the pressure transmitter, $B_{r\Delta P} = B_{\Delta P} / \Delta P = 0.25\%$. The precision limit of the pressure measurement $P_{\Delta P}$, was also assessed statistically. Using a similar equation as (B.2),

$$P_{\Delta P} = \frac{K}{n^{0.5}}\sigma = \frac{K}{n^{0.5}}\left[\frac{1}{n-1}\sum_{k=1}^{n}\left(\Delta P_k - \left(\frac{1}{n}\sum_{k=1}^{n}\Delta P_k\right)\right)^2\right]^{0.5} \qquad \text{(B.4)}$$

where K is the confidence coefficient and σ the standard deviation. Using n = 11 repeated experiments for this evaluation, the relative precision error in pressure measurement, $P_{r\Delta p} = P_{\Delta P} / \Delta P$ is estimated to be 3% at 95% confidence level

The value of the total uncertainty $E_{\Delta P}$ was computed from the square root of the sum of the squared bias and precision errors, *i.e.,*

$$E_{\Delta P} = (B_{\Delta P}{}^{2} + P_{\Delta P}{}^{2})^{05} \qquad \text{(B.5)}$$

and estimated to be 3% of the average pressure measurement.

B.4 Combined Error Assessments

To compute the errors propagated in the calculation of any parameter *R* made up of independent variables $x_1, x_2, \ldots x_n$, with corresponding relative uncertainties of $u_1, u_2, \ldots u_n$, the following relative uncertainty expression was used (Fox *et al.* 2004):

$$u_R = \sqrt{\left[\left(\frac{x_1}{R}\frac{\partial R}{\partial x_1}u_1\right)^2 + \left(\frac{x_2}{R}\frac{\partial R}{\partial x_2}u_2\right)^2 + \ldots + \left(\frac{x_n}{R}\frac{\partial R}{\partial x_n}u_n\right)^2\right]} \quad \text{(B.6)}$$

Appendix C

Supplementary Figures

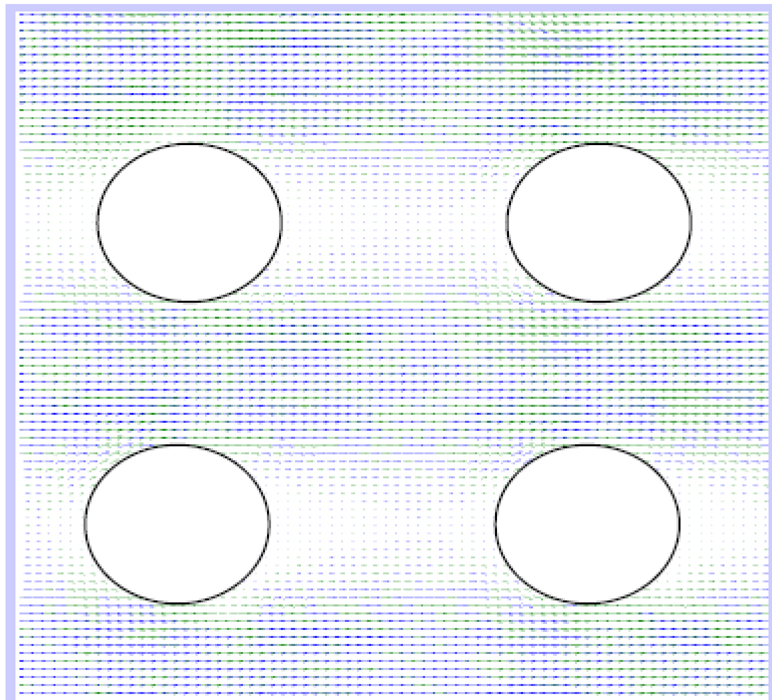

Figure C. 1: Typical PIV vector map of measurements.

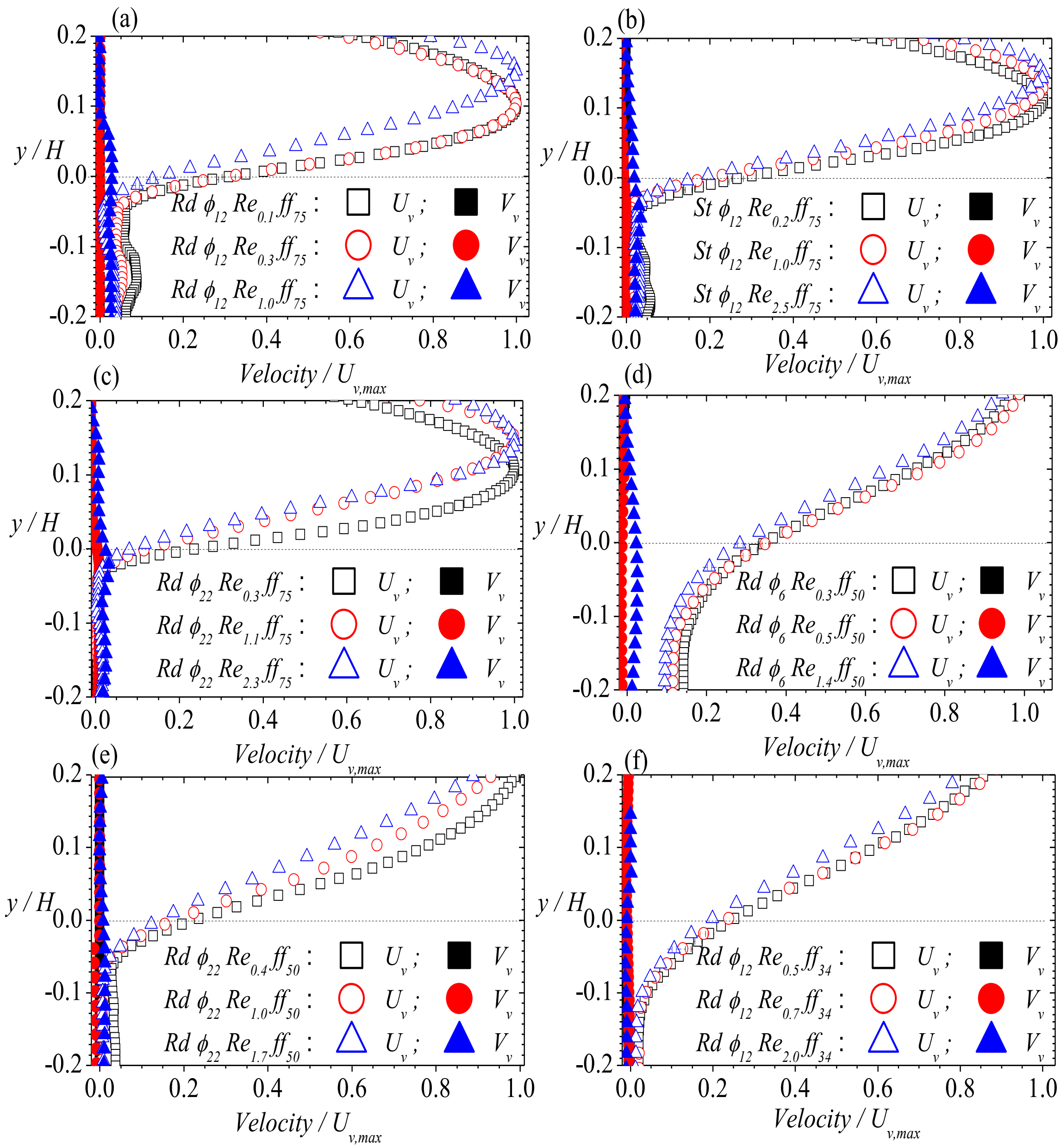

Figure C. 2: The relative magnitudes of volume averaged streamwise (U_v) and transverse (V_v) velocities for selected test conditions, showing effects of Reynolds number.